Analysis of human locomotion using analytic wavelets applied to electromyographic data from healthy controls and Parkinson's patients

Sopapun Suwansawang

PhD

University of York
Electronic Engineering

August 2018

Abstract

Human locomotion is controlled by the dynamic interaction between the human brain and spinal cord. An understanding of the basic control strategies and paradigms of normal locomotion could provide opportunity to understand and help characterise early stages of movement disorders such as Parkinson's disease. Locomotion is a stereotyped action and highly non-stationary which needs time-varying analyses. Analytic wavelets provide a powerful time-frequency analysis framework for studying time-varying properties of non-stationary neurophysiological signals, and are used in this thesis. A unified framework, which includes coherence, phase locking value (PLV), and time-resolved phase-amplitude coupling (tPAC) using generalized Morse wavelets, is developed to analyse electromyographic (EMG) recordings obtained from leg muscles during treadmill and overground walking in healthy controls and Parkinson's disease (PD) patients. A novel technique applied to coherence and PLV for removal of low frequency components due to EMG envelope modulation is then proposed. All measures have successfully been applied to three data sets, healthy human treadmill walking and human overground walking including a comparison of control subjects and PD patients. All measures provide a clear description of data from healthy treadmill locomotion. In comparison, more variability in time and frequency values are observed in analysis of overground walking data sets. The results provide new insights into the rhythmic control of locomotion in health and disease. Significant differences in features between healthy subjects and PD patients are observed in 12-20 Hz frequency range for all measures. The results from our novel technique for removal of low frequency EMG envelope modulation confirm the expectation for separating physiological mechanisms from effects due to low frequency envelope modulation of surface EMG during walking. Our results suggest that a combination of these measures could be suitable for investigating and characterising non-stationary neurophysiological data, and might be important for understanding the basic principles of human locomotion in health and disease.

Contents

List of Figures

List of Tables

Acknowledgements

I would like to acknowledge the support of the Royal Thai government scholarships (Ministry of science and technology) and Nakhon Pathom Rajabhat University, Thailand.

I wish to express my sincere gratitude to my supervisor, Dr David M Halliday, for providing me very useful advices, guidance and explanations in both the fields of neuroscience and signal processing.

I am very much thankful to Prof. Dr Natasha Maurits and Joyce Weersink, for their assistance with data collection, and their feedback on data interpretation.

I am also thank you to all Thai York friends, particularly those that have made my time in the UK more pleasant.

I will never express enough gratitude to my family and my close friends for their unconditional love, endless support and inspiration.

Declaration

I declare that this thesis is a presentation of original work and I am the sole author. This work has not previously been presented for an award at this, or any other, University. All sources are acknowledged as References.

Some parts of this thesis have been published in conference proceedings as follow:

- Suwansawang, S. and Halliday D.M., Time-frequency based Coherence and Phase Locking Value Analysis of Human Locomotion Data using Generalized Morse Wavelets. In *Proceedings of the 10th International Joint Conference on Biomedical Engineering Systems and Technologies (BIOSTEC 2017) - Volume 4: BIOSIGNALS*, pages 31-41, Porto, Portugal, February 21-23, 2017.

Chapter 1

Introduction

1.1 Motivation

Locomotion is the fundamental motor act that allows all vertebrates, including humans, to move from one place to another (Kandel et al. 2000). Locomotion can take many different forms of motor act such as flying, swimming, or walking. The motor act is required for survival such as finding food, escaping danger, and migrating to suitable environments (Kiehn & Dougherty 2013). Locomotor movements are produced by the nervous system that is controlled by the dynamic interaction between central pattern generator circuits located in the spinal cord, sensory feedback, and descending supraspinal control (Kandel et al. 2000). An understanding of the basic principles of normal locomotion can provide insight into pathological locomotor deficits.

Human movement occurs as a result of the relationship between brain and muscle activity. In other words, muscle activity is controlled by the brain and spinal cord. In many previous studies, brain activity and muscle activity were represented by an electroencephalogram (EEG) and an electromyogram (EMG), respectively (Halliday et al. 2003, Tuncel et al. 2010, Petersen et al. 2012, Artoni et al. 2017). These are powerful techniques for measurement that can be used to monitor electrical activity within the body and can help to detect and monitor nerve and muscle disorders. However, in walking, the EEG signal can be marred by noise, including cable and movement artefacts, sweating and muscle activity (Enders & Nigg 2016). This complicates analyses need techniques to deal with noise and artefacts.

Movement disorders refer to a group of neurological conditions that affect the ability to produce and control body movements. Movement disorders can be characterised by ab-

normal voluntary movements, involuntary movements, slow movement and reduced movements. There are many diseases and syndromes of movement disorder, such as Parkinson's disease, Huntington's disease, Wilson's disease, restless leg syndrome, stroke as well as Gilles de la Tourette syndrome. There is a global trend of increasing numbers of people with movement disorders. Parkinson's disease is one of the most common neurodegenerative and well-known movement disorders (Bach et al. 2011, Magrinelli et al. 2016). In 2010, 2.32 million people in Europe, 1.12 million in the United State, and 0.13 million in Canada were affected by Parkinson's disease (Bach et al. 2011). Parkinson's disease is a disease with increasing prevalence in old age, however individuals have developed Parkinson's disease in their 30s and 40s (DeMaagd & Philip 2015).

Movement disorders can be caused by damage to or disease in the central nervous system (the brain and spinal cord) that controls movement. For example, Parkinson's disease affects both motor and cognitive function (Biundo et al. 2016, Wang et al. 2017). In term of diagnosis of movement disorders, it has been found that diagnosis and treatment require not only taking a careful medical history but also performing a thorough physical and neurological examination (Hatala et al. 1997, Stone et al. 2005). Understanding human movement or how the brain controls the muscles could help in recognising the first stages of many movement disorders, such as Parkinson's disease.

One of the ways used to understand human movement in health and disease is to detect the relationship between signals that can be done by detecting amplitude, phase, and frequency. Spectral analysis techniques are commonly used in neurophysiology (Halliday et al. 2003, Pereda et al. 2005, Zhan et al. 2006, Brittain et al. 2007, Prerau et al. 2017). In addition, spectral methods have been widely used not only to investigate dependencies between signals but also to study systems displaying rhythmic behaviour (Amjad et al. 1997). In particular, coherence and phase synchrony can be derived from the results of spectral analysis techniques (Bruns 2004). A classical method in wide use to obtain a spectral representation of a given signal is the Fourier transform. Standard Fourier analysis allows the composition of a signal into frequency components but does not provide a time history of when the frequencies actually occur (Addison et al. 2009). In practice, locomotion is highly non-stationary. The frequency content of many neurophysiological signals changes rapidly with time. Wavelets are analytical methods that have been used to date in neuroscience for analysis of non-stationary signals (Le Van Quyen et al. 2001, Zhan et al. 2006, Brittain et al. 2007, Tuncel et al. 2010, Hassan et al. 2010, Nakhnikian

et al. 2016).

In recent years, the wavelet transform is a powerful time-frequency analysis suitable for analysis of non-stationary signal (Addison et al. 2009). Wavelet transforms provide time-frequency decomposition of a signal with the possibility to adjust the time-frequency resolution (Addison 2002). There are different types of the decomposition depending on the chosen wavelet transform for the signal under investigation (Addison 2002, Bruzda 2011). Continuous wavelet transform provides analysis of a signal in order to recognise local features in the data, especially in the case of signals defined over the entire real axis, providing highly redundant information (Bruzda 2011, Aguiar-Conraria & Soares 2014). The redundancy of the continuous wavelet transform may have some advantages, for example, it is possible to recover the original time series from its transform (Aguiar-Conraria & Soares 2014). The discrete wavelet transform provides a parsimonious representation of the data and is particularly useful in special discrete choice of the parameter values for time and frequency, especially in noise reduction and information compression (Bruzda 2011, Aguiar-Conraria & Soares 2014). Most studies of signal processing in neuroscience have used the continuous wavelet transforms, especially complex Morlet wavelet, to study the synchrony between different time series data (Zhan et al. 2006, Forte et al. 2008, D'Avanzo et al. 2009, Kopal et al. 2014, Gohel et al. 2016, Samiee & Baillet 2017). Recently, continuous analytic wavelets − generalized Morse wavelets are a promising class of complex-valued exactly analytic wavelet transform with vanishing support on negative frequency axis (Lilly & Olhede 2009). They are highly flexible and form a two-parameter family of wavelets that have been used for studying time-varying properties of non-stationary neurophysiological signals (Brittain et al. 2007, Nakhnikian et al. 2016).

There are a number of popular measures used to investigate and characterise non-stationary neuronal coupling. In this thesis, we focus on three measures. i) Wavelet coherence is widely used to detect time-localized common oscillations in non-stationary signals. It has been applied in studying interactions within nervous system i.e. the relationship between simultaneously recorded neural and muscular data (Zhan et al. 2006). ii) Phase synchronisation is a fundamental concept in the analysis of non-linear, chaotic and non-stationary system (Aydore et al. 2013). Phase locking value is commonly used as phase interaction measure. For example, Simões et al. (2003) applied phase locking value technique using Morlet wavelet to examine phase locking between human primary and secondary somatosensory cortices. iii) Phase-amplitude coupling measures have been

receiving increasing interest in evaluating phase-amplitude coupling in continuous electrophysiological signal obtained from the brain (Penny et al. 2008, Tort et al. 2008, 2010, Canolty & Knight 2010, Canolty et al. 2012, Pittman-Polletta et al. 2014, Dvorak & Fenton 2014, Nakhnikian et al. 2016). This method provides the frequency estimates of the oscillatory components related in phase and amplitude (Tort et al. 2008, Canolty & Knight 2010). Recently, a time-resolved measure of phase-amplitude coupling between neural oscillation, named tPAC, was proposed. This method is used to detect temporal profile and frequencies of coupled oscillatory components (Samiee & Baillet 2017).

The generalized Morse wavelets have been applied to coherence (Brittain et al. 2007) and phase-amplitude coupling analysis (Nakhnikian et al. 2016). However, to our knowledge, they have never applied to phase locking value and tPAC measures, especially in analysis of surface EMG signals during human treadmill and overground walking. In addition, we propose a novel technique applied to coherence and phase locking value that can remove low frequency components due to envelope modulation in surface EMG records for locomotion experiments. It is hoped that the methods could provide a more thorough understanding of the mechanisms involved in human walking in health and disease.

1.2 Conceptual overview of approach

For studying and understanding the nature of corticospinal interactions in normal and abnormal gait, various techniques are used to infer the coupling between ongoing cortical rhythms (LFP, EEG or MEG) and oscillations in the electrophysiological activity of the muscle (EMG). In case of recording scalp EEG during human walking can introduce motion artifacts. Thus, most studies have examined brain activations during static condition. Despite these limitations, this work intends to use EMG measured during locomotion because the correlation between muscles using paired EMG recordings, may indirectly measure cortical influence (Grosse et al. 2002, Halliday et al. 2003). Also, EMG is relatively cheap, easier to record, lighter and more comfortable as participants can perform a natural walking compared to LFP, EEG or MEG.

This work proposes the following hypothesis: *" Investigation of non-stationary neuronal coupling mechanisms underlying human locomotion in a selection of lower limb muscles gained by using analytic wavelets may improve understanding of neuronal mechanisms associated with locomotion."*

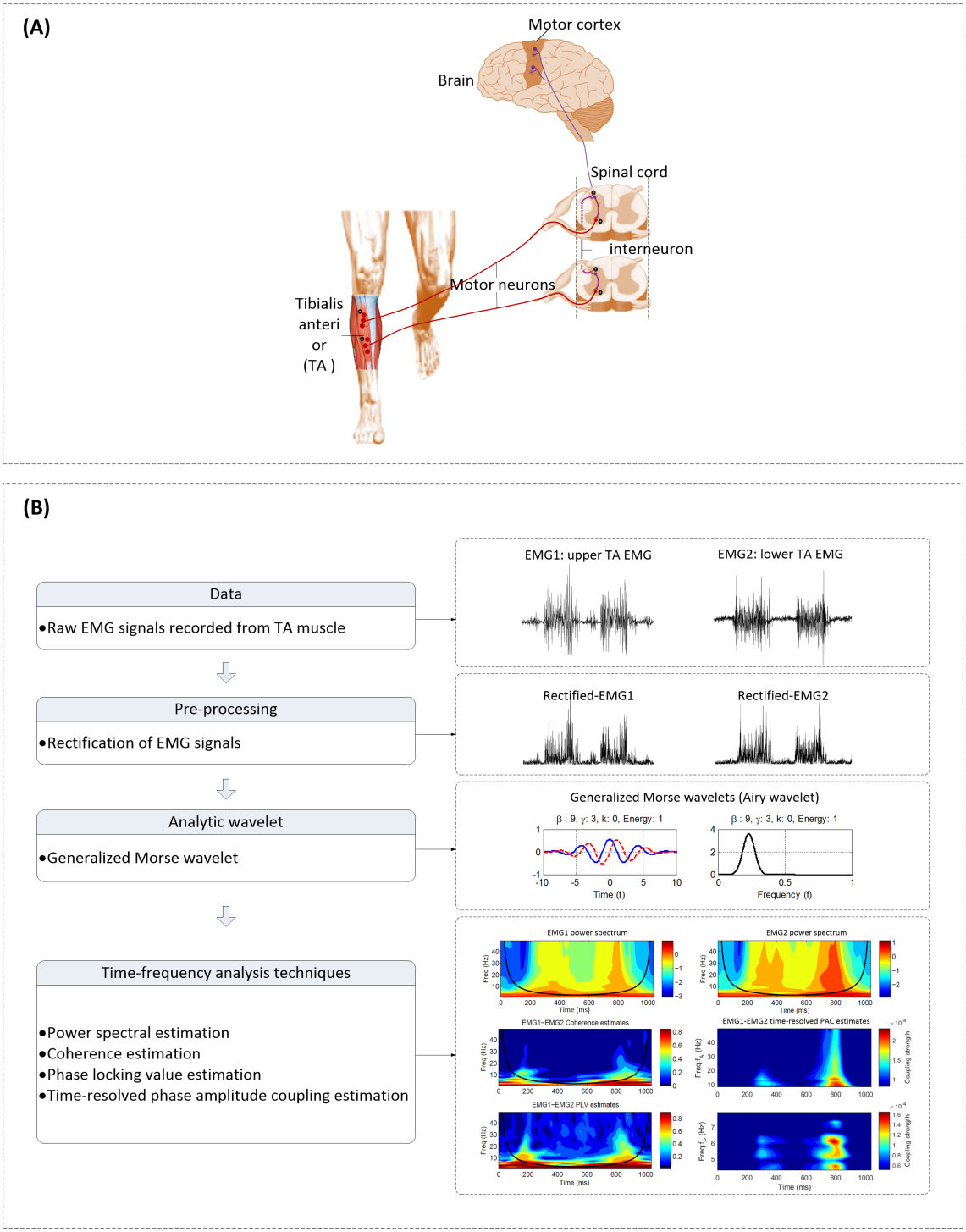

Figure 1.1: Conceptual overview of analysis of human locomotion data using analytic wavelets applied to sEMG data. (A) diagram of nervous control system of human locomotion using EMG signals and (B) overview of signal processing methods used in this thesis, see text for details.

The approach is illustrated in Figure 1.1, in this thesis data has come from paired

EMG recordings obtained from healthy control and Parkinson's disease (PD) subjects during walking. Paired bipolar surface EMG recordings were obtained from two sites over the belly of tibialis anterior (TA) muscle. We used correlation between paired surface EMG signals to look back into central nervous system to infer neural activity patterns. The EMG signals after full-wave rectification are analysed based on a unified framework, which allows the correlation structure between the paired EMG signals, by power spectrum estimation, coherence estimation, phase locking value estimation and time-resolved phase-amplitude coupling estimation using specific analytic wavelets, the generalized Morse wavelets. In particular the estimates of coherence and phase locking value, the new technique is applied to both measures for removal of low frequency components due to EMG envelope modulation. In addition, all three measures are derived from the same two-parameter family of generalized Morse wavelets. Our unified framework is used to identify any modulations in the functional coupling of motor units during walking and provide insight into the organisation of the neural pathways involved in gait patterns.

1.3 Thesis outline

The thesis is organised in six chapters. The first chapter introduces the motivation, the conceptual overview of approach and the hypothesis related to this work. A review of literature on the neurological system underlying human locomotion in normal and abnormal gait, Parkinson's disease; and a review of signal processing are in chapter two. The experimental methods and data sets: surface EMG during treadmill walking in healthy subjects and overground walking in healthy controls and PD subjects are described in chapter three. Chapter four provides details of analytical methods analysing non-stationary signals, which include generalized Morse wavelet, coherence, phase locking value and time-resolved phase amplitude coupling analysis. The results of human locomotion data analysis during treadmill walking and overground walking are presented and discussed in chapter five. Conclusions and directions for future research are included in the last chapter.

Chapter 2

Literature review

One of essential features in human life is locomotion. A common feature of human locomotion is rhythmic and alternating movements of the body (Kandel et al. 2000). Its rhythmicity makes locomotion appear to be repetitive and stereotyped. System of nerve cells responsible for the rhythmic motor patterns generation has been focused in movement neuroscience (Kandel et al. 2000). An understanding of the mechanisms underlying human locomotion could provide the opportunity to characterise an early state of many movement disorders, such as Parkinson's disease.

An analysis of human movement is a process to investigate the characteristics of human movement that relate to both normal and abnormal movement. In recent years, neurological recordings, electroencephalogram (EEG) and electromyogram (EMG), from brain and muscle activity during walking, in conjunction with time frequency analysis, have been increasingly used to investigate cortical activation patterns and corticomuscular connectivity during walking in human (Brittain et al. 2009, Petersen et al. 2012, Artoni et al. 2017). In particular movements, the recording of scalp EEG may be not always easy, for example in movement disorders (Grosse et al. 2002). The EEG signals can be marred by noise, including cable and movement artefacts, sweating and muscle activity (Grosse et al. 2002). In the study of Grosse et al. (2002) presented examples of EMG−EMG coherence. Those results suggested that the pattern of EMG−EMG coherence was qualitatively similar to the EEG−EMG coherence in the same subject. In addition, Halliday et al. (2003) provide evidence in investigating the functional coupling of motor unit during locomotion using EMG-EMG coherence analysis.

The objective of this chapter is to review the neurological system underlying human locomotion and neurological degenerative disease which consist of five main parts as follows:

nervous system, human muscles, human locomotion, Electromyogram and Parkinson's disease. In order to obtain information about electrophysiological signals, a review of signal processing is also presented in this chapter. Traditional analysis of electrophysiological signals has been conducted through the spectral analysis. Here, the classical spectral analysis is based on the Fourier transform. Also, the concepts of complex continuous wavelet transforms, Morlet wavelet, are introduced which give some characteristics to use for analysing non-stationary signals.

2.1 Neuroscience review

2.1.1 Nervous system

Anatomically, the human nervous system has two major subdivisions that are the central nervous system (CNS) and the peripheral nervous system (PNS). The CNS is the primary control centre of the body and mind. It contains the brain and spinal cord. The PNS is located outside of the CNS and consists of cranial and spinal nerves and sensory receptors. Its main function is to connect the CNS to the rest of body. Similarly, the PNS can be divided into two functional divisions, namely sensory division and motor division. The sensory division carries impulses from sensory receptors to the CNS. The motor division carries impulses from the CNS to effectors, muscles and glands, which perform an action. The motor division can be divided into two subdivisions as follows: (1) the somatic nervous system (SNS), which is involved in the voluntary (conscious) control of skeletal muscles, and (2) the autonomic nervous system (ANS), which provides involuntary (subconscious) control of cardiac muscle, smooth muscle, and glands (McKinley et al. 2015). See Figure 2.1.

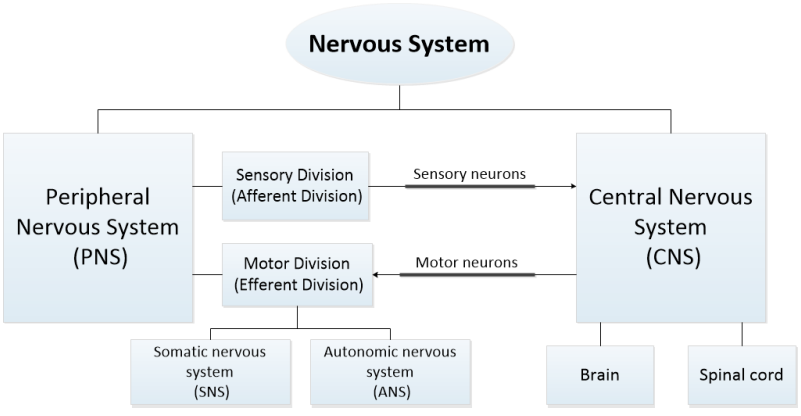

Figure 2.1: Basic structure of human nervous system adapted from (Kandel et al. 2000).

The nervous system is formed by two main classes of cells that are nerve cells, also called neurons, and satellite cells. The satellite cells are known as glial cells or glia in the brain and spinal cord (Pocock et al. 2012). Nerve cells are the principal structural and functional unit of the nervous system. Glial cells are non-neuronal cells that function to support the nervous cells.

Brain

The brain is the most important part of the CNS. It is the origin of all aspects of behaviours including body movement. The brain can be divided into three crucial divisions that are the forebrain (diencephalon and cerebral hemispheres), the midbrain, and the hindbrain (medulla, pons, and cerebellum). The midbrain and the hindbrain but excluding the cerebellum, are often referred to as the brainstem. These structures are shown in Figure 2.2

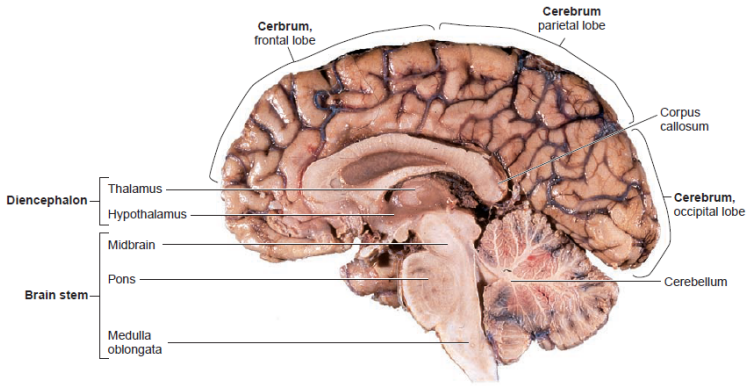

Figure 2.2: The major component of the brain. Image from McKinley et al. (2015).

Focusing on movement, one of the important brain areas that plays a role in voluntary movement is the motor cortex. In addition to motor cortex, there are many other brain regions involved in controlling movement, including cerebellum, the basal ganglia, and a large number of neuron groups located within the midbrain and brainstem. The motor hierarchy with multiple levels of control is shown in Figure 2.3 (Gazzaniga et al. (2002)). Briefly, the highest level of the hierarchy are premotor cortex and the supplementary motor area which are critical for goal-directed actions. The lower-level mechanism – the motor cortex and brainstem structures, with assistance of the cerebellum and basal ganglia, translate motor commands into movements. The lowest level is the spinal cord which provides all connections to muscles.

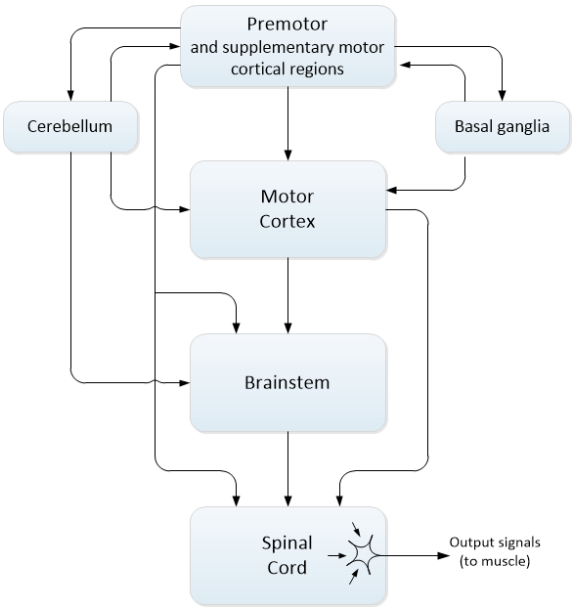

Figure 2.3: The motor hierarchy with multiple levels of control. Figure adapted from Gazzaniga et al. (2002).

- **Motor Cortex**

  The motor cortex is the region of the cerebral cortex located at the rear of the frontal lobe before the central sulcus (furrow) that separates the frontal lobe from the parietal lobe, see Figure 2.4. The motor cortex is responsible in the planning, control, and execution of voluntary movements. The motor cortex comprises the primary motor cortex, the premotor cortex, and the supplementary motor area. These motor cortical areas have motor neurons which connect to the spinal cord and brainstem. The functions of these motor neurons are responsible for producing organised movement by coordinating a number of muscle's actions.

  The primary motor cortex is located anterior to the central sulcus. It is a major source of descending projections to motor neurons in the the spinal cord and cranial nerve nuclei (Purves et al. 2001). The roles of the primary motor cortex indicate in planning or programming of voluntary movements. In general, primary motor cortex encodes the parameters that define individual movements or simple sequences of movements.

  The premotor cortex is located anterior to the primary motor cortex and has many of the same connections as the motor cortex. This region receives neuronal inputs from the sensory association cortex as well as feedback from the basal ganglia via the ventral anterior nucleus (VA) and the ventral lateral nucleus (VL) of the

thalamus. Most neuronal outputs of premotor cortex are sent to the primary motor cortex as well as to the brain stem and the spinal cord directly. The functions of the premotor cortex are usually responsible for some aspects of motor control in order to select a specific movement or sequence of movements from the repertoire of possible movements, see Purves et al. (2001, chapter 26) for more information.

The supplementary motor area (SMA) is a part of the premotor cortex that extends onto the medial side of hemisphere. The SMA is involved in selecting movements based on remembered movement sequences, programming complex movements sequences and coordinating bilateral movements.

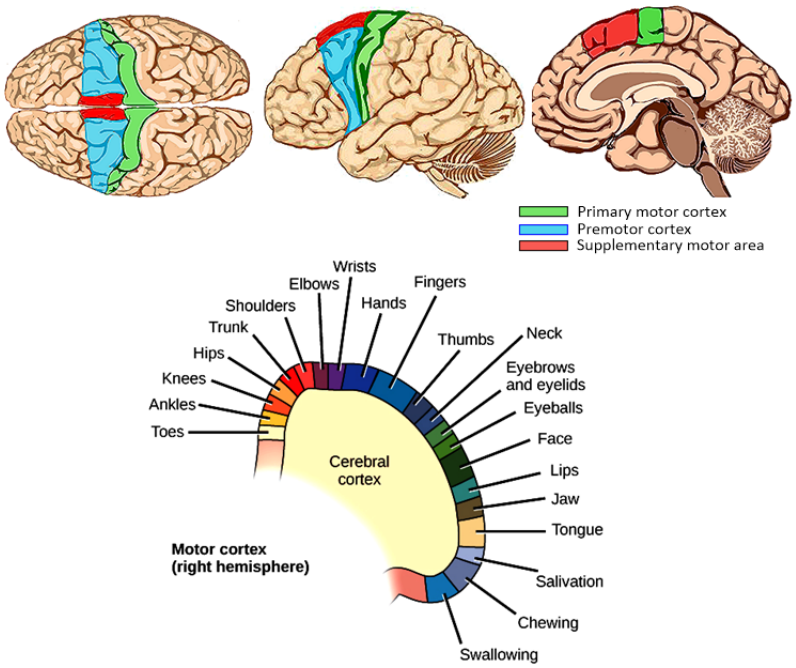

Figure 2.4: Motor cortex areas regions of the cerebral cortex in lateral, dorsal, and medial views. Figure adapted from http://neuroscience.uth.tmc.edu/s3/chapter03.html.

- **Cerebellum**

  The cerebellum is located just above the brain stem, beneath the occipital lobe at the back of the brain. The cerebellum receives information from the sensory systems of the spinal cord and other parts of the brain and then integrate these information to regulate motor movements (Kandel et al. 2000). The cerebellum has been considered a motor structure involved in the coordination of voluntary motor movement, balance and equilibrium, and muscle tone. However, the cerebellum is also known as an control error device for body movement because it corrects the errors in each movement command and imparts motor skills (Kandel et al. 2000).

- **Basal ganglia**

  The basal ganglia (Figure 2.5) is group of subcortical structures in motor control. It rests deep within the cerebral hemispheres on either side of thalamus. The role of the basal ganglia in movement is to select the appropriate motor patterns in a particular behavioural context. Overall the basal ganglia receives and processes the majority of its inputs from cerebral cortex, and then sends the results back to cerebral cortex via the thalamus. Three clusters of neurons in the basal ganglia, namely caudate nucleus, putamen, and globus pallidus are responsible for involuntary movements such as tremors, athetosis, and chorea. Therefore, the basal ganglia is studied extensively in the context neurological conditions, including Parkinson's disease (Purves et al. 2001).

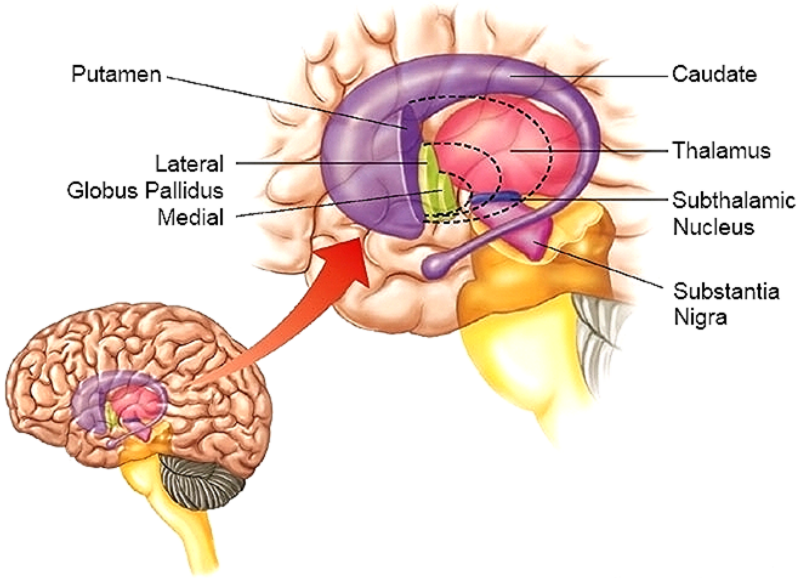

Figure 2.5: An illustration of the location of the basal ganglia within the brain. Image from http://cti.its.virginia.edu/∼psyc220/kalat/JK246.fig8.15.basal_ganglia.jpg.

- **Brainstem**

  The brainstem is one of the most fundamental regions of the human brain because it maintains the vital control of cardiac, visceral, respiratory, sensory and motor systems. In general, the brainstem is the structure that connects between the spinal cord and the brain. It consists of the midbrain, the pons, and the medulla. The brainstem has been imputed as providing important functional involvements in balance, eye movements and the maintenance of posture (Kandel et al. 2000).

Spinal cord

There are two main characteristics of spinal cord: white and grey matter. The white matter mainly includes nerve fibres passing through the spine. Nerve fibres are covered with mylin that make which facilitates faster conduction of signals. The grey matter which is butterfly shaped contains the cell bodies, see Figure 2.8 including motor neuron and interneurons. It is comprised of four main columns, including dorsal horn, intermediate column, lateral horn and ventral horn column. The ventral horn contains the lower motor neurons, namely alpha and gamma motor neurons which innervate skeletal muscle, see Figure 2.6. Alpha motor neurons receive input from a variety of sources. Focusing on the spinal cord, input to alpha motor neurons comes from descending fibers of the spinal cord and interneurons within the spinal segment (Gazzaniga et al. 2002).

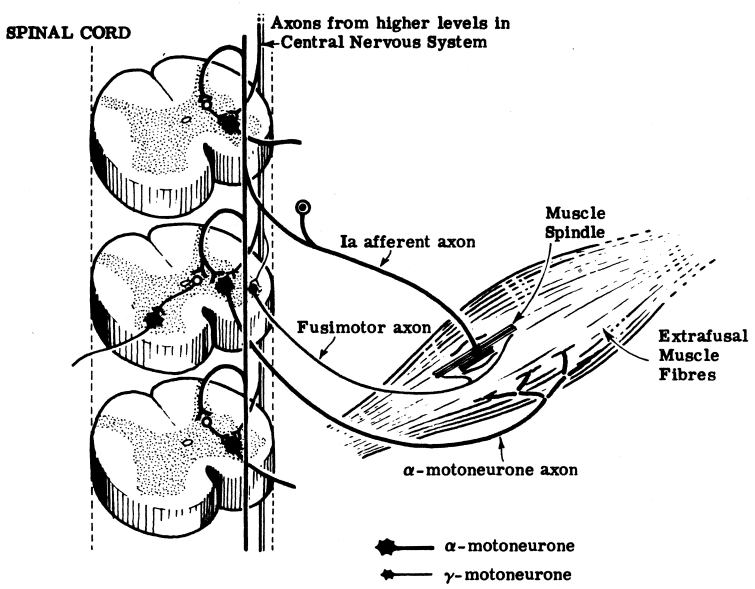

Figure 2.6: Intersegmental contralateral reflex arc in spinal cord. Image from Dr David M. Halliday, Department of Electronic Engineering, University of York, York, UK.

Central pattern generators (CPGs)

Neural circuits in the spinal cord are referred to as central pattern generators (CPGs) that when activated can produce rhythmic motor patterns including walking without sensory or descending inputs. One model of locomotor CPGs is known as the half-centre hypothesis, and proposes that a rhythmic motor pattern is produced by reciprocal inhibition between two groups of interneurons, namely an extensor half centre activating extensor motoneurons and a flexor half centre exciting flexor motoneurons, located in spinal cord

(MacKay-Lyons 2002). The half centre model gives useful information to explore how the CPG network controls movements. Previous studies on CPGs were achieved in the spinalized cat but the relevant significance of CPGs activity in control of human locomotor movements needs to be clarified (Duysens & de Crommert 1998, MacKay-Lyons 2002, Dietz 2003, Kiehn & Dougherty 2013).

Neuron

The neuron is the basic structural unit of the nervous system. A typical neuron includes three main parts: (1) a cell body or soma that contains the nucleus, (2) dendrites that act as a tool for obtaining signals from other nerve cells, and (3) an axon that transmits electrical signals known as action potentials to other neurons (Figure 2.7).

There are three major functional types of neuron in the nervous system, including motor neurons, sensory neurons, and interneurons.

Motor or efferent neurons transmit information from the CNS and turn it into muscular actions (Kandel et al. 2000). There are two sets of motor neurons, including upper and lower motor neurons. The cooperation between two types of neuron is that the upper motor neuron runs from cortex or brainstem to the ventral horn of the spinal cord and then a lower motor neuron operates from the ventral horn to the skeletal muscle. The lower motor neurons contains alpha and gamma motor neurons. Alpha motor neurons innervate extrafusal muscle fibres that cause the muscle contractions and gamma innervate intrafusal muscle fibres (Kandel et al. 2000).

Sensory or afferent neurons play a key role in perceiving stimuli from both external and internal environments of the body. This information is transmitted to the spinal cord and brain. These cells act by transforming sensory stimulus to electrical potential, a process called transduction.

Interneurons or association neurons are found exclusively in the brain and spinal cord that contain the motor and sensory neurons in neural pathways. Interneurons can be subdivided into local interneurons and relay or projection interneurons. Local interneurons have short axons and produce circuits with nearby neurons to process information within the local circuits. Projection interneurons have long axons and carry signals in one region of the brain to other regions (Kandel et al. 2000).

Figure 2.8 illustrates three major functional types of neuron in the nervous system, and an example of a reflex arc. In a reflex arc, stimuli are detected by a sensory receptor,

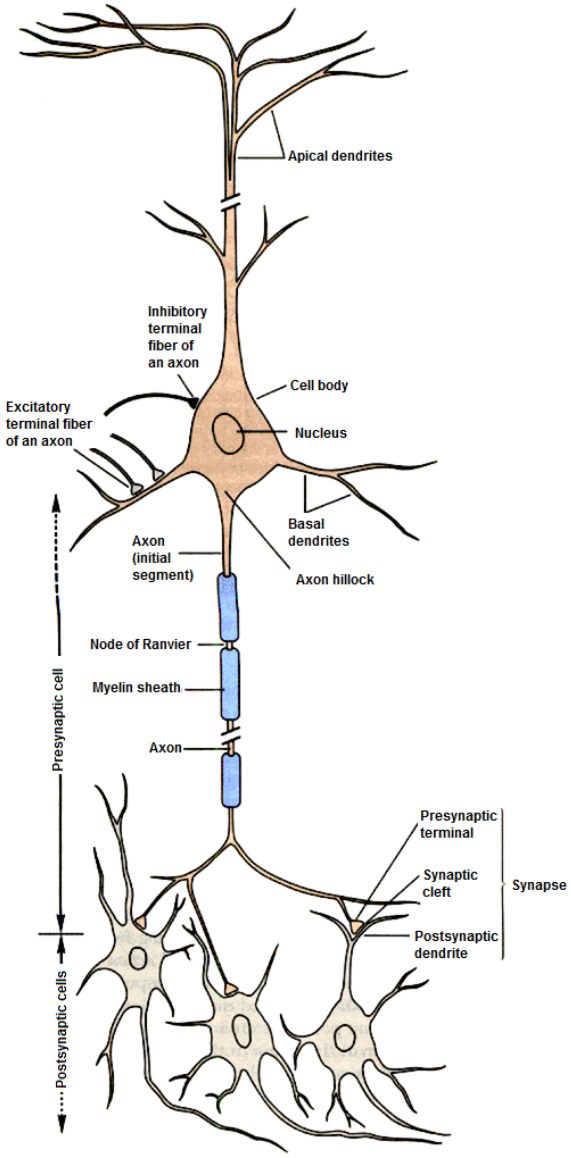

Figure 2.7: Structure of a neuron. Image from Kandel et al. (2000).

causing the production of action potentials that are carried to the CNS by an sensory neuron. Within the CNS, sensory neurons usually synapse with an interneuron. These neurons synapse with a motor neuron, which carries action potentials to the skeletal muscle effector.

Action Potential

An action potential, simply called a spike or a nerve impulse, is the means of communication between neurons (Kandel et al. 2000). The action potential is generated by a change in ion concentrations across the membrane of neuron when a neuron is stimulated. During the action potential, the voltage-gated sodium ion (Na^+) channels embedded in

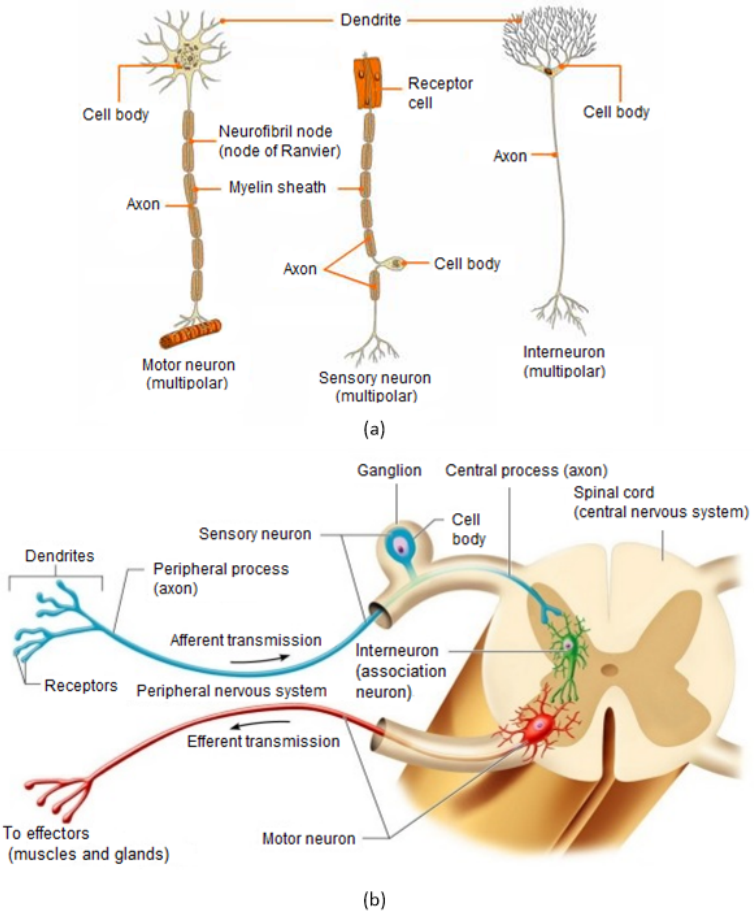

Figure 2.8: (a) Neurons classified by function and (b) example of reflex arc. Image from Marieb (2006).

the membranes of neurons open and the positive sodium cells surge into the cell. As the membrane potential reaches the peak with an amplitude of around +40 mV (after a duration of about 1 millisecond (ms)), the Na^+ channels close (Kandel et al. 2000). Then the voltage-gated potassium ion (K^+) channels are open, resulting in hyperpolarization before returning to resting potential (Trappenberg 2010). When at rest, the neuron is not sending any information. In the resting state, the sodium-potassium ions pumps actively transport Na^+ out of the cell, and K^+ into the cell so that the ions are in the correct positions, as they were originally before the neurone was stimulated. The amplitude of the resting potential varies in excitable cells and possibly ranges between -40 mv and -100 mv (typically around -70 millivolts (mv)) depending on the distribution of electrically charged ions on either side of the membrane and the selective permeability properties of the membrane (Hodgkin & Huxley 1952). Additionally, the temporal sequence of multiple action potentials is called “spike train”. Figure 2.9 shows typical form of an action potential.

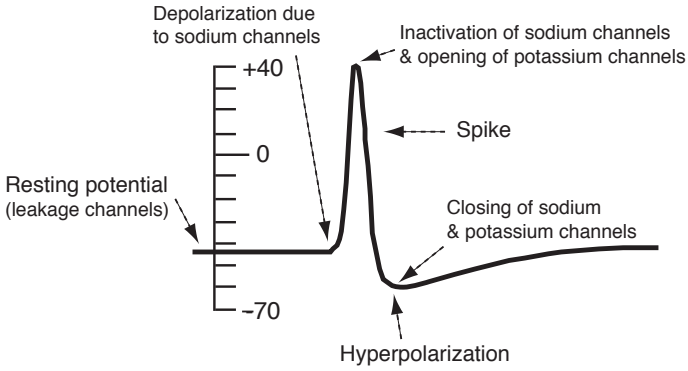

Figure 2.9: Typical form of an action potential. Image from Trappenberg (2010).

2.1.2 Human muscles

The muscular system of the human body plays an important role in movement. It can be divided into three types of muscles − skeletal muscle, cardiac muscle (heart) and smooth muscle (internal organs) (McKinley et al. 2015). Skeletal muscles are the only voluntary muscle tissue. The primary function of skeletal muscles is to support movement and maintenance of body posture and position i.e. controlling walking. The skeletal muscles involved in walking are the muscles of the lower leg (i.e. soleus, gastrocnemius, tibialis anterior/posterior, and peroneals), and the thigh/knee (i.e. vastus lateralis, medialis, obliques, and rectus femoris), see Figure 2.10.

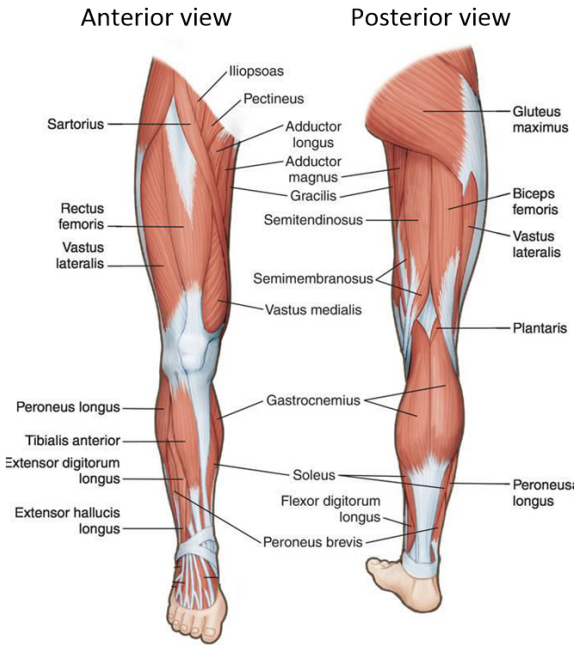

Figure 2.10: Anterior and posterior view of the muscles of human leg. Image from Weersink (2016).

Typically, see Figure 2.11 muscles consist of thousands of parallel fibers. Each fiber is supplied by a single motor neuron. In combination, a motor neuron and the group of muscle fibers (or the muscle unit) form a motor unit. In a motor unit the motor neuron branches to form neuromuscular junctions with several muscle fibers. Most individual muscles are controlled by motor neuron pool which cosists of hundreds to thousands of the motor units within the same muscle (Heckman & Enoka 2004). Electromyograms (EMG) are recorded with sensors placed on the skin over the muscles or with the needle introduced into the muscle tissue to measure the electrical activity, more detail is provided in Section 2.1.4.

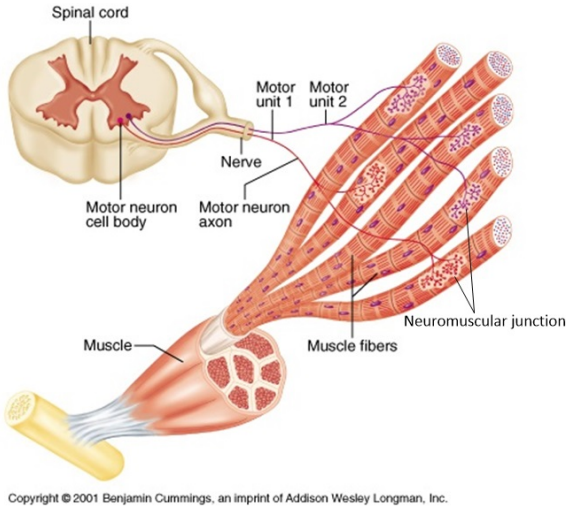

Figure 2.11: The nerve-muscle relationship. Image from `http://faculty.etsu.edu/forsman/Histologyofmuscleforweb.htm`.

2.1.3 Human locomotion

Locomotion is a fundamental skill or a basic motor act for all vertebrates that is expressed in various forms including walking, swimming, running, and hopping. Locomotor movements differ from other movements that are produced by the nervous system. For example, walking is a stereotypically repeated action while playing tennis is often non-repeated manner that it involves a complex coordination of muscles.

In 1880s, photographic techniques were used to describe locomotor movement in animals and humans. Étienne-Jules Marey and Eadweard James Muybridge used these techniques that allowed viewers to motion capture snapshots of the different locomotor movements. The sequences of pictures showed the precise timing of the movements in detail that never seen before (Kiehn & Dougherty 2013). In early twentieth century, Thomas

Graham Brown, an English neurophysiologist, concluded that neural networks within the spinal cord in the cat can generate rhythmic movements consisting of alternating flexor and extensor activity without sensory inputs. The evidence from studying many vertebrates showed that when the locomotion starts, activity in the CPGs in the spinal cord generates the exact phasing, timing and intensity cues to drive motoneuron output for simple rhythmic behaviours. Neurons in the CPG receive information from descending locomotor commands originating from neurons in the brainstem and midbrain in order to produce the rhythm and pattern of muscle contraction that is conducted to motor neurons and then to the muscles (Kiehn & Dougherty 2013).

Neural control of locomotion

A number of the neural structures controlling locomotion in vertebrates (Kiehn & Dougherty 2013) are as follows (Figure 2.12): (1) Neuronal systems in the brain play a role in selecting the behaviour. Two neuronal structures namely neurons in the mesencephalic locomotor region in the midbrain and neurons in the reticular formation in the lower brainstem are directly involved in initiating locomotor behaviour. (2) Spinal neuronal networks in the spinal cord generate the behaviour. However, the activity of the spinal neuronal networks can be adapted and fine-tuned to the environment by sensory signals. (3) Sensory signals are used in correcting and adapting the locomotor behaviour and they are sent to supraspinal structures, including the cerebellum. (4) Neural networks in the cortex take a decision in carrying out visual adjustment of locomotor movements. (5) The motor act can be modulated by neuromodulators in CPG networks that appear to play an essential roles in generating rhythmic output.

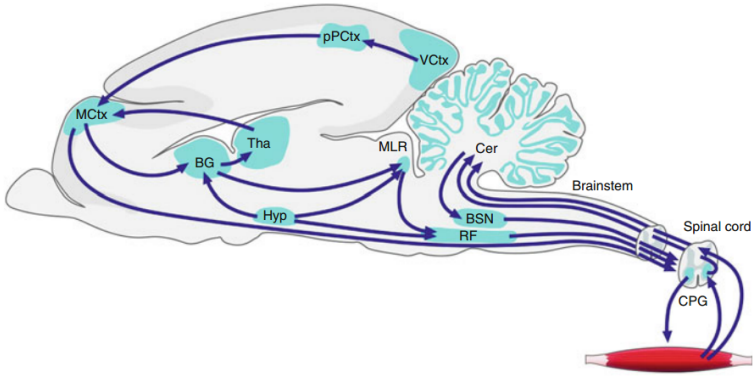

Figure 2.12: An organisation of neural structures controlling locomotion in vertebrates. Image from Kiehn & Dougherty (2013).

Sequence of basic human walking processes

Human walking is one locomotor movement that is controlled by the interaction between the nervous system (CNS and PNS) and musculoskeletal effector system. Figure 2.13 demonstrates the seven elements forming the functional basis for human walking, feedback loops have not been shown in this figure (Vaughan et al. 1999). The sequence of processes leading to walking can be summarized as follows: the gait command can be registered and activated in the CNS. The gait signals then are sent to the PNS. Skeletal muscle contractions require synaptic input from motor neurons for producing muscle contractions that develop tension. Synovial joints allow for movement produced by generating forces and moments. The joint forces and moments are organised by the rigid skeletal segments based on their anthropometry. The segments, such as the thigh, calf and foot are moved and exert forces on the external environment (generation of ground reaction forces).

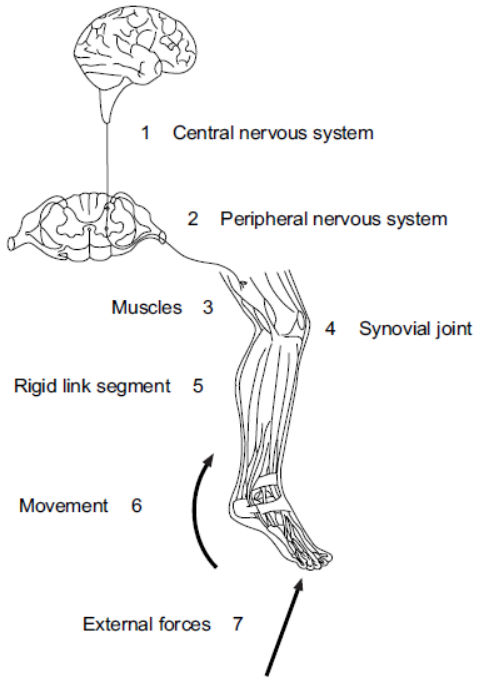

Figure 2.13: The components forming the functional basis for human walk. Image from Vaughan et al. (1999).

In natural human walking on level ground, walking cycle or gait cycle, also called stride, starts when one foot touches the floor and ends when the same foot touches the floor again. A cycle of walking involves two phases, namely stance and swing phases. The stance phase occurs when the foot contacts the ground. It constitutes about 60 percent of gait cycle which is divided into: (1) Heel strike to foot flat, (2) Foot flat through mid-

stance, (3) Mid-stance through Heel off, and (4) Heel off to Toe off. The swing phase occurs when the limb is off the ground. It constitutes 40 percent of the gait cycle which is divided into: (1) Acceleration to mid-swing and (2) Mid-swing to deceleration. The activity of each phase is illustrated in Figure 2.14. The five major muscles in the lower extremity − gluteus medius(GM), rectus femoris(RF), biceps femoris(BF), soleus(S) and tibialis anterior(TA) are also represented in Figure 2.14. The shading indicates the degree of activity on grayscale. Solid dark means most active while white means quiescent.

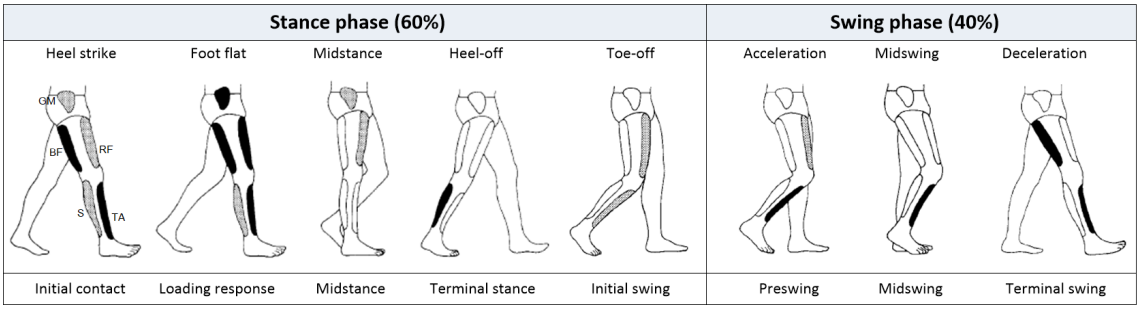

Figure 2.14: Phases of the gait cycle, showing the activity of the five major muscles in the lower extremity. Figure adapted from Vaughan et al. (1999).

2.1.4 Electromyogram

A fundamental technique in studying and understanding the behaviours of human body under normal and pathological conditions is provided by using simultaneous electrophysiology recordings. Electromyogram (EMG) is used in many fields, such as medical, neuroscience and engineering field in order to study the connectivity between neurons, neural firing patterns and diagnostic neuropathology.

The EMG signal is electrical signal affected by properties of muscles which are controlled by the nervous system. The EMG signal refers to muscle action potential that is generated in the muscle fibres during muscle contraction. Typically, one muscle includes around a thousand motor units (MUs). A MU is formed by one alpha spinal motor neuron and many thousands of muscle fibres that it innervates (Kandel et al. 2000). The activity of MU can generate the electrical changes that is called motor unit action potential (MUAP). A MUAP can be acquired by electrodes located in or on muscle mass (Figure 2.15) (De Luca et al. 2006).

There are two techniques of EMG recording that are intramuscular (needle and fine wire) and surface electrodes. The intramuscular EMG may be considered an invasive form of EMG while surface EMG is a non-invasive form of EMG. Intramuscular EMG signals

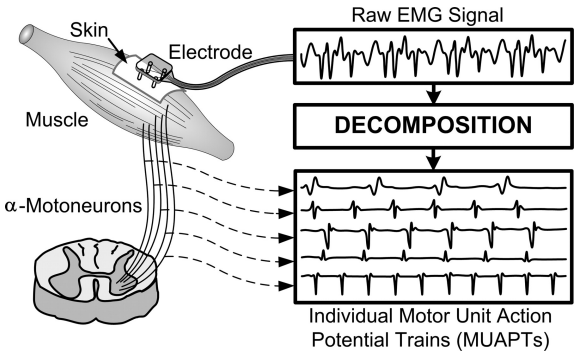

Figure 2.15: The decomposition of the surface EMG signal into its component MUAPs. Image from De Luca et al. (2006).

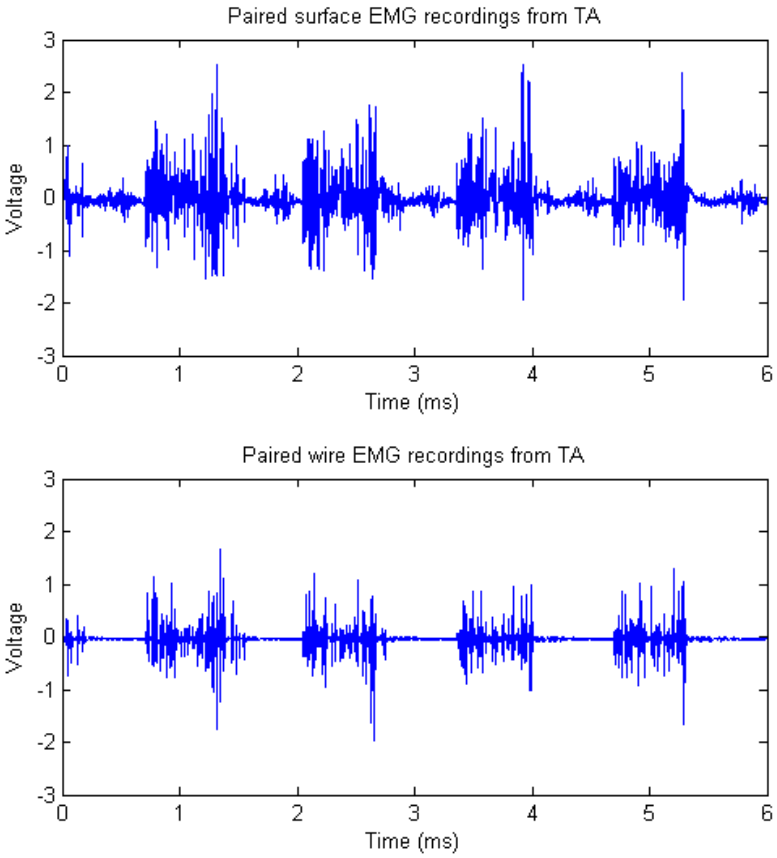

Figure 2.16: Example of surface EMG and intramuscular EMG signals which are taken from human treadmill locomotion subject, as detailed in chapter 3.

recording is used to recognize the behaviour of individual muscle fibres and motor units. Example of intramuscular EMG signal and surface EMG signal are illustrated in Figure 2.16. In contrast, surface EMG signal is a composite of all the muscle fiber action potentials occurring in the muscles underlying the skin. These EMG recording techniques have

advantages and disadvantages. For instance, the advantages of surface EMG recording are convenience and comfort while the major disadvantages are cross-talk or interference between electrodes and signal-to-noise ratio (SNR) (Perry 1998). Intramuscular EMG recording provides higher frequency content and much stronger signals, so the level of noise is reduced. Nevertheless, they are a discomfort because a fine needle is inserted directly into the muscle. The selection of an appropriate electrode depends on the use of EMG recordings.

The EMG signal is considered in terms of amplitude (a voltage-time function), frequency and phase. The amplitude of the EMG signal at any instant of time is described as random and its amplitude varies from the μV to the low mV range (Basmajian & De Luca 1985). The EMG signal has a very broad spectrum in the frequency range from 10 Hz to 1000 Hz due to significant changes in the EMG activities with muscle contractions. However, the frequency content of the EMG signal depends on factors such as type of electrodes, the timing and intensity of muscle contraction, and the distance of the electrode from the active muscle area.

Normal EMG patterns of the muscles

In clinical studies, surface EMG is an essential part of gait analysis. The knowledge of normal EMG patterns of muscle activation in the lower limbs has generally been used in clinical gait analysis, and served as a reference to explain normalities/abnormalities in human walking. The normal EMG patterns of muscle activity identified for 28 major muscles is plotted as a function of the gait cycle in Figure 2.17 (Vaughan et al. 1999). Muscles with similar phasic activity are grouped together. Most major muscle groups are active at/or around the beginning of the stance and the end of the stance and swing phases of the cycle. The stance phase starts with heel-strike (0%) while the swing phase starts with toe-off (60%). As general rule, one of the principal actions of the lower limb muscles during walking is to accelerate and decelerate the angular motions of the legs for transferring the body weight from one foot to the other.

In this thesis, we consider using correlation between paired EMG recordings from TA muscle to look back into central nervous system for inferring neural activity patterns in human locomotion. Normal EMG patterns of TA muscle in walking takes place during the swing phase and early stance phase which takes place around Heel-Strike (HS) (Woollacott et al. 1986, Halliday et al. 2003, van Asseldonk et al. 2014, Artoni et al. 2017), as seen in

Figure 2.17.

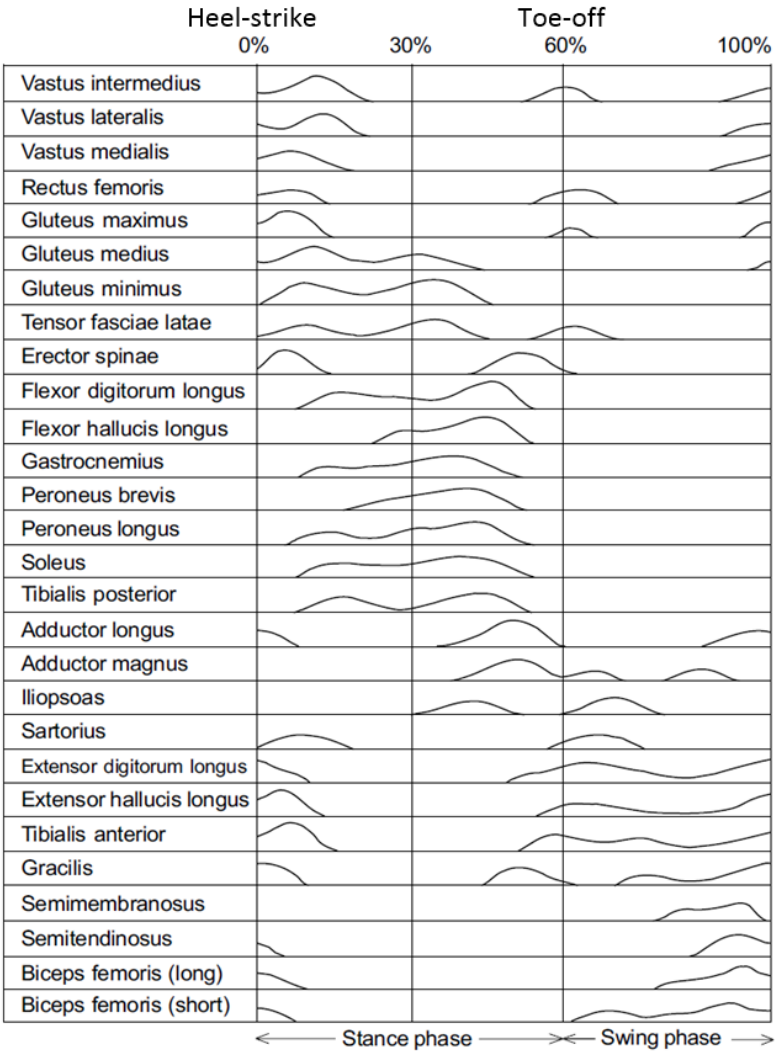

Figure 2.17: Anatomical overview of the muscles in the lower extremities (left) and filtered, rectified and normalized group averaged overview of normal EMG patterns for 28 major muscles plotted as a function of the gait cycle (right). Image from Weersink (2016).

2.1.5 Parkinson's disease

Parkinson's disease (PD) is one of the most common and well-known movement disorders. PD is a chronic disease with an increasing prevalence in old age. People with PD begin to develop symptoms in their 30s and 40s (DeMaagd & Philip 2015). Typical PD symptoms, i.e. tremor, rigidity, bradykinesia and akinesia, occur when the dopaminergic neurons in striatum are depleted. If the percentage of lost neurons becomes too great, PD symptoms will become obvious (Gazzaniga et al. 2002). Focusing on locomotion, postural and gait problems in PD consist of a characteristic shuffling and small-stepped gait, difficulty in

initiating and maintaining stepping, stooped posture, poor trunk movement and reduced arm swing (Müller et al. 1997).

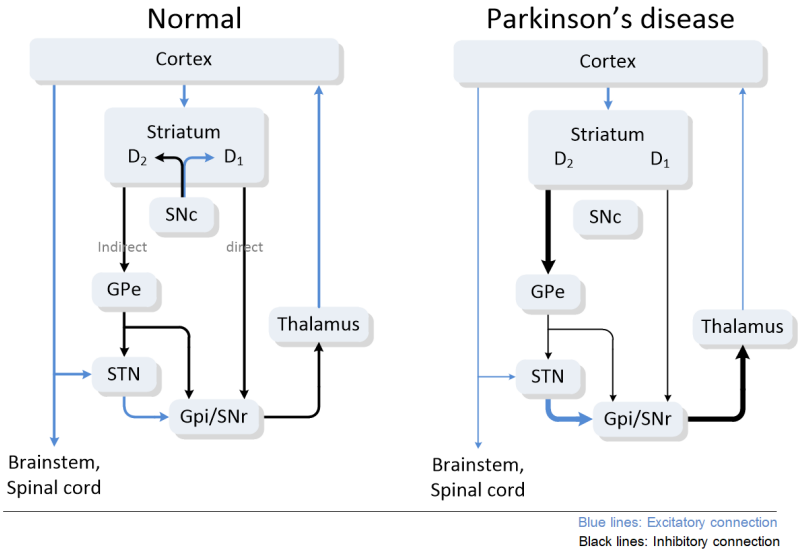

Figure 2.18: Wiring of the basal ganglia, left:normal situation, right: abnormal situation in Parkinson's disease. Figure adapted from Gazzaniga et al. (2002).

As noted earlier, PD is caused by a progressive degeneration of dopaminergic cells in the substantia nigra pars compacta (SNc), that results in dopamine depletion in the striatum. In Figure 2.18 (left), inputs from the cortex project to the striatum which serves as the input to the basal ganglia. The output from the basal ganglia originates in the globus pallidus (GPi) and the substantia nigra (SNr). Processing within the basal ganglia flows along two pathways. The direct pathway comprises direct inhibitory projections from the striatum to the GPi and SNr. The indirect pathway projects from the striatum to the GPi and SNr via the globus pallidus externa (GPe) and the subthalamic nucleus (STN). All of the output signals from the basal ganglia are inhibitory (Gazzaniga et al. 2002). The dopaminergic projections of the SNc modulate activity of both direct and indirect pathways by exciting the direct pathway via one type of dopamine receptor (D_1) and inhibiting the indirect pathway via a different type of dopamine receptor (D_2). In PD (Figure 2.18 (right)), the prominent pathology is a loss of dopaminergic cells originating in SNr and projecting to the striatum. Also, the inhibition activity along the direct pathway from the striatum to the GPi/SNr is reduced. The inhibitory output from the GPi is increased. Thus, too much inhibitory input to the Thalamus leads to a reduction in cortical activity. If about 90% of dopamine is reduced, symptoms of Parkinson, i.e. tremor, rigidity, bradykinesia and akinesia, will become obvious (Gazzaniga et al. 2002).

In summary, this section (section 2.1) specifically focuses on relevant neurological system in human locomotion that consists of (1) nervous system: brain involved in controlling movement, spinal cord and neurons (2) human muscles allowed for motions such as walking (3) human locomotion: neuron control of locomotion and sequence of basic human walking process (4) Electromyogram, including normal EMG patterns of the muscles. (5) Parkinson's disease caused by degeneration of dopaminergic neurons in the Substantia Nigra (SNc) and projecting to the striatum (Figure 2.18, right panel). Next section (section 2.2) will introduce signal processing methods that can be used to analyse time varying signals recorded during human locomotion. Section 2.2 will start from a summary on the spectral analysis based on Fourier transform, and then introduces the concepts of complex continuous wavelet transform, Morlet wavelet.

2.2 Signal processing review

Signal processing has become increasingly important in the field of neuroscience (Brittain et al. 2009, Halliday & Farmer 2010, Allen & Mackinnon 2010, Artoni et al. 2017). Analysis of the frequency content of electrophysiological signals are useful ways to examine neuronal synchrony (Grosse et al. 2002, Brittain et al. 2009). One of the most commonly used analytical tools for obtaining information about human electrophysiological signals is spectral signal analysis. Spectral analysis of EMG signals can provide useful measures for examining synchronised neuronal activity or functional states in the human motor system. The classical methods of spectral estimation are based on the Fourier transform. It has an extremely good frequency localisation but the time information is lost.

A wide range of electrophysiological signals falls into non-stationary signals whose frequency content changes over time. Such non-stationary makes the Fourier transform limited when the different window widths are needed to meet a desired resolution in time and frequency. During last decades, various time-frequency methods have been proposed. Short time Fourier transform (STFT), Hilbert transform and wavelet transform seem to be increasingly applied in dynamic neurophysiological signal analysis (Tuncel et al. 2010, Bruns 2004, Li et al. 2004, Zhan et al. 2006, Le Van Quyen et al. 2001, Le Van Quyen & Bragin 2007, Hassan et al. 2010). The STFT and the wavelet transform are used in time-frequency analysis of non-stationary signals. However, the major difference between the STFT and wavelet transform is the fixed width of the window used in the STFT but scale-dependent in the wavelet transform. Due to this difference, STFT allows only

a fixed time-frequency resolution. On the other hand, the wavelet analysis has a more precise time-frequency resolution (Addison et al. 2009, Addison 2002, Najmi & Sadowsky 1997), see Figure 2.19.

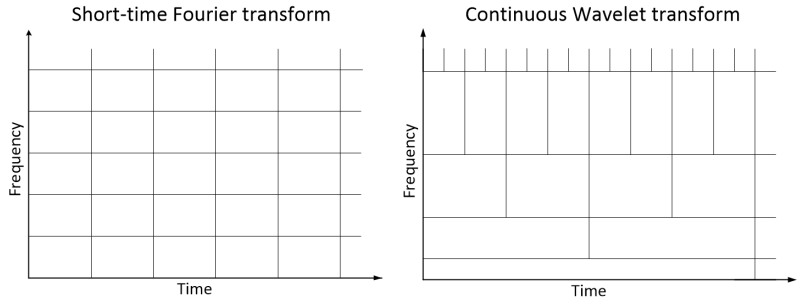

Figure 2.19: Time-frequency localization for STFT(left) and wavelet transform (right).

As described earlier, spectral analysis is traditional analysis of electrophysiological signals (Halliday et al. 1995, 2003). In recent years, wavelet transforms has been a favoured tool for analysing non-stationary electrophysiological signals (Zhan et al. 2006, Brittain et al. 2009). Here, we first review briefly the basic ideas underlying spectral analysis of stationary signals, and also provide a brief overview of the theory of the continuous wavelet transform.

2.2.1 Classical spectral analysis

Spectral analysis is one of the most widely used methods for evaluating physiological and functional states of the nervous system. In general, the investigated time series data or signals are assumed to be stationary. A single stationary signal can be characterised by estimates of the power spectrum or auto-spectrum of an individual signal and gives a frequency description of the signal. Fourier transform is usually used to determine the spectra. The signal is split into L non overlapping disjoint sections each of length T. The finite Fourier transform of the l^{th} segment $(l = 1, ..., L)$ from signal x at frequency λ is denoted by $d_x^T(\lambda, l)$ (Halliday et al. 1995) is defined as

$$d_x^T(\lambda, l) = \int_{(l-1)T}^{lT} x(t)e^{-i\lambda t}dt \approx \sum_{t=(l-1)T}^{lT-1} e^{-i\lambda t}x_t \tag{2.1}$$

The auto-spectrum of the signal is estimated as an average over segments.

$$\hat{f}_{xx}(\lambda) = \frac{1}{2\pi LT}\sum_{l=1}^{L} d_x^T(\lambda, l)\overline{d_x^T(\lambda, l)} \tag{2.2}$$

where $\hat{f}_{xx}(\lambda)$ represents the estimated auto-spectrum of time series x, with similar expressions for the estimated auto-spectrum of time series y, $\hat{f}_{yy}(\lambda)$. T is the segment length and the overbar $'-'$ on $d_x^T(\lambda, l)$ indicates a complex conjugate. The $'\wedge'$ represents an estimate. Similarly, the estimated cross-spectrum between the two signals x and y, $\hat{f}_{xy}$, can be defined by replacing $d_x^T(\lambda, l)$ with $d_y^T(\lambda, l)$ in Eq.(2.2).

The estimates of the auto and cross spectra are used to obtain the estimate of coherence. The coherence is considered as a useful method for studying the relationship between two signals in the frequency domain. Coherence analysis has been especially used to reveal the relation between muscle activity (EMG-EMG) or cortical activity and muscle (EEG-EMG) (Zhan et al. 2006, Farmer et al. 2007, James et al. 2008). The coherence can be defined as the squared magnitude of the cross-spectrum of two data sets, normalised by the product of their auto spectra (Halliday et al. 1995). Coherence functions provide a measure of linear relationship on a scale between 0 and 1 (Farmer et al. 2007). A value of 0 implies no linear correlation, with 1 implying a perfect linear association. The coherence is estimated as

$$|\hat{R}_{xy}^2(\lambda)|^2 = \frac{|\hat{f}_{xy}(\lambda)|^2}{\hat{f}_{xx}(\lambda)\hat{f}_{yy}(\lambda)} \tag{2.3}$$

The complex valued function representing the square root of equation (2.3) is called the coherency and can be estimated by

$$\hat{R}_{xy}(\lambda) = \frac{\hat{f}_{xy}(\lambda)}{\sqrt{\hat{f}_{xx}(\lambda)\hat{f}_{yy}(\lambda)}} \tag{2.4}$$

The complex valued functions can describe the phase relationship between the two signals. Phase information can be used for quantifying coupling between signals recorded simultaneously on different channels. Timing information can be obtained from the phase spectrum (Halliday et al. 1995). The estimated phase spectrum, $\hat{\phi}_{xy}(\lambda)$, is defined as the argument of the cross-spectrum

$$\hat{\phi}_{xy}(\lambda) = arg\{\hat{f}_{xy}(\lambda)\} \tag{2.5}$$

where $\hat{\phi}_{xy}(\lambda)$ can be used when there is significant coherence between the process x and y at frequency λ, and the argument of the estimated cross-spectrum in Eq.(2.5) can be obtained from the arctan function (Halliday et al. 1995).

Some assumptions are required of the data in order to formulate a confidence interval

for coherence estimates. This is essential for determining which values of coherence are significant. The value of the confidence interval may be a threshold value, the confidence interval means that the coherence can be viewed as significant if coherence value exceeds the confidence interval value. If the two signals are assumed independent and having a Gaussian distribution, the distribution of the coherence estimates is given by Gish & Cochran (1988).

$$Pr(R^2 \leq r) = 1 - (1 - r)^{K-1}, \quad 0 \leq r \leq 1 \tag{2.6}$$

where $Pr(.)$ denotes probability distribution function, r is the detection threshold value and K is the number of windows used to estimate the spectrum. For a confidence interval value of 95%, the detection threshold value for this confidence interval is computed as $r_{95\%} = 1 - 0.05^{1/(K-1)}$

2.2.2 Continuous wavelet transforms

As mentioned earlier, neurophysiological signals fall into the category of non-stationary signals whose statistical properties (mean, variance, and higher-order statistics) change with time (Zhan et al. 2006). Wavelet transforms are one of the most popular alternative time-frequency methods that can be used for analysing time series that contain non-stationary power at different frequencies (Torrence & Compo 1998). There are a number of wavelet families that are used in order to identify the appearance of oscillations and other signal properties. Wavelets can be shifted in time along the input signal. Also, they can be stretched or squeezed using a variable wavelet width for changing temporal and spectral resolution. Continuous wavelet transform (CWT) is used to explore the details of a continuous signals. Currently, the CWT are more widely used for the analysis of modulated oscillatory signals and discontinuities (Lilly & Olhede 2010).

To compute the CWT, the wavelet function called the mother wavelet is used as a basis function. A mother wavelet, $\psi(t)$ must be zero-mean and have finite energy defined as

$$\int_{-\infty}^{\infty} \psi(t)dt = 0 \tag{2.7}$$

$$E = \int_{-\infty}^{\infty} |\psi(t)|^2 dt = \infty \tag{2.8}$$

The CWT of a signal $x(t)$, $W_x(a, b)$, is defined as the convolution of $x(t)$ with a scaled

and translated version of a mother wavelet function:

$$W_x(a,b) = \int_{-\infty}^{\infty} x(t)\psi^*_{a,b}(t)dt \tag{2.9}$$

The scaled and translated version of the mother wavelet is denoted by

$$\psi_{a,b}(t) = \frac{1}{\sqrt{a}}\psi\left(\frac{t-b}{a}\right) \tag{2.10}$$

where a and b denote the scaling parameter and the translation parameter, respectively, and * denotes complex conjugate. Note that scale a should be greater than zero because negative scaling is not defined. When the scale a is adjusted, different frequency components in the signal can be extracted.

The CWT can be presented as a time-frequency representation of the signal by converting the wavelet with unit scale a scale to a characteristic frequency of the wavelet, f_0, defined as the passband centre or the central frequency of the wavelet energy spectrum (Zhan et al. 2006). The spectral components are inversely proportion to the scale a. The frequency associated with the scale a is defined by Addison et al. (2009):

$$f = \frac{f_0}{a} \tag{2.11}$$

and the time-frequency CWT expression can be given as

$$W_x(\tau, f) = \sqrt{\frac{f}{f_0}} \int_{-\infty}^{\infty} x(t)\psi^*\left(\frac{t-\tau}{f_0}\right) dt \tag{2.12}$$

where $a = f_0/f$ and $b = \tau$.

In theory, there are many wavelets with different characteristics. In practice, selecting appropriate wavelet is an important step. In case of the CWT, the Morlet wavelet is a popular choice of mother wavelet function for construction of the CWT (Najmi & Sadowsky 1997).

Morlet wavelet

The Morlet wavelet is complex valued and is often used in neurophysiological signal analysis (Li et al. 2004, Zhan et al. 2006, Hassan et al. 2010, Lachaux et al. 2002). The Morlet wavelet is commonly and widely used for spectral estimation (Lachaux et al. 2002, Li et al.

2004, Zhan et al. 2006, Allen & Mackinnon 2010, Kopal et al. 2014). The Morlet wavelet consists of a complex wave within a Gaussian envelope. The Morlet wavelet can be defined as

$$\psi(t) = \frac{1}{\sqrt[4]{\pi}} \left(e^{i2\pi f_0 t} - e^{-\frac{(2\pi f_0)^2}{2}} \right) e^{\frac{-t^2}{2}} \tag{2.13}$$

where f_0 is the central frequency of the mother wavelet. The second term in the brackets is known as the correction term which becomes negligible for values of radian frequency ($2\pi f_0 > 5$) (Addison et al. 2009) and can be ignored in practice. Previous studies have concentrated on the Morlet wavelet with $2\pi f_0 = 6$ (Torrence & Compo 1998). Similarly, values of $2\pi f_0$ between 5 and 6 are also commonly used in practice (Addison 2002). Therefore, a simple Morlet wavelet becomes

$$\psi(t) = \frac{1}{\sqrt[4]{\pi}} e^{i2\pi f_0 t} e^{\frac{-t^2}{2}} \tag{2.14}$$

The Morlet wavelet in Eq.(2.14) is a complex exponential within a Gaussian envelope, normalised by $\frac{1}{\sqrt[4]{\pi}}$. The Fourier transform of the Morlet wavelet is

$$\Psi(f) = \frac{1}{\sqrt[4]{\pi}} \sqrt{2} e^{-\frac{1}{2}(2\pi f - 2\pi f_0)^2} \tag{2.15}$$

In practice, the Morlet wavelet with $f_0 = 0.849$ Hz ($2\pi f_0 = 5.33$ rad/s) is often used. The Morlet wavelet with $f_0 = 0.849$ and its Fourier transform are shown in Figure 2.20.

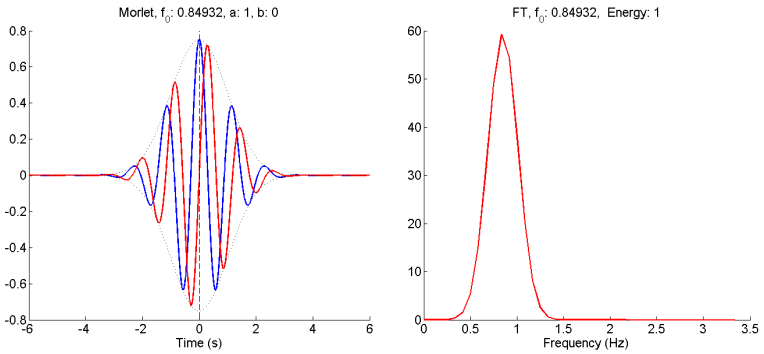

Figure 2.20: Morlet wavelet, $f_0 = 0.849$. The plot on the left gives real part (blue) and imaginary part (red) in the time domain. The plot on the right gives the corresponding function in frequency domain.

Using the well-known property of the Fourier transform and employing the convolution method, the CWT can also be represented in the frequency domain as the product of the

Fourier transform of the signal $X(f)$ and the wavelet transform $\Psi(f)$ (Zhan et al. 2006):

$$W_x(a,b) = \sqrt{a}\int_{-\infty}^{\infty} X(f)\Psi^*(af)e^{i2\pi fb}df \tag{2.16}$$

The frequency domain description of the CWT indicates that the wavelet acts as a band-pass filter with its width inversely proportional to wavelet scale. In the wavelet literature, the squared modulus of the wavelet transform is referred to as the wavelet power spectrum (Brittain et al. 2007). It is defined as:

$$S_{xx}(\tau, f) = |W_x(\tau, f)|^2 \tag{2.17}$$

Eq.2.17 is also called auto-spectra of x. The wavelet cross spectrum (the cross-wavelet-periodogram) between two signals, x and y may be constructed as:

$$S_{xy}(\tau, f) = W_x(\tau, f)W_y^*(\tau, f) \tag{2.18}$$

Transferring a concept of Fourier analysis, the wavelet power spectrum is apparent that such a quantity is in fact analogous to the periodogram (Brittain et al. 2007). To generate an estimate of the wavelet spectrum, wavelet-periodogram must undergo some form of smoothing either by ensemble averaging or locally in the time-frequency plane (Brittain et al. 2007).

When the continuous wavelet function is complex-valued, the CWT, $W_x(\tau, f)$, is also a complex-valued function which can be separated into its real part, $\Re\{W_x(\tau, f)\}$, and its imaginary part, $\Im\{W_x(\tau, f)\}$. Alternatively, the complex-valued wavelet function based on the complex variable can be defined as

$$W_x(\tau, f) = |W_x(\tau, f)|e^{i\phi_x(\tau,f)} \tag{2.19}$$

The wavelet coefficients can be described by an amplitude, $|W_x(\tau, f)|$, and phase, $\phi_x(\tau, f)$, which are

$$|W_x(\tau, f)| = \sqrt{\Re\{W_x(\tau, f)\}^2 + \Im\{W_x(\tau, f)\}^2} \tag{2.20}$$

$$\phi_x(\tau, f) = tan^{-1}\frac{\Im\{W_x(\tau, f)\}}{\Re\{W_x(\tau, f)\}} \tag{2.21}$$

The complex wavelet is necessary in order to separate the phase and amplitude information. Without the complex wavelet function, the phase is undefined.

The Heisenberg uncertainty principle

The uncertainty principle is one of the most famous idea in physics. Here, the Heisenberg uncertainty principle addresses the problem of the simultaneous resolution in time and frequency that can be attained when measuring a signal (Addison 2002). It is used to define the lower limit of time-frequency windowed resolution (Najmi & Sadowsky 1997). The spread of the wavelets in time-frequency plane can be represented by boxes that are known as Heisenberg boxes (Addison 2002). The Heisenberg boxes for the wavelet transform depend on the scale parameter a. Changing scale ,a, alters width of wavelet in time and frequency. The relationship between a and f is obtained by computing an exact expression for the response to a sinusoid (Najmi & Sadowsky 1997). This response is peaked at $a = f_0/f$, and so frequency and scale are related by Eq.(2.11). In order to describe the time-frequency localisation properties of the CWT, a time width and a frequency width of the window function or a standard deviation (radius) in time and frequency of the wavelet are denoted by σ_t and σ_f, respectively. Specifically, the product of $\sigma_t\sigma_f$ must greater than or equal to $1/4\pi$ (Addison 2002). The Heisenberg uncertainty principle establishes the lower bound as $\sigma_t\sigma_f \geq \frac{1}{2}$. The dilated wavelet at scale a has time width and frequency width equal to $a\sigma_t$ and σ_f/a, respectively. This implies that the CWT has a difference temporal and spectral resolution at each scale a although the area of the Heisenberg box is constant. Figure 2.21 shows variable resolution in time-frequency plane for the continuous wavelet transform at various scales. The spread of the energy densities of the wavelets in time domain ($|\psi_{a,b}(t)|^2$) and frequency domain ($|\psi_{a,b}(f)|^2$) can be quantified using σ_t and σ_f, respectively (Addison 2002). The Heisenberg boxes stretch for large scales which correspond to low frequencies, whereas the boxes compress for small scales which relate to high frequencies. To sum up, small scales lead to increased temporal resolution and decreased spectral resolution at high frequencies, whereas large scales give increased spectral resolution and decreased temporal resolution at low frequencies.

Cone of influence

Edge effects are common in the processing of finite-length time series. In the case of wavelet analysis, the CWT applied to a finite-length signal is usually calculated by the convolution of the signal with the wavelet function. The convolution theorem suffers from edge effects. This is due to the fact that errors will occur at the beginning and end of the wavelet transform. The region of the wavelet transform affected by edge effects is called

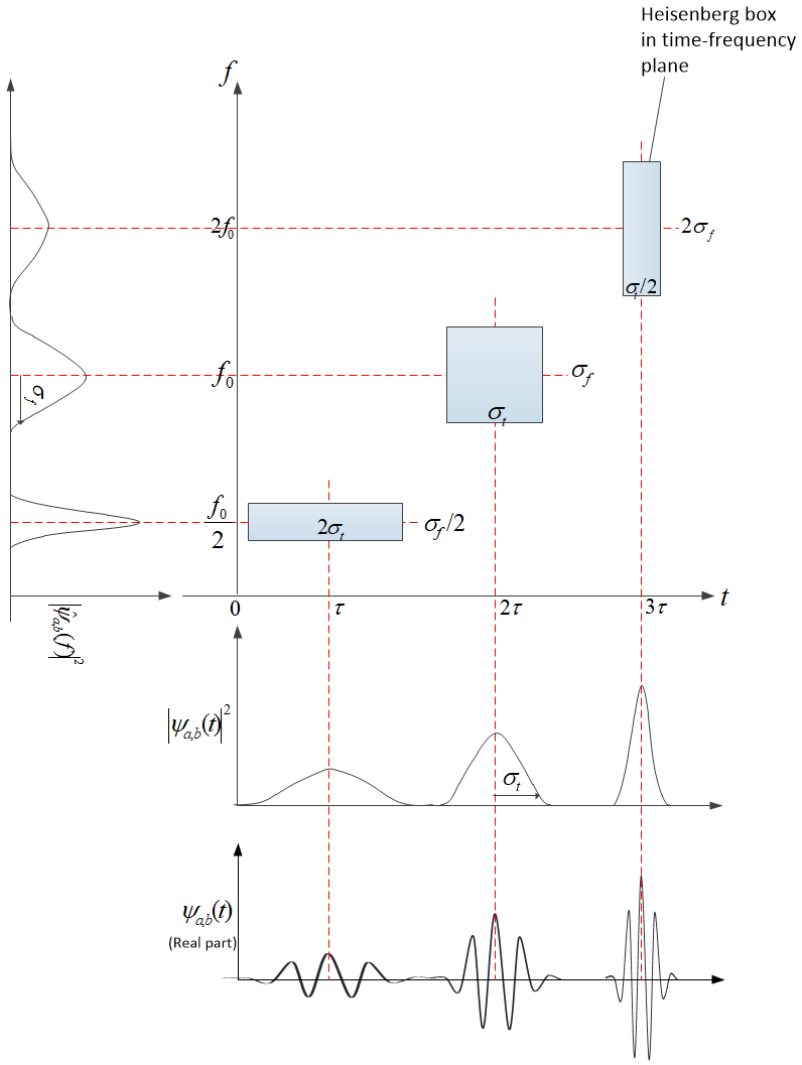

Figure 2.21: Heisenberg boxes in the time-frequency plane for the continuous wavelet transform at various scale, $a = \frac{1}{2}$, 1 and 2. Figure adapted from (Addison 2002).

the cone of influence (COI). Regions outside the COI are neglected due to edge effects.

The definition of the COI for the Morlet wavelet uses the e-folding time $\tau_a = \sqrt{2}a$ which is selected so that the wavelet power for a discontinuity at the edge drops by a factor e^{-2} (Torrence & Compo 1998).

Examples of the COI are indicated in Figure 2.22. We generate the testing signals by adding spike at the beginning and the end of 1-s and 5-s length, see Figure 2.22(top). The wavelet power spectra of testing signals in Figure 2.22(bottom) show power at the beginning and the end. The COI is indicated in Figure 2.22(bottom) by the white curved line, which can identify the possible region affected by edge effects. The power at the beginning and the end from Figure 2.22(bottom) are outside the COI that are neglected due to edge effects. These examples suggest that longer-length time series have wider

region within the COI and are less affected by edge effects.

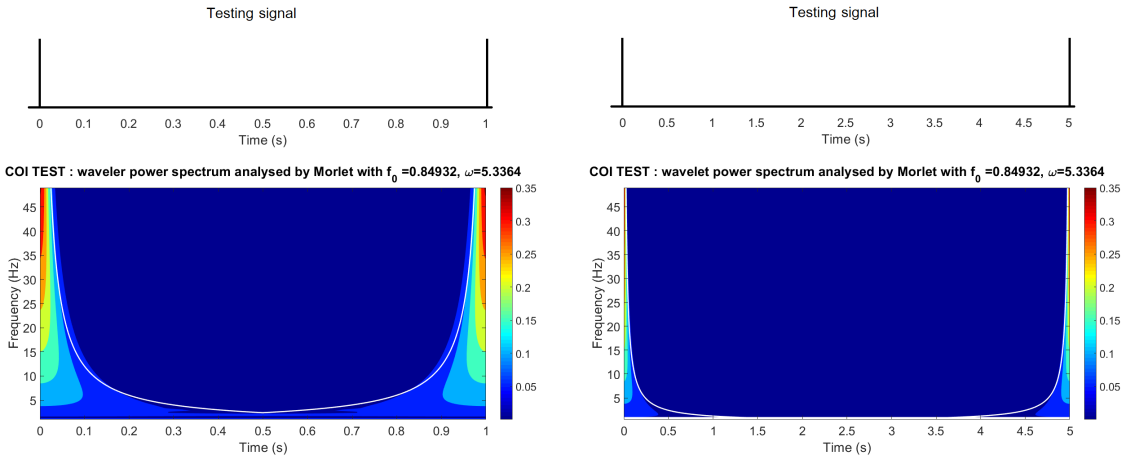

Figure 2.22: Examples of COI for wavelet power spectrum of 1-s (left) and 5-s length testing signal (right): The white curved line on contour plot indicates the COI.

2.3 Summary

This chapter is divided into two main sections. The first starts with the main section of neuroscience review (section 2.1). This section describes the background information about the neurological system underlying human locomotion in health and disease such as Parkinson's disease. Nervous system which includes i) the important brain regions involved in controlling movement in human, ii) spinal cord and neural circuits in the spinal cord − central pattern generators (CPGs), iii) neurons and the electrical properties of neuronal communication are provided in section 2.1.1. Section 2.1.2 provides details of human muscles, in particular skeletal muscles involved in walking. Section 2.1.3 describes an organisation of the neural structures controlling locomotion and sequence of basic human walking processes. Electromyogram (EMG) and normal EMG patterns of the muscles are described in section 2.1.4. In this thesis, EMG recordings from TA muscle are used as a substitute to pairs of motor unit recordings that may identify a modulation exists in the functional coupling during walking and provide a basis for investigating highly adaptive nature of human gait patterns (Halliday et al. 2003). In walking, the TA muscle is active during the swing phase and early stance phase which takes place around HS (Woollacott et al. 1986, Halliday et al. 2003, van Asseldonk et al. 2014, Artoni et al. 2017). Neuroscience review section ends with one of neurological degenerative diseases, Parkinson's disease (PD) which is common neurodegenerative and well-known movement disorders.

This is a disease with increasing prevalence in old age. Symptoms start to appear when neurons in the brain cannot produce enough of the chemical dopamine to control movement properly. The second main section (section 2.2) is to review fundamental of signal processing. The basic concept and necessary conditions of classical spectral analysis and continuous wavelet transforms are explained. Initially, classical spectral based Fourier analysis is considered. Complex continuous wavelets are one of alternative time-frequency methods for non-stationary analysis. Morlet wavelet is popular complex wavelet in the use of time-frequency techniques in processing non-stationary electrophysiological signals (Lachaux et al. 2002, Li et al. 2004, Zhan et al. 2006, Allen & Mackinnon 2010, Kopal et al. 2014). The Heisenberg uncertainty principle and cone of influence are important features of wavelet analysis. The Heisenberg uncertainty principle is used to define the lower limit of time-frequency windowed resolution (Najmi & Sadowsky 1997). The COI is used to identify the region of the wavelet transform affected by edge effects. Regions outside the COI are neglected due to edge effects. The basic concepts and necessary conditions of classical spectral analysis and continuous wavelet transforms described in this chapter are useful knowledge for understanding time-frequency analysis techniques based on analytic wavelets which will be presented in chapter 4.

Chapter 3

Experimental methods and data sets

3.1 Introduction

Human locomotion can be characterised by rhythmic activity that is governed by a series of complex interactions between the human brain and the spinal cord. These interactions can be analysed by recording electromyograms (EMG) from human muscles (Halliday et al. 2003, Petersen et al. 2010, Lodha et al. 2017). An analysis of human movement is a process to investigate the characteristics of human body movement that relates to both normal and abnormal movement (Farmer et al. 2007, Tuncel et al. 2010). Understanding human movement or how the brain controls the muscles could help in recognising the first stages of many movement disorders, such as Parkinsons disease.

Human locomotion is generated by successful initiation of gait and the continuation of steady state gait. Gait initiation is a transient procedure between a standing posture and steady-state walking. The task of gait initiation is to generate a momentum and to maintain a balance. Steady state gait is characterized by continuous gait cycles. Most studies in human walking have focused on the steady-state walking (Gwin et al. 2011, Petersen et al. 2012, Fu et al. 2014, Artoni et al. 2017). Petersen et al. (2012) and Artoni et al. (2017) report that the motor cortex and corticospinal tract contribute directly to the muscle activity observed during the periods of steady-state treadmill walking in human subjects. The task of steady-state walking provides opportunity for studying human movement and possible modifications made by age, disease, or environment.

Traditionally, gait analysis data was collected during overground walking using force

plates, 3D motion capture, and EMG (Papegaaij & Steenbrink 2017). Walking overground is more natural than walking on a treadmill. However, the use of treadmills has been increasing in order to study the neural control of human locomotion (Halliday et al. 2003, Gwin et al. 2011, Petersen et al. 2012, Castermans & Duvinage 2013, Castermans et al. 2014, Artoni et al. 2017). In clinics, the treadmill is commonly used as a tool for rehabilitation, exercise, and walking ability assessment (Khademi-Kalantari et al. 2017). Benefits of using treadmill walking for investigation of normal and pathological gait are optimal control of experimental environment, simpler use of monitoring equipment, and assessment of long-distance locomotion in a limited working volume (Carpinella et al. 2010). A number of previous studies have suggested that subjects demonstrated trends for a higher cadence, shorter step lengths and reduced preferred walking speed on a treadmill compared with overground walking (Warabi et al. 2005, Lee & Hidler 2008, Carpinella et al. 2010, Papegaaij & Steenbrink 2017). Moreover, human walking on treadmill produces a more stable and predictable gait pattern compared with overground walking (Warabi et al. 2005, Hollman et al. 2016, Papegaaij & Steenbrink 2017). It is thus thought that the treadmill might have been regulating the gait process, limiting the variability usually found in overground walking (Arsenault et al. 1986). In term of muscle activation (EMG) patterns, numerous studies reported that EMG amplitude obtained from treadmill data was slightly higher, but with lower variation than overground data (Murray et al. 1985, Arsenault et al. 1986, Khademi-Kalantari et al. 2017). Although, (Papegaaij & Steenbrink 2017) suggested that differences between treadmill and overground walking are small and typically not clinically relevant, awareness of differences between treadmill and overground are an important concern since the data from these two paradigms are employed in physiological and patho-physiological studies (Carpinella et al. 2010).

Here, we focus on the period of steady-state walking both on treadmill and overground walking. Details of experiment data and framework analysis are provided in section 3.2 and 3.3, respectively.

3.2 Data

3.2.1 Treadmill locomotion data

Data were taken from a previous study of Halliday et al. (2003). 10 of 17 experiments were successfully performed over 5 healthy subjects, age $21 - 41$ yrs, in accordance with

the Helsinki declaration. Informed consent was obtained from each participant prior to participation. Data from 7 experiments were rejected due to cross-talk between EMG recordings.

Paired bipolar surface EMG recordings (Ag-AgCl electrodes; 1 cm^2 recording area; 2 cm between poles) were obtained from two sites over the belly of tibialis anterior (TA) muscle separated by a minimum distance of 10 cm during treadmill walking. The EMG signals were amplified (gain $\sim$5 k$-$10 k), filtered (1 Hz$-$1 kHz), and stored as waveforms on a computer for later off-line analysis.

For each recording session, participants were required to maintain treadmill walking. Walking speed was constant and adjusted for each participant individually ranging from 2.9 to 3.8 km/h. All participants were familiar with treadmill walking and were given no additional instruction. A foot switch was placed under the heel of the foot to provide the precise time of heel contact during each step cycle. Recordings were made over a period of 500 seconds. All data were digitally sampled at a rate of 1 kHz or 5 kHz. A summary of the human treadmill locomotion dataset is provided in Table 3.1.

Table 3.1: Summary of dataset from healthy human treadmill locomotion experiments.

Experiment subject	Task (km/h)	Trigger count	Sampling rate (Hz)
405k1010	Walk 3.1	389	1000
406k1004	Walk 2.9	422	1000
406k1006	Walk 3.1	447	1000
417k1001	Walk 3.8	433	5000
417k1003	Walk 3.8	442	5000
418k1002	Walk 3.7	434	5000
418k1003	Walk 3.8	437	5000
419kt002	Walk 3.6	421	5000
419kt003	Walk 3.6	420	5000
419kt004	Walk 3.7	427	5000

3.2.2 Overground locomotion data

Data were taken the work of Weersink (2016), where full details of the experimental protocol can be found. 16 healthy human subjects and 9 PD patients with age < 70 years participated in the gait experiment after giving written informed consent. All healthy

subjects had no history of neurological disorder. They were excluded if they: (i) showed co-morbidity limiting walking ability, (ii) were using medication that influenced movement, or (iii) had an mini mental state exam (MMSE) score of 26 or lower. Patients with PD were confirmed to take part in the gait experiment using the following criteria: (i) PD diagnosis according to the UK Parkinson's Brain disease Society Brain Bank Criteria, (ii) able to walk properly (Hoehn & Yahr scale: stage 2-3), (iii) right handedness according to the Annett Handedness scale, (iv) self-reported absence of freezing of gait (FoG), (v) score of zero on (Dutch translation of) Giladi's FoG questionnaire, and (vi) absence of FoG on clinical examination during rapid bidirectional 360° turns and dual tasking. Participants were excluded if they: (i) suffered from another neurological or motor disorder, (ii) used medication influencing movement (other than PD), or (iii) had tremor-dominant PD. The healthy control group and PD patient group had similar age, height, weight, and sex. In addition, step frequency, stride time, stride time coefficient of variation, and swing time symmetry ratio did not differ between groups. In this thesis, 2 healthy subjects were considered unacceptable for use and were excluded from analysis because there are too many bad segments. Another 2 subjects were excluded because fewer than 100 heel strike were extracted. 1 PD patient was excluded due to technical and data collecting difficulties during the experiment. In total, 12 healthy human subjects and 8 PD patients were included for further analysis.

Paired bipolar surface EMG recordings were made from the belly of the TA muscle. EMG sensors placement and locations for obtaining EMG from TA muscle were based on the SENIAM (Surface Electromyography for the Non-Invasive Assessment of Muscles) recommendations (http://www.seniam.org). The two electrode pairs on the TA were separated by at least 10 cm to minimise the risk of cross-talk between the two pairs of recording electrodes. The subjects' skin was prepared and cleaned prior to attachment of the surface electrodes. For preparation, 3 healthy controls and 2 PD patients were asked to perform a few steps on a flat ground for investigating where and how to place all electrodes and accelerometers (ACC). A wireless EMG system was used to collect the data. EMG signals were amplified and digitally converted at a sampling rate of 256 Hz or 1024 Hz using a portable amplifier (Compumedics Neuroscan, Siesta) and sent to Profution EEG 5.0 software (Compumedics Neuroscan, Siesta) on a computer for visual on-line display and later off-line analysis.

In each of the recording sessions, overground walking was performed at each partici-

pant's preferred speed (normal and comfortable speed). Each subject was asked to walk through a hallway of length 150 m in a straight line from start to finish and back. To obtain the time of heel strike (HS) and toe-ff (TO) during walking, tri-axial ACCs were attached to the left and right ankles and one ACC was placed on the back of the lower trunk. The ACC data were recorded together with the EMG data using Profusion EEG 5.0 software. Weersink (2016) determined the time-points of HS and TO using the algorithm described by Sejdić et al. (2016). Full details of the experimental procedure are in the original study of Weersink (2016). A summary of the human overground locomotion datasets is provided in Table 3.2.

Table 3.2: Summary of dataset from human overground locomotion experiments.

Experiment subject	Group	Trigger count	Sampling rate (Hz)
#6	Healthy	128	256
#7	PD Patient	153	256
#8	PD Patient	131	256
#10	Healthy	117	256
#11	Healthy	155	1024
#12	PD Patient	134	256
#14	PD Patient	131	256
#15	Healthy	136	256
#16	Healthy	98	256
#17	PD Patient	108	1024
#18	PD Patient	111	1024
#19	Healthy	137	1024
#20	PD Patient	163	1024
#21	Healthy	160	1024
#23	PD Patient	133	1024
#24	Healthy	103	1024
#25	Healthy	135	1024
#26	Healthy	124	1024
#27	Healthy	114	1024
#28	Healthy	133	1024

3.3 Data analysis

In walking, the TA muscle is active during the swing phase and early stance phase which takes place around HS (Woollacott et al. 1986, Halliday et al. 2003, van Asseldonk et al. 2014, Artoni et al. 2017). The swing phase for every step is the segment between 60% and 100% of the gait cycle, where 0 and 100% indicate heel strike of the leg, see more details in chapter 2, section 2.1.4. In this thesis, HS for every single step are used to segment the EMG activity.

For treadmill locomotion data, Halliday et al. (2003) suggested that the TA muscle was active during swing for a period from 550 ms prior to HS until 100 ms after HS. In this thesis, if the segment length is made sufficiently large, the edge effects due to the wavelet signal processing should not be a problem. Thus, all steps are segmented into 1040 ms non-overlapping segments with 820 ms before HS and 220 ms after HS. For overground locomotion data, Weersink (2016) used the segment of 600 ms before HS until 100 ms after HS for TA-EMG/EMG coherence analysis, which corresponds to both swing and early stance phase. Here, the complete EMG data are split into 1000-ms segments, 750 ms prior to and 250 ms after HS. It is important to note that a few bad segments from overground walking are removed manually after visual inspection of the data. Prior to analysis, sEMG signals are full-wave rectified in order to allow the detection of motor unit firing patterns (Halliday & Farmer 2010, Ward et al. 2013). Examples of raw and rectified TA-EMG signals showing HS and analysis window taken from a healthy subject during treadmill locomotion and healthy and PD subjects during overground locomotion are illustrated in Figure 3.1 and 3.2, respectively.

From each walking session, individual records are analysed using the novel time-frequency analysis framework using coherence, phase locking value, and time-resolved phase-amplitude coupling via analytic wavelets for investigating and characterising non-stationary neurophysiological data. These methods are described in detail in chapter 4. The method of population or pooled analysis is then used to provide an overall summary of each subject group. A Wilcoxon rank-sum test is used to compare healthy controls and PD patients, especially in overground walking data analysis. The results from these data analysis are provided in chapter 5.

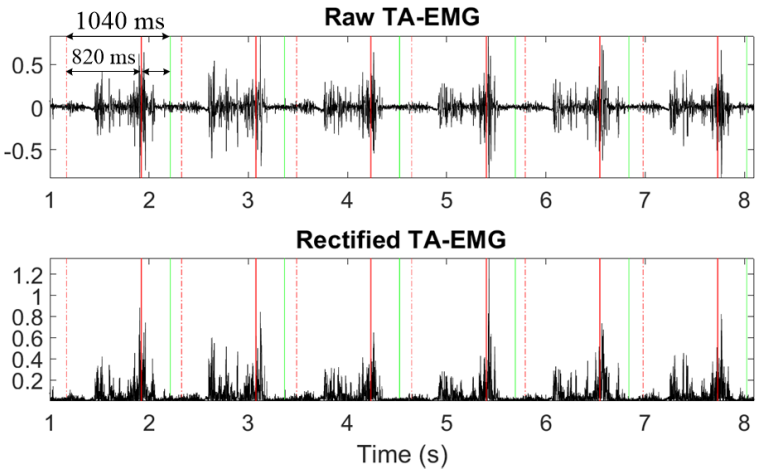

Figure 3.1: An example surface EMG signals obtained from one subject during treadmill walking, with (top) raw EMG signal and (bottom) rectified EMG signal showing analysis windows. Dash-dot red lines depict beginning of analysis window, green lines depict the end of analysis window and solid red lines depict moments of heel strike.

3.4 Summary

In this chapter, we have provided the detail of experiment data and data analysis. In brief, the treadmill dataset was collected from age matched healthy subjects, and overground datasets were collected from healthy subjects and PD patients. Paired surface EMG electrodes were placed over two sites on the ankle flexor TA. The two EMG signals over the ankle flexor can be used as a substitute for pairs of motor unit recordings that can identify any modulation in the functional coupling during walking, and provide a basis for investigating the highly adaptive nature of human gait patterns (Halliday et al. 2003). A contact switch or accelerometer signals identified heel strike. Thresholding of the heel strike record provides a sequence of trigger times. These trigger times provide a reference point within each step cycle which is used to segment the data for undertaking time-frequency analysis, where time is defined with respect to heel contact as illustrated in Figure 3.1 and 3.2. Further details of time-frequency measures used in this thesis are given in the next chapter.

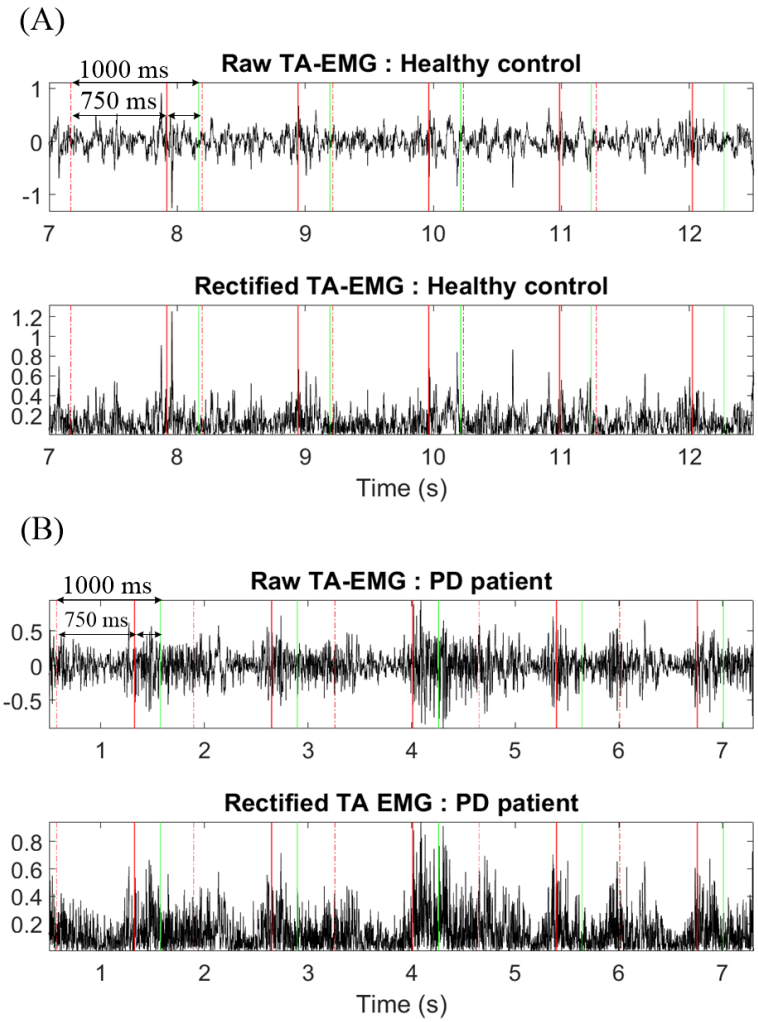

Figure 3.2: Examples of surface EMG signals obtained from (A) healthy subject and (B) PD patient during overground walking, with (top) raw EMG signal and (bottom) rectified EMG signal showing analysis window. Dash-dot red lines depict beginning of analysis window, green lines depict the end of analysis window and solid red lines depict moments of heel strike.

Chapter 4

Time-frequency analysis techniques based on analytic wavelets

Wavelet transforms provide a powerful time-frequency analysis framework which is increasingly applied in non-stationary of electrophysiological signals analysis (Le Van Quyen et al. 2001, Zhan et al. 2006, Brittain et al. 2007, Tuncel et al. 2010, Hassan et al. 2010, Aguiar-Conraria & Soares 2014). The wavelet transform is a localised transform in both time and frequency. This can be achieved by mapping a one-dimensional signal in the time domain into a two dimensional representation in time-frequency product space (Addison 2002). In recent years, analytic continuous wavelet transform − generalized Morse wavelets, have become a popular time-frequency analysis technique (Brittain et al. 2007, Lilly & Olhede 2012, Wang & Gao 2013, Aguiar-Conraria & Soares 2014). The generalized Morse wavelets are complex-valued analytic wavelet transforms containing information on both amplitude and phase, see more details in section 4.1 and Lilly & Olhede (2010).

In this chapter we consider some of the issues emerging from the analytic continuous wavelet analysis of measures such as coherence spectra, phase coherence or phase synchronisation and phase-amplitude coupling. Wavelet coherence analysis is one of the methods used to study the neural activity or interactions within nervous system i.e. the relationship between simultaneously recorded neural and muscular data (Zhan et al. 2006, Brittain et al. 2007). Coherence analysis depends on two factors: phase consistency and amplitude covariation of signals (Le Van Quyen et al. 2001). Phase synchronisation is

an alternative approach to spectral coherence. It provides the phase component that can be obtained separately from the amplitude component for a given frequency or frequency range (Le Van Quyen et al. 2001). Phase synchronisation is used to study phase relationships between physiological signals (Le Van Quyen & Bragin 2007, Lowet et al. 2016). In recent decades, wavelet phase synchronisation analysis based on Morlet wavelet transform has been developed and applied to MEG signals (Simões et al. 2003).

There is increasing interest in clarifying the interactions between neuronal oscillations of different frequencies (Tort et al. 2008, Onslow et al. 2011, Canolty et al. 2012, Voytek et al. 2013, Nakhnikian et al. 2016, Vaz et al. 2017). This form of interaction is commonly called cross-frequency coupling (CFC). One type of CFC, known as phase-amplitude coupling (PAC) or nested oscillation, occurs when the amplitude of a high frequency oscillation is modulated by the phase of a low frequency oscillation. More recently, several methods have been used to evaluate PAC on electrophysiology recordings such as electroencephalogram (EEG), local field potential (LFP) and other brain recordings (Penny et al. 2008, Tort et al. 2010, Canolty & Knight 2010, Canolty et al. 2012, Voytek et al. 2013, Pittman-Polletta et al. 2014, Dvorak & Fenton 2014, Nakhnikian et al. 2016, Samiee & Baillet 2017). Most methods investigate PAC in the frequency domain and require long segments of experimental data. Other methods for time-resolved measures of PAC between neural oscillations, referred to as event-related phase-amplitude coupling (ERPAC) (Voytek et al. 2013) and time-resolved phase-amplitude coupling (tPAC) (Samiee & Baillet 2017), are proposed. ERPAC is designed to capture the temporal evolution of task-related changes in PAC across events or between distant brain regions (Voytek et al. 2013). tPAC provides a new approach which claims high temporal resolution with capacity for estimating coupling strength, and low sensitivity to noise conditions, even for shorter data lengths (Samiee & Baillet 2017).

A unified framework as described in chapter 1 which includes three different methods of time-frequency analysis based on generalized Morse wavelets is proposed for investigating and characterising non-stationary neural coupling mechanisms underlying human locomotion. The framework uses wavelet spectra and coherence, wavelet phase locking value, and wavelet time-resolved phase-amplitude coupling. In addition, a new technique is applied to wavelet coherence and wavelet phase locking value for removal of low frequency components due to EMG envelope modulation. All three measures are derived from the same two-parameter family of generalized Morse wavelets. The use of a common

framework should facilitate comparison between the measures.

The structure of this chapter is organised as follows. First, generalized Morse wavelets are introduced. Second, a review of methodologies, with details about each of the required steps for their implementation is introduced. The three analysis methods are then studied via numerical simulation.

4.1 Generalized Morse wavelets

The choice of wavelet correlates to field of application or signal of interest. A broad class of neurophysiological signals may be modeled as modulated oscillations, using analytic signals. Continuous complex-valued wavelet transforms play a key role in analysis of modulated oscillatory signals (Lilly & Olhede 2010). As mentioned in chapter 2 pp.30, the Morlet wavelet is a commonly used complex-valued wavelet. However, the Morlet wavelet is only approximately analytic wavelet for sufficiently large radian frequency (Lilly & Olhede 2010, Wang & Gao 2013). As reported by Lilly & Olhede (2009), generalized Morse wavelets are a promising class of complex-valued exactly analytic wavelet transform with vanishing support on the negative frequency axis. The analyticity of wavelets ($\Psi(\omega) = 0$ for $\omega < 0$) is important for the analysis of strongly modulated signals, where the wavelets are required to be very narrow in time for matching the modulation timescale. Figure 4.1 and 4.2 illustrate examples of the desirable aspect for the analytic properties of the wavelet transform − a generalized Morse wavelet and a Morlet wavelet, together with their Wigner-Ville distributions[1] and instantaneous frequencies[2]. Figure 4.1 shows that these two wavelets appear indistinguishable, and their instantaneous frequencies are very nearly constant when they are fairly long in time (Lilly & Olhede 2009). In order to increase time resolution at the expense of frequency resolution, these two wavelets are reduced in time, see Figure 4.2. The Morlet wavelet's Wigner-Ville distribution exhibits leakage to negative frequencies, and its instantaneous frequency tends to fluctuate over the central window. While the generalized Morse wavelet remains analytic, its Wigner-Ville distribution has support at positive frequencies, and its instantaneous frequency is nearly constant over the central window as seen in Figure 4.2. The generalized Morse wavelets may be the best

[1] A fundamental time-frequency object which expresses the smoothing implicit in the wavelet transform (Lilly & Olhede 2009)

[2] A quantity which refects the time-varying frequency content of a modulated oscillatory signal (Lilly & Olhede 2009)

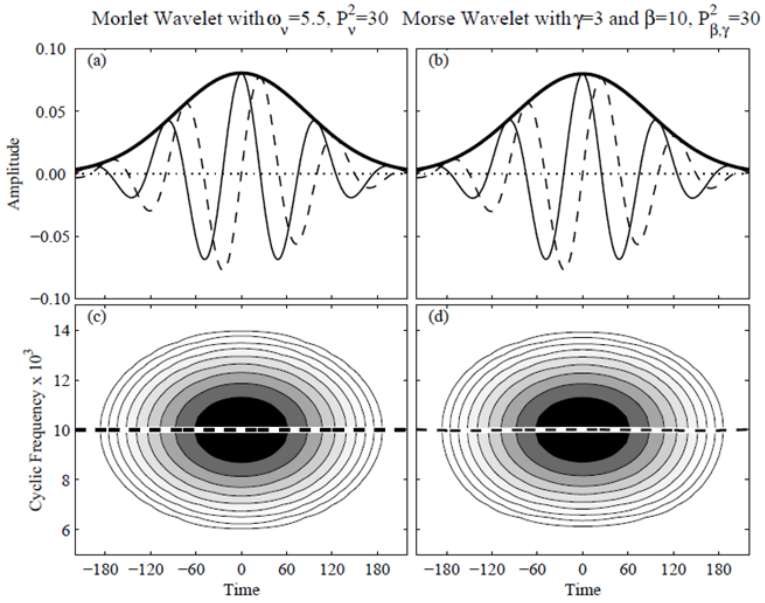

Figure 4.1: (a) Morlet wavelet with ω_v=$2\pi f_0$ =5.5 rad/s, see an expression for P_v^2 along with further details of the Morlet wavelet in text , (b) generalized Morse wavelet with $P_{\beta,\gamma}^2 = \beta\gamma$, and their respective Wigner-Ville distributions (c,d). In (a) and (b), the thick solid, thin solid, and dashed lines correspond to the magnitude, real part, and imaginary part, respectively. In (c) and (d), ten logarithmically spaced contours are drawn from the maximum value of the distribution to 1% of the value. Also, the tick dash lines in (c,d) are the wavelet instantaneous frequencies. (Images from Lilly & Olhede (2009))

choice for application to very time-localized structures compared to the Morlet wavelet, see Lilly & Olhede (2009), Olhede & Walden (2002) for details.

The generalized Morse wavelets are highly flexible and form a two-parameter family of wavelets. β and γ are two parameters controlling time-frequency localisation. The parameter β controls the time-domain decay, and γ controls the frequency-domain decay. Also, β and γ can be interpreted as a compactness parameter and a symmetry parameter, respectively (Lilly & Olhede 2009). Normally, β and γ are greater than zero. By varying β and γ, the generalized Morse wavelets provide a wide variety of forms. A definition of zeroth-order ($k = 0$) generalized Morse wavelets in the frequency domain form is provided in Olhede & Walden (2003) as

$$\Psi_{\beta,\gamma}(\omega) = \sqrt{2}H(\omega)A_{k;\beta,\gamma}\omega^{\beta}e^{-\omega^{\gamma}} \tag{4.1}$$

where $H(\omega)$ is the Heaviside unit step function and $A_{k;\beta,\gamma}$ is a normalising constant that can be expressed by

$$A_{k;\beta,\gamma} = \sqrt{\pi\gamma 2^{r}\Gamma(k + 1/\Gamma(k + r))} \tag{4.2}$$

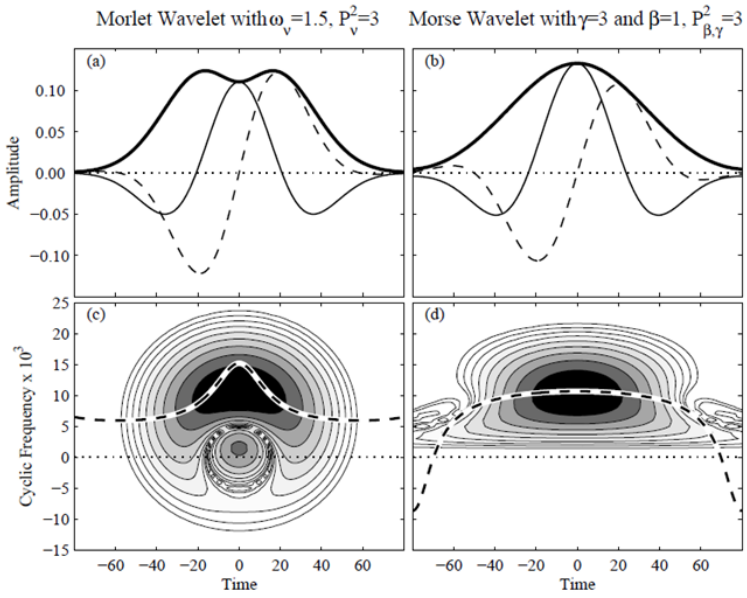

Figure 4.2: As with Figure 4.1, but the time window of wavelets are very narrow. (Images from Lilly & Olhede (2009))

where $\Gamma(\bullet)$ denotes the gamma function and $r = (2\beta + 1)/\gamma$. The maximum amplitude occurs at the peak frequency (Lilly & Olhede 2012),

$$\omega_{\beta,\gamma} \equiv \left(\frac{\beta}{\gamma}\right)^{\frac{1}{\gamma}} \tag{4.3}$$

The rescaled second derivative of the frequency-domain wavelets evaluated at its peak frequency is $P^2_{\beta,\gamma} \equiv \beta\gamma$, and $P_{\beta,\gamma}$ is called the dimensionless wavelet duration (Lilly & Olhede 2010), defined as

$$P_{\beta,\gamma} \equiv \sqrt{\beta\gamma} \tag{4.4}$$

The duration or inverse bandwidth $P_{\beta,\gamma}$ sets the number of oscillations that can fit into the time-domain wavelets centre window at its peak frequency. With increasing β at fixed γ, the wavelet becomes more oscillatory in the time domain or more tightly peaked in the frequency domain (Lilly & Olhede 2010), as seen in Figure 4.4. It is worth to note that Eq. (4.3) and (4.4) are key properties which depend only on two parameters, β and γ.

The time domain form for the generalized Morse wavelets may be expressed by the inverse Fourier transform,

$$\psi_{\beta,\gamma}(t) = \frac{1}{2\pi}\int_0^\infty \sqrt{2}A_{k;\beta,\gamma}\omega^\beta e^{-\omega^\gamma} e^{i\omega t} d\omega \tag{4.5}$$

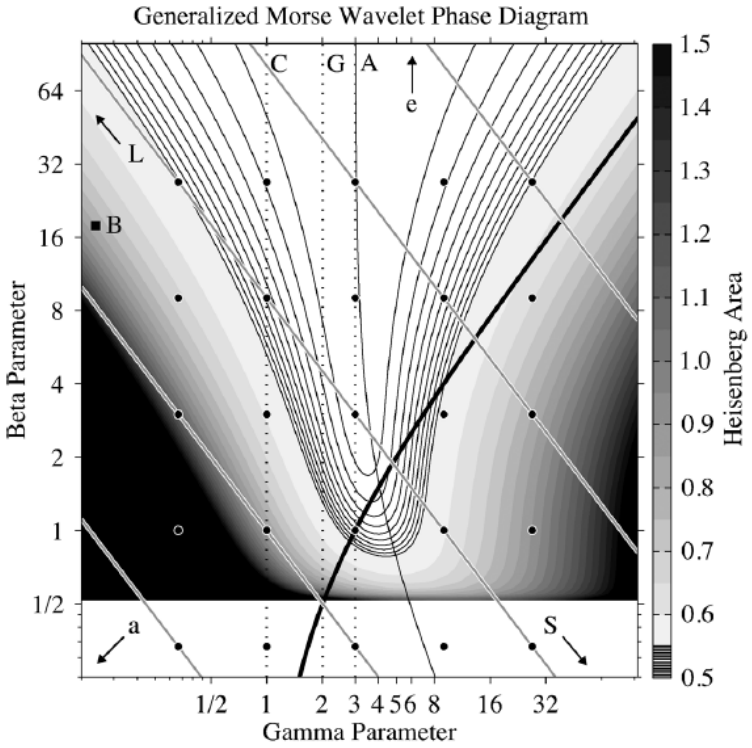

Figure 4.3: Parameter space for the generalised Morse wavelet superfamily, with the Heisenberg area shade over β and γ on log-log axes. Thin solid black lines are contours of the Heisenberg area from 0.5 to 0.55 with a spacing of 0.005. The dotted vertical lines mark the $\gamma = 1$, $\gamma = 2$ and $\gamma = 3$ wavelet families. A thin black line (a skewness curve) divides wavelet with positive skewness in the frequency domain (on the left) from those with negative skewness. Letters mark the locations of other wavelet, with arrows denoting limit, for example, 'A' for the Airy wavelets, the curve approaches the line $\gamma = 3$ with increasing β, see Lilly & Olhede (2012) for more details. Image from Lilly & Olhede (2012)

A map of generalized Morse wavelet parameter space, with the Heisenberg uncertainty area − see chapter 2 pp.33 for details, is presented in Figure 4.3. In the vicinity of the zero-skewness curve, the Heisenberg area of the generalized Morse wavelets ($A_{\beta,\gamma} \equiv \sigma_t \sigma_\omega$) approaches its theoretical lower bound at $A_{\beta,\gamma} = \frac{1}{2}$ (Lilly & Olhede 2012). With increasing β the skewness curve approaches the line $\gamma = 3$, and the Heisenberg area is very close to its lower bound. The $\gamma = 3$, called Airy wavelet family, is found to have zero asymmetry in time domain and remains nearly symmetric in the frequency domain (Lilly & Olhede 2009). The Airy wavelet family achieves a high degree of time/frequency concentration, while remaining exactly analytic. Examples of the Airy wavelet family, with $\beta = 3, 9$, and 27 are shown in Figure 4.4. The Airy wavelets not only preserve the spirit of the Morlet wavelet but also substantially outperform the Morlet for high time localisation while remaining analytic. Locations of other wavelet families and analysis functions of

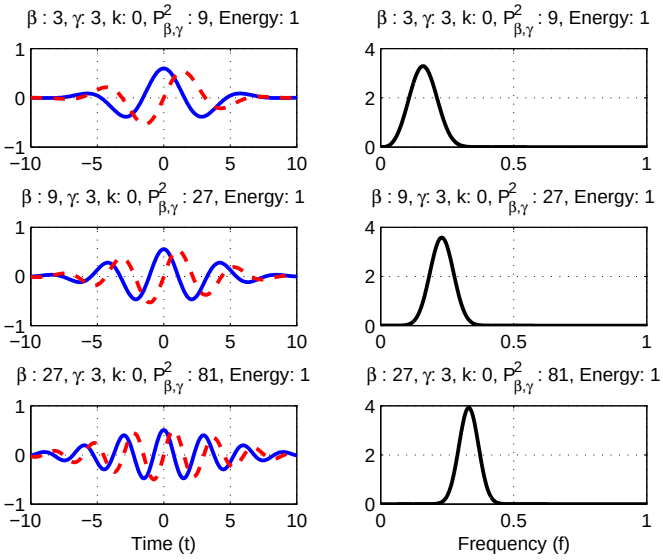

Figure 4.4: Examples of the generalized Morse wavelet for $\gamma = 3$ and $\beta = 3, 9$, and 27, with time domain form $\psi_{\beta,\gamma}(t)$ (left) and frequency domain form $\Psi_{\beta,\gamma}(\omega)$ (right). In the time domain, the solid line and the dashed line indicate the real part and the imaginary part of the wavelet, respectively. Frequency f is in cycles per second (Hz).

the generalized Morse wavelets are also indicated in Figure 4.3, for example, the Cauchy or Klauder or Paul wavelet family for the choice $\gamma = 1$, and the analytic "Derivative of Gaussian" (DoG) wavelets for $\gamma = 2$.

To explore the trade-off between time and frequency precision, the localisation measures (σ_t, σ_ω, $A_{\beta,\gamma}$, and $P^2_{\beta,\gamma}$) for some members of the generalized Morse wavelets are given in Table 4.1 and Figure 4.5. This table provides alternative choices for a particular application. For example, at fixed $P^2_{\beta,\gamma} = \beta\gamma = 12$, the Heisenberg area of $\gamma = 3$ is the most close to its lower bound for $\beta > 1$, as seen in Table 4.1. A change in behaviour between time and frequency localisation is clearly observed in Figure 4.5. The $\gamma = 3$ wavelets have an instantaneous frequency which is roughly constant, and their Wigner-Ville distributions are also roughly symmetric about the central frequency. For smaller values of γ, wavelets are concave and the instantaneous frequency takes on its maximum value at the wavelet centre, while for larger values of γ the wavelets are convex and the instantaneous frequency takes on its minimum value at the wavelet centre. The degree of concavity or convexity controls a wavelet filter which responds to signals having frequency maxima or minima at the wavelet centre. More details regarding the different roles of β and γ in controlling wavelet properties can be found in Lilly & Olhede (2009, 2010, 2012).

Table 4.1: The localisation measures for some members of the generalized Morse wavelets.

β	$\gamma = 2$				$\gamma = 3$				$\gamma = 4$			
	σ_t	σ_ω	$A_{\beta,\gamma}$	$P^2_{\beta,\gamma}$	σ_t	σ_ω	$A_{\beta,\gamma}$	$P^2_{\beta,\gamma}$	σ_t	σ_ω	$A_{\beta,\gamma}$	$P^2_{\beta,\gamma}$
1	1.732	0.337	0.583	2	2.062	0.258	0.531	3	2.287	0.228	0.522	4
3	1.483	0.347	0.514	6	2.194	0.229	0.501	9	2.706	0.186	0.503	12
4	1.464	0.348	0.510	8	2.280	0.220	0.501	12	2.884	0.174	0.503	16
6	1.446	0.350	0.506	12	2.418	0.207	0.500	18	3.168	0.158	0.502	24
10	1.433	0.351	0.503	20	2.616	0.191	0.500	30	3.581	0.140	0.501	40
20	1.423	0.352	0.502	40	2.923	0.171	0.500	60	4.243	0.118	0.501	80
30	1.420	0.353	0.501	60	3.123	0.160	0.500	90	4.691	0.107	0.500	120

Note: the formulas for σ_t, σ_f are given in Lilly & Olhede (2009) and an example code is available at http://site.google.com.site/aguiarconraria/joanasoares-wavelets/the-astoolbox.

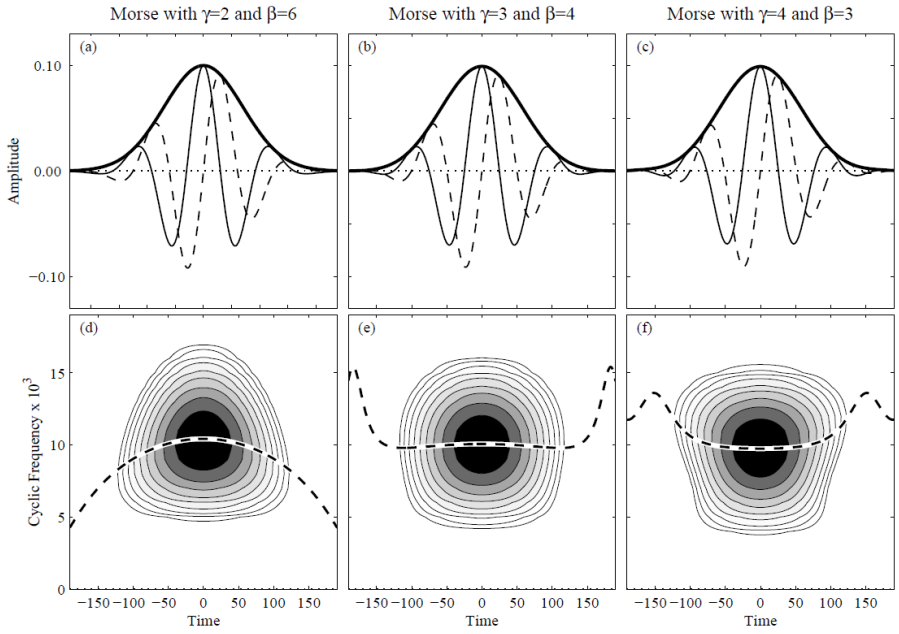

Figure 4.5: The generalized Morse wavelets in time domain (a-c) and their Wigner-Ville distributions (d-f), which have line styles and contour intervals are as Figure 4.1. All three wavelets have the same value of $P^2_{\beta,\gamma} = 12$, the values of (γ, β) are (2,6), (3,4), and (4,3), respectively. (Image from Lilly & Olhede (2009).)

In summary, Airy wavelets ($\gamma = 3$) are desirable in this work because they give wavelets having a high degree of symmetry in the frequency domain. This property may lead to good performance as previously mentioned. Increasing β at fixed γ, wavelets are more oscillatory and have a narrower bandwidth in the frequency domain. Generally, choosing a small value of β gives wavelets that are highly time-localized as opposed to frequency-

localized, as seen in Table 4.1 for the values of σ_t and σ_ω. Note that with $\gamma = 3$, β should be grater than one ($\beta > \left(\frac{\gamma-1}{2}\right)$), as stated in Olhede & Walden (2002). β is a critical parameter choice for fixed γ. An optimal value of β depends upon the particulars of the data or signals. Essentially, β controls the trade-off of time resolution against frequency resolution. In order to verify these concepts we apply generalized Morse wavelet to simulated data consisting of 0.25 s bursts of 10 Hz and 20 Hz activity followed by 0.1 s of inactivity (see Figure 4.6(A)), examples of time-frequency resolution test of each β=3, 9, 12, 18, and 27, at γ=3 are shown in Figure 4.6(B)-(F). It can be seen that $\beta = 3$ shown in Figure 4.6(B) displays the best temporal resolution. $\beta \geq$18 (Figure 4.6(E-F)) do not provide particularly good temporal resolution, especially at lower frequencies. However, the plots in Figure 4.6(E-F) show the increase in spectral resolution at higher frequencies. Therefore, lower values of β may be a good choice for a particular application which needs to have a better time localisation. If instead one wants to have good localisation both in time and frequency, for example, $\beta = 9$ and 12 in Figure 4.6(C-D) may be a reasonable choice which provides appropriate resolution both in time and frequency at two frequency components compared to other values of β. In order to achieve the best visual representation of the variability in signals, the value of β depends upon the requirements of the analysis and the particulars of the signals, such as stationary or nonstationary signals. For example, if stationary components are present in the signals (the process does not change with time), we recommend higher values of β to increase frequency resolution, as we are interested in wavelets that are highly frequency-localized as opposed to time-localized.

4.1.1 Cone of influence

As stated in chapter 2 pp.33, in practice, wavelet analysis is the convolution of the signal and the wavelet function, therefore the convolution suffers edge effects. The region of a wavelet transform affected by edge effects is called the cone-of-influence (COI). In this section, the definition of the COI is adapted from (Torrence & Compo 1998). The COI for the Morlet wavelet is chosen such that the wavelet power for a discontinuity at the edge drops by factor e^{-2}, and ensures that edge effects are negligible beyond this point. To map this approach to the generalized Morse wavelets, the e-folding time at scale s can be defined as

$$\tau'_s = \sqrt{2}s\frac{P_{\beta,\gamma}}{\omega_{\beta,\gamma}} \tag{4.6}$$

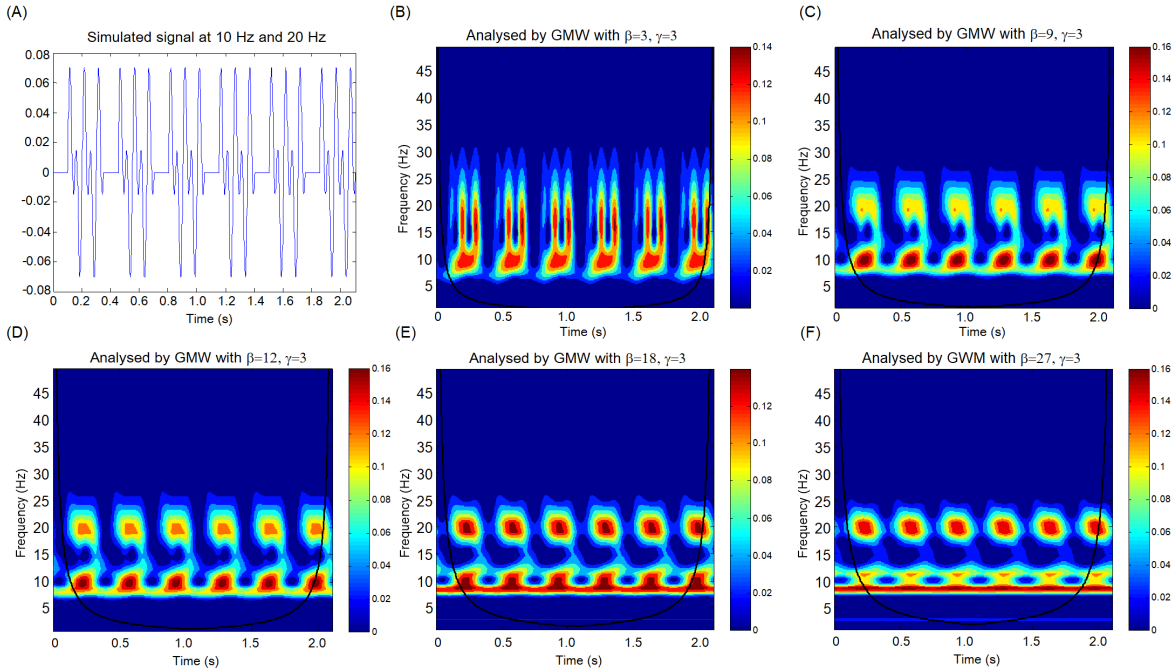

Figure 4.6: (a) Simulated signal consisting of two sinusoids at different frequencies, 10 and 20 Hz with repeated time gap of 100 ms used to determine time and frequency resolution. (b-f) Time-frequency energy distribution of each $\beta = 3, 9, 12, 18, 27$, at $\gamma = 3$ for simulated signal. Black curve line indicated the COI.

where $P_{\beta,\gamma}$ and $\omega_{\beta,\gamma}$ refer back to Eq.(4.4) and (4.3), respectively.

As seen in Eq.(4.6), the e-folding time τ_s' of the generalized Morse wavelets depends on the values of β and γ. In the case of Airy wavelets, it is important to note that differences in the parameter β can lead to changing curve for the COI. Setting β to high value to increase frequency resolution, the width of a significant area (inside the COI) becomes narrower as seen in Figure 4.7. Regions outside the COI are neglected due to edge effects.

The e-folding time τ_s' will be used to visualize the COI in time-frequency plots of the wavelet power spectra, wavelet coherence and phase locking value.

4.1.2 Choice of scales and frequencies

In practice, it is necessary to consider the scales s as proportional to an inverse frequency. In this work, computing a set of scales and frequencies is adapted from Torrence & Compo (1998). A complete range of frequencies for wavelet analysis are calculated by fractional powers of two as follows:

$$f_\ell = f_{min} 2^{\frac{\ell}{N_V}}, \quad \text{where } \ell\text{=0,1,...,}N_s - 1 \tag{4.7}$$

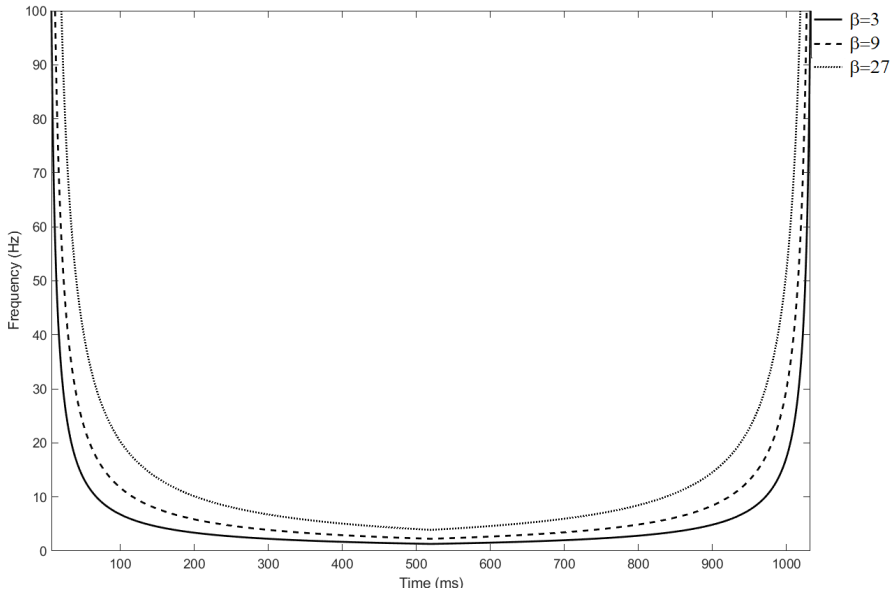

Figure 4.7: An example of the COI with different values of β.

where f_{min} is the smallest frequency in the wavelet transform. N_V is the number of voices calculated per octave, and N_s is the largest scale. Note that the appropriate range of octaves and scales depends on the maximum requested frequency in wavelet transform. The value of N_s can be calculated as follows:

$$N_s = \lfloor N_V \log_2 \left(\frac{f_{max}}{f_{min}} \right) \rfloor \tag{4.8}$$

where $\lfloor ... \rfloor$ is the floor operation, and f_{max} is the maximum frequency in the wavelet transform. The scales associated with frequencies are calculated as

$$s_\ell = \frac{\omega_{\beta,\gamma}}{2\pi f_\ell} \tag{4.9}$$

The scales of the generalized Morse wavelet correspond to a central frequency of generalized Morse wavelets ($f_0 = \frac{\omega_{\beta,\gamma}}{2\pi}$) and a range of frequencies in the wavelet analysis. An example of scale-frequency relationship is shown in Figure 4.8. Consider a wavelet analysis consisting of 8 voices per octave ($N_V = 8$), upper and lower frequency are defined. A linearly spaced frequency vector is created. The frequency values range from 1-50 Hz ($f_{min} = 1$ HZ, and $f_{max} = 50$ Hz) so the number of scales is 46, calculated by Eq.4.8. Then, the scales associated with frequencies are calculated using Eq.4.9. Figure 4.8(left) shows a plot of scale index versus scale value, and the scale values map into frequencies in this case shown as Figure 4.8(right).

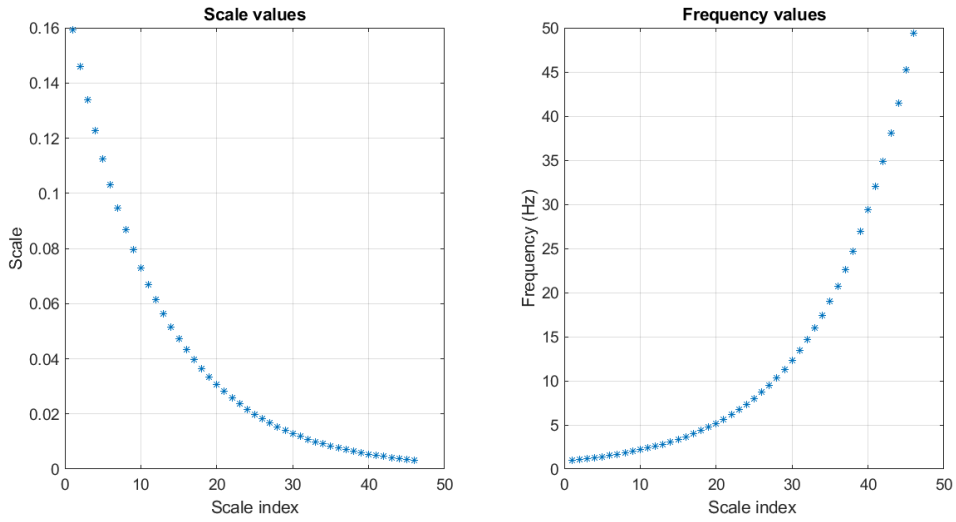

Figure 4.8: An example of relationship between scale values (left) and frequencies (right).

In summary, this section provides relevant theoretical contents on the generalized Morse wavelets which depend on two parameters (β, γ). The roles of the two parameters β and γ in controlling wavelet properties are illustrated, for example, Figure 4.5. The scales are chosen as fractional power of 2, which correspond to a central frequency of generalized Morse wavelets and a range of frequencies in the wavelet analysis. For the method, frequencies are plotted linearly in the $[f_{min}, f_{max}]$ Hz range. The COI for the generalized Morse wavelets is defined as the e-folding time as given by Eq.4.6. A particular subset of the generalized Morse wavelets, Airy wavelets ($\gamma = 3$), is found to have zero asymmetry in time domain and a high degree symmetry in frequency domain (Lilly & Olhede 2009). Here, Airy wavelet may lead to good performance for analysing time-frequency based coherence, phase locking value and time-resolved phase-amplitude coupling as described in the next sections.

4.2 Wavelet spectra and coherence estimates

In order to study the relationship between two nonstationary neuronal signals, wavelet spectra and coherence can be applied to track the time-course in nonstationary signals with varying temporal and frequency resolution. The analysis of time-frequency coherence requires estimates for the cross spectrum and auto spectra of two non-stationary processes. Considering two signals $x(t)$ and $y(t)$, the continuous wavelet transforms are $W_x(\tau, f)$ and

$W_y(\tau, f)$. The time-frequency cross spectrum between $x(t)$ and $y(t)$ signals is defined as

$$S_{xy}(\tau, f) = W_x(\tau, f)W_y^*(\tau, f) \tag{4.10}$$

and the time-frequency auto spectra of $x(t)$ and $y(t)$ signals are given as

$$S_x(\tau, f) = |W_x(\tau, f)|^2 \tag{4.11}$$

$$S_y(\tau, f) = |W_y(\tau, f)|^2 \tag{4.12}$$

The time-frequency coherence expression is obtained from Eq. (4.10), (4.11) and (4.12), the squared coherence can be calculated by the squared magnitude of the cross spectrum normalised by the auto spectra of each signal, is given by

$$|R_{xy}(\tau, f)|^2 = \frac{|S_{xy}(\tau, f)|^2}{S_x(\tau, f)S_y(\tau, f)} \tag{4.13}$$

It was suggested in Brittain et al. (2007) that coherence constructed from unsmoothed periodogram estimates will be identically equal to 1. Smoothing the spectral estimates will allow coherence to vary in the range between 0 and 1. In real situations, the auto-and cross-spectra can be estimated for a series of repeat trials that is computed by averaging across trials without smoothing within trials (Zhan et al. 2006). The procedure for estimating the time-frequency coherence is outlined in Eq. (4.14)-(4.17), see Zhan et al. (2006) for details. The time-frequency coherence is estimated from the cross spectrum $\hat{S}_{xy}(\tau, f)$ and the auto spectra $\hat{S}_x(\tau, f)$, and $\hat{S}_y(\tau, f)$ as

$$|\hat{R}_{xy}(\tau, f)|^2 = \frac{|\hat{S}_{xy}(\tau, f)|^2}{\hat{S}_x(\tau, f)\hat{S}_y(\tau, f)} \tag{4.14}$$

where

$$\hat{S}_x(\tau, f) = \frac{1}{N}\sum_{n=1}^{N} |W_{x;n}(\tau, f)|^2 \tag{4.15}$$

$$\hat{S}_y(\tau, f) = \frac{1}{N}\sum_{n=1}^{N} |W_{y;n}(\tau, f)|^2 \tag{4.16}$$

$$\hat{S}_{xy}(\tau, f) = \frac{1}{N}\sum_{n=1}^{N} W_{x;n}(\tau, f)W_{y*;n}(\tau, f) \tag{4.17}$$

where N is the number of trials. Wavelet coherence ranges between 0 and 1. 0 means no correlation, 1 means perfect correlation.

In particular, if neither x nor y is identically zero, some properties of time-frequency based coherence given in Tuncel et al. (2010) are as follows:

1) $0 \leq |R_{xy}(\tau, f)|^2 \leq 1$

2) $|R_{xy}(\tau, f)|^2 = 0$, if and only if x and y are orthogonal

3) $|R_{xy}(\tau, f)|^2 = 1$, if and only if x and y are collinear ($x = \lambda y$ for some non zero complex scalar λ.)

4) $|R_{xy}(\tau, f)|^2 = |R_{yx}(\tau, f)|^2$, for all real and complex vector x and y

5) $|R_{\lambda_1 x, \lambda_2 y}(\tau, f)|^2 = |R_{xy}(\tau, f)|^2$, for all non-zero scalars λ_1 and λ_2

Here, simulated data is generated in order to test the performance of the time-frequency coherence defined above. The data containing repeated trials uses three sine wave components embedded into white noise signals with signal-to-noise ratio (SNR) of -15 dB at 200-300 ms with 5 Hz, 400-500 ms with 25 Hz, and 700-800 ms with 40 Hz (Zhan et al. 2006) as seen in Figure 4.9. Time-frequency coherence estimates are computed using the generalized Morse wavelets with $\gamma = 3$, and $\beta = 3$, 9, and 27. Coherence is estimated from 100 trials of simulated data. A dark blue colour on time-frequency plots indicates values below the 95% confidence limit. Note that statistical significance test for coherence estimates is presented in section 4.2.1.

For the simulation results of testing data with different frequencies and time intervals, wavelet coherence estimates method can detect the correlations where the coherence has three significant peaks at 5 Hz around 200-300 ms, 25 Hz around 400-500 ms and 40 Hz around 700-800 ms, respectively as seen in Figure 4.9. In general, the wavelet transform analyses the high frequency parts with increased time resolution and low frequency with decreased time resolution (Zhan et al. 2006). In this example, visual inspection suggests that $\beta = 3$ gives a clearer time-frequency representation of the signal at low frequency 5 Hz compared with $\beta = 9$ and 27. In contrast, $\beta = 9$ and 27 give increased frequency resolution at 25 Hz and 40 Hz. It is noticed that low β leads to increased time resolution and decreased frequency resolution at high frequencies, whereas high β provides increased frequency resolution and decreased time resolution at low frequency. These characteristics relate to Heisenberg boxes, described in chapter 2, section 2.2.2. The black curved line in contour plot indicates the COI. Areas outside the COI are ignored as they may be affected

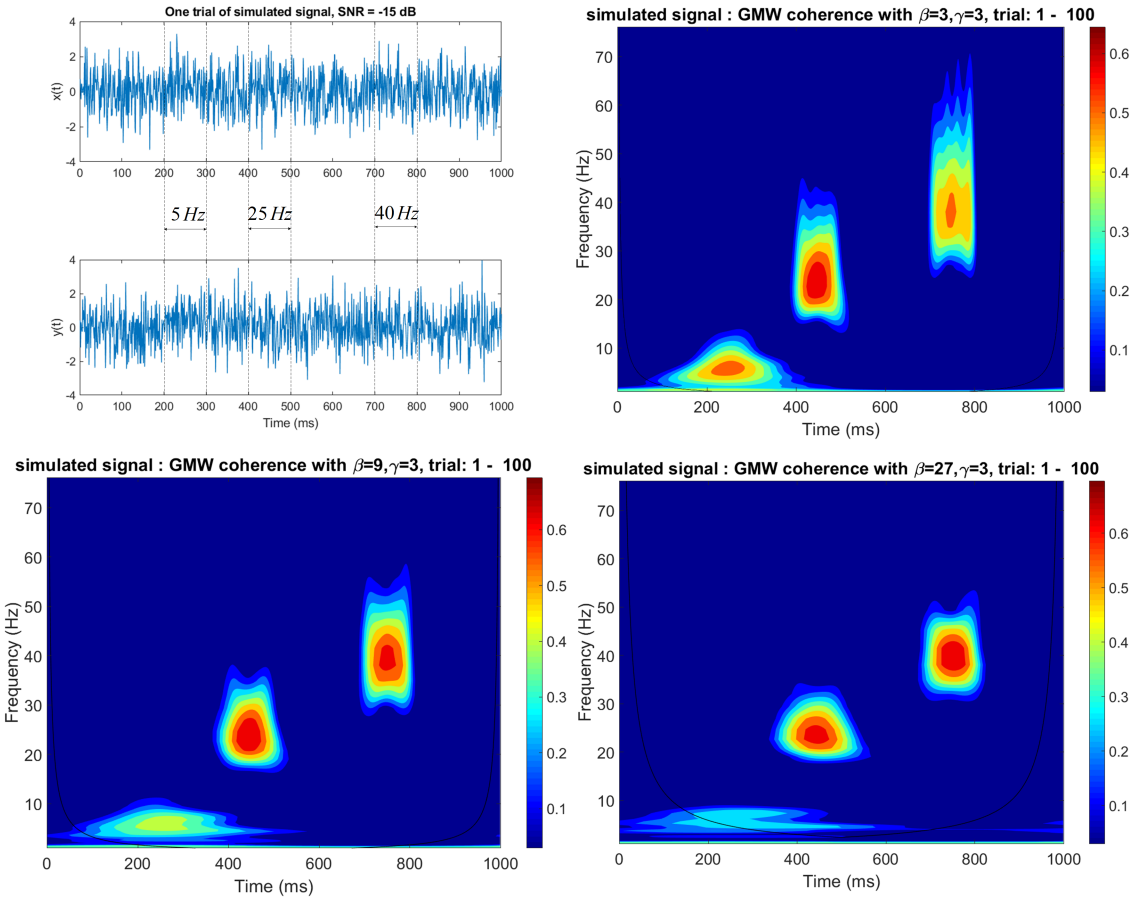

Figure 4.9: Time-frequency coherence estimates using the generalized Morse wavelets (γ = 3 and β=3, 9, and 27) for simulated data with embedded frequencies 5 Hz at times 200-300 ms, 25 Hz at 400-500 ms, and 40 Hz at 700-800 ms. The black curved line on contour plots indicates the COI. See text for more details.

by edge effects. Setting β to high value to increase frequency resolution, causes the width of area inside the COI to become narrower.

4.2.1 Confidence limits for coherence estimates

It is necessary to decide which of the coherence values are significant. A confidence interval value is a threshold value which is used to determine if the time-frequency coherence is significantly different from zero. As stated in chapter 2 pp.29, the distribution of the coherence estimate is given by Eq. (2.6) as $Pr(R^2 \leq r) = 1 - (1 - r)^{K-1}, 0 \leq r \leq 1$. If the confidence interval value of 95% is chosen, then the detection threshold value is $r_{95\%} = 1 - 0.05^{1/(K-1)}$. The $r_{95\%}$ with different number of trials, K in this study are shown in Table 4.2.

A significant value for time-frequency coherence is considered if the estimate is greater

Table 4.2: The 95% significance level for coherence with different number of trials used in this study.

no.of trials	Significance level, $\alpha = 0.05$
50	0.0593
100	0.0298
200	0.0149
300	0.0098

than the 95% confidence interval. The value of confidence limit in Table 4.2 will be used in coherence analysis in this work.

4.3 Wavelet phase locking value estimates

Phase synchronisation measures can be used to study the relationships between the phases of physiological signals. Phase synchronisation refers to the phases of two coupled oscillators that synchronise even if the amplitude fluctuations between the oscillating signals are uncorrelated (Pereda et al. 2005). Synchronisation of weakly coupled oscillating system appears as a relation between their phase and frequencies (Rosenblum & Kürths 1998). A general framework for studying phase synchronisation has three main steps (Le Van Quyen & Bragin 2007): first, pre-filtering of the raw signal with a bandpass filter around a chosen frequency value. Second, estimation of the phase of each signal. Third, quantification of the degree of phase-locking. There are two methods of phase estimation, one using complex wavelets (Le Van Quyen et al. 2001, Lachaux et al. 1999) (refer back to (4.1) and another using the Hilbert transform (HT) (Tass et al. 1998). The main difference between these two methods is that the HT is actually a filter with unit gain at every frequency. If the signal is broadband, pre-filtering in the frequency band of interest is required before applying the HT, in order to get an appropriate phase value (Pereda et al. 2005). On the other hand, pre-filtering is unnecessary when using a complex wavelet because it can act as a bandpass filter and, at the same time, provide separate values for the instantaneous amplitude and the phase (Hassan et al. 2010). In this study, phase synchronisation is based on a unified framework as described in chapter 1, section 1.2.

The phase locking value (PLV) is an important measure for investigating synchronisation of neural activity, including muscle activities detected by EMG. In particular, Tass

et al. (1998) found that phase locking between the activity of primary and secondary motor areas can be related to the coordination of antagonistic muscles.

Analytically, the interaction between two oscillating systems essentially affects the evolution of their phases if the frequencies ω_x and ω_y are in resonance for some integers p, q, indicating the ratios of possible frequency locking (for details see Wacker & Witte (2011) and Tass et al. (1998)). The existence of locking or entrainment between frequencies are close to rational relation, $p\omega_x \approx q\omega_y$ (Pereda et al. 2005). The generalised phase difference of two series is given by

$$\varphi_{p,q}(t) = p\phi_x(t) - q\phi_y(t) \tag{4.18}$$

where $\phi_x(t)$ and $\phi_y(t)$ are the unwrapped phases of the signals. The principle of phase synchronisation of periodic self-oscillatory systems corresponds to a phase locking between two systems defined as

$$\varphi_{p,q}(t) = |p\phi_x(t) - q\phi_y(t)| \leq constant \tag{4.19}$$

(4.19) is the condition for phase locking (Rosenblum et al. 2001), where p and q are small integers. This leads to $p\phi_x = q\phi_y$. As the aim is to detect functional connectivity between two signals from the same physiological system, the $p : q$ synchronisation index mostly considers the simplest case of $p = q = 1$. This is used here. An example of two oscillating signals that are almost in phase with an approximate zero phase difference is in Figure 4.10. It is clear that the amplitude of the oscillation varies, but the frequency itself remain stable. They oscillate at the same frequency and roughly the same phase around 200−250 ms, 350-400 ms and ∼900 ms, respectively.

The local phase of the generalized Morse wavelet transform for trial n at time τ and frequency f is quantified from the ratio between the imaginary part ($\Im$) and the real part ($\Re$) of the wavelet transform,

$$\phi_{x;n}(\tau, f) = \tan^{-1} \frac{\Im(W_{x;n}(\tau, f))}{\Re(W_{x;n}(\tau, f))} \tag{4.20}$$

The phase of a given time-series $x(t)$ can be defined such that it is parameterized in the range $\phi_{x;n}(\tau, f) \in [-\pi, \pi]$, with similar expressions for the phase of time-series y, $\phi_{y;n}(\tau, f)$. The phases are used to calculate the phase difference between $x(t)$ and $y(t)$ at time t. A representation of time-frequency phase locking values over N trials between the signals

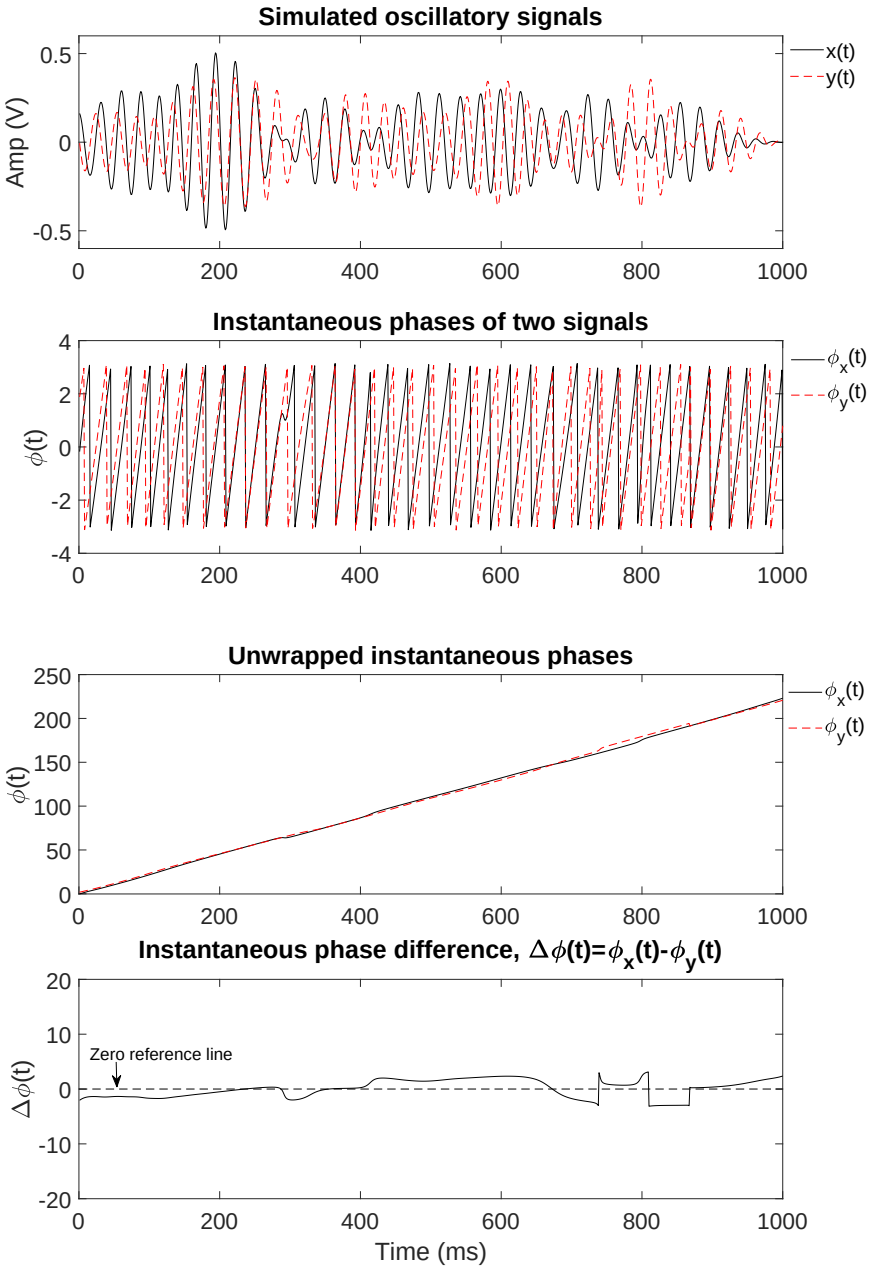

Figure 4.10: An example of two oscillatory signals and their instantaneous phases. The simulated signals are generated by using generative model of oscillatory synchronisation proposed by Lowet et al. (2016), with a centre frequency of 8 Hz, detuning frequency of 3 Hz, and coupling strength of 0.5. Step size h is set to 1 ms. Intrinsic noise is 0.05 and SNR is 250.

(Lachaux et al. 2000) is the PLV defined as

$$PLV(\tau, f) = \frac{1}{N}\left|\sum_{n=1}^{N} e^{i(\phi_{y;n}(\tau,f)-\phi_{x;n}(\tau,f))}\right| \tag{4.21}$$

PLV is a normalised measure that varies between 0 and 1, where a value of 1 means perfect

phase synchrony.

To further validate the PLV results, two illustrative examples for testing the performance of time-frequency PLV estimates are presented. The first is the same simulated data as used in Figure 4.9, and the results are presented in Figure 4.11.

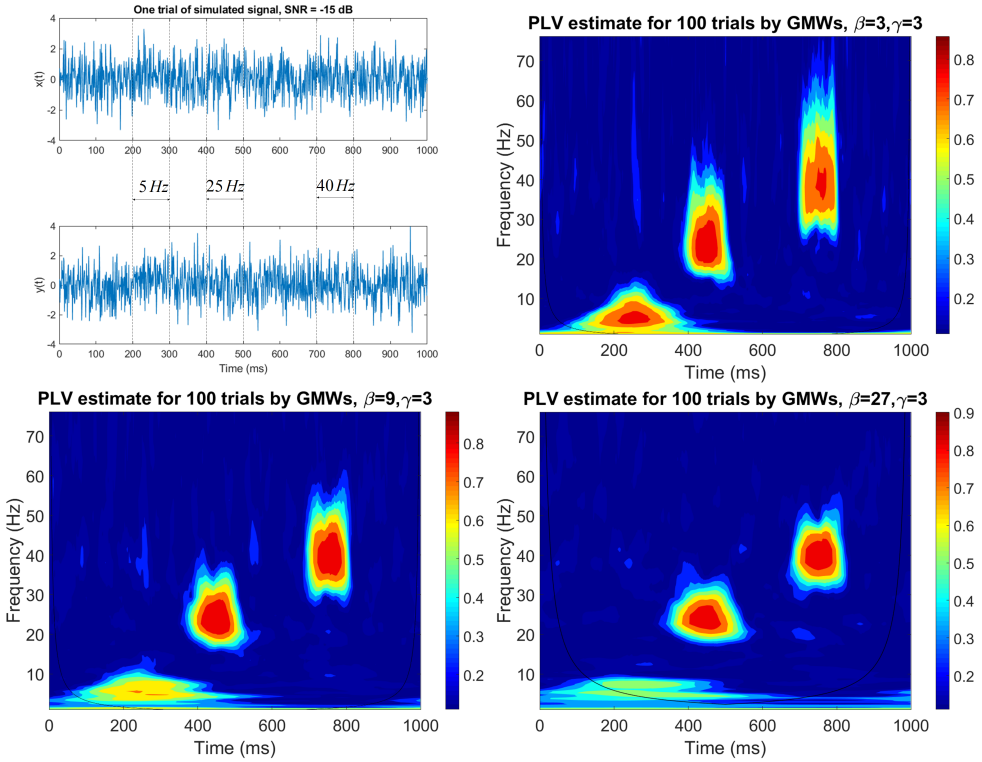

Figure 4.11: Time-frequency PLV estimates using the generalized Morse wavelets ($\gamma = 3$ and β=3, 9, and 27) for simulated data with frequency 5 Hz at time 200-300 ms, 25 Hz at 400-500 ms, and 40 Hz at 700-800 ms, compare with coherence estimates in Figure 4.9.

Figure 4.11 shows the results obtained from analysing the sine waves with 5 Hz, 25 Hz, and 40 Hz embedded into the white noises from 200-300 ms, 400-500 ms, and 700-800 ms, respectively. PLV has significant features in both time and frequency which are similar to those seen in coherence estimates in Figure 4.9. If an unbiased estimator of squared PLV is considered, PLV^2 (Aydore et al. 2013, Lowet et al. 2016), the unbiased PLV^2 estimators has similar magnitudes as the coherence estimates. For example, at $\gamma = 3$ and $\beta = 3$ the majority of PLV has peak magnitude of 0.85 at around 5 Hz, 25 Hz and 40 Hz, and peak magnitude of coherence is about 0.65. To compare the estimates of the coherence and the unbiased PLV^2 estimator, the PLV^2 is about 0.72 which is close to peak magnitude of coherence (0.65).

Secondly, simulated data with plausible and well-understood synchronisation proper-

ties are generated using the generative model of oscillatory synchronisation proposed by Lowet et al. (2016), which is very similar to the well-known Kuramoto model (Breakspear et al. 2010). The phase evolution $\phi_x(t)$ of oscillator X is defined only by its intrinsic frequency ω_x and an intrinsic phase noise process N_p^x:

$$\dot{\phi_x}(t) = \omega_x(t) + N_p^x(t) \tag{4.22}$$

In case of oscillator Y, the phase evolution $\phi_y(t)$ depends on the interaction term $(\phi_y(t) - \phi_x(t))$ and the coupling strength κ:

$$\dot{\phi_y} = \omega_y(t) + \kappa \sin(\phi_y(t) - \phi_x(t)) + N_p^y(t) \tag{4.23}$$

Then, for a given parameter set used for simulation, the instantaneous phase trace is generated by numerically solving the differential equations (Euler method). So, the discrete phase-evolution of oscillators X and Y used in this study can be defined by

$$\phi_x(t+1) = \phi_x(t) + h\left(\omega_x(t) + N_p^x(t)\right) \tag{4.24}$$

$$\phi_y(t+1) = \phi_x(t) + h\left(\omega_y(t) + \kappa \sin(\phi_y(t) - \phi_x(t)) + N_p^y(t)\right) \tag{4.25}$$

where h is step size, $\phi_x(t+1)$ and $\phi_y(t+1)$ are the value of ϕ_x and ϕ_y at each successive time step. As described above, the phase-locking properties depend on the chosen parameter ranges for intrinsic frequency differences between oscillator X and Y called detuning frequency (Δf) and coupling term κ (Lowet et al. 2016). Here, 100 datasets are created. The oscillators X and Y have a centre frequency of 8 Hz, $\Delta f = 3$ Hz, and coupling strength of 0.5. Step size h is set to 1 ms. Intrinsic noise is 0.05 and SNR is 250. Lowet et al. (2016) use frequency representation with time-frequency analysis that can see time-course of synchronisation. An example of simulated signal is shown in Figure 4.12. The signals have a segment length of 1000 ms. Time-frequency PLV estimates are computed using the generalized Morse wavelets with $\gamma = 3$, and $\beta = 3, 9$, and 27. A dark blue colour on time-frequency plots indicates values below the 95% confidence limit. Note that statistical significance test for PLV estimates is presented in section 4.3.1.

In Figure 4.12, the signals described above (Eq. (4.24) and (4.25)) are analysed. The PLV findings in this example are verified with the time-frequency coherence estimates: the results are consistent in terms of centre frequency of 8 Hz as expected seen over time

range 200-500 ms. The peaks with a distance of $\pm\ \Delta f\ =\ 3$ Hz can be observed in both coherence and PLV time-frequency plots. For setting $\beta = 3$, PLV displays the frequencies ∼5-20 Hz around 200-600 ms. With increased β (9 and 27), strong peak magnitude of phase-locking between oscillators X and Y occurs at frequencies 5-10 Hz around 200-500 ms. This suggests setting β to higher values to increase frequency resolution in coherence and PLV analysis. Here, PLV estimates have larger magnitudes and appears noisier than the coherence despite the same number of trials, see Figure 4.12(B) and (C). The confidence limit derived from surrogate data is larger for the PLV estimate than for the coherence estimate for the same number of trials. For example, the 95% confidence limit for coherence estimate in this study is 0.0298, and 0.1001 for PLV based on analysis of 100 trials, see Table 4.2 compared to Table 4.4.

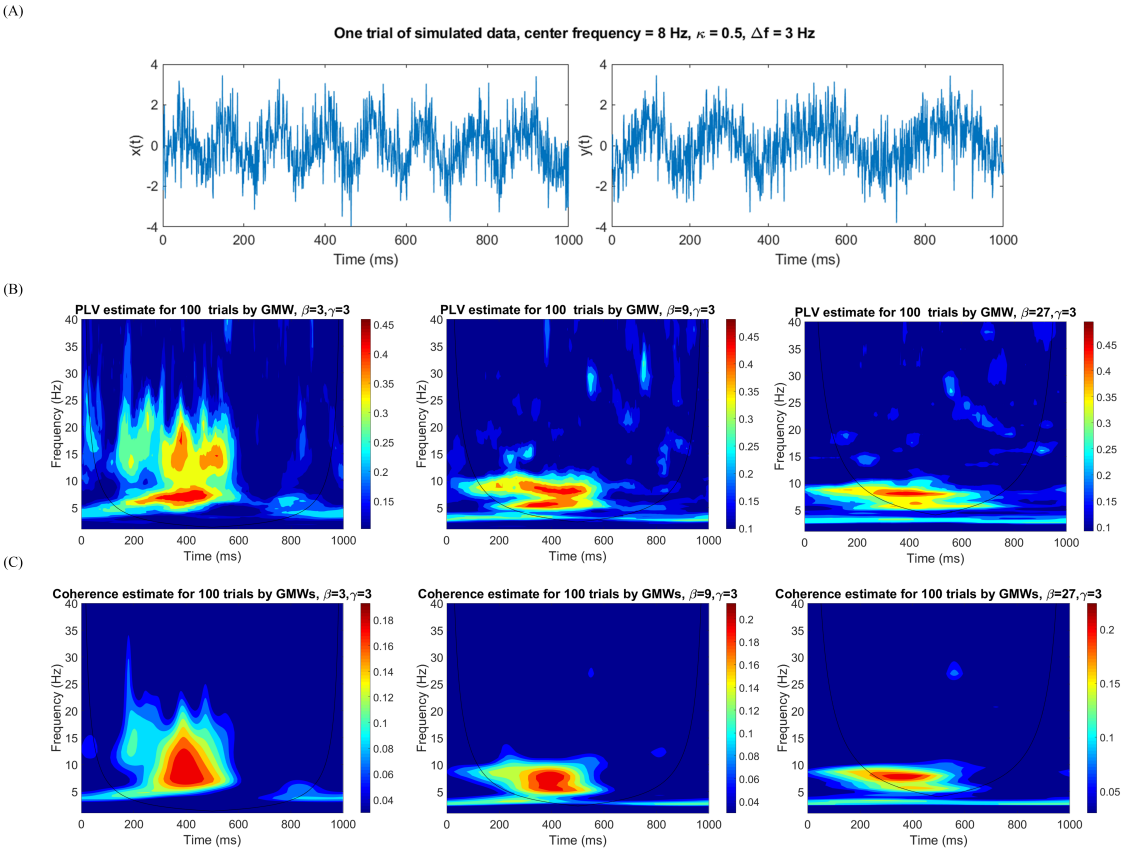

Figure 4.12: Time-frequency analysis from the generalized Morse wavelets ($\gamma\ =\ 3$ and β=3, 9, and 27) for 100 trials of simulated data using generative model of oscillatory synchronisation given by Eq 4.24 and 4.25 (A). (B) PLV estimates indicating phase-locking values, and (C) coherence estimates from the same simulated data.

4.3.1 Confidence limits for PLV estimates

The statistical significance of phase locking values is determined by using surrogate series. Lachaux et al. (1999, 2000) presented the method called phase locking statistics (PLS) in order to test the significance of the neural synchrony at each point of the time-frequency space. They tested the H_0 hypothesis that the two series of phase values ϕ_n^x and ϕ_n^y are independent. PLS used surrogate data which are created by permuting the order of all trials for signal y. The PLS indicates which the proportion of surrogate values is higher than the original PLV (between $x(t)$ and $y(t)$) for a time t. The PLV surrogate for PLS is then computed by (4.26), where K is new series of different permutations, see Lachaux et al. (1999, 2000) for details.

$$PLV_{surrogate}(\tau, f) = \frac{1}{K}\sum_{k=1}^{K}\left|\frac{1}{N}\cdot\sum_{n=1}^{N} e^{i\left(\phi_{y;perm_k(n)}(\tau,f)-\phi_{x;n}(\tau,f)\right)}\right| \tag{4.26}$$

In this thesis, experimental datasets of paired surface EMG signals are recorded during walking as reported in chapter 3. In case that walking is a stereotypically repeated action, then EMG signal from electrode 1 would not only correlate to EMG signal from electrode 2 within that trial or step cycle, but to any other steps measured by electrode 2. The shuffling trials in PLS method could not be used to explain the phase locking between paired EMG signals in this study. Here, surrogate time series for each experimental dataset are generated using a block re-sampling approach (Aru et al. 2015). The original signal $y(t)$ in each trial is split into five blocks and these blocks are sampled by random permutation. A benefit is that this procedure leads to a set of surrogates with a minimal phase distortion, see Aru et al. (2015) for details.

A significant value for PLV is considered if the PLV estimate is greater than the 95% confidence interval of the von Mises distribution (also known as the circular normal distribution (Mahan 1991)) of the mean of PLV calculated from surrogate data as described above (Aru et al. 2015). The percentage of the linear normal distribution (z=1.96) is used to give the 95% confidence interval for the mean direction in Von Mises distribution. The **CircStat**[3] toolbox for MATLAB (Berens 2009) is used in this study. Examples of these two methods used to yield the significance level for PLV calculated from simulated datasets and paired EMG datasets for a given 95% confidence level are shown in Table 4.3. The

[3]Download from https://www.jstatsoft.org/article/view/v031i10

simulated data are generated by the phase-oscillator model from the study of Lowet et al. (2016) (Eq. (4.23) and (4.24)). Paired EMG datasets are described in chapter 3.

Table 4.3: Pairwise comparison of 95% significance level for PLV between the PLS method and the proposed method.

Data sets	Significance level, $\alpha = 0.05$	
No. of trials = 100	Conventional method (PLS)	Proposed method
Simulated data		
- Centre frequency: 8 Hz	0.109	0.112
- Centre frequency: 30 Hz	0.119	0.110
EMG data		
- Treadmill data	0.620	0.097
- Overground data	0.322	0.104

Table 4.3 indicates that the confidence level calculated from both methods are similar for the simulated datasets in Figure 4.12 in contrast to EMG datasets. However, the values of confidence limit calculated from the rectified EMG data using the proposed method are nearly similar to the value of confidence limit calculated from the simulated data. This suggests the proposed method is a good choice which will be used in this study. The 95% confidence intervals in Table 4.4 are calculated from an estimate of a mean value on experimental human walking data sets, including 10 datasets of treadmill walking and 20 datasets of overground walking.

Table 4.4: The 95% significance level for PLV with different number of trials used in this study.

No. of trials	Significance level, α=0.05
50	0.1431
100	0.1001
200	0.0670
300	0.0563

Note: significance levels for n = 50 and 100 are averaged from all data sets of treadmill and overground walking, Otherwise, data from overground walking are excluded because heel strikes are fewer than 200.

As seen in Table 4.4, the value of the confidence limit depends on the number of trials.

A smaller number of trials will result in a larger confidence limit. The value of confidence limit in Table 4.4 will be used in PLV analysis in this thesis.

4.4 Practical techniques for coherence and PLV analysis

Low frequency components due to envelope modulation are an important issue when recording sEMG signals. These have frequency spectrum that contaminates a low-frequency part of the sEMG frequency spectrum, and may lead to an erroneous interpretation of the signal. In this thesis, low frequency components due to envelope modulation is defined as a low frequency (< 4 Hz) component in the sEMG envelope modulation signals. In order to enhance the coherence relationship and phase synchronisation between paired sEMG signals, low frequency component due to envelope modulation is required to be removed. Here, we propose a novel approach and practical method for coherence and PLV analysis that can separate physiological mechanisms from effects due to envelope modulation of sEMG.

4.4.1 Practical coherence analysis for removal of low frequency envelope modulation

The practical coherence analysis for removal of low frequency envelope modulation is inspired by the study of Amjad et al. (1997), who compare two coherence estimates which should be independent. In our case we compare the original coherence estimate from paired EMG signals with another derived from surrogate data. These surrogate data are calculated from the same signals $x(t)$ and $y(t)$, using Eq.(4.28), but after shuffling the order of all trials for $y(t)$. Then, Fisher's z-transform, $\tanh^{-1}$, is applied to two coherence estimates defined as

$$\hat{z} = \tanh^{-1}(|\hat{R}_{xy}(\tau, f)|) \tag{4.27}$$

where $|\hat{R}_{xy}(\tau, f)|$ is called magnitude coherency, with coherency defined by

$$\hat{R}_{xy}(\tau, f) = \frac{\hat{S}_{xy}(\tau, f)}{\sqrt{\hat{S}_x(\tau, f)\hat{S}_y(\tau, f)}} \tag{4.28}$$

where $\hat{S}_x$, $\hat{S}_y$, and $\hat{S}_{xy}$ are obtained from Eq. (4.15), (4.16), and (4.17), respectively. Coherency functions are complex valued, and both phase and amplitude coupling contribute to magnitude-squared coherence (Amjad et al. 1997). We use $\hat{D}_C$ to represent the prac-

tical coherence analysis for removal of low frequency envelope modulation. $\hat{D}_C$ is then calculated as

$$\hat{D}_C = \tanh\{\hat{z}_C - \hat{z}_{CS}\} \tag{4.29}$$

where $\hat{z}_C$ and $\hat{z}_{CS}$ are Fisher's z-transform of coherence estimates from original data and surrogate data, respectively. A priori hypothesis on the relationship between two signals is required. i) if two z transformed coherence estimates, $\hat{z}_C$ and $\hat{z}_{CS}$, have similar values, $\hat{D}_C$ will tend to be small. ii) if z_C is affected by low frequency envelope modulation component and z_{CS} is expected to be large where the low frequency envelope modulation component is consistent across segment, $\hat{D}_C$ should have significant values outside that low frequency envelope modulation.

For testing and validation, the proposed technique is illustrated by its application to simulated signals. In each example, the simulated signal is used as a substitute to EMG signal recordings. In the first example, the simulated signals, $x(t)$ and $y(t)$, are generated from a Gaussian process with the same mean and variance as the raw EMG signals modulated by activity envelopes as seen in Figure 4.13(A). The envelopes are derived from an activity envelope of rectified sEMG during locomotion, see Brittain (2007) for more details. In the second example, the simulated signals, $x(t)$, is the same data as the first example, and $y(t)$ is unmodulated white noise, as seen in Figure 4.13(B). Here, the proposed technique is expected to clarify the hypothesis stated above.

Time-frequency power spectra, coherence and practical coherence analysis for removal of low frequency envelope modulation are used in displaying features of the simulated signals and the performance of the technique calculated using averages over 100 trials. All wavelet spectral estimates have a segment length of 1024 ms, and they are computed using generalized Morse wavelets with $\gamma = 3$ and $\beta = 9$. Examples of power spectra, coherence and practical coherence analysis for removal of low frequency envelope modulation for the two examples of surrogate data in Figure 4.13 are shown in Figure 4.14. Shown in Figure 4.14(A) is the results of analysing the simulated signals in Figure 4.13(A). Wavelet power spectra of signals $x(t)$ and $y(t)$ are similar. There is an increase in power in beginning, with a reduction in the middle and then increase at the end of the time window as the envelope of the noise is modulated. Strong coherence of magnitude of 0.8 around 10-25 Hz occurs in the beginning and the end of the time window. In general, coherence estimate should be independent when two signals are Gaussian white noise. In this example, uncorrelated white noises are used, however, coherence reflects amplitude modulation of white noise.

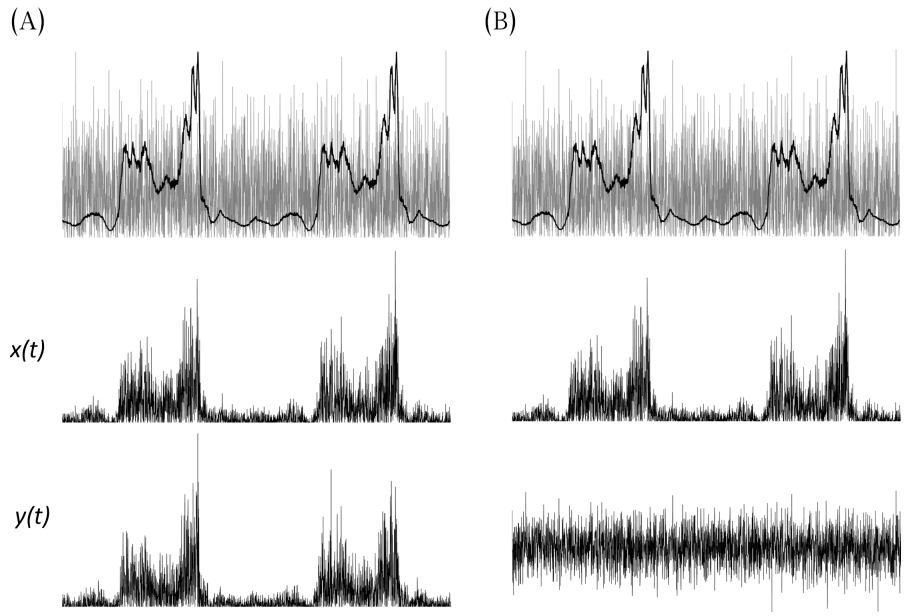

Figure 4.13: Examples of simulated signals for two time windows or two trials. Top row shows process for obtaining simulated data (e.g. EMG activity envelopes (heavy line) and Gaussian noise (thin line) for (A) and (B). Middle row shows simulated data for $x(t)$, multiplying a Gaussian noise and envelopes both in (A) and (B). Bottom row shows simulated data for $y(t)$, same as $x(t)$ for (A), a Gaussian noise for (B). Assumed sampling rate is 1 ms. See text for details.

It is likely to be caused by envelope modulation of the two simulated signals. Let us assume that envelope modulation is the explanation for this coherence. Shuffling the trials should not affect the coherence which have the same envelope modulation for each trial. Thus, the practical coherence analysis for removal of low frequency envelope modulation is below 0.2 (lower plot), which suggests two estimates are similar. For the second example, the results in Figure 4.14(B) indicates that there is no coherence between the simulated signals. Since only one signal is modulated, we would expect that there is no coherence. The practical coherence analysis for removal of low frequency envelope modulation in this example presents the same analyses as in Figure 4.14(A). For comparison of significant coherence between these two examples, we found that the coherence in Figure 4.14(A) is very large (nearly 1) while the coherence in Figure 4.14(B) is reduced to 0.2, as seen in colourbar of each figure. Briefly, the proposed technique confirms the expectation for comparison of coherence estimates. If two coherence estimates are similar ($z_C \cong z_{CS}$), the practical coherence analysis for removal of low frequency envelope modulation ($\hat{D}_C$) is small or near zero indicating that the original coherence maybe affected by envelope modulation. Figure 4.14(B) show that the practical coherence analysis for removal of low

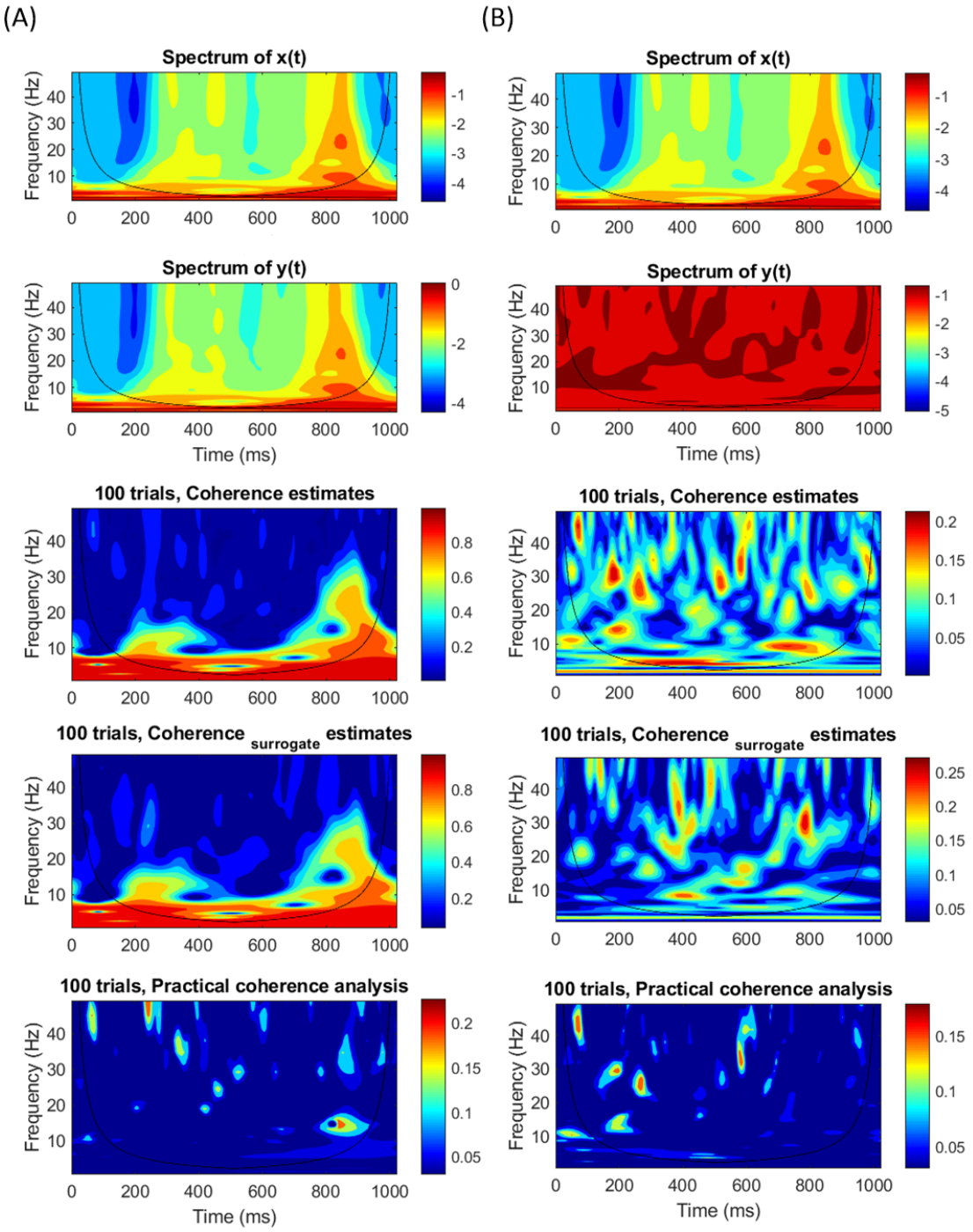

Figure 4.14: Power spectra, coherence and practical coherence analysis for removal of low frequency envelope modulation are calculated using averages over 100 trials of simulated data from Figure 4.13. Two top rows show power spectra of $x(t)$ and $y(t)$, respectively. Third row shows coherence estimates of original simulated signals. Fourth row show coherence estimates of surrogate data. Bottom row shows practical coherence analysis for removal of low frequency envelope modulation. Black line curve in each figure indicates COI. A dark blue colour on time-frequency plots indicates values below the 95% confidence limit.

frequency envelope modulation tends to be near zero when there is no coherence between two uncorrelated signals.

To further understand the nature of the practical coherence analysis for removal of low frequency envelope modulation, we consider a practical example of using the proposed technique. An example of its application to real sEMG data is demonstrated. Here, rectified sEMG signals (Figure 4.15(A)) obtained from one subject treadmill walking (see more detail in chapter 3) are used to validate the reliability of the proposed technique. EMG-EMG wavelet spectral and practical coherence analysis for removal of low frequency envelope modulation are computed using the same parameter setting as the simulation above. An example of EMG signals and the results are shown in Figure 4.15. Interestingly, wavelet power spectra (Figure 4.15(B)) and coherence estimate (Figure 4.15(C) top) roughly give similar aspects as power spectra and coherence estimates shown in Figure 4.14(A). However, coherence estimates of surrogate data in this example shows peak around low frequency ($\approx$ 3 Hz) over step cycle (Figure 4.15(C)(middle)). Thus, the practical coherence analysis for removal of low frequency envelope modulation indicates that low frequency ($<$ 4 Hz) component disappears, and a distinct 8-20 Hz correlation located around early and late swing of step cycles remains. This has been demonstrated to represent a rhythmic modulation of motor unit activity (Halliday et al. 2003). The proposed technique not only provides useful information of modulation of motor unit activity but also removes low frequency envelope modulation component ($<$ 4 Hz).

In conclusion, we propose a novel technique for removal of low frequency envelope modulation in coherence analysis. The technique compares the original coherence estimate from paired EMG signals with another derived from surrogate data. We demonstrate the technique with synthesized data and real sEMG data. The results show that the proposed technique could be used in the removed of low frequency components of sEMG records.

4.4.2 Practical PLV analysis for removal of low frequency envelope modulation

As already mentioned, both PLV and coherence have been employed in experimental studies to assessed the relationship between pairs of recorded neural oscillations. The performance of these two measures has already been discussed in previous sections (see section 4.2 and 4.3). With the use of simulations, the PLV provides equivalent information to the coherence regarding the two signals. Theoretically, both the magnitude of the

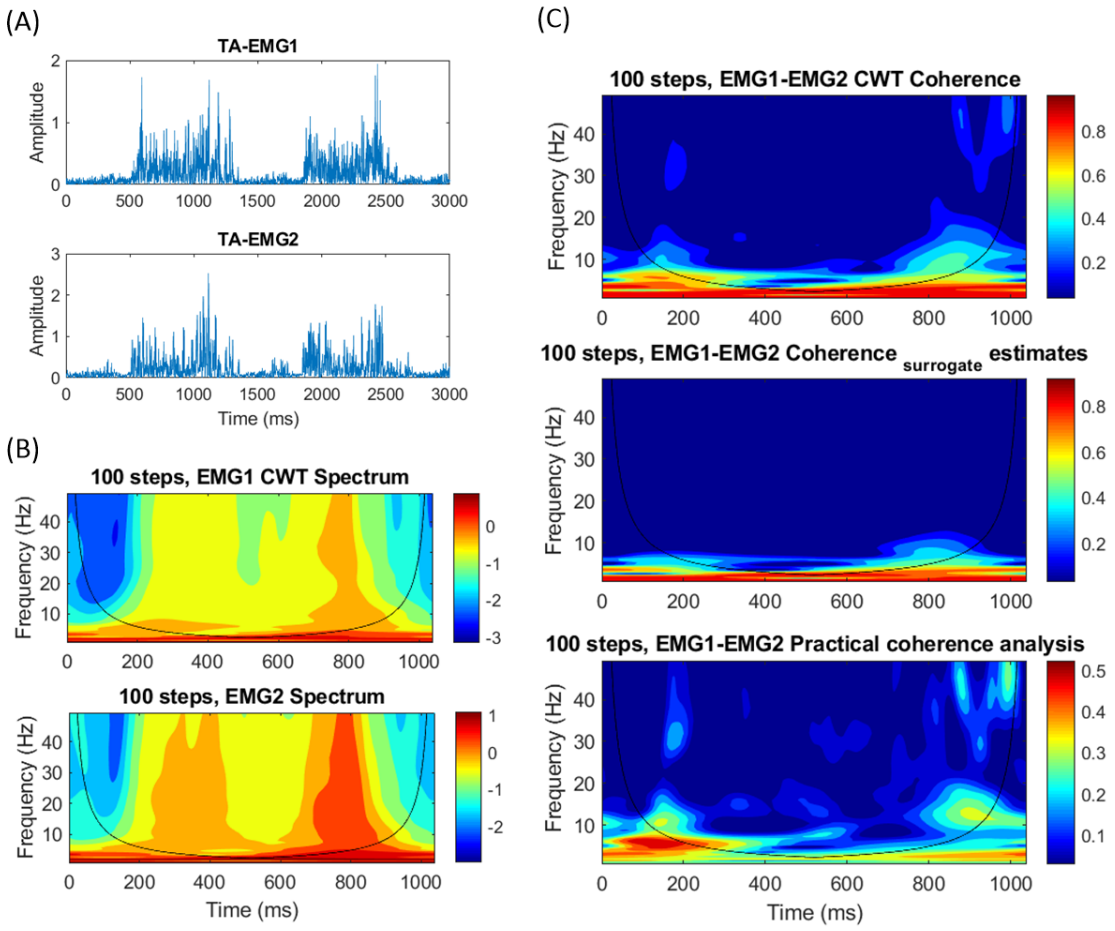

Figure 4.15: EMG-EMG wavelet spectral and practical coherence for removal of low frequency envelope modulation component analysed from 100-step cycles, which segmented into 1024 ms non overlapping epochs from one subject during treadmill walking. (A) an example of paired sEMG signals after rectification and (B) estimates of spectra for each EMG channel, (C) time-frequency coherence and practical coherence analysis for removal of low frequency envelope modulation plots.

coherence and the PLV lie in the interval between 0 and 1. Further, the study of Aydore et al. (2013) suggest that PLV and coherence are equivalent measures. Thus, it appears reasonable to expect that the practical technique for coherence could also be applied to PLV analysis.

The practical PLV analysis for removal of low frequency envelope modulation uses $z-$ transform as variance stabilizing transform for PLV and the same procedures as the practical coherence analysis for removal of low frequency envelope modulation except using Eq.4.21 instead of Eq.4.28 for computing the original PLV estimates and PLV estimates from surrogate data (trial-shuffling within signal $y(t)$). For testing the performance of the practical PLV analysis for removal of low frequency envelope modulation, it will be applied

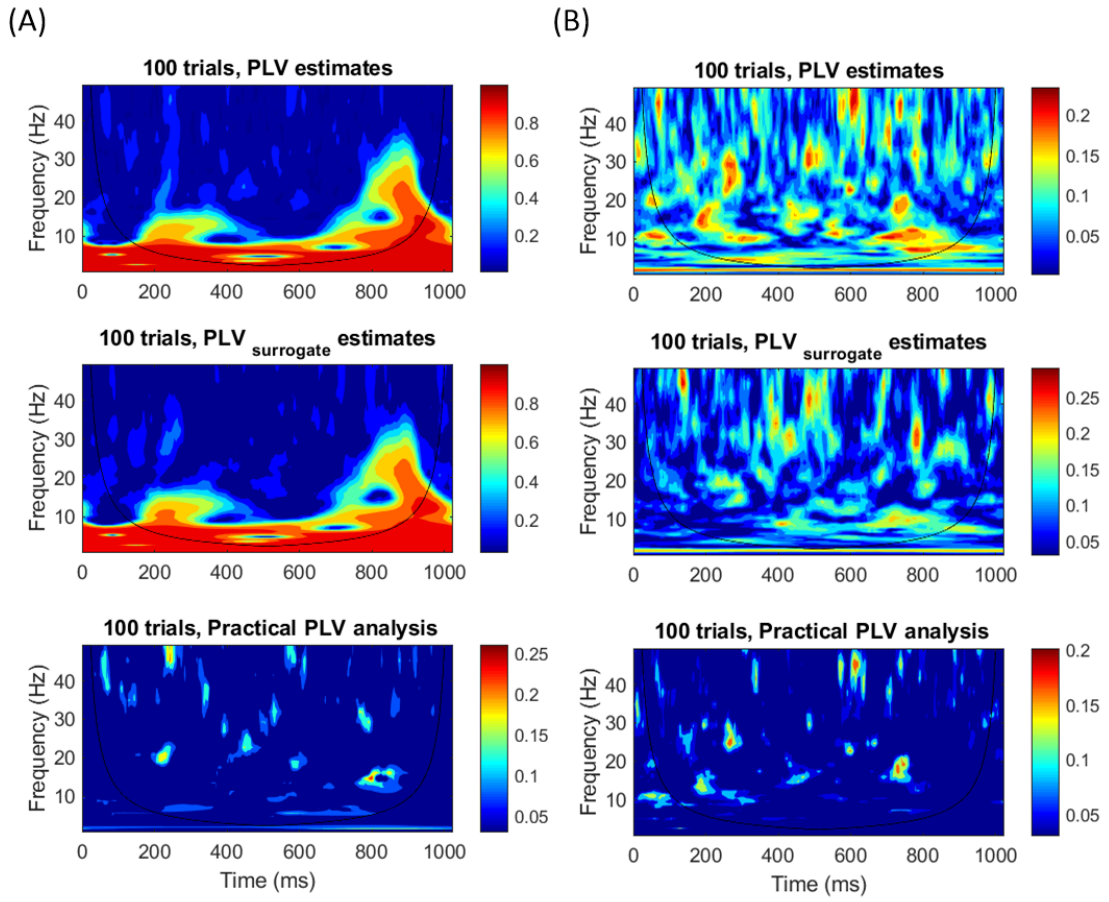

Figure 4.16: PLV and practical PLV analysis for removal of low frequency envelope modulation component are calculated using averages over 100 trials of simulated data from Figure 4.13(A) and (B). Top row shows PLV estimates of original simulated signals. Middle row show PLV estimates of surrogate data. Bottom row shows practical PLV analysis for removal of low frequency envelope modulation. Black line curve in each figure indicates COI.

to the same data used in the practical coherence analysis for removal of low frequency envelope modulation. Figure 4.16 and Figure 4.17 show in section 4.4.1, original PLV estimates, PLV estimates of surrogate data, and practical PLV analysis for removal of low frequency envelope modulation from the simulated signals shown in Figure 4.13, and the experimental data shown in Figure 4.15(A), respectively. The practical PLV analysis for removal of low frequency envelope modulation provides similar information as the practical coherence analysis for removal of low frequency envelope modulation although the practical PLV analysis for removal of low frequency envelope modulation appears to exhibit more fluctuation than the practical coherence analysis for removal of low frequency envelope modulation, see Figure 4.15 compared to Figure 4.17.

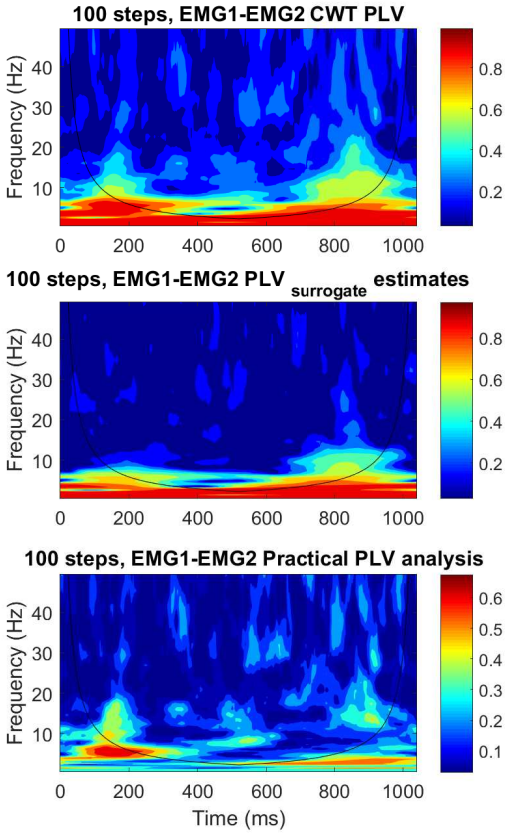

Figure 4.17: EMG-EMG practical PLV analysis for removal of low frequency envelope modulation in treadmill locomotion data. Details are as indicated in the captions and in Figure 4.15.

Practical coherence analysis and practical PLV analysis for removal of low frequency envelope modulation are novel techniques which provide a method for removal of low frequency envelope modulation in sEMG records. Three examples shown in section 4.4.1 and 4.4.2 are presented, the first example uses two amplitude modulations of Gaussian noise modulated by the same amplitude envelope, the second uses only one amplitude modulation and uncorrelated Gaussian noise, the third uses the real sEMG data. The results analysed from the simulated data suggest two coherence estimates have similar values (both are large (≈0.8) for the first example and both are small (≈0.2) for second example). Thus, the practical coherence and PLV analysis for removal of low frequency envelope modulation is small (≈0.2), see Figure 4.14 and 4.16. The results from real sEMG data analysis show that original coherence presents a rhythmic modulation of motor unit activity (8-20 Hz) around early and late swing and a low frequency component ($< 4Hz$), coherence estimates of surrogate data present low frequency ($<$ 4 Hz) throughout the step

cycle, practical coherence and PLV analysis for removal of low frequency component show a distinct 8-20 Hz during early and late swing, but the low frequency components (< 3 Hz) disappear as illustrated in Figure 4.15 and 4.17. The results from this study may be used to separate physiological mechanisms from effects due to envelope modulation. Further details for analysing real sEMG data are provided in chapter 5.

4.5 Wavelet time-resolved phase-amplitude coupling estimates

Phase-amplitude coupling (PAC) is used to study interaction between neuronal oscillations at different frequencies. Measures of PAC can monitor the relationship between the oscillatory activities where the phase of lower-frequency oscillations modulates the amplitude of higher-frequency oscillations (Canolty & Knight 2010). There are several methods for calculating PAC measures. Here, mean vector length proposed by Canolty & Knight (2010) is used to describe the standard steps in the computation of PAC measures. Then, time-resolved PAC proposed by Samiee & Baillet (2017) is considered as a technique in order to investigate and characterise non-stationary neuronal activities underlying human walking in this thesis. Mean vector length and time-resolved PAC in this thesis rely on the generalized Morse wavelets. Throughout the following sections the amplitude and the phase frequencies under analysis are denoted by f_A and f_P, respectively. PAC detection relies on filtering signals for particular frequencies. For instance, a signal filtered at the two particular frequencies (f_A and f_P) denoted as x_{f_A} and x_{f_P}, respectively.

4.5.1 Mean vector length

Mean vector length (MVL) is defined as a modulation index based on the complex variable (Penny et al. 2008, Canolty et al. 2006). The complex-valued wavelet function based on the complex variable can be defined as

$$Z_{f_P,f_A} = |A_{f_A}(\tau)| \cdot e^{i\phi_{f_P}(\tau)} \tag{4.30}$$

Eq.(4.30) could be used to extract a phase-amplitude coupling measure where A_{f_A} is the envelope of higher-frequency oscillations, and ϕ_{f_P} is the phase of lower-frequency oscillations. After extracting ϕ_{f_P} and A_{f_A}; each component of A_{f_A} in time is represented by the length of the complex vector, whereas component of ϕ_{f_P} in the same time point

is represented by the vector angle. Then, the estimation of absolute value of the mean vector over N trials is given by

$$MVL = \frac{1}{N}\sum_{n=1}^{N}\left|\overline{Z}_{f_P,f_A,n}\right| \tag{4.31}$$

where $\overline{Z}_{f_P,f_A,n}$ is vector sum of $Z_{f_P,f_A,n}$ across all time samples for trial n. This MVL is used to measure the degree of phase-amplitude synchronisation across frequency bands. See Canolty et al. (2006) for more details.

A significance value for the modulation index can be calculated by using a surrogate series approach. Canolty et al. (2006) compared the actual mean vector of a complex time series defined as (4.30) to a set of surrogate means created by offsetting A_{f_A} and ϕ_{f_P} by some large time lag T (i.e., the surrogate vector is defined by $A_{f_A}(t+T)e^{i\phi_{f_P}(t)}$; see supplementary material of Canolty et al. (2006) for more details). Then, a normalized modulation index is defined as

$$MVL_{NORM} = \frac{MVL - \mu}{\sigma} \tag{4.32}$$

where μ is the mean of the surrogate lengths, and σ is their standard deviation. Canolty et al. (2006) suggested that MVL_{NORM} is insensitive to the marginal distributions of A_{f_A} and ϕ_{f_P}, and is sensitive only to their joint distribution.

The general procedure for computation of PAC using generalized Morse wavelets is shown in Figure 4.18. First, the instantaneous amplitude envelope of the higher-frequency oscillation and instantaneous phase of the lower-frequency oscillation are calculated by obtaining an analytic representation of the original signal. Here, the wavelet transform naturally converts a signal to its analytic representation, and also filters the signal in a single step. Each scaled wavelet acts as a bandpass filter which inversely relates to oscillatory frequency as discussed in 4.1.2. Higher scales produce broader wavelets in time space which can increase the wavelength in contrast to lower scales. Secondly, the instantaneous amplitude and phase are extracted from the analytic representation, and then calculated as the absolute value and the phase angle of the analytic signal, respectively. PAC measures in the frequency domain are typically represented with a comodulogram plot, which shows the level of coupling strength between phase/amplitude pairs in pseudocolour scale. The x-axis represents the frequencies analysed as phase frequency: f_P, and the y-axis represents the frequencies analysed as amplitude frequency: f_A.

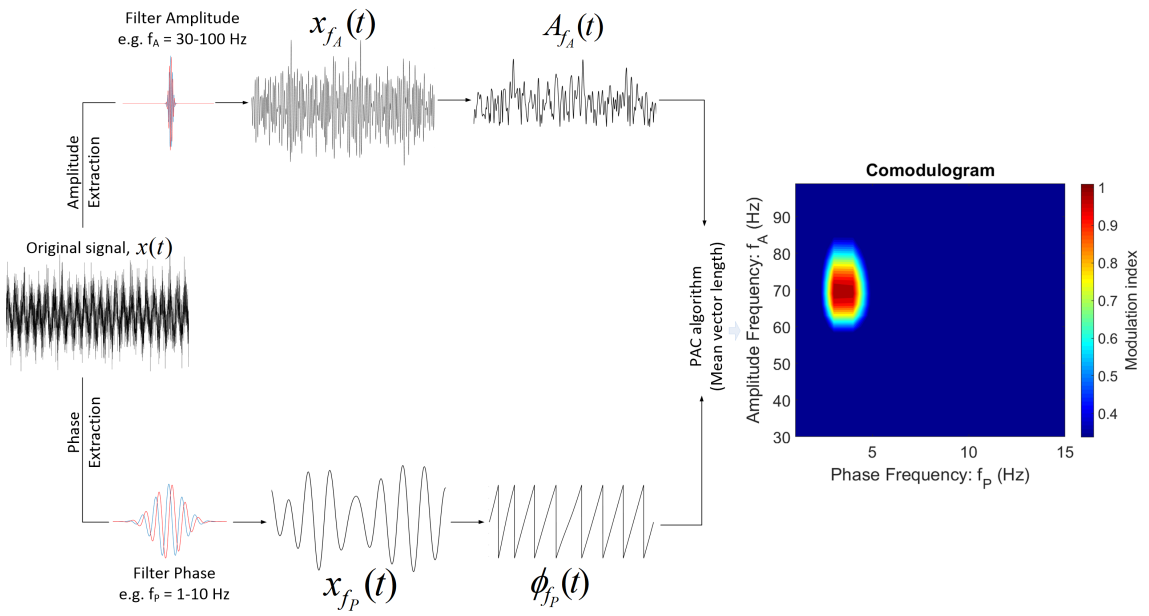

Figure 4.18: Graphical overview of PAC analysis. The original signal containing power at $f_P = 3Hz$ and $f_A = 70Hz$, which is generated using the model explained in (4.35) and (4.36), is separated into frequency components of interest via the generalized Morse wavelets: an amplitude signal x_{f_A} and a phase signal x_{f_P}, from which their amplitude envelope A_{f_A} and phase ϕ_{f_P} are extracted. Then, the coupling between phase and amplitude is quantified using mean vector length algorithm to produce a modulation index value. The modulation index is represented by comodulogram plot which pseudocolour scales indicates coupling strength shown at right.

4.5.2 Time-resolved phase-amplitude coupling

Time-resolved PAC (tPAC) is a method to resolve PAC measures in time. The approach is inspired by Samiee & Baillet (2017) and Özkurt & Schnitzler (2011). Özkurt & Schnitzler (2011) suggest that a MVL−MI algorithm which includes a normalization factor corresponding to the instantaneous amplitude envelope of the higher-frequency oscillation, A_{f_A}, is more resilient to measurement noise (see Özkurt & Schnitzler (2011) for more details). Here, an estimation of tPAC using a frequency map adapted from Samiee & Baillet (2017) and Özkurt & Schnitzler (2011) is defined by

$$tPAC(f_A, f_P) = \frac{1}{N}\sum_{n=1}^{N}\left(\frac{|\overline{Z}_{f_A,f_P,n}|}{\sqrt{\overline{A_{f_A}^2}}}\right) \tag{4.33}$$

where $\overline{Z}_{f_P,f_A,n}$ is vector sum of $Z_{f_P,f_A,n}$ across all time samples for trial n. The estimation of tPAC in time-frequency map can be calculated by

$$tPAC = \frac{1}{N}\sum_{n=1}^{N}\left(\frac{|Z_{f_A,f_P,n}|}{\sqrt{\overline{A^2_{f_A}}}}\right) \tag{4.34}$$

where N is the number of trials, $Z_{f_A,f_P,n}$ is from (4.30), and $\overline{A^2_{f_A}}$ is mean value of $A^2_{f_A}$.

Steps in the computation of tPAC have a similar approach to the flow for computing PAC. Additionally, the principle of the tPAC procedure requires additional steps as the f_P with strongest phase-amplitude coupling with f_A bursts in each trial is searched for automatically using a power spectrum estimate (Samiee & Baillet 2017). A spectrum range of interest for f_P and f_A should be defined either linearly or logarithmically. If in each trial, the amplitude of f_A oscillations is coupled to the phase of a slower oscillation at frequency f_P, then the power spectrum density (P_A) of A_{f_A} is expected to feature a peak at f_P. Also, a peak around f_P shall be expected in the power spectrum density of original signal (P_x). P_A and P_x are calculated using discrete-Fourier transform (DFT) averaged over trials. Due to the presence of edge effects at the start and the end of time-series created by wavelet filtering, sufficient zero-padding is included around trials, i.e. the number of time points is set to equal or larger than next biggest power of 2 of the data length, see Samiee & Baillet (2017) for more details. In this study, the tPAC procedure based on the generalized Morse wavelets is summarised in Figure 4.19.

The analysis in Figure 4.18 and 4.19 are demonstrated using simulated time series with a single PAC frequency pairing of 3 Hz and 70 Hz. As seen in their comodulogram plot, the advantage of using tPAC analysis (Figure 4.19), as compared to standard PAC analysis (Figure 4.18) is that tPAC method displays a smaller area of significant coupling between an amplitude of 70 Hz and phase of 3 Hz. The dominant $f_P \sim 3$ Hz is represented in the tPAC comodulogram as seen in Figure 4.19 compared to Figure 4.18. Most importantly, tPAC method also measures the coupling strength over time. The coupling is observed between f_P=3 Hz and f_A=70 Hz over time (1 second), as seen in time-frequency plot. Interestingly, tPAC detects the power of faster oscillations indeed modulated by the phase of the slow rhythm. It is clearly seen that bursts of couplings present in time-frequency plot vary according to the 3-Hz f_P cycle.

In order to test the performance of the tPAC method using the generalized Morse wavelets, simulated data with controlled PAC parameters are used. It is generated using

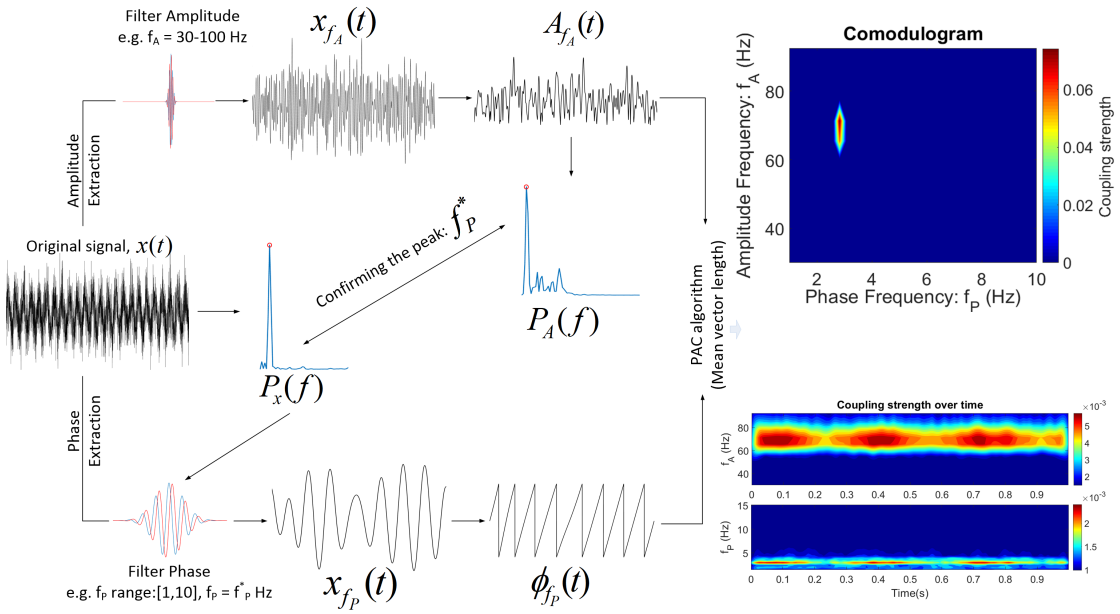

Figure 4.19: Graphical overview of tPAC method. Details are stated in text and in Figure 4.18. Additionally, to determine the dominant frequency f_P^*; the power spectrum P_A is estimated and its peaks are extracted. Also, the power spectrum P_x is estimated, and is used for finding the highest peak in P_A that co-occurs with a peak in P_x (Samiee & Baillet 2017). Note: values in time-frequency tPAC plot are not bounded in the range [0, 1] due to scaling, see Eq 4.34.

the method of Tort et al. (2010) which is modelled as

$$x(t) = \overbrace{K_{f_P}\sin(2\pi f_P t)}^{x_{f_P}(t)} + \overbrace{A_{f_A}(t)\sin(2\pi f_A t)}^{x_{f_A}(t)} + \varepsilon(t) \tag{4.35}$$

where $\varepsilon(t)$ is additive noise, and

$$A_{f_A} = 0.5[K_{f_A}(1-\chi)\sin(2\pi f_P t) + A_{f_A}(t) + \chi + 1] \tag{4.36}$$

K_{f_P} and K_{f_A} are constant which determine the maximal amplitude of f_P and f_A, respectively. The parameter $\chi \in [0, 1]$ controls the intensity of the coupling: $\chi = 0$ represents maximum coupling while $\chi = 1$ is no coupling.

Here, the original signal is constructed with length of 2 s, sampling rate of 1000 Hz. Multiple modes of coupling in the study of Samiee & Baillet (2017) are applied for this testing, which are: during the first half of the signal (1 s), the phase of slow oscillation at $f_{P_1} = 9$ Hz is coupled to the amplitude of a faster oscillation at $f_{A_1} = 115$ Hz. In the second half, the first coupling mode is terminated and two other modes appeared simultaneously with $f_{P_2} = 13$ Hz, $f_{A_2} = 145$ Hz, $f_{P_3} = 5$ Hz, and $f_{A_3} = 87$ Hz, respectively. The signal-

to-noise ratio is set to 6 dB, and the preferred coupling phase in the three modes are $270°, 0°, 180°$, respectively. The coupling parameter (χ) in each mode are 0.5, 0.2, and zero, respectively. The frequency ranges of interest for f_P and f_A in the tPAC analysis are defined linearly as ranges $[1, 15]$ Hz and $[40, 200]$ Hz, respectively. The wavelet parameters, β is set to 3,9, and 27, and γ is 3.

Figure 4.20 illustrates the tPAC analysis outcome on the synthesized data. Time-frequency maps reveal three coupling modes which there are areas of significant coupling between f_A=115 Hz and f_P=9 Hz during the time of 0-1 s, and the significant coupling between f_A=145 Hz, f_P=13 Hz and f_A=87 Hz, f_P=5 Hz occur during the time of 1-2 s, as seen in tPAC coupling strength maps for f_A and f_P vs. time (Figure 4.20(B)). The dominant coupling in each modes vary according to slow rhythm, for example, during the first half of the signal (1 s duration), the signal is averaged time locked to the troughs of the 9-Hz f_P cycle. The tPAC comodulogram (Figure 4.20(C)) is also reconstructed, as typical, non time-resolved appreciation of PAC in signal. It also shows three coupling modes, (f_P=5 Hz,f_A=87 Hz), (f_P=9 Hz,f_A=115 Hz), and (f_P=13 Hz,f_A=145 Hz). As noted in section 4.1, changing the value of β changes the frequency resolution of the corresponding wavelets. Setting β to low value, the frequency resolution is decreased. Here, the results show that tPAC method is less accurate in detecting the coupling for $\beta = 3$. tPAC returns accurate results for setting value of β to 27, see Figure 4.20(B-C)(top) compared to Figure 4.20(B-C)(bottom). Note that a dark blue colour on comodulogram and time-frequency plots indicates values below the 95% confidence limit. Statistical significance test for tPAC is described in 4.5.3.

4.5.3 Confidence limits for tPAC estimates

To determine statistical significance of tPAC estimates, surrogate data are generated following the approach of Aru et al. (2015) and Samiee & Baillet (2017). Here, the amplitude information (A_{f_A}) in each trial is first split into five blocks. Then, these blocks are randomly permuted to yield a surrogate dataset. Further, the phase and amplitude information of the original data are shuffled randomly between the different frequency components (Thengone et al. 2016). For each shuffled phase information obtained from the i^{th} frequency is randomly matched with the shuffled amplitude data from j^{th} frequency, where i and j are pseudorandom integers. The tPAC parameter estimates within the 95^{th} percentile of the surrogate distribution are considered statistically significant.

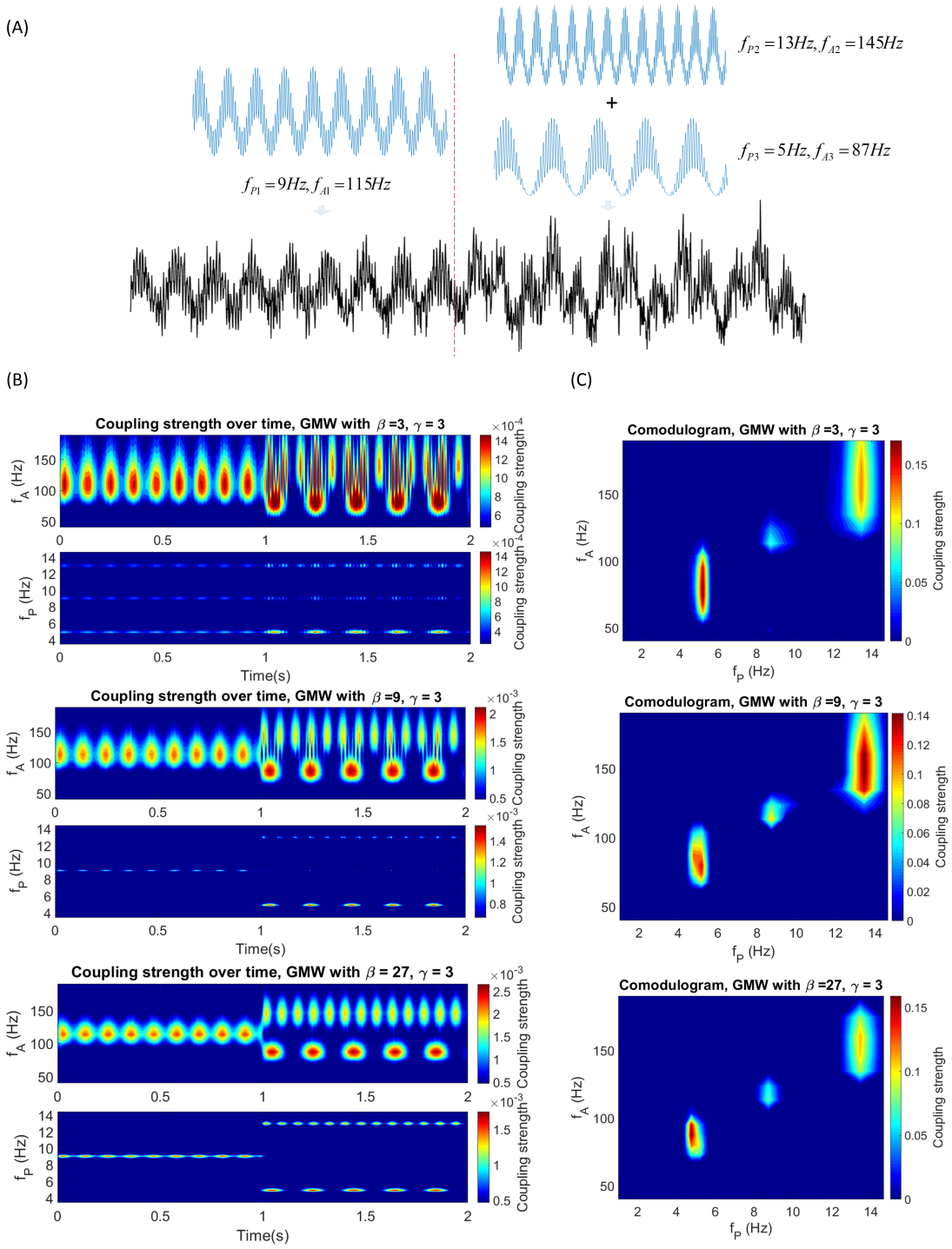

Figure 4.20: An example of tPAC analysis outcome on a synthesized data. (A) A synthesized data including three different coupling modes, see text for more details. (B) tPAC coupling strength maps for f_A and f_P vs. time, note these are not bounded in the range [0, 1], see Eq 4.34. (C) tPAC comodulogram. The 95% confidence limit for tPAC time-frequency plane is 0.47×10^{-3}, and 0.01 for tPAC comodulogram.

4.6 Summary

This chapter has reviewed relevant theoretical aspects of analytic wavelets − generalized Morse wavelets. Changes in parameters β and γ relate to temporal and spectral resolution in the time-frequency plane. Adjustment of these will alter the resolution in time and frequency. A particular subset of the generalized Morse wavelets, Airy wavelets (γ=3), are used in this thesis because they have zero asymmetry in time domain and are nearly symmetric in the frequency domain. In addition, the Airy wavelets not only preserve the spirit of the Morlet wavelet but also substantially outperform the Morlet for high time localisation while remaining analytic (Lilly & Olhede 2010, 2012). Optimal value of β depends upon the requirement of the analysis. To increase time resolution, we recommend setting β to low value. To increase frequency resolution, we recommend a relatively high value of β.

Three measures of time-frequency analysis, wavelet spectra and coherence, wavelet phase locking value, and wavelet time-resolved phase-amplitude coupling, are proposed. To have a better understanding, all methods are demonstrated by experiments on simulated signals. From the results given by these three methods, it has proved that the methods are able to successfully detect localised correlation in time-frequency plane. Coherence and PLV estimates in this chapter provide a similar description of the same signals. This finding is consistent with the study of Mezeiová & Paluš (2012), who suggested that coherence and phase synchronization provided essentially the same information. Although the PLV estimates have larger magnitudes than the coherence estimates, the unbiased PLV^2 estimator shows that the value of PLV^2 is close to the magnitude of coherence estimates, see section 4.3. The confidence limit derived from surrogate data is larger for the PLV estimates than for the coherence estimates for the same number of trials. Coherence and PLV estimates for removal of low frequency envelope modulation may be used to separate physiological mechanisms from effects due to low frequency envelope modulation of sEMG, as seen in Figure 4.15 and Figure 4.17. tPAC method is used to measure time-resolved parameters of PAC in signals. tPAC in time-frequency plane reveals time course of coupling cross-frequency expressed in the signal, see Figure 4.19 and 4.20. All three measures are derived using the Airy wavelet (γ=3) and setting β= 3, 9, and 27, it is noticed that low β leads to increased time resolution and decreased frequency resolution at high frequency, whereas high β provides increased frequency resolution and decreased time resolution at low frequency. Interestingly, in particular tPAC analysis, tPAC method

is more accurate in detecting the coupling for setting β to higher value. Note that for method of time-resolved phase-amplitude coupling, only time-frequency analysis (f_p and f_A vs. time) will be used in this thesis.

All three techniques can serve as a useful tool for investigating and characterising the interactions between non-stationary neurophysiological data such as surface EMG recorded during walking. The techniques are applied to surface EMG data from human treadmill and overground walking in next chapter. Airy wavelet with $\beta = 9$ is used as a compromise value for calculating all three measures, coherence, PLV, and tPAC.

Chapter 5

Application of time-frequency analysis to human locomotion data

In walking, a vast literature exists regarding the use of EMG analysis to detect a contribution from cortical motor commands to muscle activity observed in steady-state walking (see Halliday et al. (2003), Brittain et al. (2009), Petersen et al. (2010), Lodha et al. (2017) for example). Evidence suggests that the frequency of EMG-EMG coherence reflects common oscillatory drive to motoneurones from difference sources i.e. beta and gamma frequencies associated with oscillatory drive from sensorimotor cortex. Furthermore, Petersen et al. (2010) have reported that EMG signals are less noisy and the source of activity is known compared with EEG signals.

In this thesis, the rhythmic modulation of motor unit activity, which reflects contributions from rhythmic cortical activity, obtained from paired surface EMG recordings over the ankle flexor TA is acquired with the goal of studying and investigating neuronal coupling mechanisms associated with locomotion. Features from theta (4-8 Hz), alpha (8-12 Hz), low-beta (12-20 Hz), high-beta (20-30 Hz), and gamma (30-45 Hz) frequency bands are extracted and analysed to identify any modulations in the functional coupling of motor units during walking. All analyses may also provide insight into the organisation of the neural pathways involved in gait patterns.

In this chapter, time-frequency power spectrum, coherence, PLV and tPAC estimates presented in chapter 4 are used to assess the rhythmic modulation of motor unit activity during treadmill and overground walking in several data sets from normal healthy adult subjects and PD patients. The results of applying these methods are used to display the rhythmic modulation of motor unit firing which are contained in the EMG signals. To

summarise the correlation structure in each group of subjects, the individual estimates are combined, or pooled, into a single representative estimate. Note that the method of pooled coherence analysis is described in Amjad et al. (1997). All analyses are implemented using MATLAB (The MathWorks, Natick, MA).

5.1 Human treadmill walking

The data set analysed in this section comes from the study of Halliday et al. (2003). This data set has been analysed and the novelty here is in application of time varying measures. The two EMG signals over the ankle flexor can be used as a substitute for pairs of motor unit recordings which can identify any modulation in the functional coupling during walking, and provide a basis for investigating the highly adaptive nature of human gait patterns (Halliday et al. 2003). EMG recordings were digitally sampled at rate of 1000 and 5000 Hz. Recordings were made over a period of 500 seconds. A contact switch identified heel strike. Thresholding of the heel strike (HS) record provides a sequence of trigger times. These trigger times provide a reference point within each step cycle which is used to segment the data for undertaking time-frequency analysis, where time is defined with respect to heel contact. Further details of experiments are given in chapter 3, section 3.2.1. Example of rectified EMG signals and analysis window obtained from one subject during treadmill walking is demonstrated in Figure 3.1.

Halliday et al. (2003) applied estimates of coherence function and estimates of the cumulant density function to characterise the correlation between the EMG signals in the frequency domain and the time domain, respectively. Each step cycle was divided into three different non-overlapping segments each lasting 200 ms corresponding to early, mid, and end swing. The results demonstrate that the TA/TA coherence consist of a significant low-frequency component (<8 Hz) present in early and late swing together with peaks of coherence arising between 8-15 and 15-20 Hz. Also, a small broad peak close to 30 Hz is observed. Here, to obtain functional insight into the neuronal network responsible for the 8-20 Hz rhythmic components we present the novel analysis of these data focusing on time-frequency analysis using continuous wavelets.

Time-frequency power spectrum, coherence and PLV both with and without removal of low frequency component due to EMG envelope modulation, and tPAC are computed using generalized Morse wavelets with $\gamma = 3$ and $\beta = 9$. Experiments sampled at 5000 Hz have been down-sampled to 1000 Hz in order to construct pooled estimates. Note that

to construct pooled estimates, the individual estimates must be defined upon the same sample size and sampling rate. The standard practice of rectification of surface EMG signals has been a commonly used pre-processing procedure that allows detection of EMG coherence (Halliday & Farmer 2010) and is used here. EMG-EMG spectra, PLV and tPAC analysis are calculated using averages over 100-step cycles. All steps are segmented into 1040 ms segments with 820 ms before heel trigger and 220 ms after heel trigger, as seen in Figure 3.1 (chapter 3). The time scale on time-frequency plots is labelled as 0-1040 ms, heel triggers are at 820 ms in these plots. Thus, all plots cover swing phase including early, mid, and late swing for each step cycle. The EMG-EMG coherence, PLV, and tPAC analysis are considered significant if above the 95% confidence limits, calculated using Eq.(2.6) for coherence, in section 4.3.1 for PLV, and in section 4.5.3 for tPAC. Significant coherence, PLV, and tPAC are observed at frequencies $\leq$ 50 Hz, including theta, alpha, beta, and gamma frequency bands. Note that tPAC is applied to the data with f_P and f_A frequency ranges of interest, $[4-8]$ Hz and $[8-50]$ Hz, respectively.

5.1.1 Results from treadmill walking

Examples of time-frequency power spectra, coherence, PLV, and tPAC from 3 subjects walking at 4 km/h are shown in Figure 5.1(A)-(D), respectively. The results suggest that there is an increase in power in early, with a reduction in the middle and then increase in late swing of the step cycle (Figure 5.1(A)). Plot of estimated coherence before removal of low frequency envelope modulation component (Figure 5.1(B)(top)) shows that the strongest coherence (≈ 0.8) is at frequency < 5 Hz. This low frequency component persists across the swing phase. In addition, weaker coherence (> 0.6) between 8 and 20 Hz occurs in early ($\approx$ 200-400 ms) and late swing ($\approx$ 800 ms), for example, e417k1001 (centre) and e419kt002 (right). However, coherence magnitude of e406k1004 (left) in the early swing is smaller when compared to mid and end swing. In figure 5.1(B)(bottom), coherence estimates after removal of low frequency envelope modulation component indicates that some of the low frequency might be related to EMG envelop modulation, while coherence between 8 and 20 Hz in early and late swing is clearly seen in these plots. Some regions of coherence are outside the COI, therefore potential edge effects should be taken into account. Figure 5.1(C) shows that the PLV has significant features in both time and frequency which are similar to those seen in coherence estimates for each subject. A significant low-frequency (< 4 Hz) component is present throughout the step cycle as

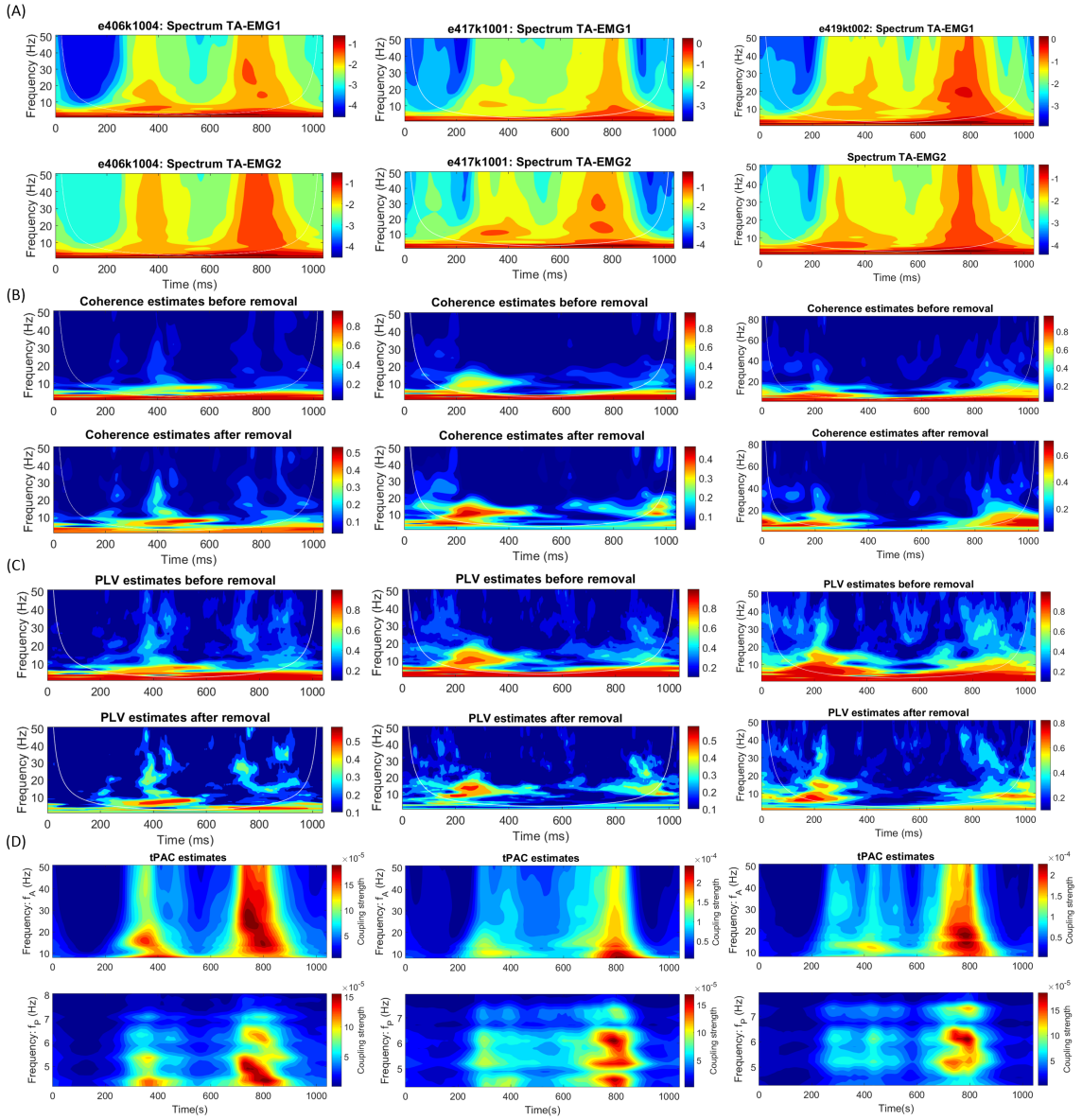

Figure 5.1: Examples of individual subjects analysed from 100-step cycles, segmented into 1040 ms nonoverlapping epochs during treadmill walking. The time scale on time-frequency plots is labelled as 0-1040 ms, heel triggers are at 820 ms. Columns represent records while rows represent (A) spectral estimates, (B) and (C) time-frequency individual coherence and PLV plots, including (top) before and (bottom) after removal of low frequency envelope modulation component, respectively, (D) individual time-frequency tPAC plots, note these are not bounded in the range [0, 1], see Eq 4.34. A dark blue colour on time-frequency plots indicates values below the 95% confidence limit for coherence, PLV, and tPAC.

shown in Figure 5.1(C)(top). A distinct 8-20 Hz frequency component is present during early and late swing in these PLV estimates. Also, some low frequency components disappear after removal of low frequency envelope modulation as illustrated clearly in Figure 5.1(C)(bottom). tPAC analysis is used to detect timing and frequencies of coupled os-

cillatory components: a slower oscillation (f_P) and a faster oscillation (f_A), where the amplitude of faster oscillations is coupled to the phase of slower oscillation. Figure 5.1(D) shows that strongest tPAC couplings are observed between $f_P \sim$ 4-6 Hz (theta band) and $f_A \sim$ 8-30 Hz (alpha and beta bands) during late swing. tPAC coupling strength in late swing encompasses not only frequency components of motor unit correlation between 8 Hz and 20 Hz, but also higher frequencies (>30Hz). In addition, there is another smaller coupling between $f_P \sim$ 4-6 Hz and $f_A \sim$ 8-20 Hz during early swing. Interestingly, we observed that tPAC follows a trend similar to that observed in the power spectra.

Some features shown on individual estimates in Figure 5.1 are common across all subjects as illustrated in summary time-frequency diagrams (Figure 5.2). These diagrams show maximum values of coherence and PLV after removal of low frequency envelope modulation components and tPAC at a given time and frequency band analysed from 100-step cycles for 10 records. For the majority of records ($\geq$ 7 records), maximum coherence and maximum PLV in Figure 5.2(top and middle) are observed at 4-20 Hz and 8-30 Hz around early swing (∼200 ms) and late swing (around heel contract ∼800-900 ms), respectively. Two of the records (#e406k1004 and #e406k1006) have maximum coherence and PLV at 4-20 Hz during the mid swing, ∼400-600 ms. The other frequency band, high-beta, is also observed during the late swing in only a few records. The tPAC analysis in Figure 5.2(bottom) highlights the coupling strength between the 4-8 Hz (theta band) and 8-12 Hz (alpha band) around 300-400 ms and the 4-8 Hz (theta band) and 8-45 Hz (alpha, beta and gamma bands) at ∼800 ms (around heel trigger) across all 10 records. A few subjects (3 subjects) display coupling between theta band and low-beta band around 400 ms.

Results over individual subjects during treadmill walking for all three measures are represented in Appendix A.

In summarising the correlations within data sets, individual estimates are combined into pooled estimates. The interpretation of pooled parameter estimates is similar to those for individual parameter estimates, except any inferences relate to the population as a group level (as opposed to the individual level). Here, the pooled estimates have been calculated across 10 records using a total of 1000 steps, 100 from each record. Pooled results are presented in Figure 5.3 for the three analysis methods. The pooled results from Figure 5.3 provide an overview of this data set. Both pooled and individual results demonstrate similar trends, which involve 8-20 Hz alpha and beta frequencies during early

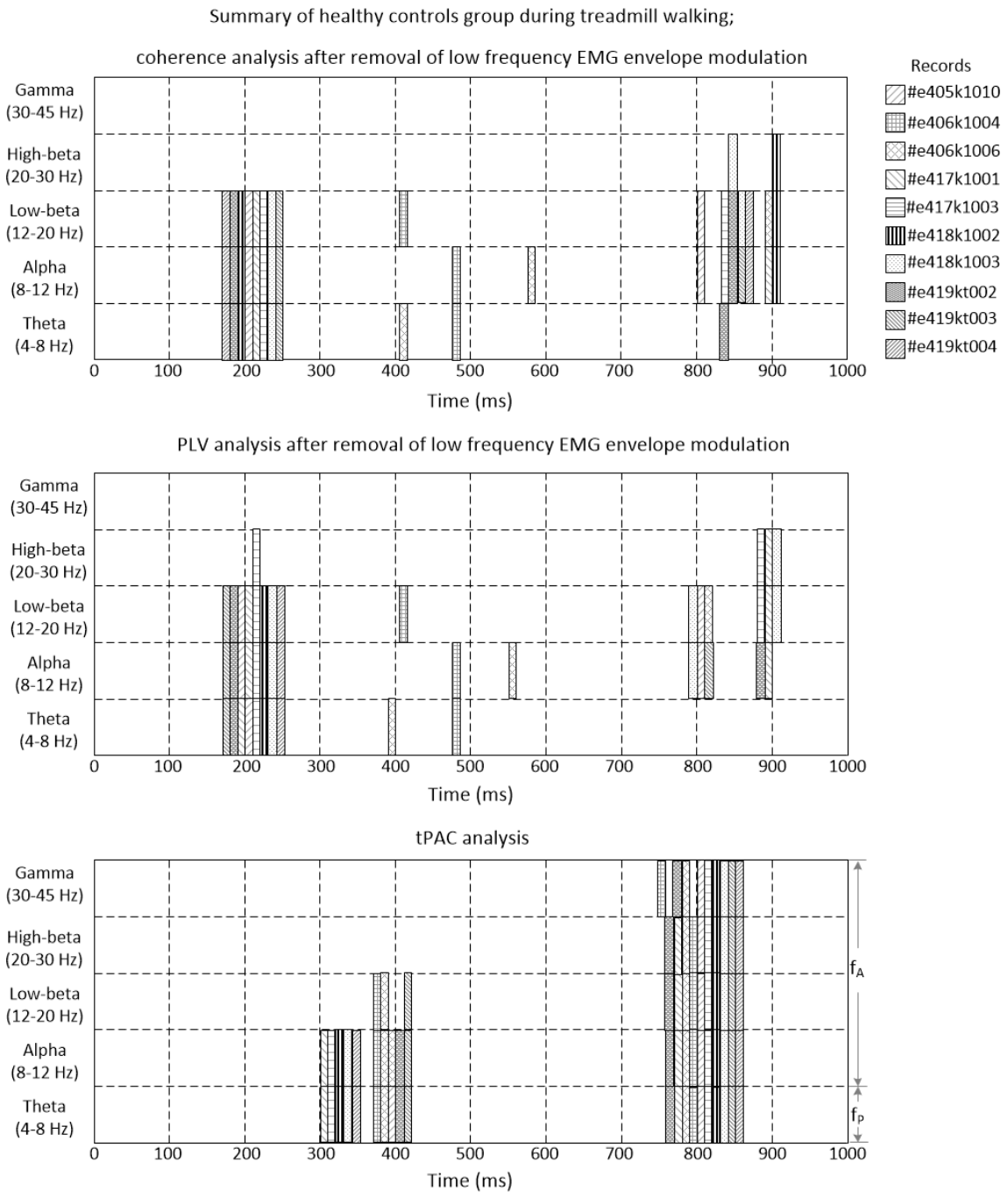

Figure 5.2: Summary time-frequency diagram of healthy subjects whose data showed maximum coherence and PLV after removal of low frequency envelope modulation component, and tPAC from 100-step cycles for 10 records during treadmill walking at 5 frequency bands [theta (4-8 Hz), alpha (8-12 Hz), low-beta (12-20), high-beta (20-30), gamma (30-45 Hz)]. Shaded bar for each record represents location of significant features at a given time and frequency band.

and late swing in coherence and PLV. In tPAC coupling is observed between $f_P \sim$ 5.5-6.5 Hz and $f_A \sim$ 8-50 Hz with the strongest coupling between $f_P \sim 6$ Hz and $f_A \sim 8$ Hz and between $f_P \sim 6$ Hz and $f_A \sim 20$ Hz during late swing. Significant peaks in all analyses

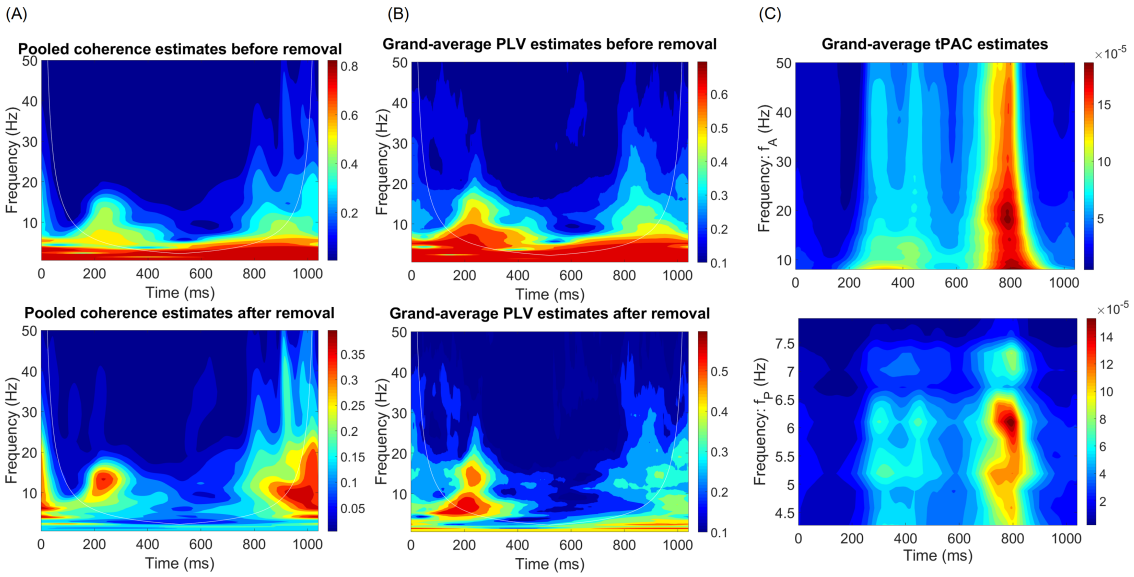

Figure 5.3: Pooled and grand-average analyses across 10 records during treadmill walking for 1000 steps. (A) Pooled coherence analysis before and after removal of low frequency envelope modulation component. (B) Grand-average PLV analysis before and after removal of low frequency envelope modulation component. (C) Grand-average tPAC analysis,note these are not bounded in the range [0, 1], see Eq 4.34. A dark blue colour on time-frequency plots indicates values below the 95% confidence limit for coherence, PLV, and tPAC.

are observed in early and late swing phase. To highlight the significant features, Table 5.1 summarises the pooled estimates in different frequency bands. Note that to avoid wavelet edge effects only values inside the COI are presented in the Table 5.1. The results of coherence and PLV estimates before removal of low frequency envelope modulation component have peak magnitude at frequency $\sim$ 4 Hz while the results of coherence and PLV estimates after removal of low frequency envelope modulation component show peak magnitude at $\sim$ 8-15 Hz around early swing. Also, significant coherence and phase synchrony are found in other frequency bands ($\sim$ 22-35 Hz) in late swing. Some regions of significant values are seen outside the COI, and are probably due to edge effects. Although the results of tPAC present significant coupling in all frequency bands, it is worth noting that the coupling strength is concentrated in distinct frequency bands, showing peak values of around 0.020×10^{-2} at 8-20 Hz and 0.015×10^{-2} around $\sim$ 6 Hz and $\sim$ 30 Hz. These strong coupling strengths are observed during late swing in all frequency bands. These frequency components are prominent around heel contact ($\sim$ 790-820 ms).

Table 5.1: Pooled peak time-frequency for all analyses of healthy subjects during treadmill walking before and after removal of components due to low frequency envelope modulation component.

Frequency bands	Coherence estimates	
	Before removal	After removal
4 - 8 Hz	0.680; 4 Hz; 650 ms	0.216; 6.73 Hz; 210 ms
8 - 12 Hz	0.528; 8.00 Hz; 225 ms	0.355; 11.31 Hz; 235 ms
12 - 20 Hz	0.460; 13.45 Hz; 240 ms	0.362; 13.45 Hz; 235 ms
20 - 30 Hz	0.231; 22.63 Hz; 815 ms	0.214; 22.63 Hz; 933 ms
30 - 45 Hz	0.214; 34.90 Hz; 920 ms	0.211; 34.90 Hz; 920 ms
Frequency bands	PLV estimates	
	Before removal	After removal
4 - 8 Hz	0.660; 4 Hz; 222 ms	0.560; 7.34 Hz; 217 ms
8 - 12 Hz	0.634; 8.00 Hz; 215 ms	0.572; 8.00 Hz; 210 ms
12 - 20 Hz	0.523; 13.45 Hz; 235 ms	0.521; 14.67 Hz; 230 ms
20 - 30 Hz	0.311; 22.63 Hz; 855 ms	0.294; 22.63 Hz; 910 ms
30 - 45 Hz	0.252; 32.00 Hz; 820 ms	0.231; 32.00 Hz; 820 ms
Frequency bands	tPAC estimates	
4 - 8 Hz	0.016×10^{-2}; 6.10 Hz; 790 ms	
8 - 12 Hz	0.020×10^{-2}; 8.00 Hz; 815 ms	
12 - 20 Hz	0.019×10^{-2}; 18.22 Hz; 790 ms	
20 - 30 Hz	0.018×10^{-2}; 20.75 Hz; 789 ms	
30 - 45 Hz	0.015×10^{-2}; 30.64 Hz; 790 ms	

5.1.2 Discussion of treadmill walking

The methods have been used to characterise the correlation structure in experimental data consisting of paired surface EMG signals during treadmill walking. The main finding is that all proposed methods are able to detect localised correlation in the time-frequency plane. Time-frequency coherence and PLV estimates in this section provide a similar description of the data. The results obtained are similar to Fourier based analysis time-frequency estimates in Halliday et al. (2003), where functional coupling of motor unit during locomotion is investigated. This demonstrated the presence of 8-15 Hz frequency

components of motor unit correlation. Here, we see similar frequencies in time-frequency coherence and PLV localised in early and late swing. In tPAC analysis, the results indicate that theta oscillation ($f_P \sim 6$ Hz) is strongly coupled to alpha and low-beta rhythms ($f_A \sim$ 8-20 Hz) during late swing. In addition, significant coupling is between $\sim$ 6 Hz and $\sim$ 20-45 Hz, specifically around heel contact. These frequency components partly overlap with the frequency ranges in the study of Petersen et al. (2012), who provide evidence in investigating the functional coupling between the motor cortex and TA muscles at 8-12 and 24-40 Hz in swing phase during treadmill walking. This finding is consistent with their suggestion that the motor cortex and the corticospinal tract contribute to the control of walking. Our findings show that tPAC can be used to investigate the functional coupling between two EMG signals from TA muscle during walking.

With respect to timing, we found that coherence and phase synchrony are present around 210-240 ms ($\sim$ 600 ms before heel trigger) and 820-910 ms (around heel trigger). This is largely in agreement with the study of Halliday et al. (2003), where coherence is present during early and late swing, and absent during mid swing. Further, we found maximum coupling strength in tPAC analysis around 790-815 ms (just prior to heel trigger). The temporal profiles for all three measures are approximately 50 ms prior heel strike to 120 ms after heel strike, which reflect rhythmic neural activity associated with a particular phase of locomotion, corresponding to late swing and early stance.

By using a novel approach for removal of low frequency envelope modulation components in coherence and PLV, we found that a low frequency component < 4 Hz is removed while other features remain unchanged. This technique gives advantage in terms of extracting low frequency envelope modulation component from sEMG recordings, and detecting rhythmic modulation of motor unit activity. The results in Figure 5.1 and 5.3 confirm that our novel analysis may be suitable for practical application of coherence and PLV analysis of EMG signals during walking. The techniques are applied to overground walking in next section.

5.2 Human overground walking

The three time-frequency measures used in treadmill locomotion data analysis are now applied to data from human overground walking. Data from 12 healthy control participants and 8 PD patients during walking under ecologically valid circumstances were collected by Weersink (2016). In brief, all of the healthy subjects had normal neurodevelopmental

history. All PD patients were diagnosed by a movement disorders specialist according to UK Brain Bank criteria (Hughes et al. 1992). In addition, they are able to walk properly, had right handedness according to Annett Handedness scale and absence of freezing of gait. All participants were instructed to walk at their preferred walking speed. The participants were asked to continually walk through a hallway of 150 metres in a straight line on level ground from start to finish and back. EMG from the bilateral anterior tibial (TA) muscles were recorded at sampling rates of 256 Hz or 1024 Hz, and stored for off-line analysis. Weersink (2016) determined the exact time of heel strike (HS) using an approach introduced by Sejdić et al. (2016). Further details of these experiments are given in chapter 3.

Data analysis was undertaken using similar methods to those described in section 5.1. In brief, the data have been up-sampled off-line to a common sampling rate of 1024 Hz in order to construct pooled estimates. Full wave rectification of surface EMG is used. The EMG signals are split into 100 non-overlapping segments or step cycles of length 1000 ms with 750 ms before HS and 250 ms after HS. All analyses are computed across all 12 subjects for healthy control and 8 subjects for PD. Pooled estimates are used to summarise the correlation structure in each group of subjects. The results of each group are provided in section 5.2.1. Significant features determined using same approach as section 5.1.

5.2.1 Results from overground walking

Based on previous results for paired TA-EMG analysis of treadmill locomotion data, our expectations for this experiment are: i) to see similar results for control subjects, for example, modulation of the magnitude of correlations over the swing cycle, the strongest correlations at the beginning and end, and the patterns of 8-20 Hz common modulation of EMG during locomotion, and ii) to provide any insight into differences in EMG activities in healthy control participants and PD patients.

Healthy controls group

An example of the rectified EMG signal and analysis window obtained from the TA muscle of a single healthy control subject during overground walking is provided in chapter 3, Figure 3.2(A). The signal appears slightly different from treadmill locomotion. EMG amplitude obtained from overground data is not as strongly modulated as in treadmill data and EMG signals from overground walking data appear more variable. The power spectra,

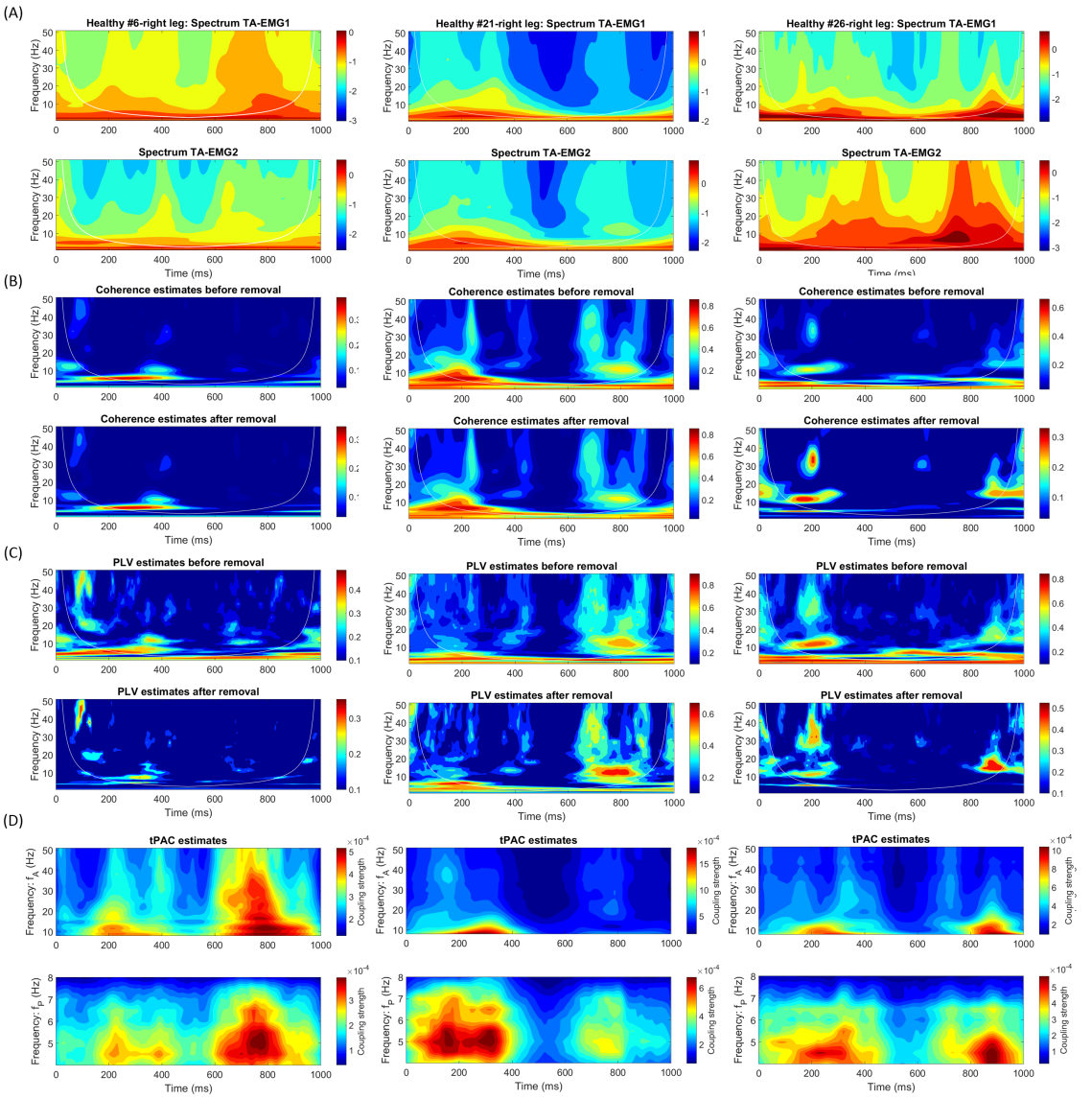

Figure 5.4: Examples of individual healthy subjects analysed from 100-step cycles, segmented into 1000 ms nonoverlapping epochs during overground walking. The time scale on time-frequency plots is labelled as 0-1000 ms, heel triggers are at 750 ms. Columns represent records while rows represent (A) spectral estimates, (B) and (C) time-frequency individual coherence and PLV plots, including (top) before and (bottom) after removal of low frequency envelope modulation component, respectively, (D) individual time-frequency tPAC plots, note these are not bounded in the range [0, 1], see Eq 4.34. A dark blue colour on time-frequency plots indicates values below the 95% confidence limit for coherence, PLV, and tPAC.

coherence, PLV and tPAC estimates are shown in Figure 5.4(A)-(D) for 3 representative subjects. Figure 5.4(A) shows increased power during early swing (200-400 ms), as well as during late swing and early stance (700-900 ms). During mid swing (500-600 ms) the power decreased. The frequencies of ∼6-12 and ∼30-40 Hz are observed in the beginning of swing (∼200-400 ms), and frequencies of ∼ 15-20 Hz occur around early stance phase (800-

900 ms) in coherence (Figure 5.4(B)). The features shown in coherence (Figure 5.4(B)) are also seen in PLV (Figure 5.4(C)). The frequency range $\sim$ 40-50 Hz around 100 ms in subject #6 is clearly seen in PLV plot in contrast to coherence estimates, see Figure 5.4(B) and (C)(left)).

The low-frequency component ($<$ 4 Hz) presented throughout the step cycle in Figure 5.4(B and C)(centre and right)) and the frequency range $\sim$ 6-8 Hz around 600-800 ms in Figure 5.4(B and C (top))(centre and right)) are removed by low frequency envelope modulation substitution.

In case of tPAC analysis (Figure 5.4(D)), the data show strongest coupling between $f_P \sim$ 4-5 Hz and $\sim$ 8-15 Hz at early swing ($\sim$ 200-400 ms) in subject #21 (column 2) and late swing in subject #6 (column 1) and subject #26 (column 3). Also, there are other smaller coupling modes between $f_P \sim$ 4-5 Hz and $f_A \sim$ 10-12 Hz around 200-400 ms in subject #6 (column 1) and subject #26 (column 3), and between $f_P \sim$ 4-5 Hz and $f_A \sim$ 20-40 Hz around 600-800 ms in subject #6 (column 1). As mentioned in section 5.1, it is interesting to note that tPAC analysis for overground walking data also shows a similar trend to that observed in the power spectra.

As mentioned earlier, EMG signals from overground walking data appear more variable than treadmill data. So, the results from individual coherence, PLV and tPAC estimates during overground walking show variability both in time and frequency values as seen in Figure 5.4. To represent the dominant features for all individual subjects, the summary time-frequency diagrams of three measures are shown in Figure 5.5. In Figure 5.5(top) and (middle), coherence and PLV are present at times $\sim$ 100-400 ms and $\sim$ 600-900 ms. Several subjects ($\geq$5 subjects) have maximum coherence and PLV values at frequencies 4-30 Hz around early swing ($\sim$ 200 ms) and late swing (around heel contract $\sim$700-800 ms), these features are similar to coherence and PLV analysis in treadmill walking data. In tPAC analysis (Figure 5.5(bottom)), strongest coupling in the majority of subjects (11 out of 12) are observed between f_P : 4-8 Hz and f_A : 8-12 Hz at times $\sim$ 700-900 ms. In this time interval, features between f_P : 4-8 Hz and f_A : 12-45 Hz component also appear across several subjects ($>$7 subjects). In addition, these frequency bands are also observed at times $\sim$ 100-200 ms and $\sim$ 300-400 ms. Only few subjects (2 subjects) display features around 600 ms.

Results over individual subjects during overground walking for all three measures are represented in Appendix B, section B.1.

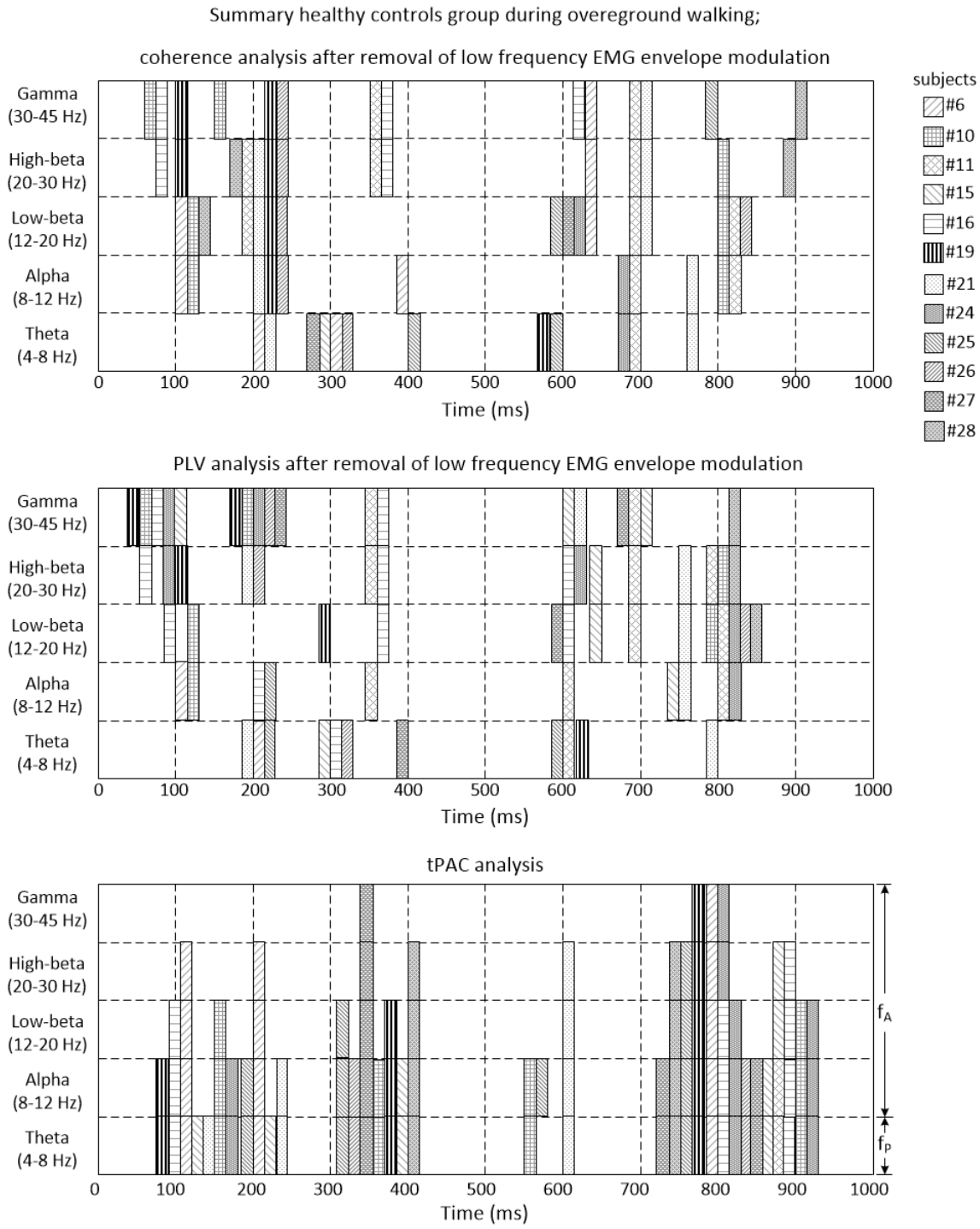

Figure 5.5: Summary time-frequency diagram of healthy subjects whose data showed maximum coherence and PLV after removal of low frequency envelope modulation, and tPAC from two legs (200-step cycles) for 12 subjects during overground walking at 5 frequency bands [theta (4-8 Hz), alpha (8-12 Hz), low-beta (12-20), high-beta (20-30), gamma (30-45 Hz)]. Shaded bar for each record represents location of significant features at a given time and frequency band.

In order to summarise the correlation parameters, individual estimates from two-leg swings are pooled. Here, the pooled estimates are calculated across 12 subjects for 2400 steps, 200 steps from each subject (100 steps per leg). Summary of results from pooled estimates in each method are presented in Table 5.2 and Figure 5.6. Based on Figure 5.6, there are two major coherence components in pooled results, around 100 ms at 20-25 Hz, and 735-900 ms at $\sim$ 8 Hz. In addition, weaker 25-45 Hz coherence are observed at times 650-700 ms. For PLV estimates, grand-average PLV estimates after removal of low frequency envelope modulation display dominant peaks at 11-30 Hz and 25-45 Hz frequencies at times 100-150 ms and 650-700 ms, respectively. Interestingly, the results of pooled coherence estimates are slightly different from the results of grand-average PLV estimates for this group. The comparison between pooled coherence estimates and grand-average PLV estimates indicates that $\sim$ 8 Hz at time $\sim$ 800 ms is observed only in coherence analysis. Strong low frequencies $<$ 4 Hz in PLV is removed by low frequency envelope modulation correction. The results of grand-average tPAC are similar to those seen in individual results, which exhibit dominant coupling between $f_P \sim$ 4-6 Hz and 8-15 Hz around 200-400 ms and 740-950 ms, respectively.

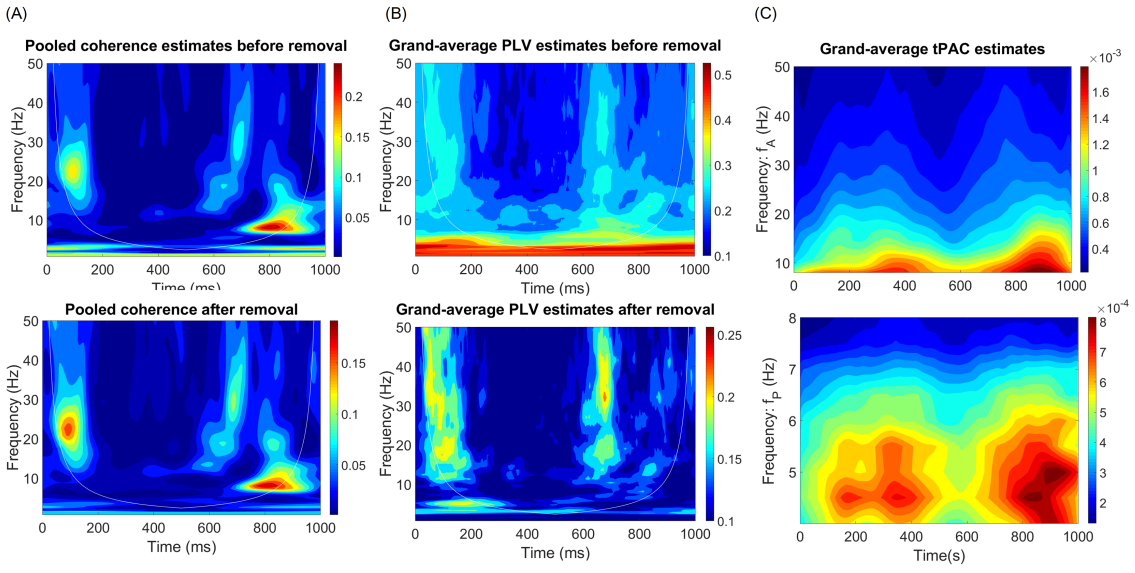

Figure 5.6: Pooled analyses across 12 healthy subjects during overground walking for 2400 steps. (A) Pooled coherence analysis before and after removal of low frequency envelope modulation. (B) Grand-average PLV analysis before and after removal of low frequency envelope modulation. (C) Grand-average tPAC analysis, note these are not bounded in the range [0, 1], see Eq 4.34. A dark blue colour on time-frequency plots indicates values below the 95% confidence limit for coherence, PLV, and tPAC.

Table 5.2: Pooled peak time-frequency for all analyses of healthy control subjects during overground walking before and after removal of low frequency envelope modulation component.

Frequency bands	Coherence estimates	
	Before removal	After removal
4 - 8 Hz	0.206; 7.34 Hz; 803 ms	0.167; 7.34 Hz; 813 ms
8 - 12 Hz	0.241; 8.00 Hz; 798 ms	0.191; 8.00 Hz; 803 ms
12 - 20 Hz	0.156; 20.75 Hz; 90 ms	0.156; 20.75 Hz; 90 ms
20 - 30 Hz	0.167; 22.63 Hz; 95 ms	0.165; 22.63 Hz; 95 ms
30 - 45 Hz	0.102; 32.00 Hz; 690 ms	0.100; 32.00 Hz; 690 ms
Frequency bands	PLV estimates	
	Before removal	After removal
4 - 8 Hz	0.394; 6.17 Hz; 680 ms	0.157; 6.73 Hz; 250 ms
8 - 12 Hz	0.329; 8.72 Hz; 710 ms	0.171; 11.31 Hz; 130 ms
12 - 20 Hz	0.304; 13.45 Hz; 835 ms	0.223; 17.45 Hz; 100 ms
20 - 30 Hz	0.289; 29.34 Hz; 80 ms	0.222; 29.34 Hz; 95 ms
30 - 45 Hz	0.295; 34.90 Hz; 670 ms	0.232; 32.00 Hz; 675 ms
Frequency bands	tPAC estimates	
4 - 8 Hz	0.085×10^{-2}; 5.00 Hz; 900 ms	
8 - 12 Hz	0.189×10^{-2}; 8.00 Hz; 890 ms	
12 - 20 Hz	0.151×10^{-2}; 12.34 Hz; 890 ms	
20 - 30 Hz	0.088×10^{-2}; 20.75 Hz; 885 ms	
30 - 45 Hz	0.060×10^{-2}; 30.64 Hz; 790 ms	

To provide a more comprehensive summary across the dataset of overground walking in healthy control subjects, peak pooled time-frequency coherence, PLV and tPAC magnitudes and timings are provided in Table 5.2. Pooled coherence estimates give similar features before and after removal of low frequency envelope modulation components; stronger coherence is observed at $\sim$ 8 Hz during early stance ($\sim$ 800 ms), medium coherence occurs in frequency range 20-23 Hz at the beginning of the swing cycle, coherence decreases at higher frequencies (>30 Hz). In contrast, an increase in higher frequencies (>30 Hz) is seen around 670 ms in grand-average PLV estimates. Removal of low frequency

envelope modulation component has greater impact on PLV, see Table 5.2. Focusing on grand-average PLV estimates after removal, peak magnitudes between 0.17 and 0.22 are observed in the ∼11-30 Hz frequency range around 95-130 ms. A decrease in magnitude (0.15) at ∼ 7 Hz is observed around 250 ms. For grand-average tPAC estimates, stronger coupling strengths in f_A band are found at ∼ 8-12 Hz, while lower coupling strengths are at frequencies > 30 Hz. tPAC coupling is present during late swing and early stance (around 795-910 ms) in all frequency bands, f_P 4-8 Hz and f_A 8-45 Hz. Although the results in this section display more variability in time and frequency values as clearly seen in Figure 5.5 compared with the results of healthy records from treadmill walking data in Figure 5.2, some features are similar to treadmill and also the frequency components of motor unit correlation (8-20 Hz) are observed during early and late swing in most subjects. Overall, the EMG activity in the TA muscle from healthy control data during overground walking is observed in frequency range from 5 Hz to 35 Hz with distinct peaks in early swing, late swing and early stance phase.

PD patients group

In this section, time-frequency analysis of the data from 8 PD patients during overground walking is undertaken using similar methods to those described in healthy controls. An example of the rectified EMG signal and analysis window obtained from the TA muscle of a single PD patient during overground walking is provided in chapter 3, Figure 3.2(B) which a general form of sEMG signals is similar to healthy controls. The EMG power spectra, coherence, PLV and tPAC estimates from 3 subjects are shown in Figure 5.7(A)-(D), respectively. The coherence and PLV estimates in these 3 subjects exhibit considerable difference. For example, PLV estimates show more fluctuations. In addition, low frequency component (< 4 Hz) is obviously seen only in PLV before removal of low frequency envelope modulation component. Peak magnitudes of coherence and PLV estimates at frequencies ∼8-15 Hz are observed around 200-400 ms in 3 subjects and around 600-800 ms in 2 subjects (#7 and #20, Figure 5.7(B-C)(column 1 and 3)). In addition, subject #20, has strong features at frequencies > 30 Hz around 200 ms in coherence and PLV plots. In tPAC estimates, strongest couplings are between f_P ∼5 Hz and f_A ∼ 8 Hz at times 200-400 ms in 2 subjects (#7 and #20). In contrast, strongest coupling mode in subject #8 are between f_P ∼ 7 Hz and f_A ∼20-30 Hz at times ∼ 800. Broad variability in frequency and time is found in plots of individual coherence and PLV estimates for the patient group

as summarised in Figure 5.8.

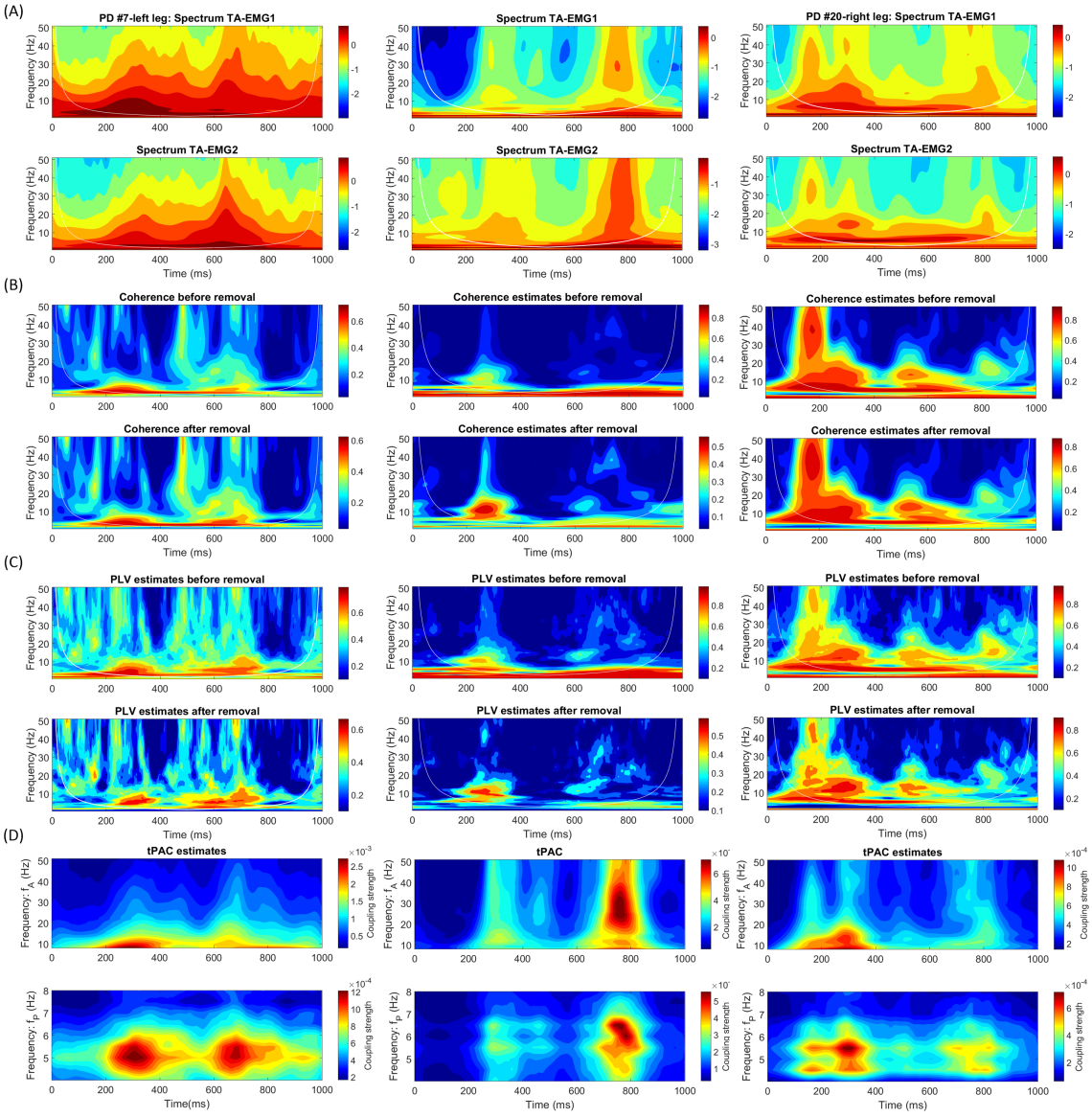

Figure 5.7: Examples of individual PD subjects analysed from 100-step cycles, segmented into 1000 ms nonoverlapping epochs during overground walking. The time scale on time-frequency plots is labelled as 0-1000 ms, heel triggers are at 750 ms. Columns represent records while rows represent (A) spectral estimates, (B) and (C) time-frequency individual coherence and PLV plots, including (top) before and (bottom) after removal of low frequency envelope modulation component, respectively, (D) individual time-frequency tPAC plots, note these are not bounded in the range [0, 1], see Eq 4.34. A dark blue colour on time-frequency plots indicates values below the 95% confidence limit for coherence, PLV, and tPAC.

Figure 5.8(top) shows that maximum coherences in most subjects (7 subjects) occur in all frequency bands at time $\sim$ 100-350 ms and $\sim$ 500-700 ms (This time range is earlier compared to healthy controls). In addition to these components, $\sim$ 12-45 Hz is evident in 4

subjects at time $\sim$ 100-200 ms. All frequency bands are observed around 200-350 ms and $\sim$ 600 ms in $>$ 4 subjects. Only one subject displays maximum coherence in frequency $\sim$ 30-45 Hz around 900 ms. For PLV analysis (Figure 5.8(middle)), the results are more diffuse. However, some features are consistent with those seen in Figure 5.8(top). For instance, $\sim$ 12-45 Hz around 100-200 ms and 4-45 Hz around $\sim$ 200-350 ms and $\sim$ 600 ms are evident in 4 subjects. Only one subject displays peak PLV in 30-45 Hz around 900 ms. Other features appear significant in only 2 subjects. For tPAC analysis (Figure 5.8(bottom)), a clear representation of significant coupling mode is seen across most subjects between f_P $\sim$ 4-8 Hz and $f_A \sim$ 8-30 Hz at time $\sim$ 200-400 ms, where dominant coupling is observed between f_P :4-8 Hz and f_A : 8-20 Hz around $\sim$ 300-400 ms. In addition, 7 subjects display significant coupling mode between f_P :4-8 Hz and $f_A \sim$ 8-45 Hz at times $\sim$ 750-900 ms. Only few subjects show significant coupling modes between $f_P \sim$ 4-8 and $f_A \sim$ 8-20 Hz around $\sim$ 100 ms (1 subject) and $\sim$ 500-600 ms (2 subjects). Generally, the existence of distinct rhythmic components within 8-20 Hz frequency bands during early swing, late swing and early stance seen in healthy controls are still observed in the patients with PD, but there is a slight difference in timing between healthy controls and PD, especially in coherence and PLV analysis.

Results over individual PD subjects during overground walking for all three measures are represented in Appendix B, section B.2.

As in the analysis of overground walking data from healthy subjects, pooled estimates and grand averages are also used here to summarise the correlation parameters within each group. Figure 5.9 shows pooled coherence estimates, grand-average PLV estimates, and grand-average tPAC estimates, which are calculated from two legs (8 subjects, 1600 steps, 100 steps per leg). The pooled coherence plots show clear coherence in the frequency range $\sim$20-40 Hz around 50-100 ms. Furthermore, weaker coherence between 12 Hz and 20 Hz occurs in $\sim$ 450-600 ms. Grand-average PLV estimates have dominant features at $\sim$ 8-15 Hz around $\sim$ 200-250 ms, and $10-15$ around $\sim$ 600 ms. Some significant values are also observed in frequency range $>$ 20 Hz around 100-300 ms, and $\sim$ 8-10 Hz at $\sim$ 900 ms which most of them are outside the COI. Interestingly, the plot of grand-average PLV estimates after removal of low frequency envelope modulation presents strongest magnitudes in low frequency range $\sim$ 1-3 Hz throughout the step cycle. Although this low frequency feature is outside the COI, it is important to notice that this frequency component disappears in grand-average PLV after removal of low frequency envelope modulation component for

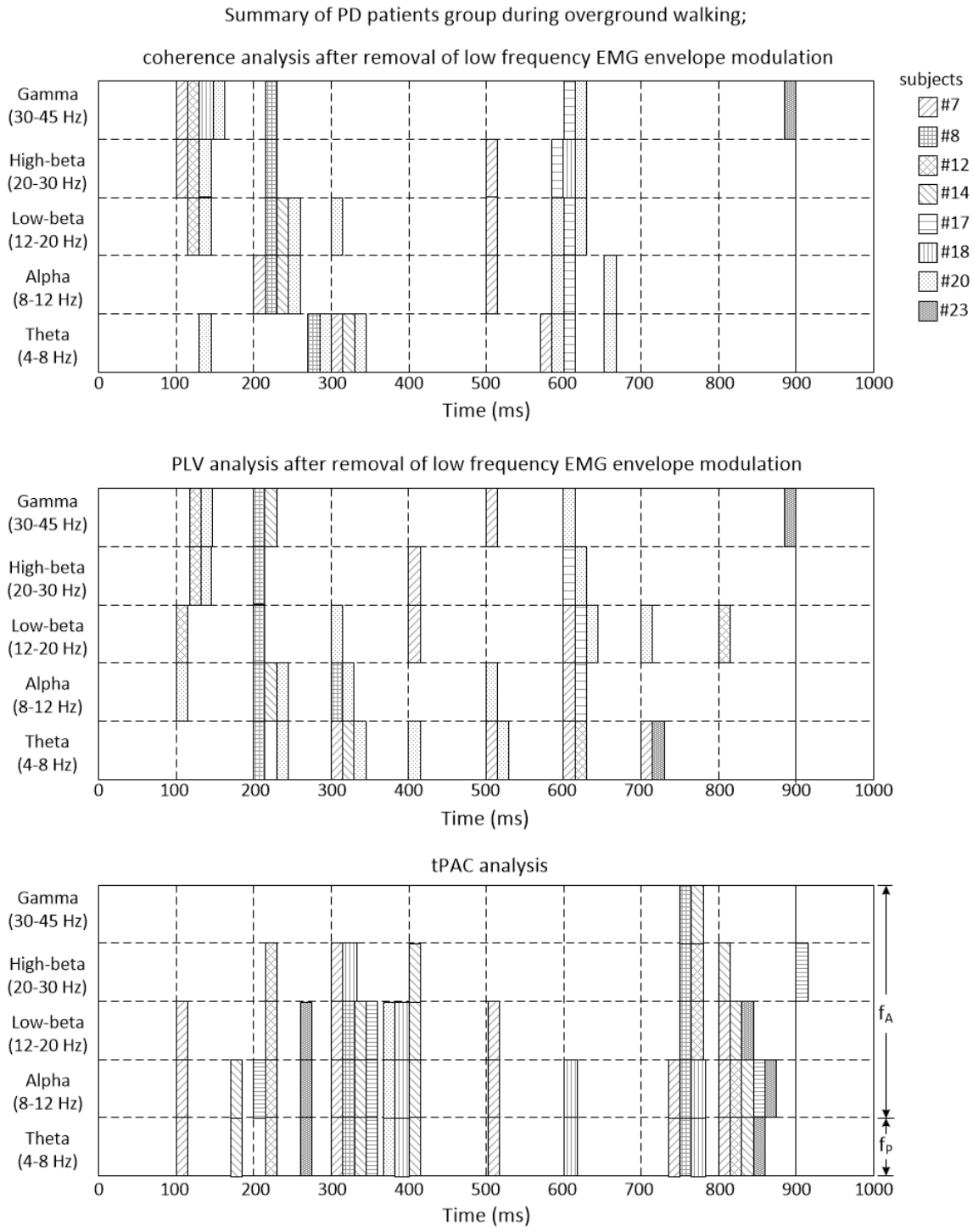

Figure 5.8: Summary time-frequency diagram of PD subjects whose data showed maximum coherence and PLV after removal of low frequency envelope modulation, and tPAC from two legs (200-step cycles) for 8 subjects during overground walking at 5 frequency bands [theta (4-8 Hz), alpha (8-12 Hz), low-beta (12-20), high-beta (20-30), gamma (30-45 Hz)]. Colour bar for each record represents features at a given time and frequency band.

healthy control data, see Figure 5.6(B) or Figure 5.3(B) for comparison. For grand-average tPAC estimates, the results suggest that stronger coupling strengths are observed between

frequency range $f_P \sim$ 4-6 Hz and $f_A \sim$ 8-15 Hz around $\sim$ 300-400 ms and $\sim$ 800-900 ms. The features shown in all pooled and grand-average estimates here are consistent with summary time-frequency diagram in Figure 5.8 for PD patients group.

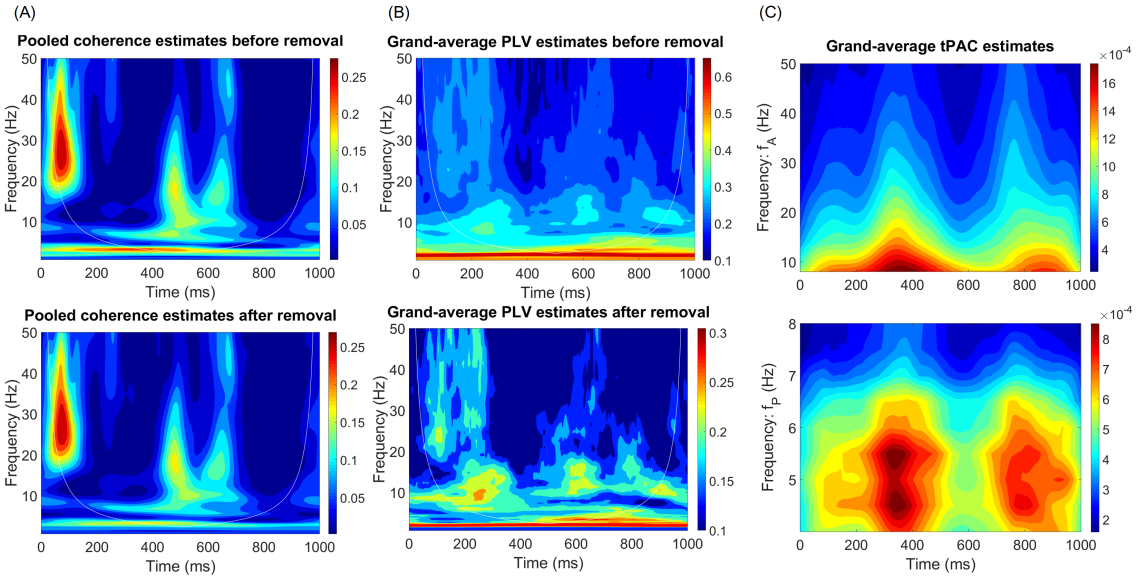

Figure 5.9: Pooled analyses across 8 PD subjects during overground walking for 1600 steps. (A) Pooled coherence analysis before and after removal of low frequency envelope modulation. (B) Grand-average PLV analysis before and after removal of low frequency envelope modulation. (C) Grand-average tPAC analysis, note these are not bounded in the range [0, 1], see Eq 4.34. A dark blue colour on time-frequency plots indicates values below the 95% confidence limit for coherence, PLV, and tPAC.

To summarise the significant features across the PD data set, Table 5.3 provides pooled peak time-frequency coherence, PLV and tPAC magnitudes and timing. In coherence estimates, we found that stronger coherences (> 0.2) are in frequency range $\sim$ 20-32 Hz at $\sim$ 70-76 ms, and lower coherences (~ 0.1) in frequency range $\sim$ 6-10 Hz at $\sim$ 446-530 ms. In PLV analysis, grand-average PLV suggest peak values are in frequencies $\sim$ 4 Hz and $\sim$ 8-38 Hz in time $\sim$ 100-260 ms and $\sim$ 600-725 ms, respectively. In tPAC analysis, stronger couplings ($> 0.1 \times 10^{-2}$) are in frequency range $f_A\sim$ 8-20 Hz at $\sim$ 340-360 ms, and lower couplings ($\sim 0.08{\times}10^{-2}$) at $f_P \sim 5$ Hz and $f_A \sim 30$ Hz at 345 ms and 326 ms, respectively. Although three measures suggest different features, it is clear that all three measures show time gap of 200-300 ms between two regions of strong features, with time range 400-600 ms using time scale in Figure 5.9. In addition, the results of grand-average tPAC estimates show strong features around 320-360 ms for all frequency bands.

Table 5.3: Pooled peak time-frequency for all analyses of PD subjects during overground walking before and after removal of low frequency envelope modulation component.

Frequency bands	Coherence estimates	
	Before removal	After removal
4 - 8 Hz	0.159; 6.73 Hz; 456 ms	0.128; 6.73 Hz; 446 ms
8 - 12 Hz	0.170; 10.37 Hz; 520 ms	0.160; 10.37 Hz; 530 ms
12 - 20 Hz	0.222; 20.75 Hz; 68 ms	0.218; 20.75 Hz; 70 ms
20 - 30 Hz	0.275; 26.91 Hz; 75 ms	0.269; 26.91 Hz; 76 ms
30 - 45 Hz	0.255; 32.00 Hz; 73 ms	0.249; 32.00 Hz; 74 ms
Frequency bands	PLV estimates	
	Before removal	After removal
4 - 8 Hz	0.458; 4.00 Hz; 606 ms	0.245; 4.36 Hz; 725 ms
8 - 12 Hz	0.373; 8.72 Hz; 250 ms	0.260; 9.51 Hz; 244 ms
12 - 20 Hz	0.327; 13.45 Hz; 280 ms	0.236; 13.45 Hz; 265 ms
20 - 30 Hz	0.307; 22.63 Hz; 116 ms	0.232; 24.68 Hz; 100 ms
30 - 45 Hz	0.294; 34.90 Hz; 107 ms	0.209; 38.00 Hz; 116 ms
Frequency bands	tPAC estimates	
4 - 8 Hz	0.089×10^{-2}; 5.00 Hz; 345 ms	
8 - 12 Hz	0.182×10^{-2}; 8.00 Hz; 360 ms	
12 - 20 Hz	0.151×10^{-2}; 12.34 Hz; 345 ms	
20 - 30 Hz	0.108×10^{-2}; 20.75 Hz; 347 ms	
30 - 45 Hz	0.079×10^{-2}; 30.64 Hz; 326 ms	

Comparison of healthy controls and PD patients groups

In order to determine statistically significant differences in features between the two groups −healthy controls and PD patients, a Wilcoxon rank-sum test (also called Mann-Whitney U test) is used. This statistical test is a popular non-parametric statistical analysis that is used for variables with non-normal distributions (Vickers 2005). Estimates of population coherence, PLV, and tPAC are obtained by averaging each pooled estimate for five frequency bands (theta, alpha, low-beta, high-beta, and gamma). Only features above the 95% confidence limits and within the COI are chosen for further processing. The Wilcoxon rank-sum test is conducted at the 5% significance level including the coherence

and PLV after removal of low frequency envelope modulation component, and tPAC in the five frequency bands. The resulting figures for comparison of healthy controls and PD patients are created using the toolbox notBoxPlot (Campbell 2017). The difference in features of paired surface EMG signals between healthy controls and PD patients during overground walking for each data analysis method is shown in Figure 5.10.

In coherence analysis (Figure 5.10(top)), there are significant differences of coherence values in theta, low-beta, high-beta, and gamma frequency bands. Coherence values in alpha band are lower in PD patients than in healthy controls. When PLV analysis is considered, phase synchrony in alpha band is higher in PD patients than healthy controls in contrast to coherence. As can be seen in Figure 5.10(middle), there are significant difference of phase correlations at the lower frequency bands (< 20 Hz), and there are no differences between two groups in higher frequencies (20-45Hz). In contrast, for the tPAC coupling strength values obtained at frequencies < 12 Hz there are no differences between healthy controls and PD patients, the coupling scores have greatly significant differences at high frequencies (20-45 Hz).

In conclusion, the findings of time frequency analysis suggest that patterns of 8-12 Hz and 12-20 Hz common modulation of EMG are observed in healthy controls and patients with PD during overground walking. Although three proposed measures used in this thesis suggest significant differences in features between healthy controls and PD patients during overground walking, it is interesting to note that all three measures suggest significant differences in low-beta band (12-20 Hz). In addition, coherence and tPAC analysis display significant differences in high-beta (20-30 Hz) and gamma (30-45 Hz) bands while coherence and PLV analysis display significant difference in theta band (4-8 Hz), as seen in Figure 5.10. With respect to timing, our findings suggest that the time gap between two regions of strong features in PD patients is shorter than healthy controls for coherence and PLV estimates, time gap of 200-300 ms for PD and time gap of 300-400 ms for control, with time window ranges around 400-600 ms for PD patients and around 400-700 ms for healthy controls using time scale on time frequency plots as labelled 0-1000 ms, with heel trigger is at 750 ms.

5.2.2 Discussion of overground walking

As expected from ordinary coherence analysis, the results of healthy controls in this section display a distinct 8-15 Hz and 15-20 Hz, frequency components of motor unit correlation.

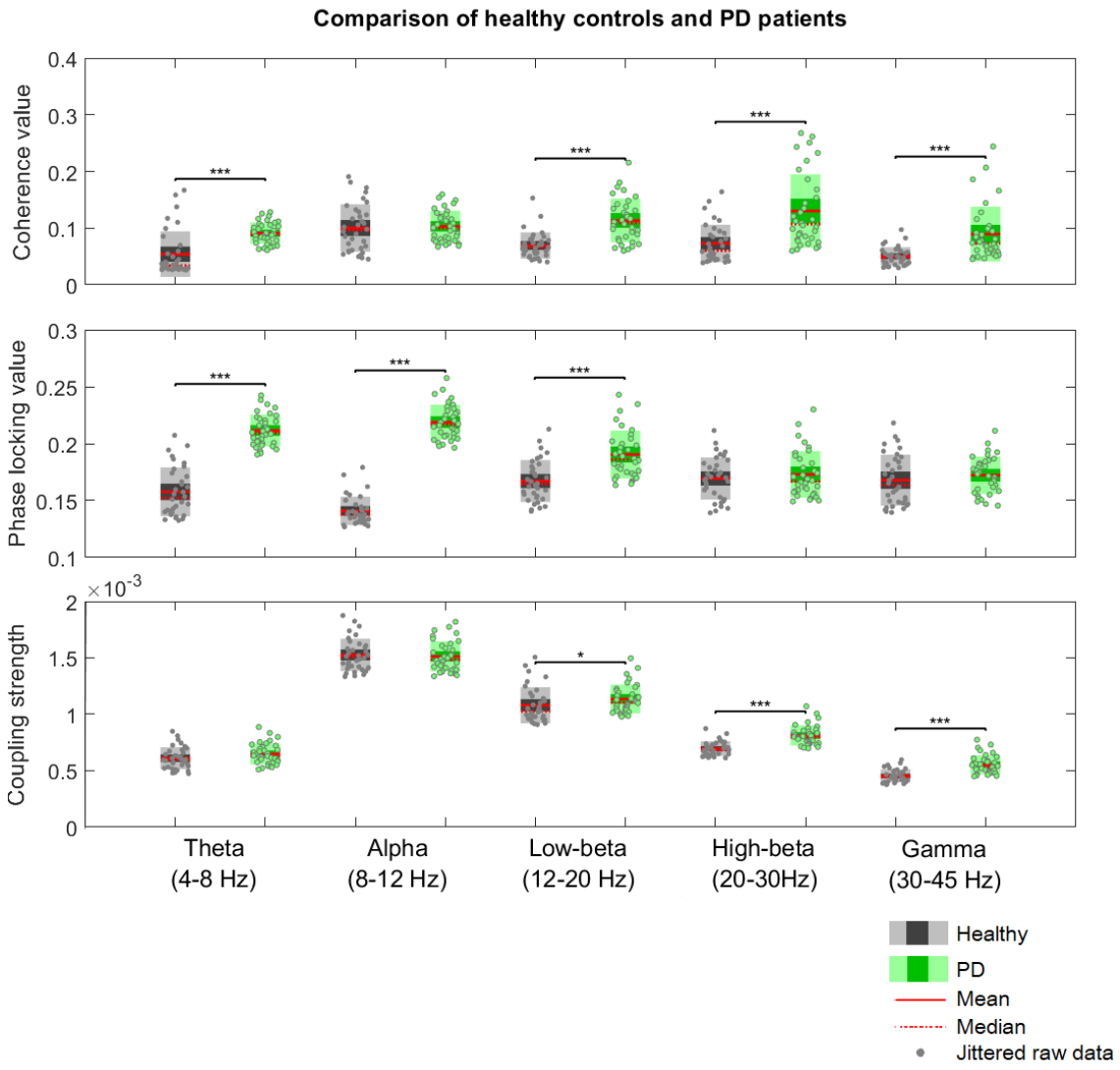

Figure 5.10: Boxplots comparing coherence (top panel), PLV (middle panel) and tPAC (bottom panel) values for healthy controls and PD patients. In boxplot, darker colour boxes indicate one standard deviation in the respective group. The lighter colour boxes indicate the 95 % confidence intervals of the arithmetic mean values. An asterisk represents a significance level of $p < 0.05$, two asterisks denote a significance level of $p < 0.01$, and three asterisks represent a significance level of $p < 0.001$. (Wilcoxon Rank Sum Test)

These frequency components are present during swing phase (early and late swing) and early stance phase, which are similar to that from data analysis during ordinary coherence analysis of treadmill walking (Halliday et al. 2003, Artoni et al. 2017).

In PD, the frequency components of motor unit correlation at 8-12 Hz are also observed. It is interesting to note that low frequency coherence and PLV (<6 Hz) displaying significant features is more clearly seen in PD patients group compared to healthy control group. In addition, the results from coherence and tPAC analysis show that beta band

(12-30 Hz, subdivided into low and high beta) and low gamma band (30-45 Hz) are greatly enhanced in comparison with healthy controls, as clearly seen in Figure 5.10(top and bottom). Clinically, the majority of patients with PD are affected by tremor, bradykinesia, and rigidity (Baumann 2012, Helmich et al. 2012, Little et al. 2012). In term of frequency content, tremor can be found in 4-12 Hz (Baumann 2012, Beudel et al. 2015), which can vary from low (4-6 Hz) to high (8-10 Hz) (Helmich et al. 2012). However, Beudel et al. (2015) suggested that PD tremor is related to low gamma oscillations. In recent years, there is growing evidence linking beta activity at rest and beta changes in response to treatment for bradykinesia and rigidity (Eusebio et al. 2012, Little & Brown 2014, Beudel et al. 2015, Little et al. 2012). Recent studies suggest that tremor seems to be an independent symptom of PD, which may have a distinct underlying pathophysiology to that of bradykinesia and rigidity (Stochl et al. 2008, Beudel et al. 2015). In term of timing, we found the time gap between two regions of strong features in PD patients group is shorter compared to controls group (time gap of 200-300 ms for PD and time gap of 300-400 ms for control, with time ranges 400-600 ms and 400-700 ms using time scale on time frequency plots of 0-1000 ms, with heel trigger of 750 ms). Dominant features in grand-average tPAC are present around 300-400 ms for PD patients group while they are present around 800-900 ms for controls group. These temporal profiles might be useful to characterise gait problems in PD, for example, shuffling and small-step gait, and difficulty in initiating and maintaining stepping.

As a walking task, however, in contrast to treadmill walking, we found that low frequency envelope modulation component during overground walking is weaker, as seen in time-frequency coherence and PLV before removal of low frequency envelope modulation effects. Time-frequency coherence and PLV analysis of EMG data recorded during overground walking, especially in PD patients, detect different features, as clearly seen in Figure 5.9 compared to Figure 5.6. However, our novel analysis for removal of low frequency envelope modulation component in coherence and PLV can be used to separate physiological mechanisms from effects due to amplitude modulation of sEMG as previously discussed in treadmill data analysis.

To summarise, the three time-frequency methods used in treadmill locomotion data analysis can be applied to the data set of overground walking in healthy control and PD patients. The results from overground walking data appear more variable than treadmill walking data, but all measures highlight specific features in time-frequency plane. Inter-

estingly, PLV analysis of PD patients data shows more variability in time and frequency values (Figure 5.8). Surprisingly, low frequency components (< 4 Hz) are observed in grand-average PLV after removal of low frequency envelope modulation of PD patients in contrast to healthy controls, see Figure 5.9 compared to Figure 5.6. The significant difference in features of paired surface EMG signals between healthy controls and PD patients determined by a Wilcoxon rank-sum test is observed in low-beta band (12-20 Hz) for all measures (Figure 5.10).

5.3 Summary

In this chapter, time-frequency based coherence, PLV and tPAC analysis using generalized Morse wavelets are applied to pairs of sEMG signals recorded from leg muscles (TA muscles) during treadmill and overground walking in healthy and PD human subjects. Low frequency EMG envelope modulation component in coherence and PLV analysis can be removed by comparing the original coherence or PLV from paired EMG signals with another derived from surrogate data, see more detail in chapter 4, section 4.4. One main finding is that all three time-frequency methods can detect the rhythmic modulation of motor unit activity, the alpha band (8-12 Hz) and low-beta band (12-20 Hz) in particular, across all datasets. These frequency components are prominent around heel contact, which reflect rhythmic neural activity associated with a particular phase of locomotion. The specific features described here match those observed in (Halliday et al. 2003). The results from all measures suggest the statistically significant difference between healthy and PD groups to be in the low-beta band (12-20 Hz).

Within the healthy treadmill locomotion dataset, all measures provide a clear description of the data. Coherence and PLV analysis detect similar features across all records. In addition, high frequencies > 30 Hz at late swing and early stance phase are evident in tPAC analysis for all records. A strong low frequency component due to EMG envelope modulation (<4 Hz) has been previously observed in coherence and PLV analysis before removal of low frequency envelope modulation component. See section 5.1 and Appendix A for more details in treadmill locomotion. During overground walking, more variability in time and frequency values are observed. Coherence and PLV analysis suggest different features are present especially in PD patients. In tPAC analysis, high frequency component (> 30 Hz) is evident in a few subjects. The low-frequency effect from EMG envelope modulation (<4 Hz) is rarely observed compared to treadmill walking. See section 5.2

and Appendix B for more details of overground locomotion. In this thesis, there may be several factors for the different results between treadmill and overground walking data. For example, data were collected from the different participant groups, measurements and data collection systems (number of study participants, sensor, sampling rate). Treadmill locomotion may take place in a controlled environment (a fixed speed) and put a limit on participant's vision and motion in comparison with overground walking.

In conclusion, our results suggest that a combination of three methods would be suitable for investigating and characterising non-stationary neuronal coupling mechanisms underlying human locomotion. Our novel approach for removal of low frequency envelope modulation component in coherence and PLV gives advantages in terms of extracting low frequency EMG envelope modulation from physiological mechanisms, and detecting the rhythmic modulation of motor unit activity. tPAC analysis is a new time-frequency method for estimating cross frequency phase-amplitude coupling in EMG signals during walking. Here, it produces results equivalent to those seen in power spectra. All three measures suggest significant differences between healthy controls and PD patients in low-beta band (12-20 Hz). These findings might be important for understanding the basic principles of human locomotion in health and disease.

Chapter 6

Conclusion and future work

6.1 Conclusion

This thesis has focused on investigating non-stationary neuronal coupling mechanisms underlying human locomotion in a lower limb muscles. EMG are recorded from two locations of the tibialis anterior (TA) muscle during human treadmill and overground walking in healthy controls and Parkinson's patients. Correlation between paired surface EMG recordings is used to look back into central nervous system to infer neural activity patterns during human locomotion.

The analysis of the data is based on a unified framework summarised in chapters 1 and chapter 4. Estimates of coherence, phase locking value (PLV), and time-resolved phase-amplitude coupling (tPAC) are performed to characterise features of the surface EMG signals during walking. These three different measures are derived from the same two-parameter family of generalized Morse wavelets, Airy wavelets ($\gamma = 3$) with β=9. To our knowledge, Airy wavelets have never been applied to these three measures in analysis of surface EMG signals during human treadmill and overground walking in health and disease. In addition, a novel technique applied to wavelet coherence and wavelet phase locking value for removal of low frequency components due to EMG envelope modulation is proposed. Details of all measures based on the generalized Morse wavelets which are studied via numerical simulation are presented in chapter 4.

Simulation results given by coherence, PLV and tPAC estimates based on generalized Morse wavelets (chapter 4) show that all measures are able to successfully detect localised correlation in the time-frequency plane. Wavelet coherence and PLV estimates give similar results for the same surrogate signals, see section 4.2 and 4.3 for more details. Wavelet

tPAC in time-frequency plane displays the time-course of cross-frequency coupling expressed in a surrogate signal, see section 4.5 for more details. The results from our novel technique, called practical coherence analysis and practical PLV analysis for removal of low frequency envelope modulation, confirm the expectation for separating physiological mechanisms from effects due to low frequency envelope modulation of surface EMG, see section 4.4 for more details. In summary, wavelet coherence, wavelet PLV and wavelet tPAC may be used to track time-localised common oscillations in non-stationary neurophysiological signals with varying time and frequency resolution. Practical coherence and practical PLV analysis for removal of low frequency envelope modulation may be used to analyse surface EMG data during treadmill and overground walking.

The results of human locomotion data analysis during treadmill walking and overground walking are presented and discussed in chapter 5. Within the healthy treadmill locomotion dataset, the main finding is that all measures are able to detect localised correlation in the time-frequency plane, and provide a clear description of the data. Wavelet coherence and PLV estimates provide information which is consistent with the study of Halliday et al. (2003) based on Fourier methods. Rhythmic modulation of motor unit activity, in alpha (8-12 Hz) and low-beta bands (12-20 Hz), are observed during early and late swing phase. Interestingly, tPAC analysis shows that not only theta oscillations ($f_P \sim 6$ Hz) are strongly coupled to alpha and low-beta rhythms ($f_A \sim$ 8-20 Hz) during late swing, but also reveals significant cross-frequency coupling between theta band ($f_P \sim 6$ Hz) and high-beta and gamma bands ($f_A \sim$ 20-45 Hz), specifically around heel contact. These frequency components (20-45 Hz) at late swing partly overlap with the frequency ranges in the study of Petersen et al. (2012), who provide evidence investigating the functional coupling between the motor cortex and TA muscles at 8-12 and 24-40 Hz in the swing phase during treadmill walking. See section 5.1 for more details of treadmill locomotion. Within the overground walking datasets, the results from the time-frequency measures appear more variable in time and frequency than for the treadmill walking data, but all measures highlight specific features in the time-frequency plane. The frequency components of motor unit correlation (8-20 Hz) during swing and early stance phases are observed in healthy controls and PD patients. However, in wavelet coherence and PLV analysis, timing where the distinct rhythmic components within 8-20 Hz frequency bands occur is different between healthy controls and PD patients. With respect to timing, wavelet coherence and PLV estimates suggest that the time gap between two regions of

strong features in PD patients is shorter than healthy controls, time gap of 200-300 ms for PD and time gap of 300-400 ms for control, with time window ranges around 400-600 ms for PD patients and around 400-700 ms for healthy controls using a time scale on time frequency plots of 0-1000 ms, with heel trigger is at 750 ms. It is interesting to note that PLV analysis of PD patients data shows more variability in time and frequency values than coherence. In tPAC analysis, dominant couplings are between theta band ($f_P \sim 5$ Hz) and the alpha and low-beta bands ($f_A \sim$ 8-20 Hz) around 300-400 ms for PD patients group while they are present around 800-900 ms for controls group. These temporal profiles might be useful to characterise walking abnormalities in patients with PD. All measures suggest that the statistically significant difference in features between healthy controls and PD patients, determined by a Wilcoxon rank-sum test, is in low-beta band (12-20 Hz). This frequency band may be both causally and quantitatively important in the motor impairment of PD (Little & Brown 2014). See section 5.2 for more details of overground locomotion.

Focusing on the effects due to amplitude modulation of surface EMG, we noticed that EMG amplitude obtained from overground data is not as strongly modulated as in treadmill data, see chapter 3 for details. The results from wavelet coherence and wavelet PLV before removal of low frequency EMG envelope modulation component during overground walking show that low frequency envelope modulation effects are weaker than treadmill walking, see section 5.2 compared to section 5.1.1 for both treadmill and overground walking. Using a novel approach for removal of low frequency EMG envelope modulation component in wavelet coherence and wavelet PLV, we found that low frequency components (<4 Hz) are removed while other features remain unchanged, as clearly seen in time-frequency coherence and PLV after removal of low frequency EMG envelope modulation component plots (chapter 5 and Appendices). These results suggest that our novel techniques give advantage in terms of extracting low frequency EMG envelope modulation component from surface EMG recordings, and detecting rhythmic modulation of motor unit activity. However, it is important to note that low frequency components ($<$ 4 Hz) are observed in PLV after removal of low frequency envelope modulation of PD patients in contrast to healthy controls. It is possible that these low frequency components may reflect different physiological mechanisms, which can be separated from the effects due to low frequency envelope modulation of surface EMG.

Three measures in this thesis have successfully been applied to three data sets in order

to identify modulations in the functional coupling of motor units during treadmill and overground walking in normal and Parkinsons disease subjects. The results have provided complementary insight into the organisation of the neural pathways involved in gait patters in health and disease.

6.2 Future work

According to the useful results obtained from the unified framework, as stated in chapter 1, and applied in chapter 5, the research presented in this thesis has raised a number of questions that could be developed for future work. This section briefly describes some interesting ideas, which are worth investigating further. These are:

- An advantage of generalized Morse wavelets is that they are a two-parameter family of exactly analytic continuous wavelets. Two parameters, β and γ, control the shape of time-frequency localisation. In this thesis, choosing γ =3 is desirable because it gives wavelets having zero symmetry in time domain and a high degree symmetry in frequency domain, a property that tends to lead to good performance (Lilly & Olhede 2009). Varying β with fixed γ controls the trade-off of time resolution against frequency resolution. It would be good to do a systematic study to address the effect of turning of parameters β and γ on a range of data.

- According to the results obtained in chapter 5, our results suggest all measures give useful information and are suitable for investigation of non-stationary neuronal coupling mechanisms underlying human locomotion. Although this thesis is constrained to EMG acquired during walking, this approach could be applied to other physiological data such as local field potential (LFP), electroencephalography (EEG) and magnetoencephalography (MEG).

- EMG recordings used in this thesis were taken from 2 sites on the tibialis anterior muscle during walking. Exploration of alternate muscle groups, for example, soleus, biceps femoris, iliopsoas and rectus femoris, would also be interesting to use in investigation of non-stationary neuronal coupling mechanisms underlying human locomotion.

- This thesis has focused on the experimental datasets of paired surface EMG signals during walking. Since walking is a stereotypically repeated action, then an EMG

signal from sensor 1 would not only correlate to EMG signal from sensor 2 within that trial or step cycle, but to any other steps measured by sensor 2. The published statistical method for PLV, called phase locking statistic (PLS), could not explained by phase locking between paired EMG signals in this thesis. We proposed the technique adapted from Aru et al. (2015) to calculate the confidence limit for PLV and tPAC. It would be interesting to adapt the test of statistical significance level of PLV or tPAC used in this thesis to other data which has the same behaviour as EMG data recorded during walking.

- Practical coherence and practical PLV for removal of low frequency EMG envelope modulation component are new techniques. In this thesis, we use the statistical significance level methods described in section 4.2.1 for coherence and described in section 4.3.1 for PLV to calculate the confidence limit. It would be interesting to construct specific statistical measures for these techniques.

- The results from practical coherence and practical PLV for removal of low frequency EMG envelope modulation show that low frequencies < 4 Hz can be separated from physiological mechanisms during walking. Thus, the use of practical coherence and PLV for removal low frequency EMG envelope modulation could be extended to inform the selection of the band of interest for f_P in tPAC analysis.

- Samiee & Baillet (2017) suggest that tPAC provides high temporal resolution, the capacity of estimating coupling strength, and low sensitivity to noise conditions obtained with the short data lengths. They suggested that the minimum length of analysis window should be set to at least one cycle of the minimum of slow frequency component (f_P^*). In addition, they claimed that increasing the window length from 2 cycles of f_P^* to 4 and 8 cycles leads to similar results. It should therefore be possible to apply tPAC to natural patterns of walking, which will involve only short segments (or small number of steps) of EMG recordings. In this thesis, tPAC analysis is calculated using averages over 100-step cycles so it is possible that lower than 100-step, for example, 20, 40, 60, or 80 steps, could be analysed. Also, it is possible that tPAC could be used to analyse EMG data from different walking speeds.

The unified framework for analysing non-stationary signals using generalized Morse wavelets has considerable potential for application to both clinical and non-clinical EMG data. The current findings have been reviewed, and suggestions for future research are

made. It is hoped that new insights into the rhythmic control of locomotion in health and disease presented in this thesis have scope for further development.

Appendix A

Results over individual subjects during treadmill walking

This section presents the results over individual subjects (EMG recordings from subjects 405k1, 406k1, 417k1, 418k1, and 419kt) during treadmill walking for all measures, including power spectra, coherence and PLV before/after removal of low frequency due to EMG envelope modulation, and tPAC analysis.

A.0.1 Healthy subjects

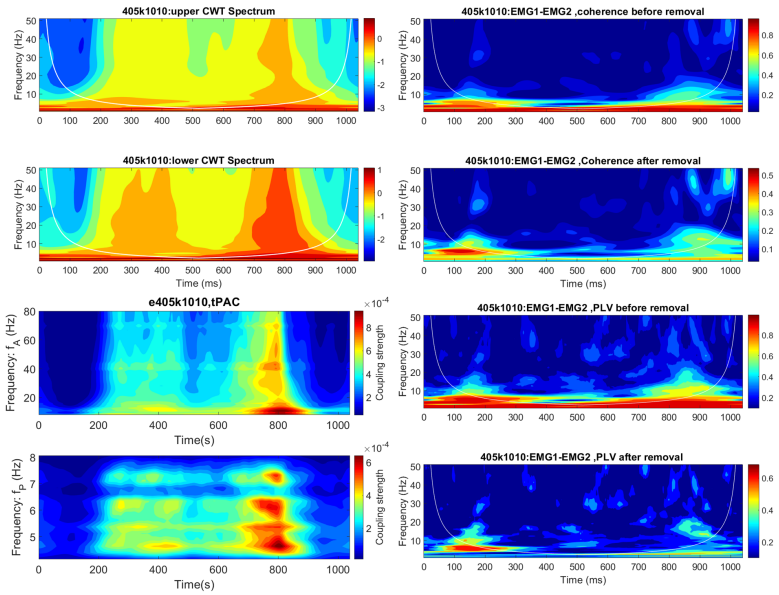

Figure A.1: Power spectra, coherence and PLV before/after removal of low frequency envelope modulation component, and tPAC for healthy subject 405k1010 during overground walking. See figure for details.

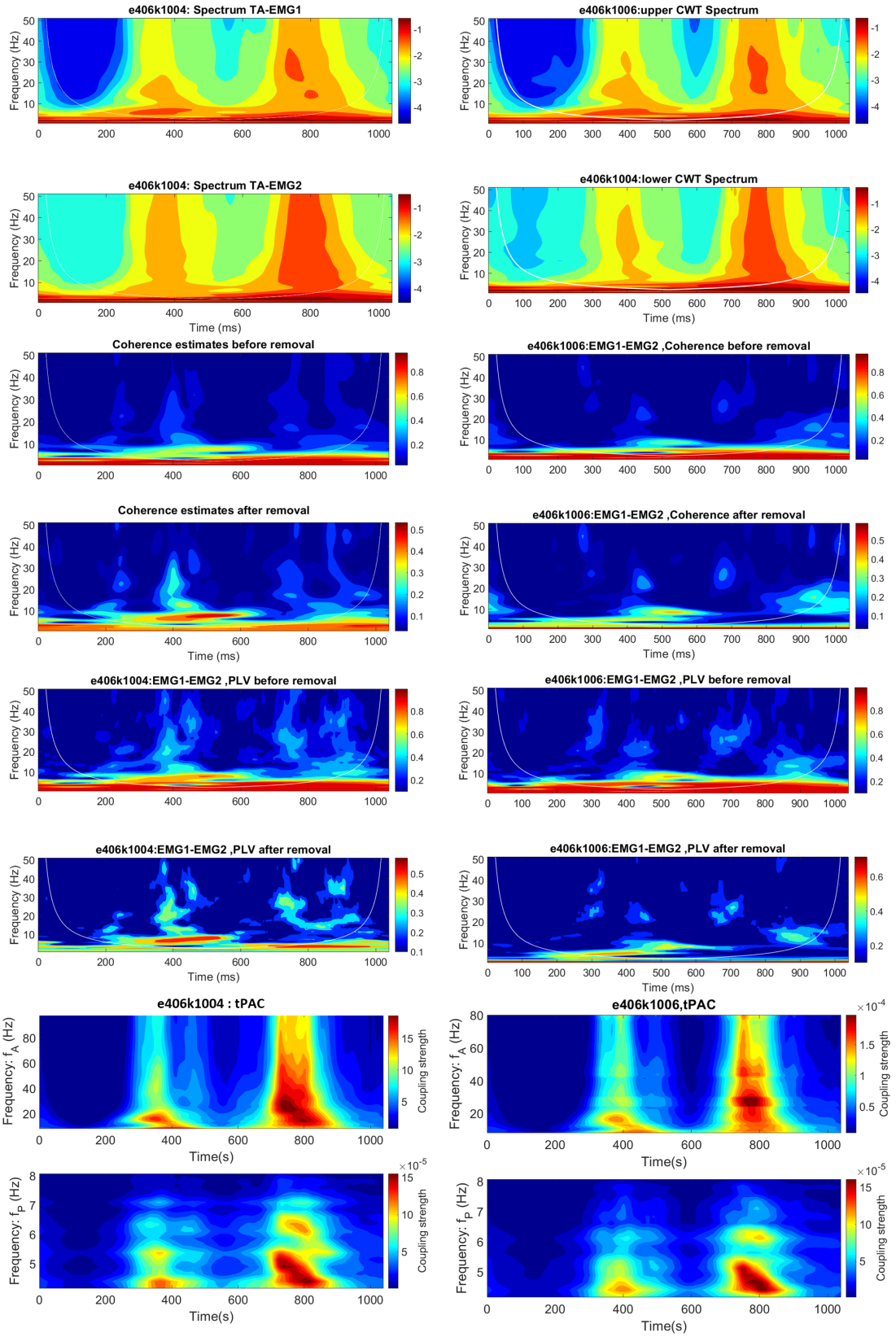

Figure A.2: Power spectra, coherence and PLV before/after removal of low frequency envelope modulation component, and tPAC for healthy subject 406k1004 (left column) and 406k1006 (right column) during overground walking. See figure for details.

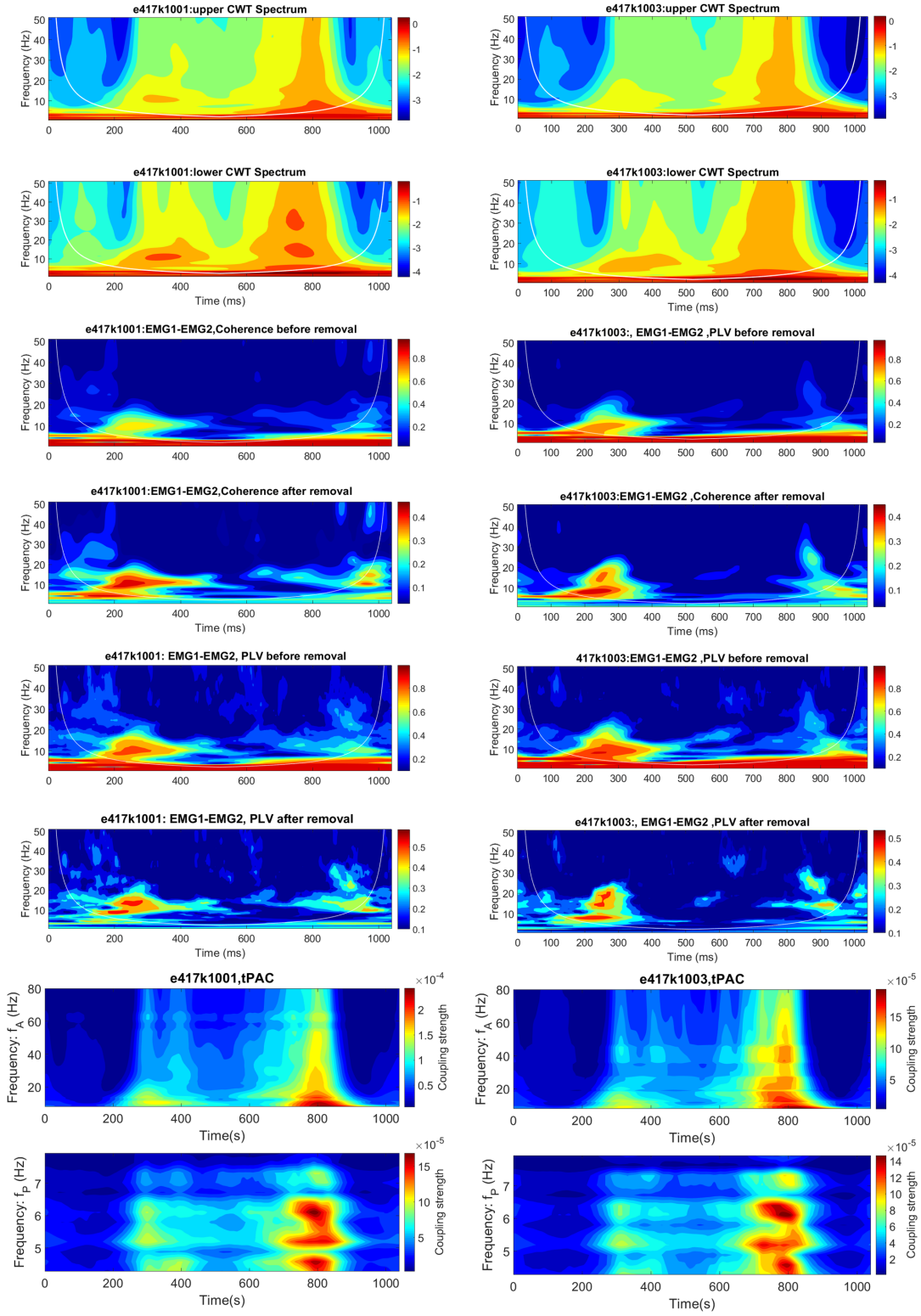

Figure A.3: Power spectra, coherence and PLV before/after removal of low frequency envelope modulation component, and tPAC for healthy subject 417k1001 (left column) and 417k1003 (right column) during overground walking. See figure for details.

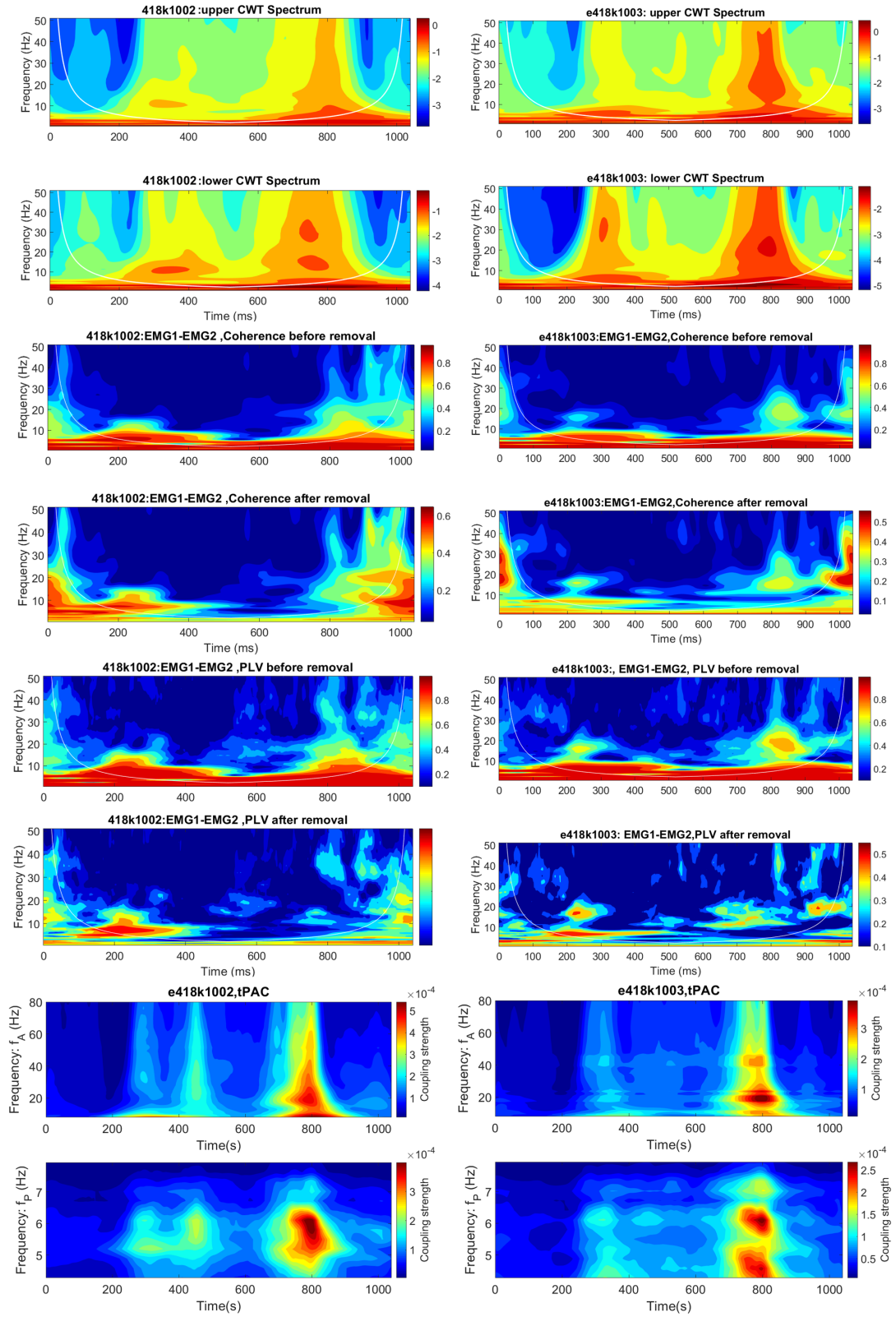

Figure A.4: Power spectra, coherence and PLV before/after removal of low frequency envelope modulation component, and tPAC for healthy subject 418k1002 (left column) and 418k1003 (right column) during overground walking. See figure for details.

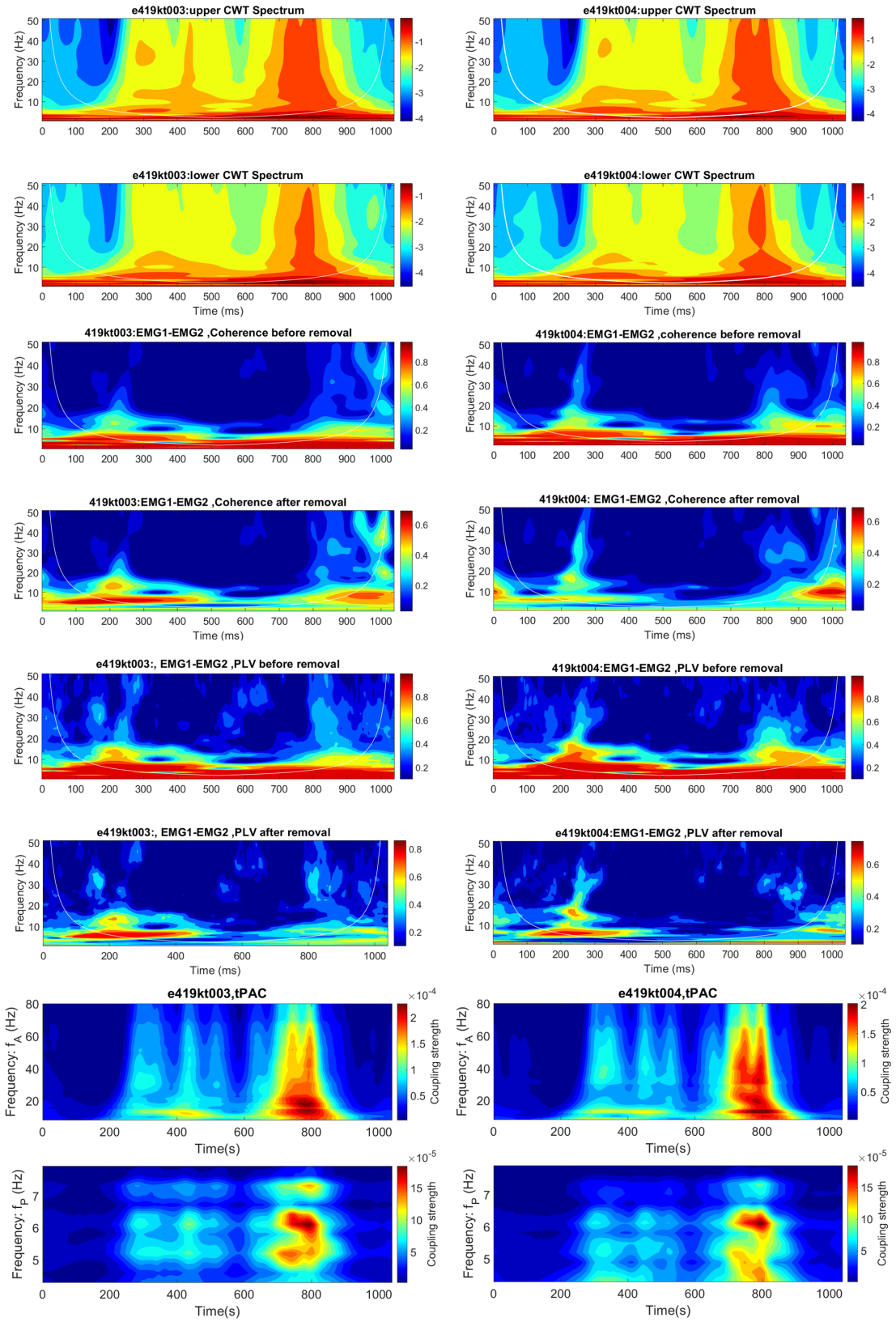

Figure A.5: Power spectra, coherence and PLV before/after removal of low frequency envelope modulation component, and tPAC for healthy subject 419kt003 (left column) and 419kt004 (right column) during overground walking. See figure for details.

Appendix B

Results over individual subjects during overground walking

This section presents the results over individual subjects during overground walking for all measures, including power spectra, coherence and PLV before/after removal of low frequency due to EMG envelope modulation, and tPAC analysis.

B.1 Healthy controls

EMG recordings from 12 healthy subjects , #6, #10, #11, #15, #16, #19, #21, #24, #25, #26, #27, and #28.

B.2 PD patients

EMG recordings from 8 PD patients, #7, #8, #12, #14, #17, #18, #20, and #23.

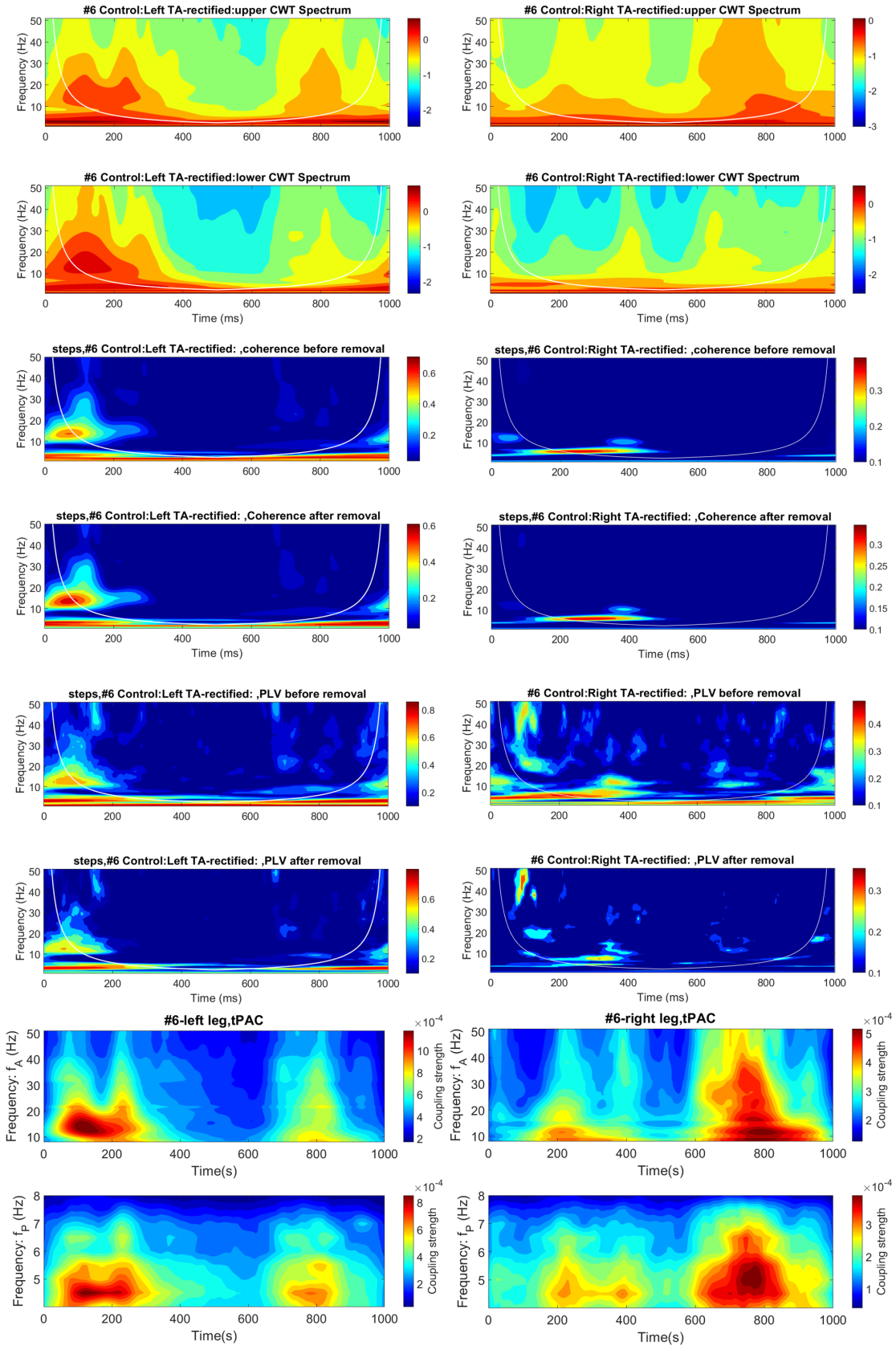

Figure B.1: Power spectra, coherence and PLV before/after removal of low frequency envelope modulation component, and tPAC for healthy subject #6 left leg (left column) and right leg (right column) during overground walking. See figure for details.

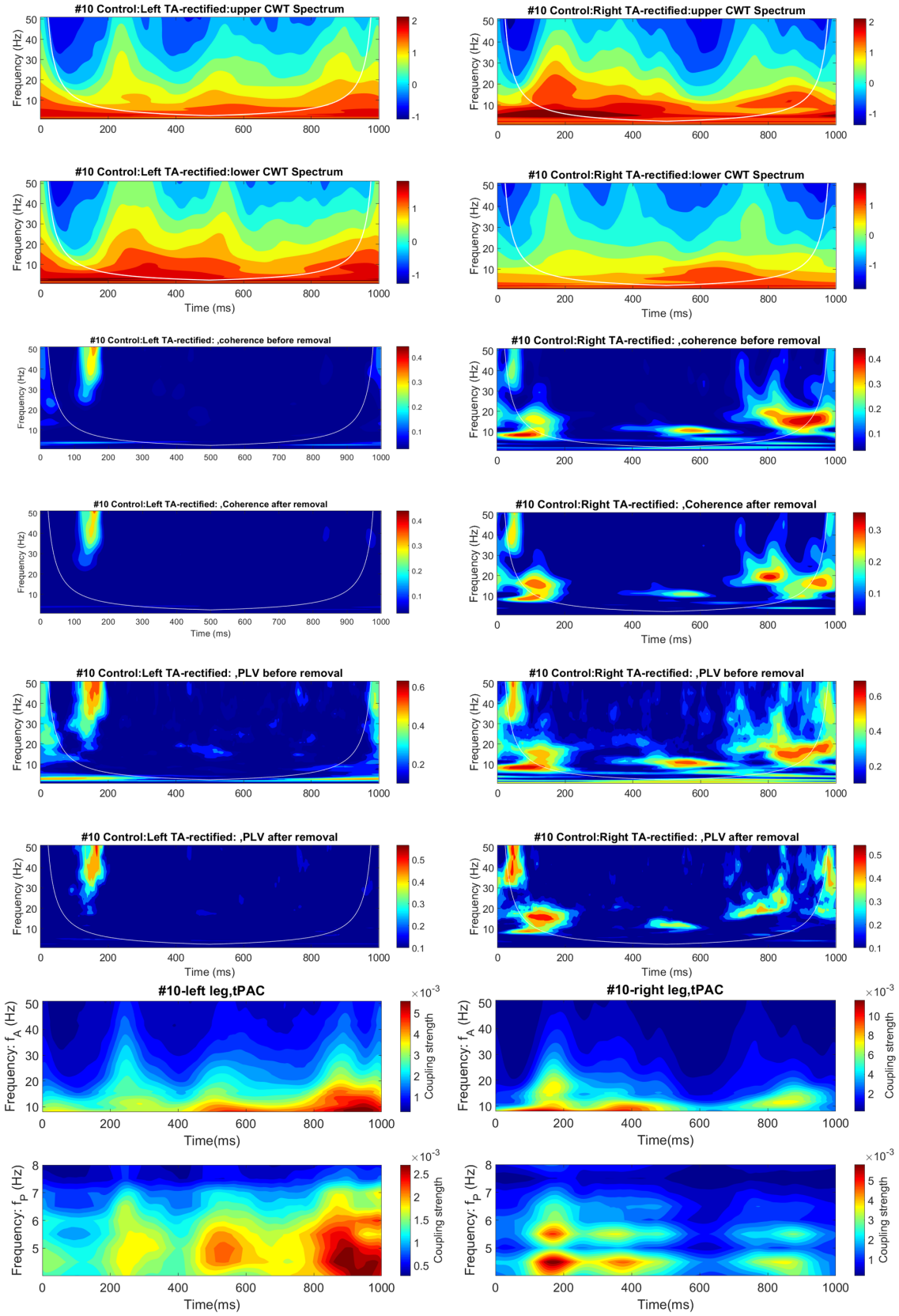

Figure B.2: Power spectra, coherence and PLV before/after removal of low frequency envelope modulation component, and tPAC for healthy subject #10 left leg (left column) and right leg (right column) during overground walking. See figure for details.

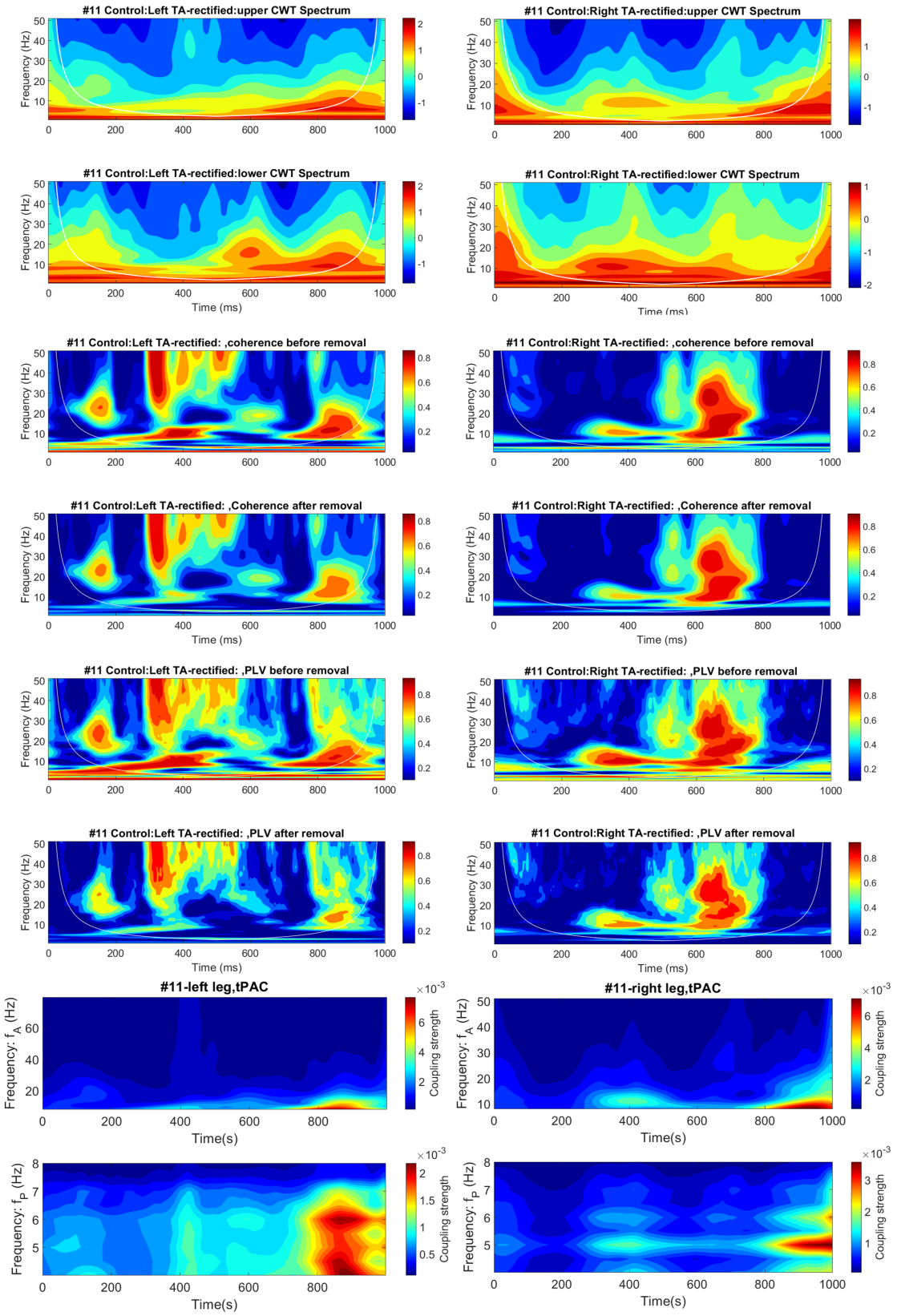

Figure B.3: Power spectra, coherence and PLV before/after removal of low frequency envelope modulation component, and tPAC for healthy subject #11 left leg (left column) and right leg (right column) during overground walking. See figure for details.

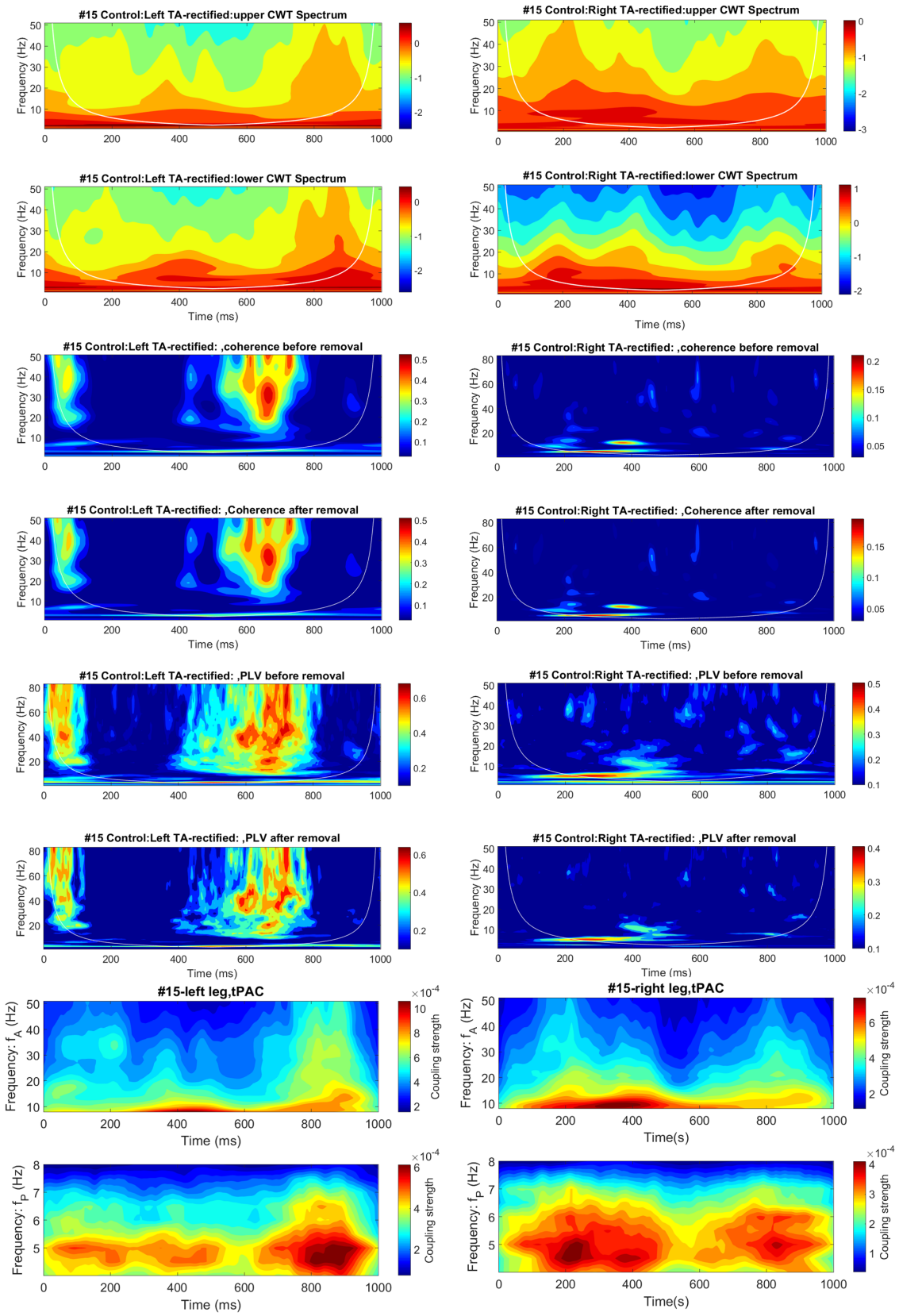

Figure B.4: Power spectra, coherence and PLV before/after removal of low frequency envelope modulation component, and tPAC for healthy subject #15 left leg (left column) and right leg (right column) during overground walking. See figure for details.

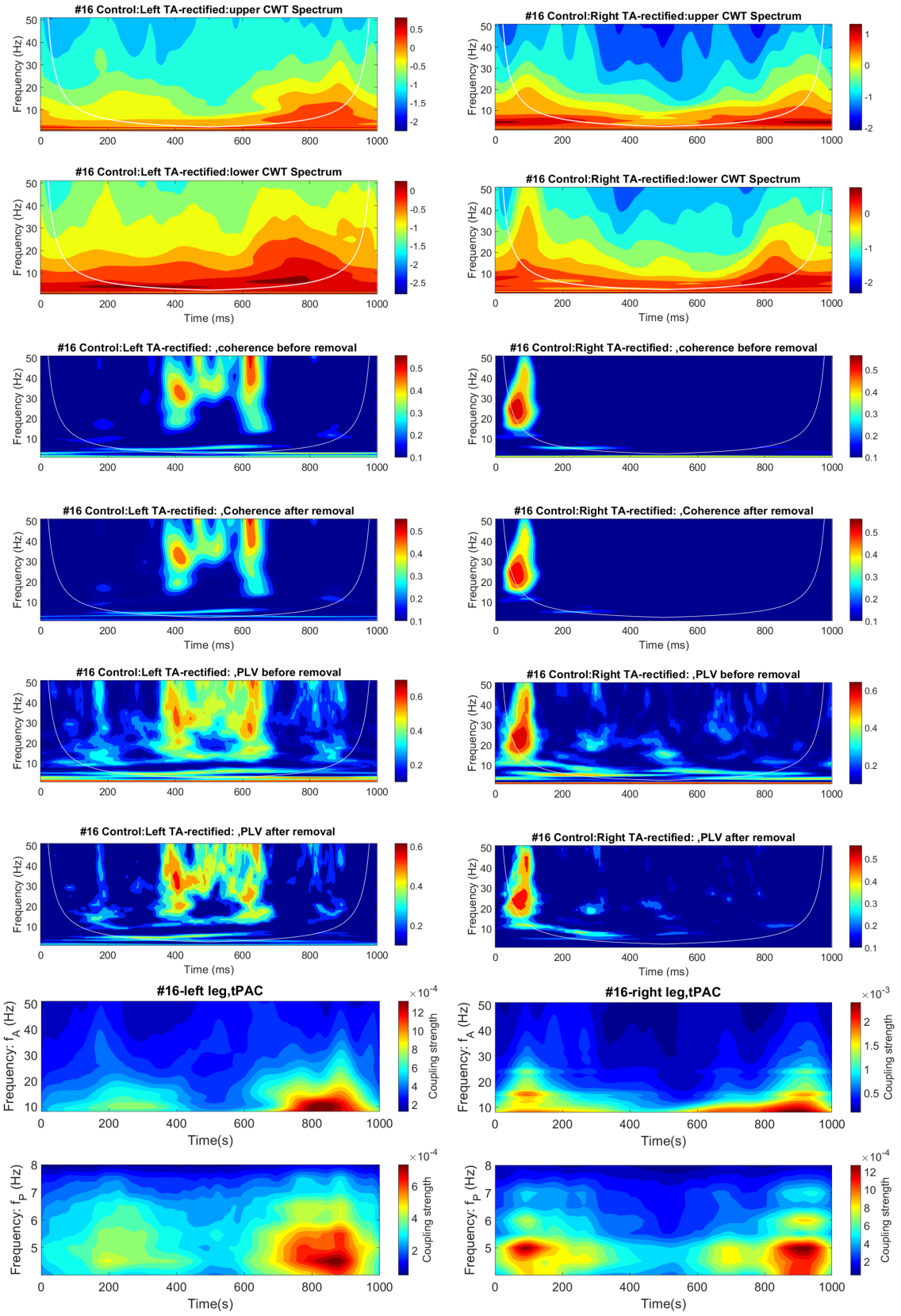

Figure B.5: Power spectra, coherence and PLV before/after removal of low frequency envelope modulation component, and tPAC for healthy subject #16 left leg (left column) and right leg (right column) during overground walking. See figure for details.

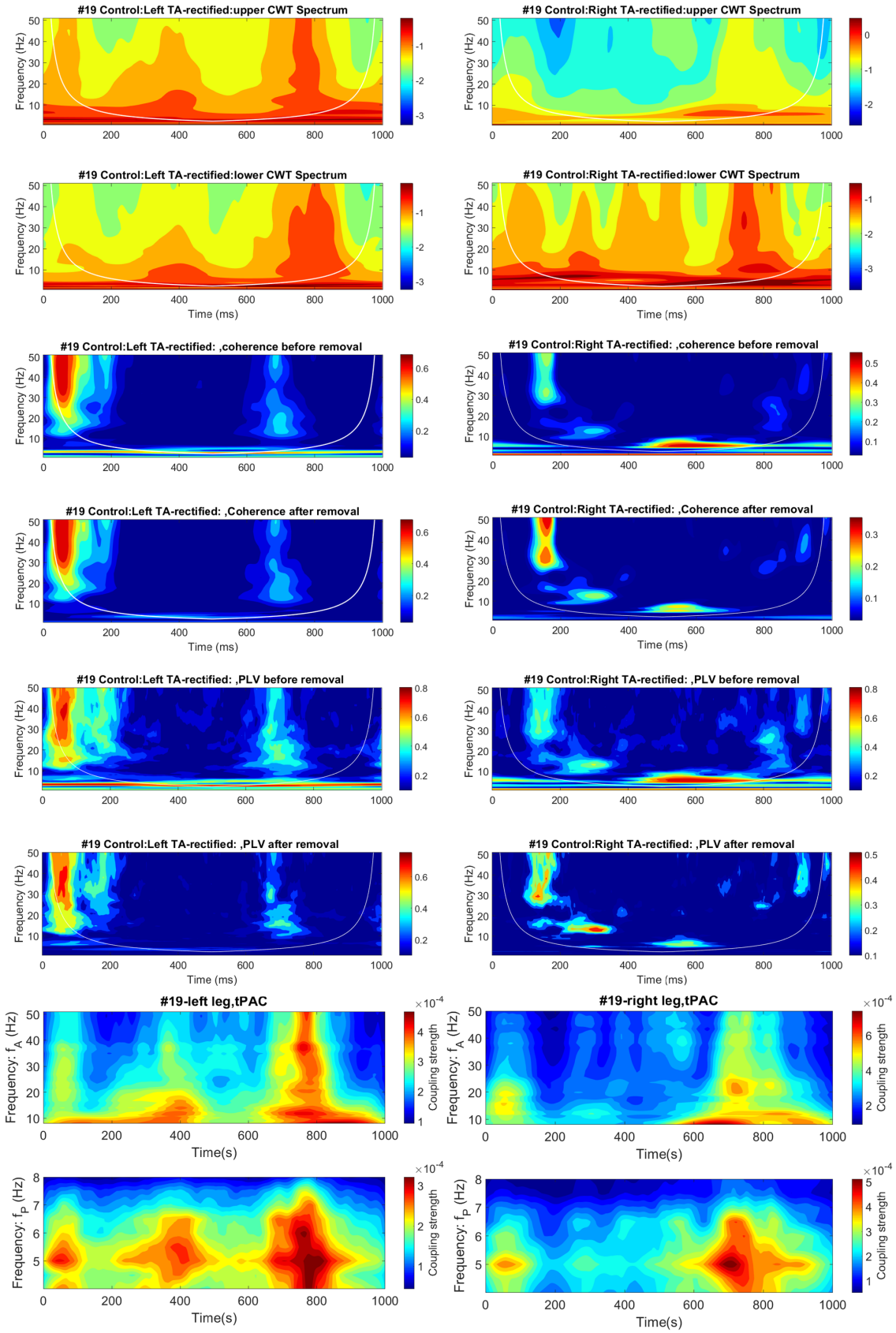

Figure B.6: Power spectra, coherence and PLV before/after removal of low frequency envelope modulation component, and tPAC for healthy subject #19 left leg (left column) and right leg (right column) during overground walking. See figure for details.

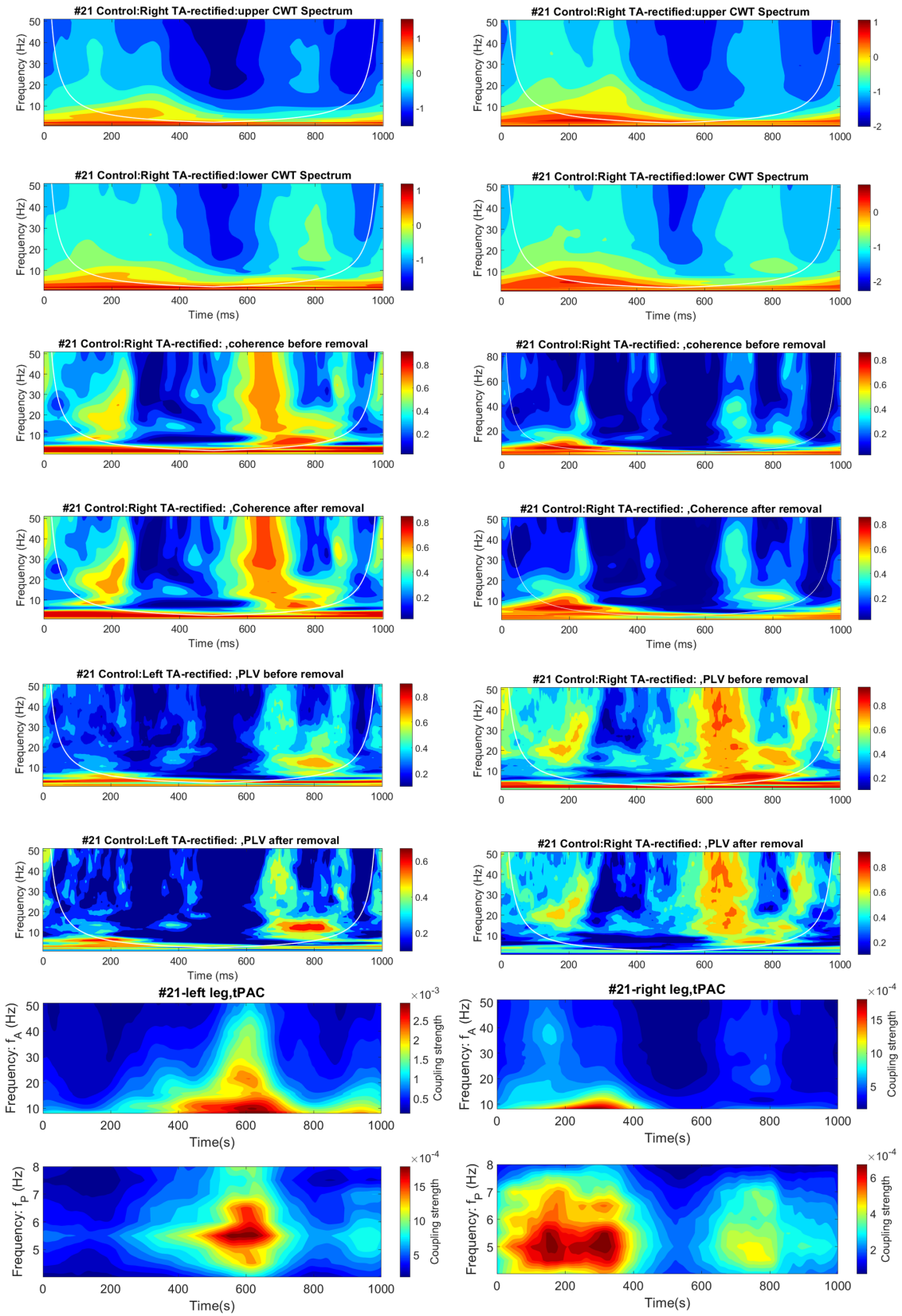

Figure B.7: Power spectra, coherence and PLV before/after removal of low frequency envelope modulation component, and tPAC for healthy subject #21 left leg (left column) and right leg (right column) during overground walking. See figure for details.

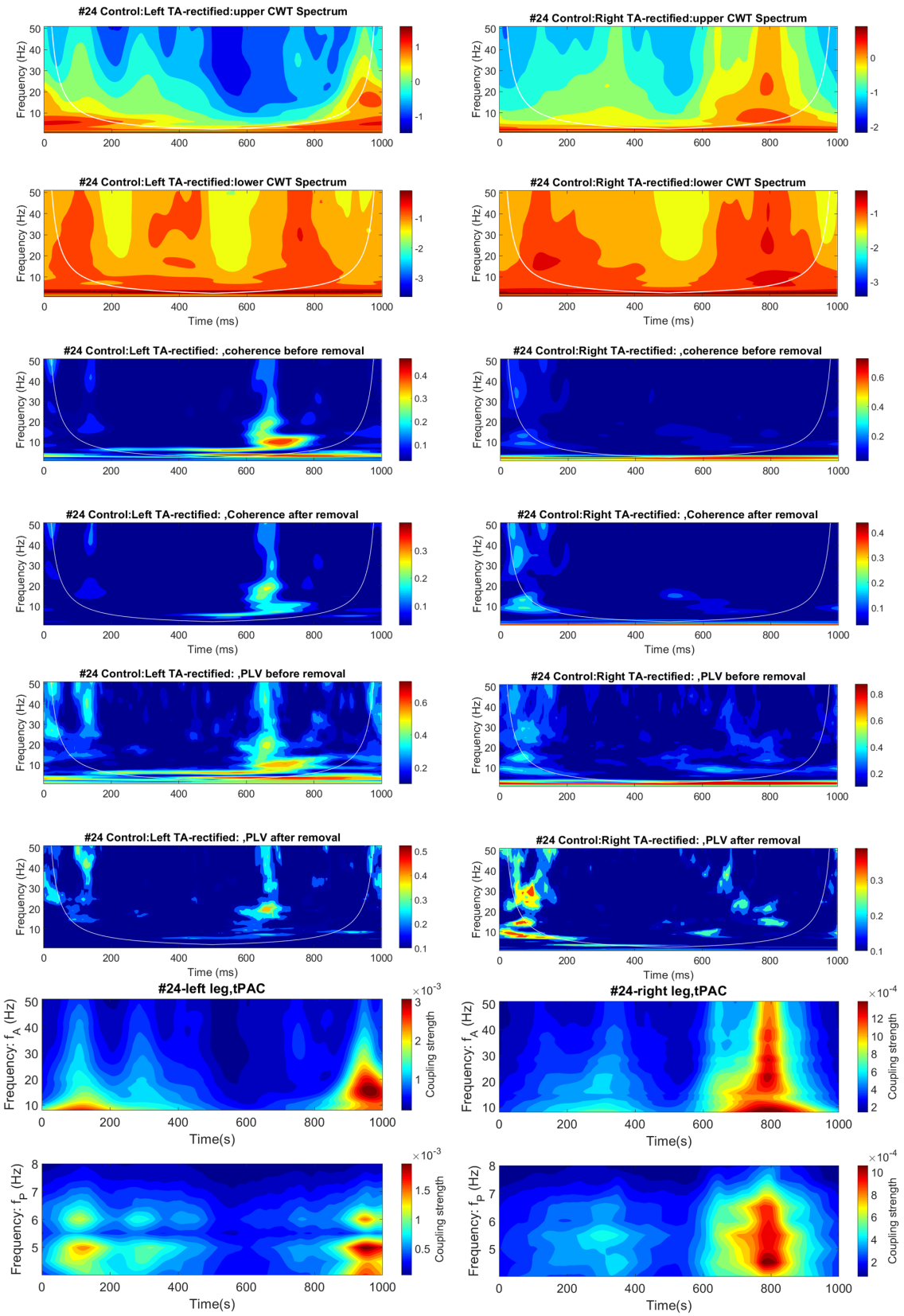

Figure B.8: Power spectra, coherence and PLV before/after removal of low frequency envelope modulation component, and tPAC for healthy subject #24 left leg (left column) and right leg (right column) during overground walking. See figure for details.

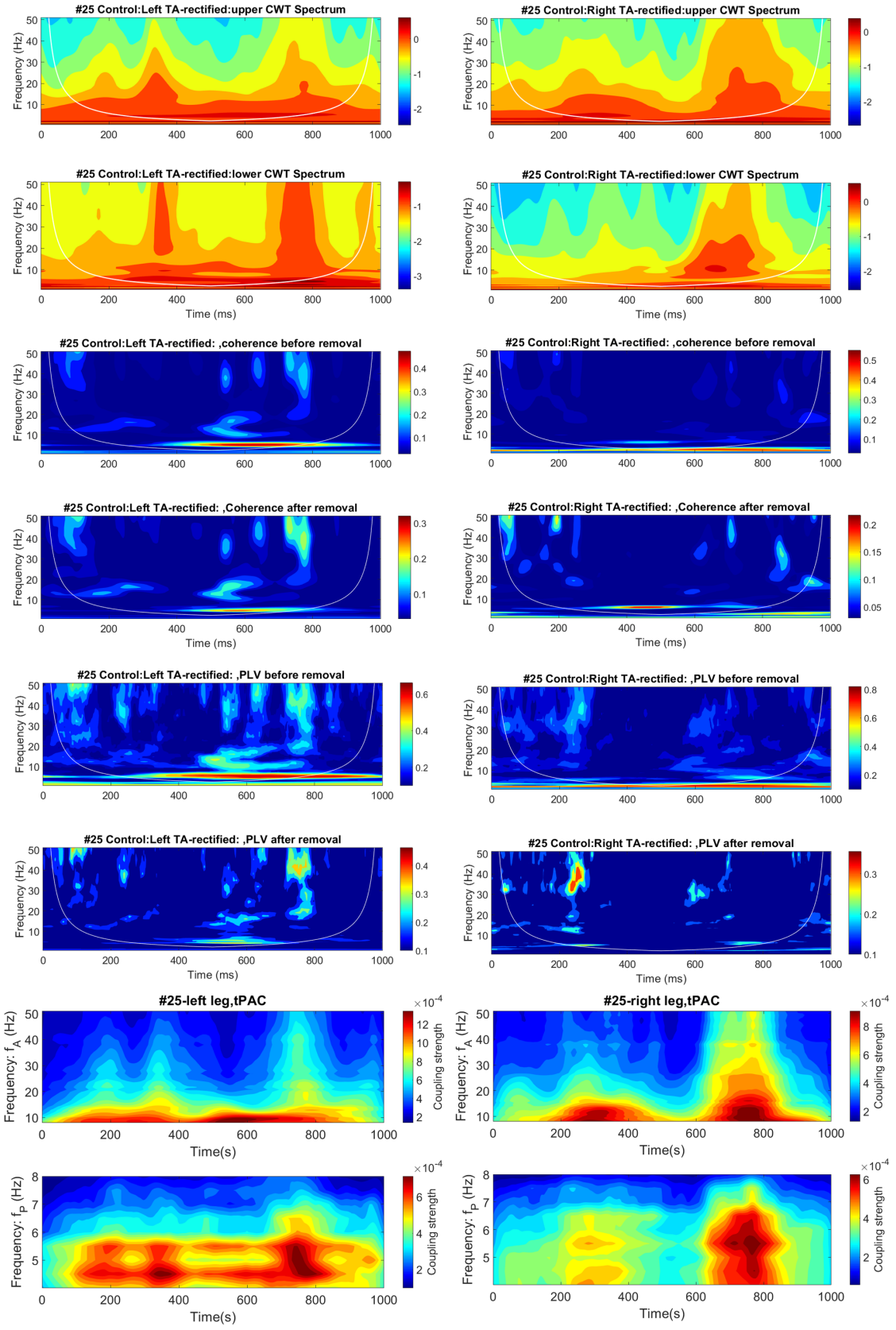

Figure B.9: Power spectra, coherence and PLV before/after removal of low frequency envelope modulation component, and tPAC for healthy subject #25 left leg (left column) and right leg (right column) during overground walking. See figure for details.

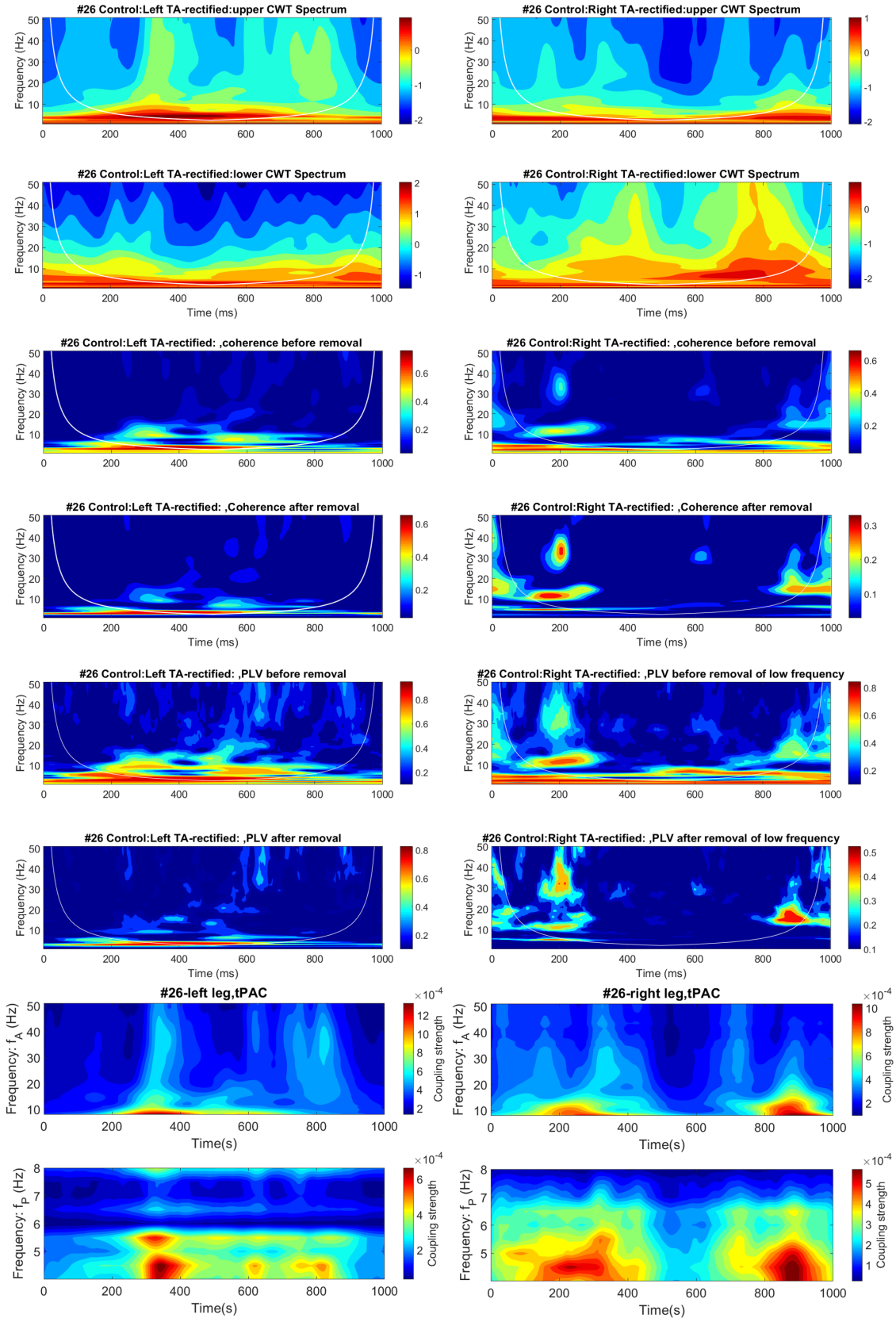

Figure B.10: Power spectra, coherence and PLV before/after removal of low frequency envelope modulation component, and tPAC for healthy subject #26 left leg (left column) and right leg (right column) during overground walking. See figure for details.

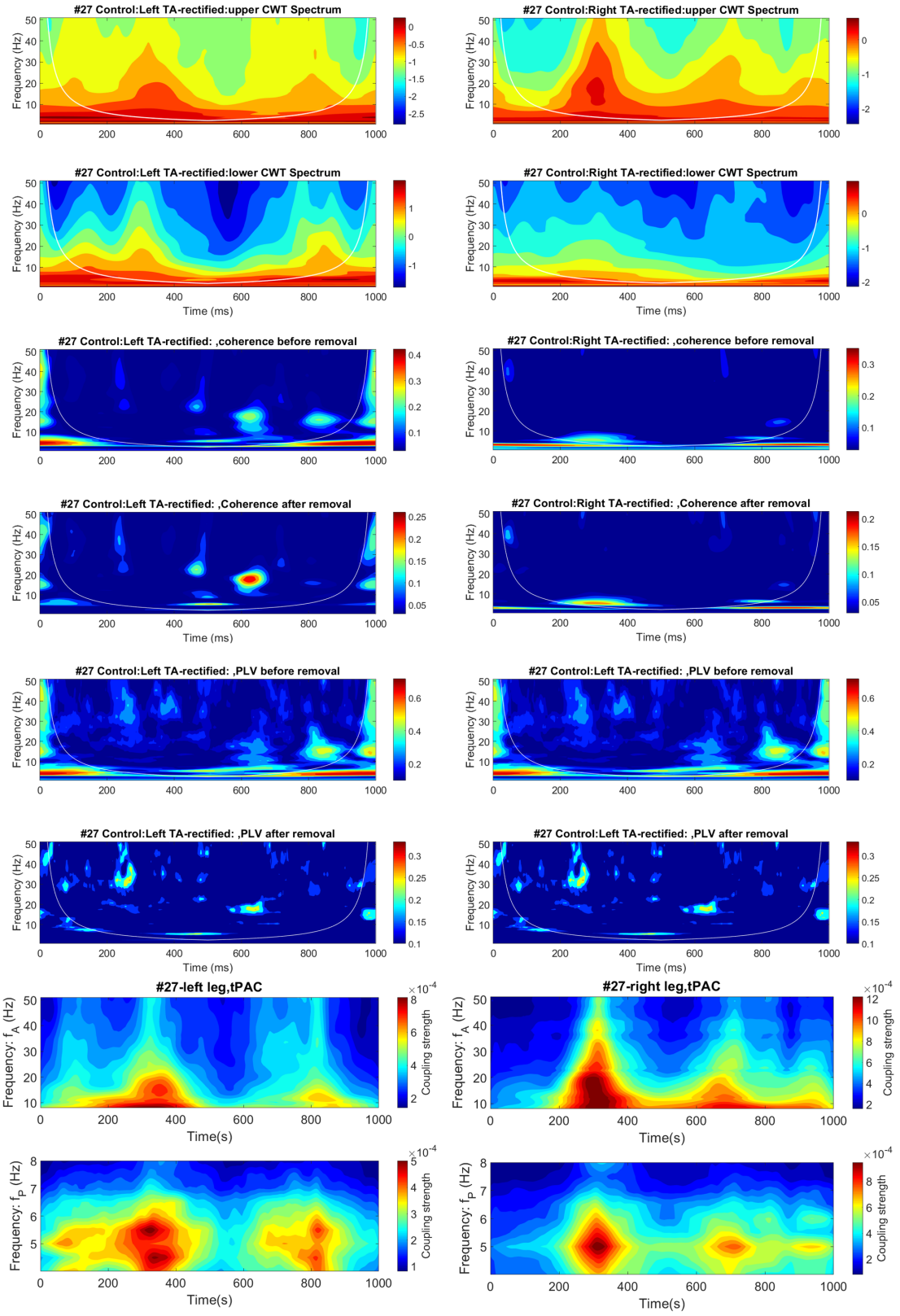

Figure B.11: Power spectra, coherence and PLV before/after removal of low frequency envelope modulation component, and tPAC for healthy subject #27 left leg (left column) and right leg (right column) during overground walking. See figure for details.

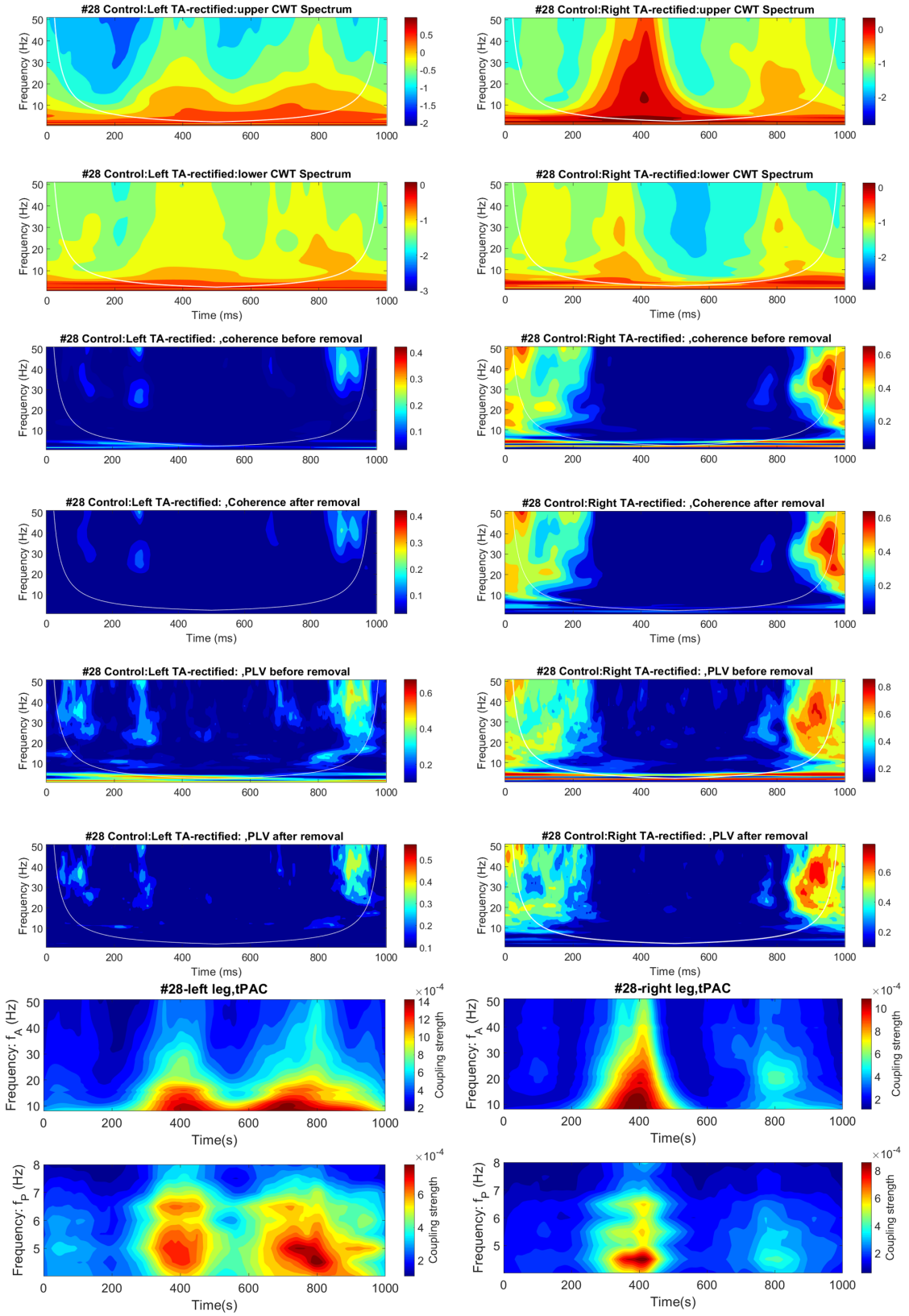

Figure B.12: Power spectra, coherence and PLV before/after removal of low frequency envelope modulation component, and tPAC for healthy subject #28 left leg (left column) and right leg (right column) during overground walking. See figure for details.

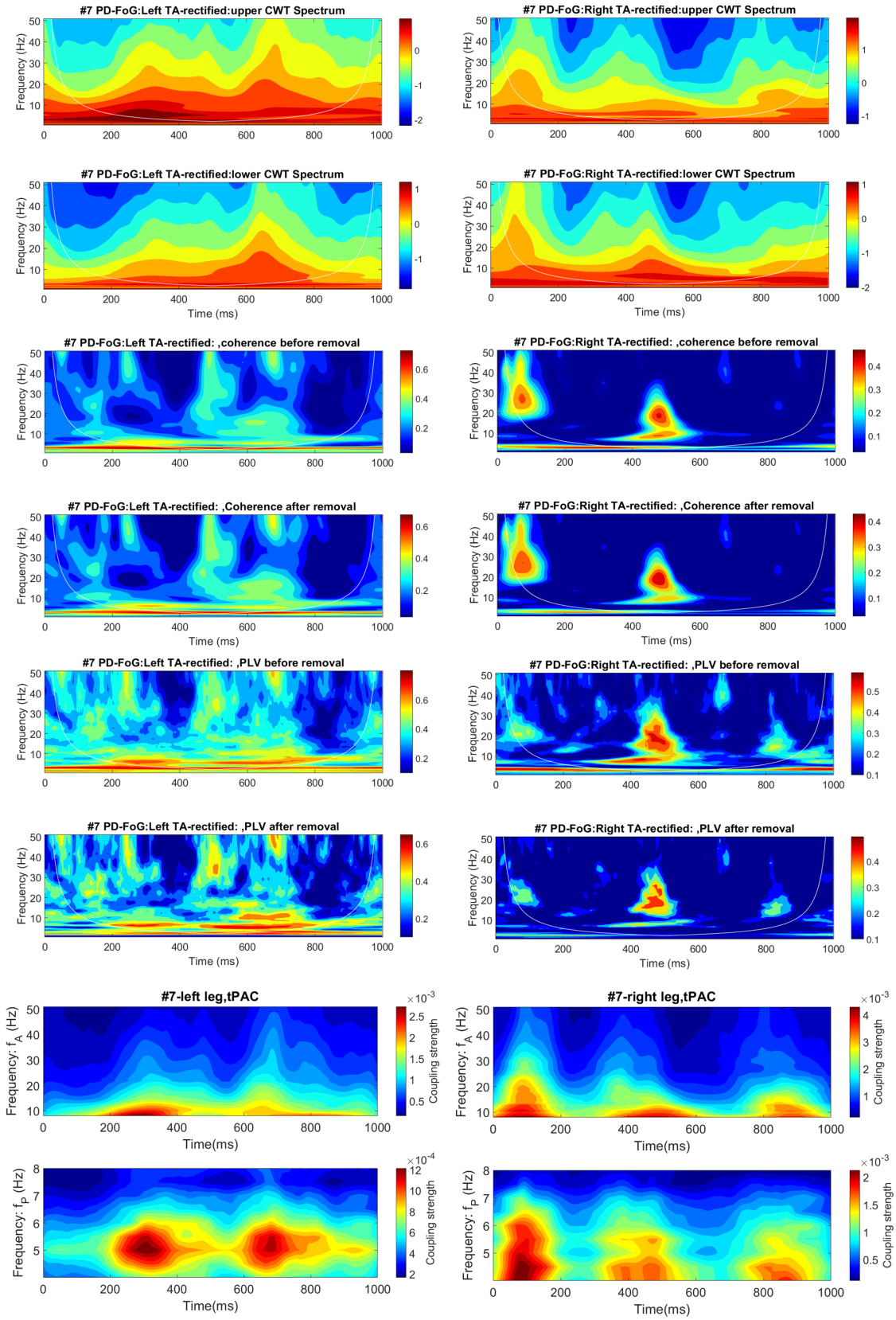

Figure B.13: Power spectra, coherence and PLV before/after removal of low frequency envelope modulation component, and tPAC for PD patient #7 left leg (left column) and right leg (right column) during overground walking. See figure for details.

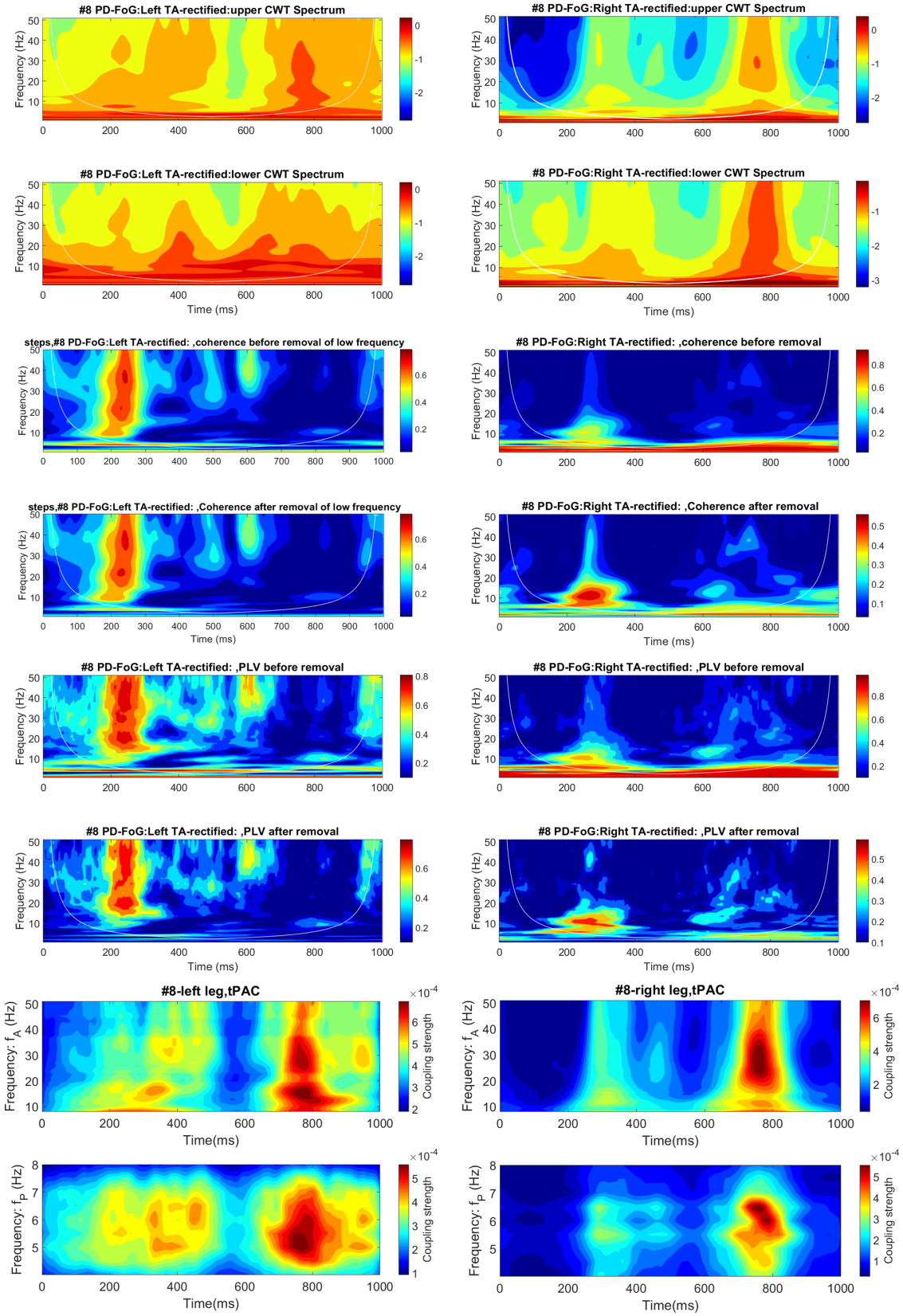

Figure B.14: Power spectra, coherence and PLV before/after removal of low frequency envelope modulation component, and tPAC for PD patient #8 left leg (left column) and right leg (right column) during overground walking. See figure for details.

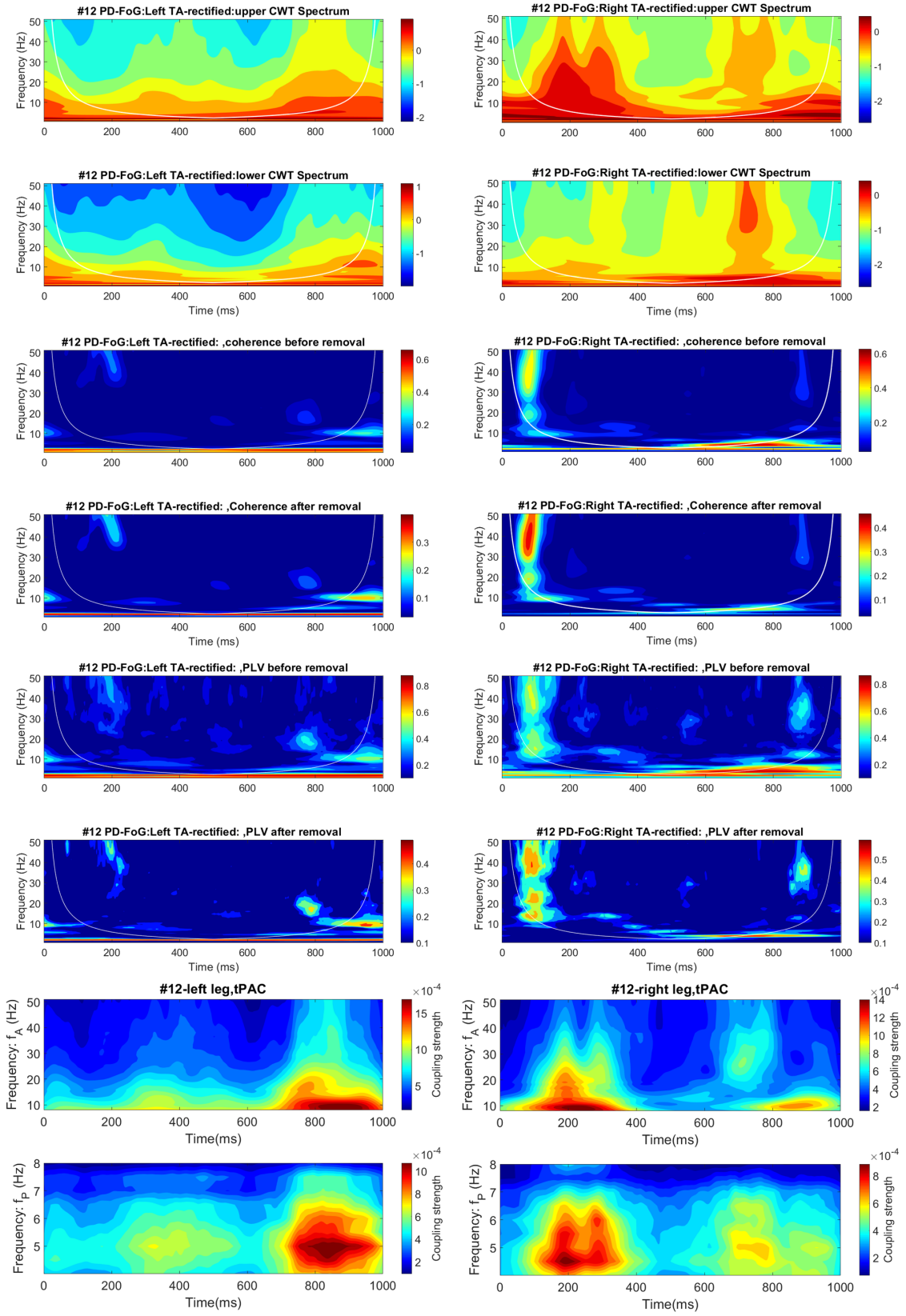

Figure B.15: Power spectra, coherence and PLV before/after removal of low frequency envelope modulation component, and tPAC for PD patient #12 left leg (left column) and right leg (right column) during overground walking. See figure for details.

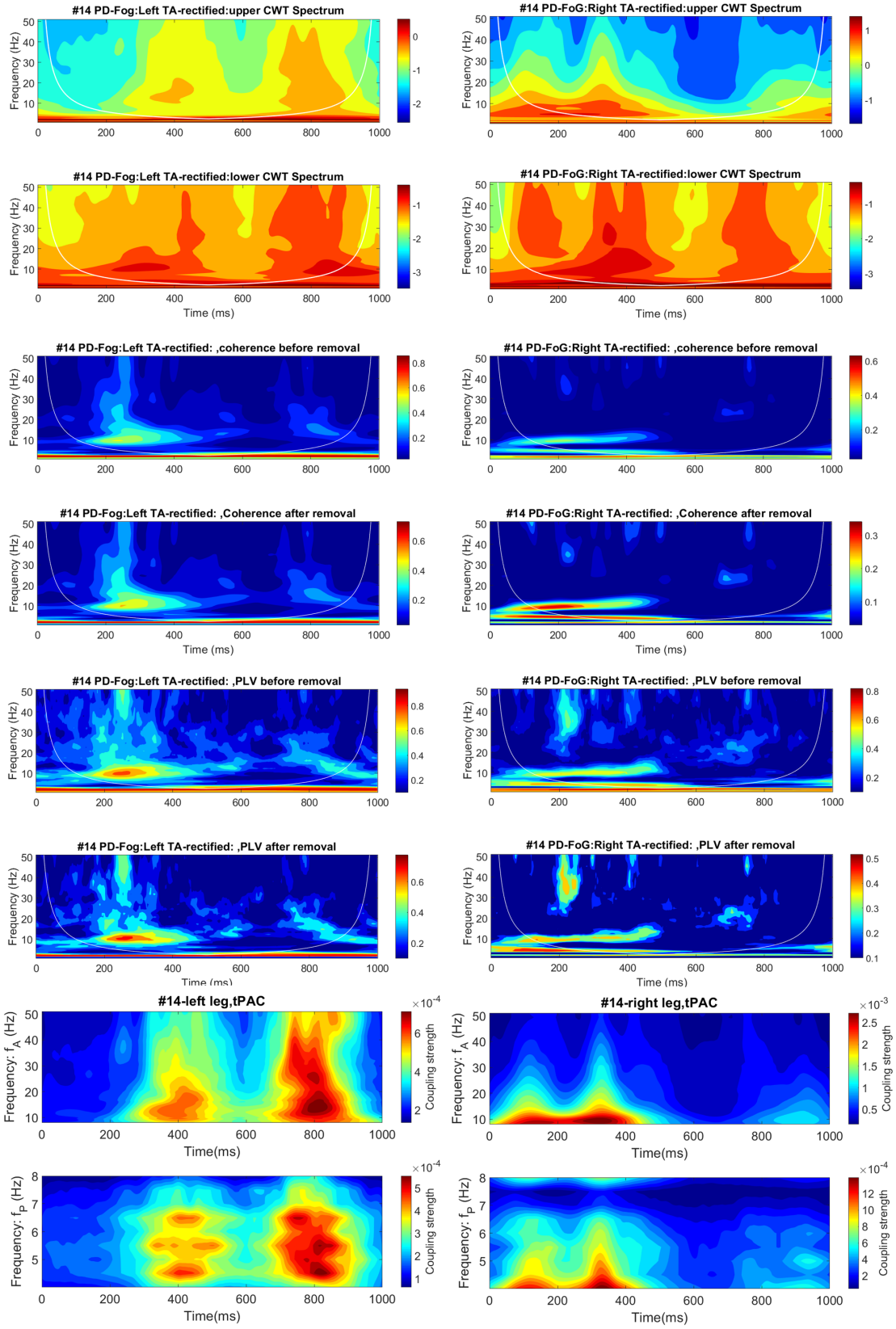

Figure B.16: Power spectra, coherence and PLV before/after removal of low frequency envelope modulation component, and tPAC for PD patient #14 left leg (left column) and right leg (right column) during overground walking. See figure for details.

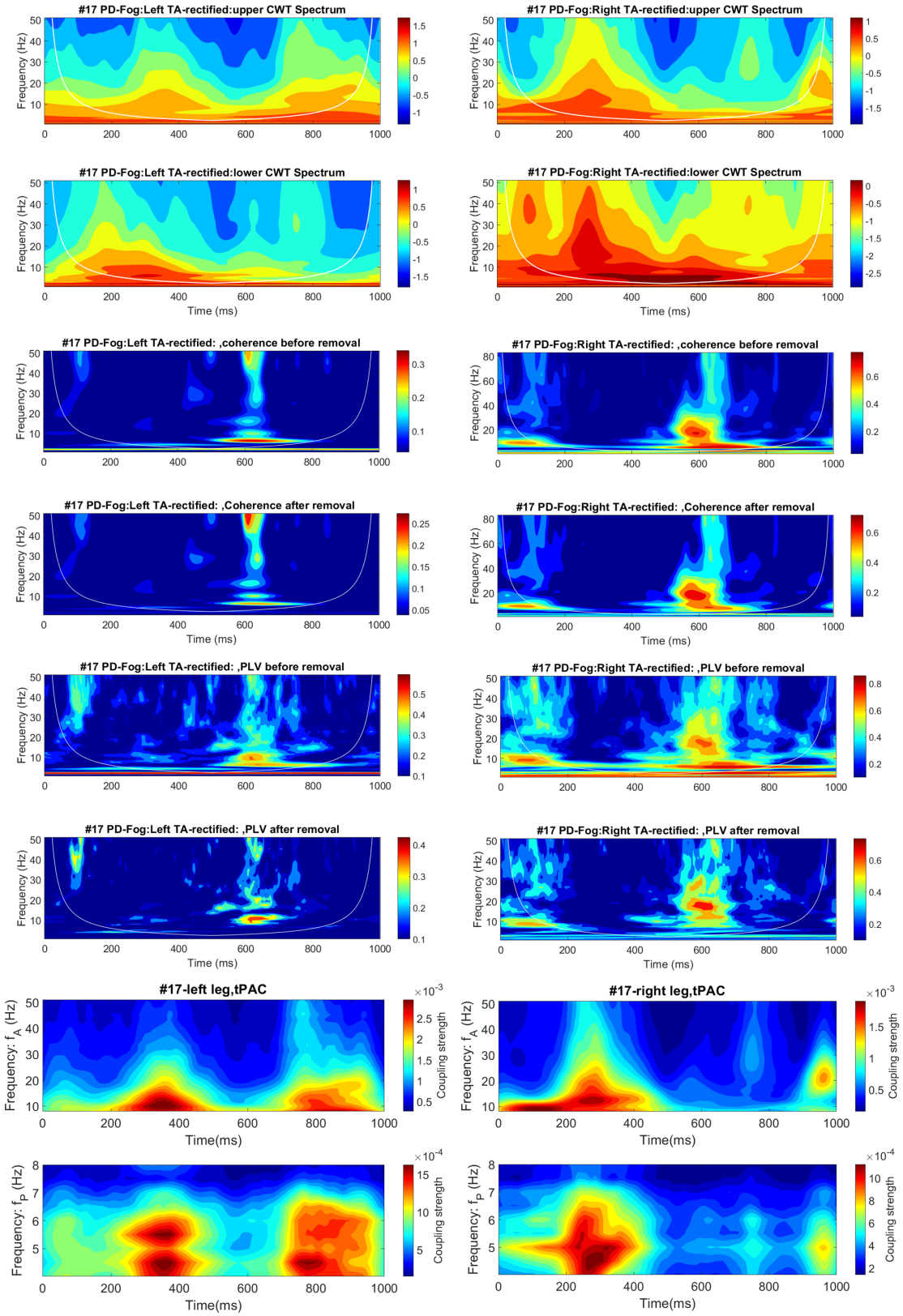

Figure B.17: Power spectra, coherence and PLV before/after removal of low frequency envelope modulation component, and tPAC for PD patient #17 left leg (left column) and right leg (right column) during overground walking. See figure for details.

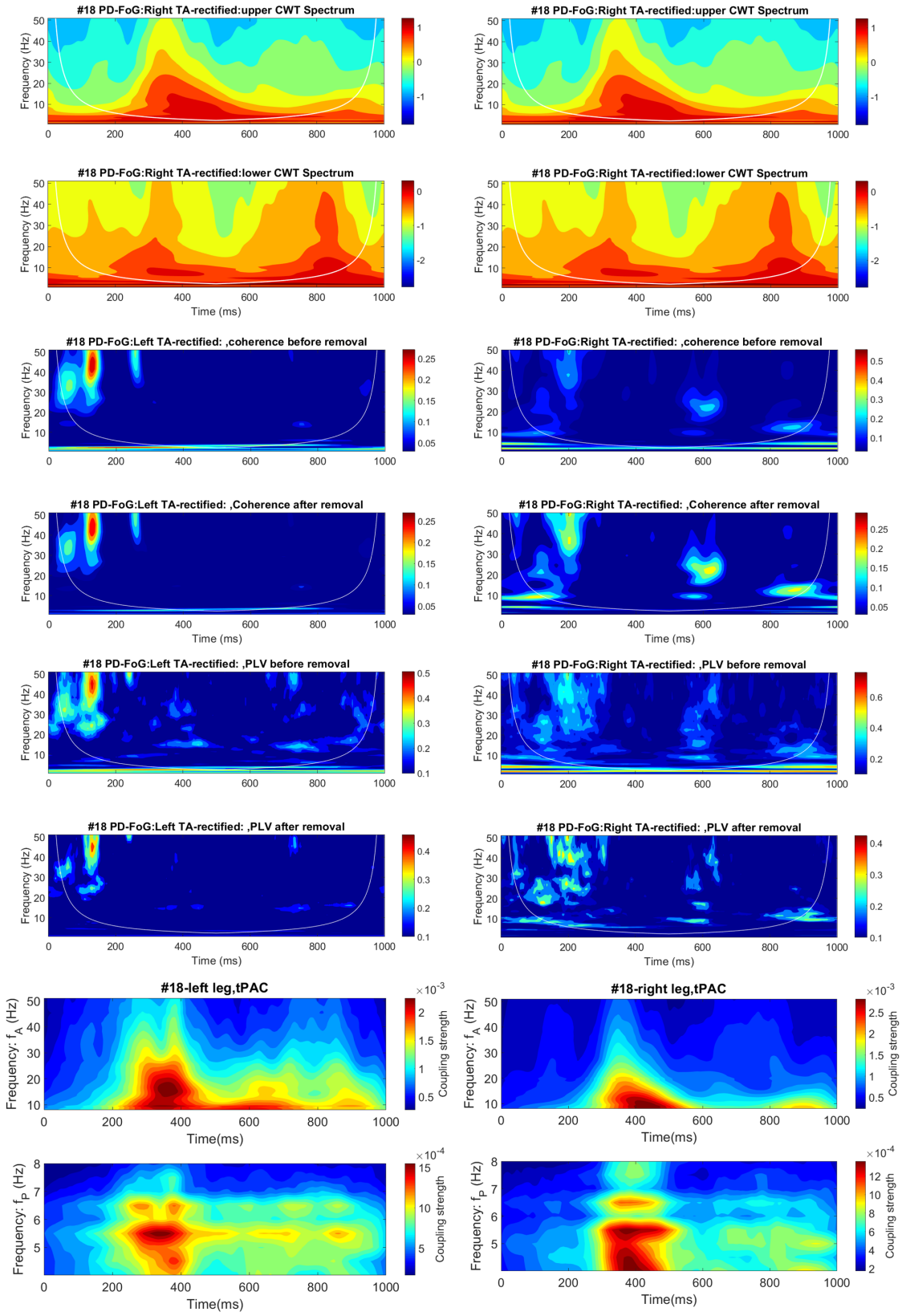

Figure B.18: Power spectra, coherence and PLV before/after removal of low frequency envelope modulation component, and tPAC for PD patient #18 left leg (left column) and right leg (right column) during overground walking. See figure for details.

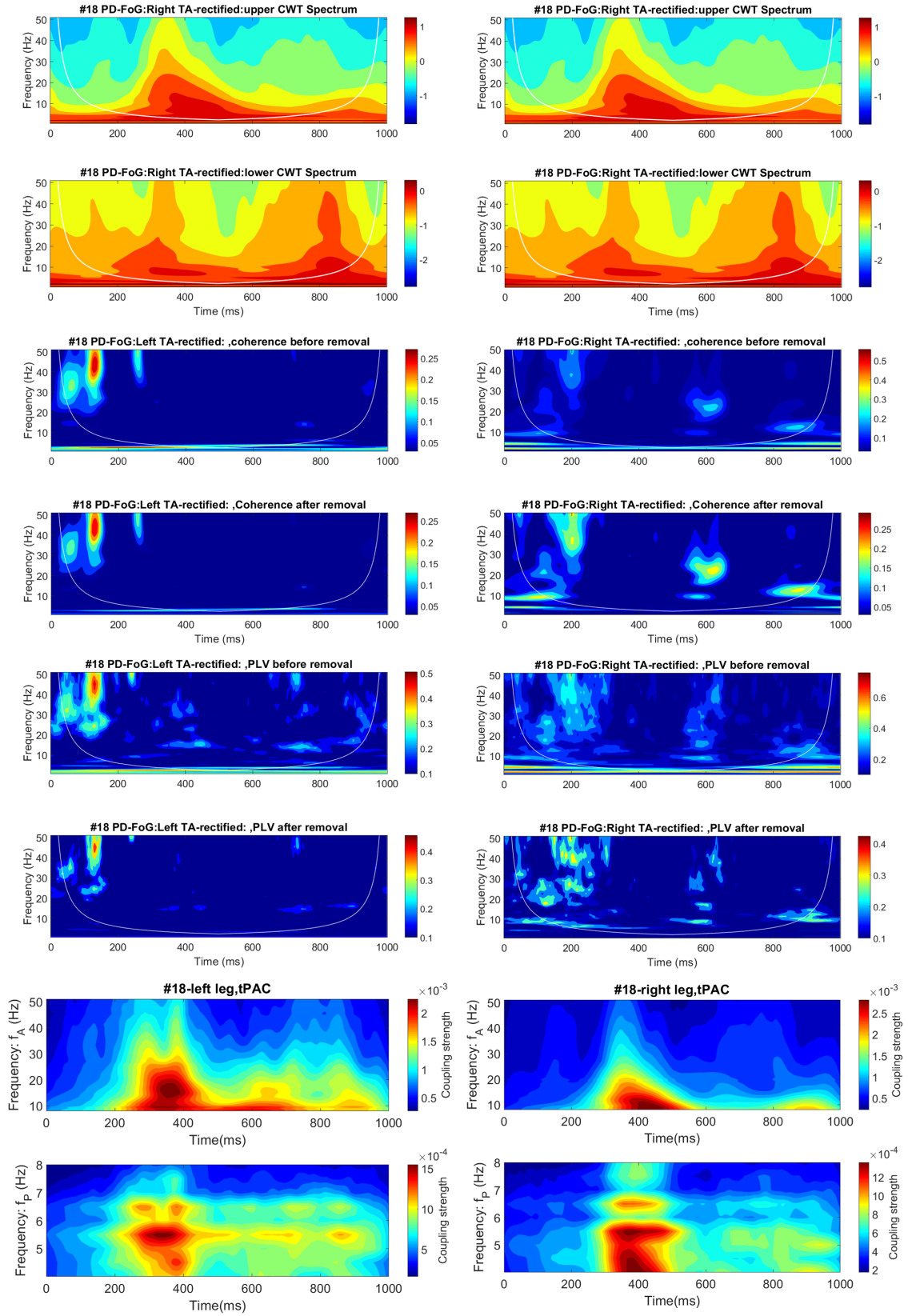

Figure B.19: Power spectra, coherence and PLV before/after removal of low frequency envelope modulation component, and tPAC for PD patient #20 left leg (left column) and right leg (right column) during overground walking. See figure for details.

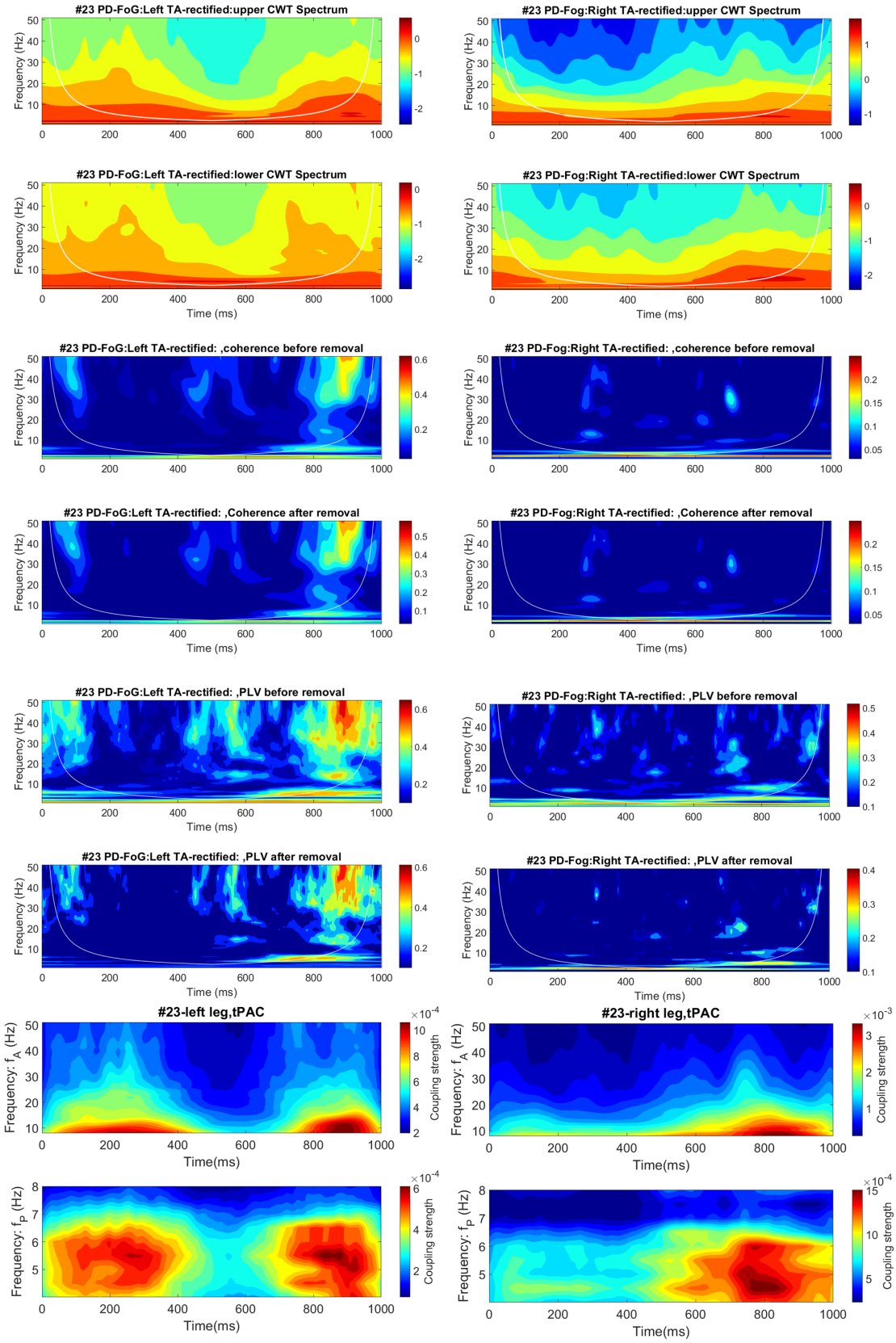

Figure B.20: Power spectra, coherence and PLV before/after removal of low frequency envelope modulation component, and tPAC for PD patient #23 left leg (left column) and right leg (right column) during overground walking. See figure for details.

References

Addison, P. (2002), *The illustrated wavelet transform handbook*, IOP Publishing Ltd.

Addison, P., Walker, J. & Guido, R. (2009), 'Time-frequency analysis of biosignals', *IEEE Engineering in Medicine and Biology Magazine* pp. 14–29.

Aguiar-Conraria, L. & Soares, M. (2014), 'The continuous wavelet transform: moving beyond uni- and bivariate analysis', *Journal of Economic Surveys* **28**(2), 344–375.

Allen, D. & Mackinnon, C. (2010), 'Time-frequency analysis of movement-related spectral power in eeg during repetitive movements: A comparison of methods', *J. Neurosci. Methods* **186**, 107–115.

Amjad, A., Halliday, D., Rosenberg, J. & Conway, B. (1997), 'An extended difference of coherence test for comparing and combining several independent coherence estimates: theory and application to the study of motor units and physiological tremor', *Journal of Neuroscience Methods* **73**, 69–79.

Arsenault, A. B., Winter, D. A. & Marteniuk, R. G. (1986), 'Treadmill versus walkway locomotion in humans: an EMG study', *Ergonomics* **29**, 665–676.

Artoni, F., Fanciullacci, C., Bertolucci, F., Panarese, A., Makeig, S., Micera, S. & Chisari, C. (2017), 'Unidirectional brain to muscle connectivity reveals motor cortex control of leg muscles during stereotyped walking', *NeuroImage* **159**, 403–416.

Aru, J., Aru, J., Priesemann, V., Wibral, M., Lana, L., Pipa, G., Singer, W. & Vicente, R. (2015), 'Untangling cross-frequency coupling in neuroscience', *Curr. Opin. Neurobiol* **31**, 51–61.

Aydore, S., Pantazis, D. & Leahy, R. (2013), 'A note on the phase locking value and its properties', *Neuroimage* **74**, 231–244.

Bach, J., Ziegler, U., Deuschl, G., Dodel, R. & Doblhammer-Reiter, G. (2011), 'Projected numbers of people with movement disorders in the years 2030 and 2050', *Movement Disorders* **26**(12), 2286–2290.

Basmajian, J. & De Luca, C. (1985), *Muscles alive-Their function revealed by electromyography*, Williams & Wilkens, Baltimore.

Baumann, C. R. (2012), 'Epidemiology, diagnosis and differential diagnosis in parkinsons disease tremor', *Parkinsonism and Related Disorders* **18**(suppl.1), S90–S92.

Berens, P. (2009), 'Circstat: A matlab toolbox for circular statistics', *Journal of Statistical Software* **31**(10), 1–21.

Beudel, M., Little, S., Pogosyan, A., Ashkan, K., Foltynie, T., Limousin, P., Zrinzo, L., Hariz, M., Bogdanovic, M., Cheeran, B., Green, A. L., Aziz, T., Thevathasan, W. & Brown, P. (2015), 'Tremor reduction by deep brain stimulation is associated with gamma power suppression in parkinson's disease', *Neuromodulation: Technology at the Neural Interface* **18**(5), 349–354.

Biundo, R., Weis, L. & Antonini, A. (2016), 'Cognitive decline in parkinsons disease: the complex picture', *npj Parkinson's Disease* **2**, 1–7.

Breakspear, M., Heitmann, S. & Daffertshofer, A. (2010), 'Generative models of cortical oscillations: neurobiological implications of the kuramoto model', *Frontiers in Human Neuroscience* **4**, 190.

Brittain, J.-S. (2007), *The non-stationary analysis and characterisation of neurological systems involved in human locomotion*, PhD's thesis, University of York.

Brittain, J.-S., Catton, C., Conway, B., Nielsen, J., Jenkinson, N. & Halliday, D. (2009), 'Optimal spectral tracking-with application to speed dependent neural modulation of tibialis anterior during human treadmill walking', *Journal of Neuroscience Methods* **177**, 334–347.

Brittain, J.-S., Halliday, D., Conway, B. & Nielsen, J. (2007), 'Single-trial multiwavelet coherence in application to neurophysiological time series', *IEEE Transactionson Biomedical Engineering* **54**(5), 854–862.

Bruns, A. (2004), 'Fourier-, hilbert- and wavelet-based signal analysis: are they really different approaches?', *J. Neurosci. Methods* **137**, 321–332.

Bruzda, J. (2011), 'Some aspects of the discrete wavelet analysis of bivariate spectra for business cycle synchronisation', *Economics* **16**, 1–46.

Campbell, R. (2017), 'File exchange-matlab central [internet]'.
URL: *http://uk.mathworks.com/matlabcentral/fileexchange/26508-notboxplot*

Canolty, R., Cadieu, C., Koepsell, K., R.T., K. & Carmena, J. (2012), 'Multivariate phase-amplitude cross-frequency coupling in neurophysiological signals', *IEEE Trans Biomed Eng* **59**(1), 8–11.

Canolty, R., Edwards, E., Dalal, S., Soltani, M., Nagarajan, S., Kirsch, H., Berger, M., Barbaro, N. & Knight, R. (2006), 'High gamma power is phase-locked to theta oscillations in human neocortex', *Science* **313**, 1626–1628.

Canolty, R. & Knight, R. (2010), 'The functional role of cross-frequency coupling', *Trends Cogn Sci* **14**(11), 506–515.

Carpinella, I., Crenna, P., Rabuffetti, M. & Ferrarin, M. (2010), 'Coordination between upper- and lower-limb movements is different during overground and treadmill walking', *Eur J Appl Physiol* **108**, 71–82.

Castermans, T. & Duvinage, M. (2013), 'Corticomuscular coherence revealed during treadmill walking: further evidence of supraspinal control in human locomotion', *The journal of Physiology* **591**(6), 1407–1408.

Castermans, T., Duvinage, M., Cheron, G. & Dutoit, T. (2014), 'About the cortical origin of the low-delta and high-gamma rhythms observed in eeg signals during treadmill walking', *Neuroscience Letters* **561**, 166–170.

D'Avanzo, C., Tarantino, V., Bisiacchi, P. & Sparacino, G. (2009), 'A wavelet methodology for eeg time-frequency analysis in a time discrimination task', *International Journal of Bioelectromagnetism* **11**(4), 185–188.

De Luca, C., Adam, A., Wotiz, R., Gilmorw, L. & Nawab, S. (2006), 'Decomposition of surface emg signals', *Journal of Neurophysiology* **96**, 1646–1657.

DeMaagd, G. & Philip, A. (2015), 'Parkinsons disease and its management: Part 1: Disease entity, risk factors, pathophysiology, clinical presentation, and diagnosis', *Pharmacy and Therapeutics* **40**(8), 504–532.

Dietz, V. (2003), 'Spinal cord pattern generators for locomotion', *Clinical Neurophysiology* **114**, 1379–1389.

Duysens, J. & de Crommert, H. W. V. (1998), 'Neural control of locomotion; part 1: The central pattern generator from cats to humans', *Gait and Posture* **7**, 131–141.

Dvorak, A. & Fenton, A. (2014), 'Toward a proper estimation of phaseamplitude coupling in neural oscillations', *J. Neurosci. Methods* **225**, 42–56.

Enders, H. & Nigg, B. M. (2016), 'Measuring human locomotor control using emg and eeg: Current knowledge, limitations and future considerations', *European Journal of Sport Science* **16**(4), 416–426.

Eusebio, A., Cagnan, H. & Brown, P. (2012), 'Does suppression of oscillatory synchronisation mediate some of the therapeutic effects of dbs in patients with parkinson's disease?', *Frontiers in Integrative Neuroscience* **6**, 47.

Farmer, S., Gibbs, J., Halliday, D., Harrison, L., James, L., Mayston, M. & Stephens, J. (2007), 'Changes in emg coherence between long and short thumb abductor muscles during human development', *J Physiol* **579**, 389–402.

Forte, J. D., Bui, B. V. & Vingrys, A. J. (2008), 'Wavelet analysis reveals dynamics of rat oscillatory potentials', *Journal of neuroscience methods* **169**, 191–290.

Fu, C., Suzuki, Y., Kiyono, K., Morasso, P. & T., N. (2014), 'An intermittent control model of flexible human gait using a stable manifold of saddle-type unstable limit cycle dynamics', *J.R. Soc. Interface* **11**(101), 1–16.

Gazzaniga, M., Ivry, R. & Mangun, G. (2002), *Cognitive neuroscience: The biology of the mind*, second edn, New York: Norton.

Gish, H. & Cochran, D. (1988), 'Generalised coherence', *International Conference on Acoustics, Speech, and Signal Processing* **5**, 2745–2748.

Gohel, B., Lim, S., Kim, M.-Y., min An, K., Kim, J.-E., Kwon, H. & Kim, K. (2016), 'Evaluation of phase-amplitude coupling in resting state magnetoencephalographic signals: Effect of surrogates and evaluation approach', *Frontiers in Computational Neuroscience* **10**, 1–13.

Grosse, P., Cassidy, M. & Brown, P. (2002), 'EEGEMG, MEGEMG and EMGEMG frequency analysis: physiological principles and clinical applications', *Clinical Neurophysiology* **113**(10), 1523–1531.

Gwin, J. T., Gramann, K., Makeig, S. & Ferris, D. P. (2011), 'Electrocortical activity is coupled to gait cycle phase during treadmill walking', *NeuroImage* **54**, 1289–1296.

Halliday, D., Conway, B., Christensen, Hansen, N., Petersen, N. & Nielsen (2003), 'Functional coupling of motor units is modulated during walking in human subjects', *J Neurophysiol* **89**, 960–968.

Halliday, D. & Farmer, S. (2010), 'On the need for rectification of surface EMG', *J Neurophysiol* **103**, 3547.

Halliday, D., Rosenberg, J., Amjad, A., Breeze, P., Conway, B. & Farmer, S. (1995), 'A framework for the analysis of mixed time series/point process data-theory and application to the study of physiological tremor, single motor unit dischatges and electromyograms', *Prog Biophy Mol Biol* **64**, 237–278.

Hassan, M., Terrien, J., Karlsson, B. & Marque, C. (2010), 'Interactions between uterine emg at different sites investigated using wavelet analysis: comparison of pregnancy and labor contraction', *EURASIP J. Adv. Signal Process* **17**, 1–9.

Hatala, R., Kane, S.-L. & Meade, M. O. (1997), 'An evidence-based approach to the clinical examination', *J Gen Intern Med* **12**(3), 1–12.

Heckman, C. & Enoka, R. M. (2004), *Physiology of the motor neuron and the motor unit*, Vol. 4 of *Handbook of Clinical Neurophysiology*, Elsevier, pp. 119–147.

Helmich, R. C., Hallett, M., Deuschl, G., Toni, I. & Bloem, B. R. (2012), 'Cerebral causes and consequences of parkinsonian resting tremor: a tale of two circuits?', *Brain* **135**, 3206–3226.

Hodgkin, A. & Huxley, A. (1952), 'A quantitative description of membrane current and its application to conduction and excitation in nerve', *J Physiol.* **117**(4), 500–544.

Hollman, J. H., Watkins, M. K., Imhoff, A. C., Braun, C. E., Akervik, K. A. & Ness, D. K. (2016), 'A comparison of variability in spatiotemporal gait parameters between treadmill and overground walking conditions', *Gait & Posture* **43**, 204–209.

Hughes, A., Daniel, S., Kilford, L. & Lees, A. (1992), 'Accuracy of clinical diagnosis of idiopathic parkinson's disease: a clinico-pathological study of 100 cases', *BMJ Publishing Group Ltd* **55**(3), 181–184.

James, L., Halliday, D., Stephens, J. & Farmer, S. (2008), 'On the development of human corticospinal oscillations: age-related changes in eeg-emg coherence and cumulant', *EUR J NEUROSCI* **27**, 3369–3379.

Kandel, E., Schwartz, J., Jessell, T., Siegelbaum, S. & Hudspeth, A. (2000), *Principles of neural science*, fourth edn, McGraw-Hill Medical.

Khademi-Kalantari, K., Rahimi, F., Hosseini, S. M., Baghban, A. A. & Jaberzadeh, S. (2017), 'Lower limb muscular activity during walking at different speeds: Over-ground versus treadmill walking: A voluntary response evaluation', *Journal of Bodywork & Movement Therapies* **21**, 605–611.

Kiehn, O. & Dougherty, K. (2013), *Neuroscience in the 21st Century: Section 1, Locomotion: circuits and physiology*, Springer New York.

Kopal, J., Vyšata, O., Burian, J., Schätz, M., Procházka, A. & Vališ, M. (2014), 'Complex continuous wavelet coherence for eeg microstates detection in insight and calm meditation', *Consciousness and Cognition* **30**, 13–23.

Lachaux, J., Lutz, A., Rudrauf, D., Cosmelli, D., Le Van Quyen, M., Martinerie, J. & Varela, F. (2002), 'Estimating the time-course of coherence between single-trial brain signals: an introduction to wavelet coherence', *Neurophysiol Clin* **32**, 157–174.

Lachaux, J., Rodriguez, E., Le van Quyen, M., Lutz, A., Martinerie, J. & Varela, F. (2000), 'Studying single-trials of phase synchronous activity in the brain', *International Journal of Bifurcation and Chaos* **10**(10), 2429–2439.

Lachaux, J., Rodriguez, E., Martinerie, J. & Varela, F. (1999), 'Measuring phase synchrony in brain signals', *Hum. Brain Mapp* **8**, 194–208.

Le Van Quyen, M. & Bragin, A. (2007), 'Analysis of dynamic brain oscillations: methodological advances', *Trends in Neurosciences* **30**(7), 365–373.

Le Van Quyen, M., Foucher, J., Lachaux, J., Rodriguez, E., Lutz, A., Martinerie, J. & Varela, F. (2001), 'Comparison of hilbert transform and wavelet methods for the analysis of neuronal synchrony', *J. Neurosci. Methods* **111**, 83–98.

Lee, S. J. & Hidler, J. (2008), 'Biomechanics of overground vs. treadmill walking in healthy individuals', *J Appl Physiol* **104**, 747–755.

Li, X., Yao, X., Fox, J. & Jefferys, J. (2004), 'Interaction dynamics of neuronal oscillations analysed using wavelet transforms', *J. Neurosci. Methods* **160**, 178–185.

Lilly, J. & Olhede, S. (2009), 'High-order properties of analytic wavelets', *IEEE Transactions on signal processing* **57**(1), 146–160.

Lilly, J. & Olhede, S. (2010), 'On the analytic wavelet transform', *IEEE Transactions on Information Theory* **56**, 4135–4156.

Lilly, J. & Olhede, S. (2012), 'Generalized morse wavelet as a superfamily of analytic wavelets', *IEEE Transactions on Signal Processing* **60**(11), 6036–6041.

Little, S. & Brown, P. (2014), 'The functional role of beta oscillations in Parkinson's disease', *Parkinsonism and Related Disorders* **20**(1), S44–S48.

Little, S., Pogosyan, A., Kuhn, A. & Brown, P. (2012), 'Beta band stability over time correlates with parkinsonian rigidity and bradykinesia', *Experimental Neurology* **236**, 383–388.

Lodha, N., Chen, Y.-T., McGuirk, T. E., Fox, E. J., Kautz, S. A., Christou, E. A. & Clark, D. J. (2017), 'EMG synchrony to assess impaired corticomotor control of locomotion after stroke', *Journal of Electromyography and Kinesiology* **37**, 35–40.

Lowet, E., Roberts, M., Bonizzi, P., Karel, J. & Weerd, P. (2016), 'Quantifying neural oscillatory synchronization: A comparison between spectral coherence and phase-locking value approaches', *PLoS one* **11**(1), 1–37.

MacKay-Lyons, M. (2002), 'Central pattern generation of locomotion: A review of the evidence', *Physical Therapy* **82**, 69–83.

Magrinelli, F., Picelli, A., Tocco, P., Federico, A., Roncari, L., Smania, N., Zanette, G. & Tamburin, S. (2016), 'Pathophysiology of motor dysfunction in parkinsons disease as the rationale for drug treatment and rehabilitation', *Parkinson's Disease* pp. 1–16.

Mahan, R. (1991), *Circular Statistical Methods: Applications in Spatial and Temporal Performance Analysis*, Georgia Univ. Dept. Psychol.

Marieb, E. (2006), *Essentials of human anatomy & physiology*, eighth edn, Pearson Education, Inc, San Francisco.

McKinley, M., O'Loughlin, V. & Bidle, T. (2015), *Anatomy & Physiology: An Integrative Approach textbook*, second edn, McGraw-Hill Education.

Mezeiová, K. & Paluš, M. (2012), 'Comparison of coherence and phase synchronization of the human sleep electroencephalogram', *Clin Neurophysiol* **123**(9), 1821–1830.

Müller, V., Mohr, B., Rosin, R., Pülvermuller, F., Müller, F. & Birbaumer, N. (1997), 'Shot-term effects of behavioral treatment on movemet initiation and postural control in parkinson's disease: A controlled clinical study', *Movement disorders* **12**(3), 306–314.

Murray, M., Spurr, G., Sepic, S., Gardner, G. & L.A., M. (1985), 'Treadmill vs floor walking: kinematics, electromyogram, and heart rate', *J Appl Physiol* **59**, 87–91.

Najmi, A. & Sadowsky, J. (1997), 'The continuous wavelet transform and variable resolution time-frequency analysis', *The Johns Hopkins APL Tech. Dig.* **18**(1), 134–140.

Nakhnikian, A., Ito, S., Dwiel, L., Grasse, L., Rebec, G., Lauridsen, L. & Beggs, J. (2016), 'A novel cross-frequency coupling detection method using the generalized morse wavelets', *J. Neurosci. Methods* **269**, 61–73.

Olhede, S. & Walden, A. (2002), 'Generalized morse wavelets', *IEEE TRANSACTIONS ON SIGNAL PROCESSING* **50**(11), 2661–2669.

Olhede, S. & Walden, A. (2003), 'Polarization phase relationships via multiple morse wavelet. i fundamentals', *Proc. Roy. Soc. Lond* **60**(11), 6036–6041.

Onslow, A., Bogacz, R. & Jones, M. (2011), 'Quantifying phase-amplitude coupling in neuronal network oscillations', *Prog Biophys Mol Biol* **105**(1-2), 49–57.

Özkurt, T. & Schnitzler, A. (2011), 'A critical note on the definition of phaseamplitude cross-frequency coupling', *Journal of Neuroscience Methods* **201**(2), 438–443.

Papegaaij, S. & Steenbrink, F. (2017), 'Clinical gait analysis:treadmill-based vs overground'.

URL: *https://static.hocoma.com/wp-content/uploads/2017/06/Motek-whitepaper-2017-05-03-SCREEN.pdf*

Penny, W., Duzel, E., Miller, K. & Ojemann, J. (2008), 'Testing for nested oscillation', *J. Neurosci. Methods* **174**(1), 50–61.

Pereda, E., Quiroga, R. & Bhattacharya, J. (2005), 'Nonlinear multivariate analysis of neurophysiological signals', *Prog Neurobiol* **77**, 1–37.

Perry, J. (1998), *The Contribution of Dynamic Electromyography to Gait Analysis: Section 2, Chapter 1, Gait Analysis in the Science of Rehabilitation*, books.google.com.

Petersen, T. H., Willerslev-Olsen, M., Conway, B. & Nielsen, J. (2012), 'The motor cortex drives the muscles during walking in human subjects', *The Journal of Physiology* **590**(Pt 10), 2443–2452.

Petersen, T., Kliim-Due, M., Farmer, S. & Nielsen, J. (2010), 'Childhood development of common drive to a human leg muscle during ankle dorsiflexion and gait', *The Journal of Physiology* **588**(22), 4387–4400.

Pittman-Polletta, B., Hsieh, W.-H., Kaur, S., Lo, M.-T. & Hu, K. (2014), 'Detecting phase-amplitude coupling with high frequency resolution using adaptive decompositions', *J. Neurosci. Methods* **226**, 15–32.

Pocock, G., Richards, C. & Richards, D. (2012), *Human physiology*, fourth edn, Oxford University Press, Oxford.

Prerau, M. J., Brown, R. E., Bianchi, M. T., Ellenbogen, J. M. & Purdon, P. L. (2017), 'Sleep neurophysiological dynamics through the lens of multitaper spectral analysis', *Physiology* **32**, 60–92.

Purves, D., Augustine, G., Fitzpatrick, D., Katz, L., LaMantia, A.-S., McNamara, J. & Williams, S. (2001), *Neuroscience*, second edn, Sunderland (MA): Sinauer Associates.

Rosenblum, M. & Kürths, J. (1998), Analysing synchronisation phenomena from bivariate data by means of the hilbert transform, *in* 'Nonlinear Analysis of Physiological data', Springer, pp. 91–99.

Rosenblum, M., Pikovsky, A., Kurths, J., Schäfer, C. & Tass, P. (2001), Chapter 9 phase synchronization: From theory to data analysis, *in* F. Moss & S. Gielen, eds, 'Neuro-Informatics and Neural Modelling', Vol. 4 of *Handbook of Biological Physics*, North-Holland, pp. 279–321.

Samiee, S. & Baillet, S. (2017), 'Time-resolved phase-amplitude coupling in neural oscillations', *NeuroImage* **159**, 270–279.

Sejdić, E., Lowry, K. A., Bellanca, J., Perera, S., Redfern, M. S. & Brach, J. S. (2016), 'Extraction of stride events from gait accelerometry during treadmill walking', *IEEE J Transl Eng Health Med.* **4**, 1–11.

Simões, C., Jensen, O., Parkkonen, L. & Hari, R. (2003), 'Phase locking between human primary and secondary somatosensory cortices', *Proceedings of the National Academy of Sciences* **100**(5), 2691–2694.

Stochl, J., Boomsma, A., Ruzicka, E., Brozova, H. & Blahus, P. (2008), 'On the structure of motor symptoms of parkinson's disease', *Movement Disorders* **23**(9), 1307–1312.

Stone, J., Carson, A. & Sharpe, M. (2005), 'Functional symptoms and signs in neurology: assessment and diagnosis', *J Neurol Neurosurg Psychiatry* **76**(Suppl I), i2–i12.

Tass, P., Rosenblum, M., Weule, J., Kurths, J., Pikovsky, A., Volkmann, J., Schnitzler, A. & Freund, H.-J. (1998), 'Detection of n:m phase locking from noisy data: Application to magnetoencephalography', *Phys. Rev. Lett.* **81**(15), 3291–3294.

Thengone, D., Gagnidze, K., Pfaff, D. & Proekt, A. (2016), 'Phase-amplitude coupling in spontaneous mouse behavior', *PLOS ONE* **11**(9), 1–19.

Torrence, C. & Compo, G. (1998), 'A practical guide to wavelet analysis', *Bulletin of the American Meteorological Society* **79**, 61–78.

Tort, A., Komorowski, R., Eichenbaum, H. & Kopell, N. (2010), 'Measuring phase-amplitude coupling between neuronal oscillation of different frequencies', *J Neurophysiol* **104**(4), 1195–1210.

Tort, A., Kramer, M., Thorn, C., Gibson, D., Kubota, Y., Graybiel, A. & Kopell, N. (2008), 'Dynamic cross-frequency couplings of local field potential oscillations in rat striatum and hippocampus during performance of a t-maze task', *PNAS* **105**(51), 20517–20522.

Trappenberg, T. (2010), *Fundamentals of computational neuroscience*, second edn, Oxford University Press, Oxford.

Tuncel, D., Dizibuyuk, A. & Kiymik, M. (2010), 'Time frequency based coherence analysis between eeg and emg activities in fatigue duration', *Journal of Medical Systems* **34**(2), 131–138.

van Asseldonk, E. H., Campfens, S. F., Verwer, S. J., van Putten, M. J. & Stegeman, D. F. (2014), 'Reliability and agreement of intramuscular coherence in tibialis anterior muscle', *PLOS ONE* **9**, 1–10.

Vaughan, C., Davis, B. & O'Connor, J. (1999), *Dynamics of human gait*, second edn, Kiboho Publishers, Cape Town, South Africa.

Vaz, A., Yaffe, R., Wittig Jr, J., Inati, S. & Zaghloul, K. (2017), 'Dual origins of measured phase-amplitude coupling reveal distinct neural mechanisms underlying episodic memory in the human cotex', *NeuroImage* **148**, 148–159.

Vickers, A. (2005), 'Parametric versus non-parametric statistics in the analysis of randomized trials with non-normally distributed data', *BMC Medical Research Methodology* **5**(35), 1–12.

Voytek, B., D'Esposito, M., Crone, N. & Knight, R. (2013), 'A method for event-related phase/amplitude coupling', *NeuroImage* **64**, 416–424.

Wacker, M. & Witte, H. (2011), 'On the stability of the n:m phase synchronization index', *IEEE Transactions on Biomedical Engineering* **58**(2), 332–338.

Wang, P. & Gao, J. (2013), 'Extraction of instantaneous frequency from seismic data via the generalized morse wavelets', *Journal of Applied Geophysics* **93**(Supplement C), 83–92.

Wang, Y.-X., Zhao, J., Da-Ke, Peng, F., Wang, Y., Yang, K., Liu, Z.-Y., Liu, F.-T., Wu, J.-J. & Wang, J. (2017), 'Associations between cognitive impairment and motor dysfunction in parkinsons disease', *Brain Behav* **7**(6), 1–7.

Warabi, T., Kato, M., Kiriyama, K., Yoshida, T. & Kobayashi, N. (2005), 'Treadmill walking and overground walking of human subjects compared by recording sole-floor reaction force', *Neuroscience Research* **53**, 343–348.

Ward, N. J., Farmer, S. F., Berthouze, L. & Halliday, D. M. (2013), 'Rectification of emg in low force contractions improves detection of motor unit coherence in the beta-frequency band', *Journal of Neurophysiology* **110**(8), 1744–1750.

Weersink, J. (2016), *Brain-body interaction during locomotion in Parkinson patients compared to controls: a combined EEG-EMG study*, Master's thesis, University Medical Center Groningen.

Woollacott, M. H., Shumway-Cook, A. & Nashner, L. M. (1986), 'Aging and posture control: Changes in sensory organization and muscular coordination', *The International Journal of Aging and Human Development* **23**(2), 97–114.

Zhan, Y., Halliday, D., Jiang, P., Liu, X. & Feng, J. (2006), 'Detecting time-dependent coherence between non-stationary electrophysiological signal-a combined statistical and time-frequency approach', *J. Neurosci. Methods* **156**, 322–332.